

DESIGN OF AN AIRCRAFT LANDING SYSTEM USING DUAL-FREQUENCY GNSS

A DISSERTATION

SUBMITTED TO THE DEPARTMENT OF AERONAUTICS AND
ASTRONAUTICS AND THE COMMITTEE ON GRADUATE STUDIES

OF STANFORD UNIVERSITY

IN PARTIAL FULFILLMENT OF THE REQUIREMENTS

FOR THE DEGREE OF

DOCTOR OF PHILOSOPHY

Hiroyuki Konno

December 2007

© Copyright 2008 Hiroyuki Konno
All Rights Reserved

I certify that I have read this dissertation and that, in my opinion, it is fully adequate in scope and quality as a dissertation for the degree of Doctor of Philosophy.

Per K. Enge
(Principal Advisor)

I certify that I have read this dissertation and that, in my opinion, it is fully adequate in scope and quality as a dissertation for the degree of Doctor of Philosophy.

Stephen M. Rock

I certify that I have read this dissertation and that, in my opinion, it is fully adequate in scope and quality as a dissertation for the degree of Doctor of Philosophy.

Samuel P. Pullen

Approved for the University Committee on Graduate Studies.

ABSTRACT

In the civil aviation community, there is a strong demand for new all-weather navigation aids to support aircraft precision approach and landing. The Local Area Augmentation System (LAAS) developed by the U.S. Federal Aviation Administration (FAA) is one such navigation aid that uses the Global Positioning System (GPS) as a means to estimate aircraft locations. As a safety-of-life system, LAAS is required to provide very high levels of accuracy, integrity, continuity, and availability. In particular, the integrity requirement of one undetected navigation failure in a billion approaches has been the most critical challenge for realizing and certifying this system. Tremendous efforts have been devoted to develop methods to guarantee integrity in the presence of various potential anomalies that might threaten LAAS-aided landing. Currently, almost all these risks are sufficiently mitigated by existing integrity methods. One issue that remains is the risk due to ionosphere anomalies. The central focus of this research is to create and evaluate a method that fully mitigates the safety risk due to ionosphere anomalies.

To defend against ionosphere anomalies, this dissertation introduces novel integrity algorithms that take advantage of GPS modernization. Currently, GPS is undergoing major changes to enhance civil and military user capabilities, and these improvements include adding new GPS civil signals. The frequency diversity obtained from these additional signals makes possible multiple-frequency techniques, among which this research focuses on two types of dual-frequency carrier-smoothing methods: Divergence-Free Smoothing, and Ionosphere-Free Smoothing. Using combinations of these two smoothing methods, this research designs integrity algorithms for ionosphere

anomalies that satisfy the integrity requirements for Category II and III precision approach.

The first algorithm introduced in this dissertation is based on Ionosphere-Free Smoothing. Simulations show that this algorithm can only obtain 96% to 99.9% availability at best over a broad region of Conterminous United States (CONUS). However, a key benefit of this algorithm is that the resulting availability is not a function of the ionosphere condition. The second algorithm, in contrast, is based on Divergence-Free Smoothing. Simulations show that this algorithm will achieve more than 99.9% availability over more than 70% of CONUS under nominal ionosphere conditions. However, it has the potential to lose availability under severe ionosphere conditions. Taking advantage of these two algorithms, this research introduces a LAAS system architecture that implements both Ionosphere-Free Smoothing and Divergence-Free Smoothing and switches between them based on the best estimate of the current ionosphere state obtained by an ionosphere monitor that is also designed in this research. With this “hybrid” architecture, Category III LAAS can achieve more than 99.9% availability over more than 70% of CONUS under nominal ionosphere conditions and more than 96% availability over 100% of CONUS under severe ionosphere conditions while meeting all integrity requirements.

ACKNOWLEDGEMENTS

I would like to thank my adviser, Professor Per Enge, for his intellectual guidance, advice, and support throughout the course of my doctoral program. He gave me the freedom to pursue my own course of research and shared my enthusiasm for this research. His technical insight, leadership, and humor made the Stanford GPS Laboratory an ideal place to pursue GPS related research, one in which I could develop my skills as a GPS engineer, a writer, and a critical thinker through the rich learning experience in this laboratory.

I would also like to thank Professor Stephen Rock for his review of this dissertation. His accurate and constructive comments for this research have improved it. In addition, his enlightening control class is the one that I enjoyed the most at Stanford. I also extend my gratitude to the other members of my thesis defense committee, Professor Claire Tomlin and Professor Umran Inan, for their perceptive commentary.

Dr. Sam Pullen, I do not have any words that fully express my gratitude to him. He is not only my mentor but also a good friend. He offered me a deep and wide collection of knowledge about GPS and LAAS. He was always within reach and unselfish with his time when I needed his help. Much of the work in this dissertation would have been impossible without the valuable input from him.

I am also grateful for the help and friendship of former and current members in the GPS Laboratory. I would especially like to thank LAAS team members: Ming Luo, Jason

Rife, Jiyun Lee, Young Shin Park, and Shankar Ramakrishnan. Discussions with these friends gave me many ideas. Many colleagues outside the LAAS team also supported my work. I would like to thank Dr. Todd Walter and Seebany Datta-Barua for providing their knowledge about ionosphere anomalies. Thanks also to Doug Archdeacon and Godwin Zhang for their technical support for computer problems and to Sherann Ellsworth and Dana Parga for their administrative help.

The work in this dissertation was sponsored by a research grant from the Federal Aviation Administration LAAS Program Office. Their financial support is gratefully acknowledged.

I would very much like to thank many friends outside the GPS Laboratory including Sei Higuch, Andre and Ines Marta, James Overduin, Tomo Koyanagi, Joo Sook Hwang, and Young Han Lee. Thanks are extended to the Silicon Valley Japanese Ski Freak folks including Daisuke Terasawa, Hiro Minami, and Shinji Sato. Life at Stanford has been a truly enjoyable experience due to these friends. Special thanks go to people at Information and Science Techno-System Co., Ltd. Japan, including Dr. Fumio Shinohara and Mr. Masaki Usami, for their support and friendship.

Last but not least, I would like to thank my family. Thanks to my parents, Yukio and Hiromi, for their endless sacrifice and love in supporting me through my life, and to my brother, Toshi, for his friendship and encouragement. Above all, my deepest thanks go to my wife, Yoko, for the help, advice, encouragement, and love that she has given me over the course of my studies at Stanford. It is to my family that I dedicate this dissertation.

CONTENTS

ABSTRACT	iv
ACKNOWLEDGEMENTS.....	vi
CONTENTS.....	viii
LIST OF FIGURES	xi
LIST OF TABLES	xiv
 CHAPTER 1	
Introduction	1
1.1 Background.....	3
1.2 The Global Positioning System	4
1.2.1 System Overview.....	4
1.2.2 Differential GPS	8
1.2.3 GPS Modernization	10
1.3 Local Area Augmentation System.....	10
1.3.1 System Overview.....	11
1.3.2 Ionosphere Anomalies: The Technical Challenge of this Research.....	13
1.4 Related Research	15
1.4.1 Integrity Methods using Single-Frequency GPS.....	16
1.4.2 Ionosphere Mitigation Techniques using Dual-Frequency Signals.....	17
1.5 Contributions	18
1.6 Reader's Guide	20
 CHAPTER 2	
Local Area Augmentation System (LAAS).....	25
2.1 System Requirements	26
2.2 Accuracy	29
2.2.1 GPS Range Measurements	29
2.2.2 Accuracy Improvement: Carrier Smoothing and DGPS	38

2.2.3 Model of Positioning Error.....	43
2.3 Integrity Methodology	52
2.3.1 System Architecture from Integrity Perspective	53
2.3.2 Protection Level Concept	57
2.3.3 Integrity Methods for H ₂ Risks.....	61
2.4 Summary	62
CHAPTER 3	
Ionosphere Threat Model.....	65
3.1 Threat Model Parameter Definitions	66
3.2 Ionosphere Anomaly Data Analysis	68
3.3 Threat Model Used in This Research	73
CHAPTER 4	
Carrier-Smoothing Methods: Assessment of Ionosphere Impact	74
4.1 Geometrical Specification of LAAS Operation Affected by Ionosphere Wave Front.....	76
4.2 Theoretical Impact Assessment for Single-Frequency Carrier Smoothing	81
4.3 Theoretical Impact Assessment for Dual-Frequency Carrier Smoothing.....	86
4.3.1 Overview of New Civil Signals.....	86
4.3.2 Divergence-Free Smoothing.....	89
4.3.3 Ionosphere-Free Smoothing	92
4.4 Empirical Demonstration of Ionosphere Impact.....	94
4.4.1 Experimental Setup	95
4.4.2 Impact Evaluation Results	100
4.5 Summary	110
CHAPTER 5	
Ionosphere-Free Based Architecture	113
5.1 VPL Equation for IFree-Based LAAS.....	114
5.2 Availability Simulation Method	118
5.3 Simulation: Settings, Results, and Discussions	122
5.3.1 Simulation Settings.....	122
5.3.2 Results and Discussions	130
5.4 Summary	134
CHAPTER 6	
Divergence-Free Based Architecture	136
6.1 Overview of Integrity Method for DFree-Based LAAS	138
6.2 Ionosphere Change Rate Monitor	142
6.3 Undetectable Ionosphere Wave Fronts and the Worst-Case Condition for the Monitor	148
6.4 Derivation of VPL_{iono}	157
6.5 Availability Simulations: Results and Discussions	165
6.6 Summary	170

CHAPTER 7

Enhanced System: Hybrid Dual-Frequency LAAS	173
7.1 Hybrid Dual-Frequency System Architecture	174
7.2 Switching Strategy between DFree and IFree	175
7.2.1 Switching Strategy I	176
7.2.2 Switching Strategy II	177
7.2.3 Switching Strategy III	178
7.3 Summary	182

CHAPTER 8

Conclusion.....	184
8.1 Core Research Contributions	184
8.1.1 Evaluation of DFree and IFree Considering Ionosphere Anomalies.....	185
8.1.2 IFree-based LAAS.....	187
8.1.3 DFree-based LAAS	188
8.1.4 Enhanced System: Hybrid Dual-Frequency LAAS.....	189
8.2 Suggestions for Future Work.....	190
8.2.1 Research on Ionosphere Anomalies	190
8.2.2 Effects of Adding Extra Satellites	191
8.3 Summary	192

APPENDIX A

Continuous Approximation of Smoothing Filter	194
---	------------

APPENDIX B

Method to Compute B-values.....	196
--	------------

APPENDIX C

Verification of Undetectable Conditions.....	198
C.1 Undetectable Condition for Two Satellites	198
C.2 Undetectable Condition for Three Satellites	203

BIBLIOGRAPHY	209
---------------------------	------------

LIST OF FIGURES

Figure 1.1: News about Chaos at Heathrow Airport from BBC ONLINE	2
Figure 1.2: The Global Positioning System (GPS)	5
Figure 1.3: Schematic of Differential GPS	8
Figure 1.4: Scatter Plots of Horizontal Positioning Errors	9
Figure 1.5: System Overview of LAAS (the original figure is found in [FAAwebsite])	11
Figure 1.6: Vertical Ionosphere Error Distribution.....	14
Figure 1.7: Contributions of this Dissertation and Related Research Areas.....	21
Figure 1.8: Organization of Dissertation.....	22
Figure 2.1: Approach and Landing with Alert Limits	27
Figure 2.2: Schematic of L1 Signal Generation.....	31
Figure 2.3: Thin-Shell Model and Geometrical Conversion from Slant Ionosphere Error to Vertical Ionosphere Error	36
Figure 2.4: Block Diagram of Error Reduction Process in LAAS.....	38
Figure 2.5: Filter Structure of Carrier-Smoothing	40
Figure 2.6: Coordination System for LAAS Position Estimation.....	44
Figure 2.7: Airborne Accuracy Designators	48
Figure 2.8: Ground Accuracy Designators ($M = 1$)	50
Figure 2.9: LAAS Integrity Allocation Tree.....	54
Figure 2.10: System Architecture from Integrity Perspective	56
Figure 2.11: Integrity Determination Using Protection Level.	58
Figure 2.12: Position Error Distribution under Fault-Free Conditions and VPL_{H0}	59
Figure 2.13: Biased-Distribution Due to Single Reference-Receiver Failure.	61
Figure 3.1: Matlab-Generated Visualization of Vertical Ionosphere Error Distribution	67
Figure 3.2: Simplified Model of Ionosphere Anomaly.....	68
Figure 3.3: WRS Network	69
Figure 3.4: CORS Network and Selected Clusters	70
Figure 3.5: Ionosphere Error Evolution during 11/20/03 Ionosphere Storm in Northern Ohio and Southern Michigan.....	71
Figure 4.1: Ionosphere Effect on LAAS-aided Landing.....	75
Figure 4.2: Baseline Geometry of LAAS-aided Landing under Ionosphere Anomaly	77

Figure 4.3: Moving direction of ionosphere wave front and ionosphere delay difference between airborne and ground signals	79
Figure 4.4: Two-Satellite Affected Case.....	80
Figure 4.5: Block Diagram of SFCS	81
Figure 4.6: Signal Power Spectra of Three Civil Signals	87
Figure 4.7: Block Diagram of DFree	90
Figure 4.8: Block Diagram of IFree.....	93
Figure 4.9: Experimental Antenna Locations	95
Figure 4.10: Simulated Landing Situation	97
Figure 4.11: Injected Ionosphere Error	98
Figure 4.12: Satellite Geometry of Time Slot #1	101
Figure 4.13: Residual Ranging Error for Time Slot #1 (nominal case)	102
Figure 4.14: Vertical Position Error during Time Slot #1 (nominal case).....	103
Figure 4.15: Lowest-Elevation Satellite is Affected by an Ionosphere Wave Front .	104
Figure 4.16: Residual Ranging Error after Injecting Artificial Ionosphere Error (Time Slot #1)	104
Figure 4.17: Vertical Position Error after Injecting Artificial Ionosphere Error (Time Slot #1)	105
Figure 4.18: Satellite Geometry of Time Slot #2	106
Figure 4.19: Residual Ranging Error for Time Slot #2 (nominal case).....	107
Figure 4.20: Positioning Error during Time Slot #2 (nominal case)	108
Figure 4.21: Vertical Position Error for Expanded Time Slot (nominal case)	108
Figure 4.22: Residual Ranging Error after Injecting Artificial Ionosphere Error (Time Slot #2)	109
Figure 4.23: Positioning Error after Injecting Artificial Ionosphere Error (Time Slot #2)	110
Figure 5.1: IFree-Based LAAS Integrity Allocation Tree	114
Figure 5.2: Ratio of σ_{IF} to σ_{L1} as a Function of κ_{L15}	117
Figure 5.3: Hypothetical Constellation and Satellite Geometry	120
Figure 5.4: Difference of Relative Position of Satellites with Respect to Antenna When Assuming Two Different Epochs	127
Figure 5.5: IFree-Receiver Models Used in Simulations.....	128
Figure 5.6: Simulation Result for Case #1	131
Figure 5.7: Simulation Result for Case #2.....	131
Figure 5.8: Simulation Result for Case #3.....	132
Figure 5.9: Simulation Result for Case #4.....	132
Figure 5.10: Simulation Result for Case #5	133
Figure 5.11: Simulation Result for Case #6	133
Figure 6.1: Two Types of Divergence-Free (DFree) Filters	139
Figure 6.2: Block Diagram of Integrity Method	140
Figure 6.3: Ionosphere Change Rate Estimated from Empirical Data.....	144
Figure 6.4: Cumulative Distribution Function of Normalized Change Rate	145
Figure 6.5: Threshold of Ionosphere Monitor.....	147
Figure 6.6: Step Response of Ionosphere Monitor	148
Figure 6.7: LAAS Operation Affected by Ionosphere Wave Front.....	149

Figure 6.8: Monitor Threshold in Terms of Ionosphere Spatial Gradient	150
Figure 6.9: Undetectable Condition	151
Figure 6.10: Undetectable Condition for Two Satellites (Top View).....	152
Figure 6.11: Undetectable Condition for Three Satellites (Top View).....	153
Figure 6.12: IPP Geometry the Investigation Searched for (Two-Satellite Case)	155
Figure 6.13: IPP Geometry the Investigation Searched for (Three-Satellite Case) ...	155
Figure 6.14: Relationship between VPL_{iono} and Vertical Position Error Distribution	159
Figure 6.15: Simulation Result for L1-Based DFree (24-SV Constellation).....	166
Figure 6.16: Simulation Result for L5-Based DFree (24-SV Constellation).....	166
Figure 6.17: Simulation Result for 30-SV Constellation (00:00:00)	168
Figure 6.18: Simulation Result for 30-SV Constellation (10:00:00)	168
Figure 6.19: Sample Satellite Geometry over SFO (04:34:00 UTC on July 1, 1993).....	169
Figure 7.1: Hybrid Dual-Frequency System Architecture	174
Figure 7.2: Example Satellite Geometry over SFO	179
Figure 7.3: Count of Advantaged Sub-Geometries.....	181
Figure 7.4: Count of Disadvantaged Sub-Geometries	181
Figure 7.5: Difference of Advantaged minus Disadvantaged Sub-Geometries	182
Figure 8.1: Failure Test Results from Injecting a Simulated Ionosphere Anomaly into Nominal Test Data.....	186
Figure 8.2: Availability of IFree-Based LAAS.....	187
Figure 8.3: Availability of DFree-Based LAAS	189
Figure C.1: Undetectable Condition for Two Satellites.....	199
Figure C.2: Velocity of an Ionosphere Wave Front That Moves with Two IPPs.....	200
Figure C.3: Schematic of Process (2) (Computing d)	201
Figure C.4: Investigation Result for Memphis.....	202
Figure C.5: Undetectable Condition for Three Satellites.....	204
Figure C.6: Schematic of Process Steps (2) through (4) (Computing $v_{i,j}$, dv , and d_{max})	205
Figure C.7: Investigation Result for Memphis.....	207
Figure C.8: Investigation Results for JFK International Airport and Los Angeles International Airport.....	208

LIST OF TABLES

Table 1-1: Summary of Errors in GPS Measurements	7
Table 2-1: Requirements for Precision Approach and Landing	29
Table 2-2: Summary of Errors in GPS Measurements, Including Those in Carrier-Phase Measurements	33
Table 2-3: Airborne Accuracy Designator Parameters	48
Table 2-4: Ground Accuracy Designator Parameters	50
Table 3-1: Currently Confirmed Ranges of Threat Model Parameters	72
Table 3-2: Threat Model Parameters Used in This Research	73
Table 4-1: Experimental Time Slots (Date: February 22, 2007)	100
Table 4-2: Summary of Worst Residual Ionosphere Error at Decision Point	111
Table 5-1: Summary of Eight Possible Constellation States	121
Table 5-2: Orbital Parameters of Current 24-Satellite Constellation [Dod]	123
Table 5-3: Historical Probabilities of Satellite Outages [Dod]	124
Table 5-4: Orbital Parameters of Current 30-Satellite Constellation [Massatt]	125
Table 5-5: Assumed Probabilities of Satellite Outages for 30-Satellite Constellation	126
Table 5-6: Summary of Simulation Conditions	129
Table 6-1: Dates for Data Taking on Durand Rooftop	143
Table 6-2: Summary of Input Parameters for VPL_{iono}	162
Table 6-3: Summary of VPL Equations (4 Reference-Receiver Configuration)	164
Table 6-4: Location of Each Satellite in Sample Geometry	169
Table 7-1: Location of Each Satellite in Example Geometry	179
Table 7-2: VPL_{DFree} for Each Sub-Geometry	180
Table C-1: Summary of Investigation Results	203

CHAPTER 1

Introduction

At the end of the year 2006, a Portuguese friend of mine and I planed to have a Christmas party at his apartment on the Stanford campus. His wife, who was doing her Ph.D. research in Portugal, was to visit him during that vacation and to join our party, and it was on her way to the United States that an unfortunate thing happened. She was stranded at Heathrow airport (London) for two days because of a thick fog that caused more than 300 flights to be cancelled, bringing misery to tens of thousands of Christmas passengers (see Figure 1.1). She eventually managed to obtain a flight and arrived at Stanford in the morning of the party (although it took several more days for her baggage to reach her). Of course, the main topic of conversation at the party was about the travel chaos. However, she was so elegant as to speak of the story pleasantly without spoiling the happy mood with grumbles. Just as a tiny complaint, she finished her talk, saying with a sigh, “why are aircraft so weak to bad weather?” I said in response, “that is the motivation of my research.”

This dissertation discusses an all-weather navigation aid for aircraft precision approach and landing using satellite-based positioning systems.

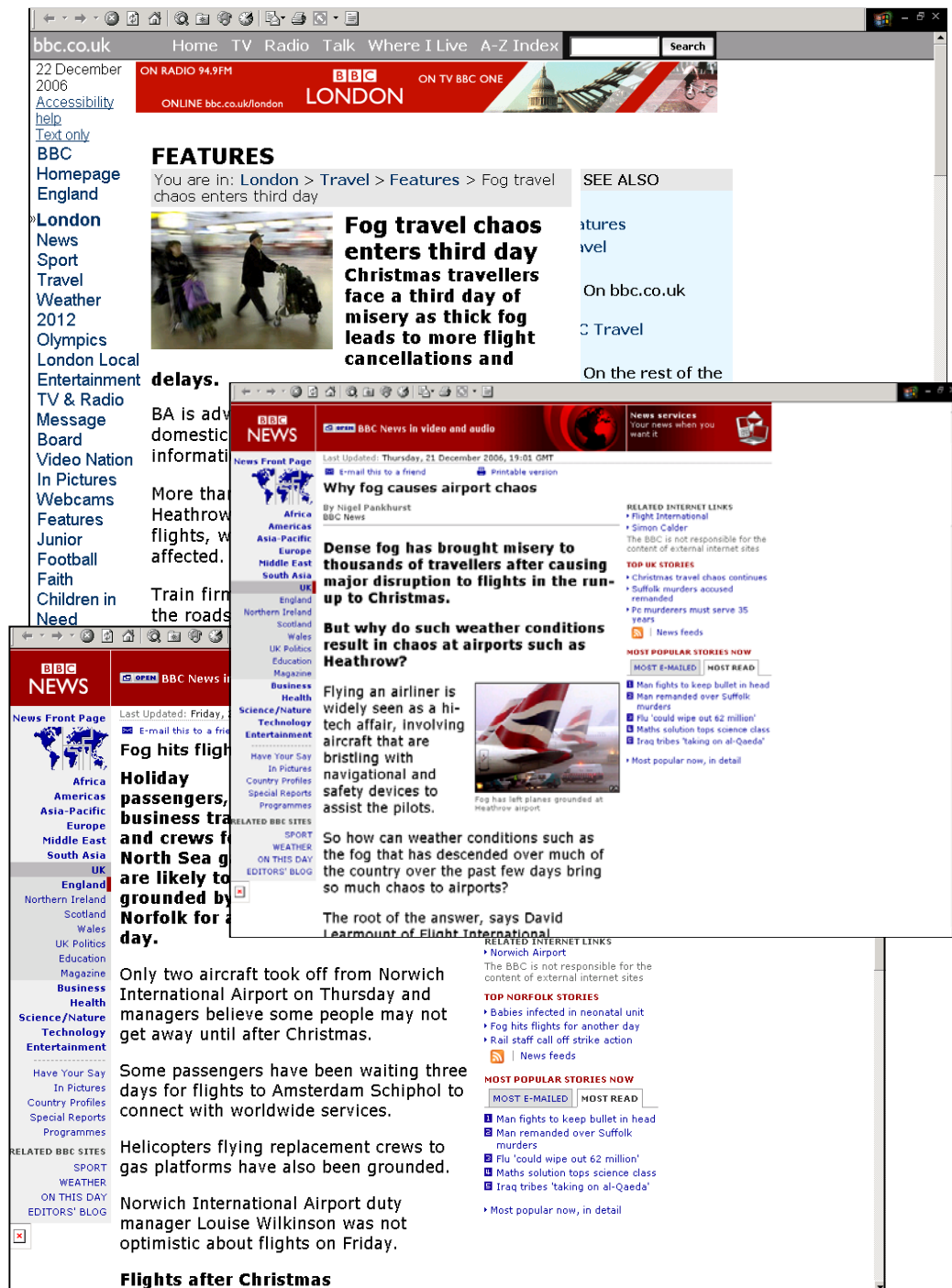


Figure 1.1: News about Chaos at Heathrow Airport from BBC ONLINE

A thick fog over the Heathrow airport prevented more than 300 aircraft from landing and taking off for more than three days, affecting tens of thousands Christmas season passengers.

1.1 Background

In 1991, the United States made a formal commitment to the International Civil Aviation Organization (ICAO) to make the Global Positioning System (GPS) available on a continuous and worldwide basis [Misra(Chapter 2)]. Over the next fifteen years, the civil aviation community in the U.S. has invested in prospective applications of GPS that provide positioning information to pilots through all phases of flight, bringing GPS closer to becoming the primary system for civil aviation navigation. Among these applications is the Federal Aviation Administration's *Local Area Augmentation System* (LAAS), a navigation system that aims to support zero-visibility precision approach and landing.

As a safety-of-life system, LAAS is required to provide very high levels of accuracy, safety, and reliability. In particular, satisfying the stringent safety requirement of “one undetected navigation failure in a billion approaches” has been the most critical challenge for realizing and certifying this system. The vast majority of LAAS research efforts have developed methods to guarantee safety in the presence of various potential anomalies that threaten LAAS-aided landing, and thanks to these efforts, almost all of these risks are now sufficiently mitigated. A small gap that remains, however, is the risk due to ionosphere anomalies. Currently, no method has been demonstrated that can mitigate errors induced by anomalous ionosphere behavior during strong geomagnetic storms to the degree required for safe operation during zero-visibility precision landing. The central focus of this research, hence, is to create and evaluate a method that fully mitigates the safety risk due to ionosphere anomalies.

To tackle this problem, this research takes advantage of technologies that will be available in the near future. Currently, GPS is undergoing amazing changes to enhance civil user capabilities, and these changes are expected to be completed within the next ten years. These improvements include adding new GPS signals that provide the benefit of frequency diversity, and frequency diversity makes possible various techniques to

solve ionosphere-related problems. This research proposes a solution to the ionosphere anomaly problem, based on the new capabilities of multiple-frequency GPS.

It is now legitimate to refer to the title of this dissertation—*Design of an Aircraft Landing System Using Dual-Frequency GNSS*. Obviously, “Aircraft Landing System” is a generic expression of LAAS; while GNSS, which stands for “Global Navigation Satellite Systems,” is a generic name for GPS-like satellite-based navigation systems including *Galileo*, an European satellite navigation system that is expected to be fully deployed in the next ten years and is designed to provide interoperability with GPS [Misra(Chapter 3), Hein06a, Grohe]. Although more than 90% of the discussion from the next section through Chapter 7 focuses on GPS and LAAS, the generic terms in the title apply just as well because the technical challenge dealt with in this research is common for all LAAS-like GNSS-based landing systems, and because the methods developed in this dissertation are theoretically applicable to all such systems. Expansion from the GPS/LAAS context to the more generic context will be discussed in the last chapter along with the recommendations for future work.

1.2 The Global Positioning System

This section provides an overview of GPS and focuses on two issues that are important to this research: the concept of Differential GPS (DGPS) and the outlines of ongoing GPS Modernization. DGPS is a vital technique with which LAAS improves positioning accuracy significantly. GPS Modernization is the process of gradually improving GPS that will enhance the capabilities of civil aviation applications. This research takes account of the benefits of this modernization.

1.2.1 System Overview

The Global Positioning System (GPS) is a satellite-based navigation system consisting of a 24-satellite constellation (see Figure 1.2) plus active (broadcasting) spare satellites. All GPS satellites have extremely accurately synchronized clocks and broadcast ranging

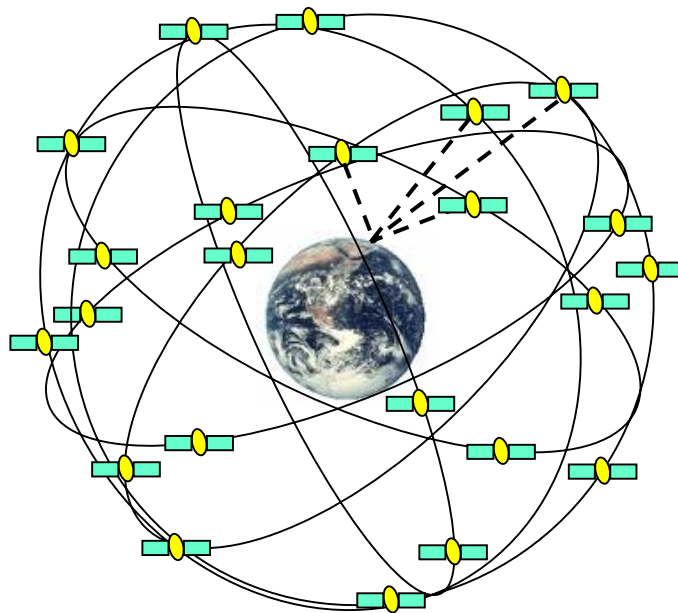


Figure 1.2: The Global Positioning System (GPS)

signals with their estimated positions. The fundamental navigation technique for GPS is to use *one-way* ranging from the GPS satellites [Parkinson].

Currently, each GPS satellite transmits two ranging signals on the top of the two radio frequency carriers, referred to as Link 1 (L1) and Link 2 (L2), whose frequencies are 1575.42 MHz and 1227.60 MHz, respectively. The ranging signal on L1 is for civil use; the other on L2 is for military use (the signal is encrypted). The L1 signal is a composite binary signal including a navigation message and a ranging code. The navigation message consists of data such as the satellite ephemeris (orbit) parameters, satellite clock bias parameters, and the satellite health status. The ranging code is a binary sequence that is unique to each satellite and provides the mechanism to identify each satellite in the constellation. For a given satellite, a user receiver measures the range by matching (correlating) the incoming signal with a user-generated replica signal and measuring the travel time of the ranging signal [Parkinson].

In order to measure the true transit time, the receiver clock must be synchronized with the satellite clock. However, considering the deviation of the receiver clock from the satellite clock to be an unknown, receivers are released from this onerous requirement. The receiver clock bias shifts the observed transit times for all satellites by the same amount. The corresponding ranges are thus all too short, or too long, by a common amount, and are called *pseudoranges*. Because the clock bias is common for all measurements, it can be the forth unknown in addition to the three coordinates of position. As a consequence, a user receiver needs to obtain pseudoranges from at least four satellites to solve for all the four unknowns.

If each pseudorange corresponds to the true distance to the satellite plus the receiver clock bias, users could compute their exact locations. In reality, however, the pseudorange is contaminated by various errors that are grouped as follows [Misra(Chapters 2 and 5)]:

- errors in the parameter values broadcast by a satellite in its navigation message,
- uncertainties associated with the propagation medium (such as the ionosphere and the troposphere) which affects the travel time of the signal from a satellite to the receiver,
- receiver noise which affects the precision of a measurement, and multipath from reflecting surfaces in the vicinity of the antenna.

Typical values of these errors are summarized in Table 1-1. Because the measured pseudoranges are erroneous, the resulting position is also erroneous. According to the GPS performance standard [Dod], the global average of the positioning accuracy in the horizontal direction is equal or less than 13 meters, and the accuracy in the vertical direction is equal or less than 22 meters (these accuracies are specified in terms of 95% error bound). GPS applications for zero-visibility precision landing, hence, require significant improvement in accuracy.

Table 1-1: Summary of Errors in GPS Measurements

Group	Source	Potential Error Size
1	Satellite clock model	Modeling error: 2 m (rms)
	Satellite ephemeris prediction	Component of the ephemeris error along the line of sight: 2 m (rms)
2	Ionosphere	<p>Error on the measurement: 2 – 30 m</p> <p>The error varies depending upon the elevation angle; the lower the elevation angle is, the larger the error is, because the propagation path length of a signal through the ionosphere decreases with the elevation angle.</p> <p>The error also depends upon the user geomagnetic latitude; the closer the user is to the geomagnetic equator, the larger the error is.</p> <p>The error also depends upon the time of the day (larger in day time) and the solar activity.</p>
	Troposphere	<p>Error on the measurement: 2 – 25 m</p> <p>The error varies depending upon the elevation angle; the lower the elevation angle is, the larger the error is, because the propagation path length of a signal through the troposphere decreases with the elevation angle.</p> <p>The error also depends upon the user altitude; the higher the user is, the larger the error is.</p>
3	Multipath	0.5 – 1 m (in a “clean” environment)
	Thermal noise	0.25 – 0.5 m (rms)

(The original data are found in [Misra] Table 5.4)

1.2.2 Differential GPS

To improve positioning accuracy, LAAS uses a classical technique called Differential GPS (DGPS). DGPS takes advantage of the fact that measurement errors associated with the satellite-broadcast parameters and the signal propagation medium (Groups 1 and 2 in Table 1-1) are similar for users separated by tens or even hundreds of kilometers [Misra(Chapters 2 and 5)]. These errors are often referred as *spatially correlated errors*. The closer two users are; the more similar are their spatially correlated errors.

Figure 1.3 shows the basic concept of DGPS. As shown in this figure, DGPS uses a reference station whose position is precisely known. Based on the receiver position and

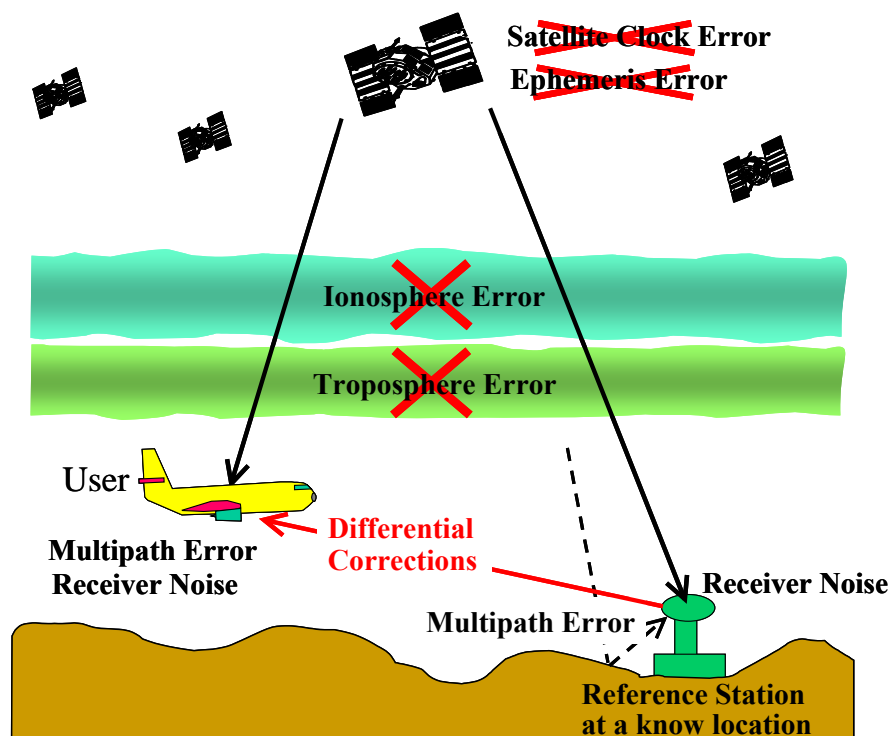


Figure 1.3: Schematic of Differential GPS

Spatially correlated errors such as the satellite clock offset, the ephemeris error, the ionosphere error, and the troposphere error are almost completely cancelled through DGPS.

the satellite positions provided by the ranging signals, the reference station can estimate the total ranging error for each satellite. These error estimates (generally called *differential corrections*) are then made available to users in the vicinity of the station. By calibrating spatially correlated errors with these differential corrections, each user reduces the ranging error and consequently improves the position estimation. As described above, the closer a user is to the reference station, the higher the benefit from DGPS. Figure 1.4 shows a typical improvement in positioning accuracy resulting from the use of DGPS. The left-hand plot shows typical positioning errors of stand-alone GPS, which spread widely within a 5-meter radius. In contrast, as shown in the right-hand plot, the positioning errors are concentrated within a 2-meter radius for the case of DPGS in which the user is located 25 km from the reference station.

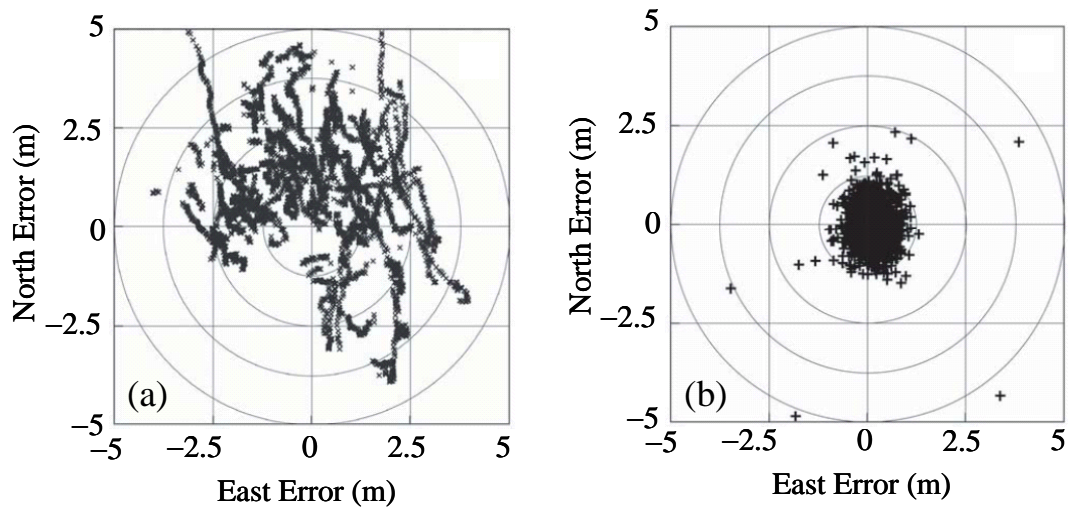


Figure 1.4: Scatter Plots of Horizontal Positioning Errors

(a) Stand-alone GPS position estimation and (b) DGPS position estimation with 25-kilometer separation between the reference station and the user. The original plots are shown in [Misra] Figure 6.6 and Figure 6.7.

1.2.3 GPS Modernization

As the importance of GPS increases within various fields, civil users have lobbied hard for additional capabilities and have pressed for changes in system design and policies [Misra(Chapter 3)]. In response, then-Vice President Gore announced plans for GPS modernization in 1998. GPS has been undergoing continuous system improvement since that time. This improvement is the result of many changes, including, in particular, the improvement of GPS constellation and ground-control-station management, and the addition of new civil signals [Enge03, Pullen04]. These new civil signals have great significance for this research.

Over the next ten years, a second civil signal on L2 (1227.60 MHz) and a third civil signal on L5 (1176.45 MHz) will join the current civil signal on L1 (1575.42 MHz). These new signals provide mainly three benefits: (1) they improve the fundamental signal acquisition and tracking performance of receivers, (2) they add redundancy against radio frequency interference, and (3) they enable techniques for mitigating the ionosphere errors that currently limit the accuracy of GPS. In particular, this research makes use of the third benefit. More specifically, this research uses several techniques enabled by multiple-frequency GPS to overcome technical challenges caused by potential ionosphere anomalies.

This section has presented an overview of GPS, including the very basics of DGPS and an introduction to GPS modernization. More details of these issues will be described as they come up in subsequent chapters. The attention is now turned to LAAS.

1.3 Local Area Augmentation System

The Federal Aviation Administration's Local Area Augmentation System (LAAS) is a DGPS-based augmentation to GPS to support aircraft navigation within the region around an airport equipped with LAAS (approximately 45 km radius). Its primary use is supporting precision-approach and departure procedures and hopefully other terminal-

area operations. This section introduces LAAS and provides an overview of the ionosphere anomaly problem, which is the focus of this research.

1.3.1 System Overview

Traditionally, instrument-aided precision approaches are classified into three categories—Category I, II, and III—based both on the altitude to which navigation systems provide guidance to pilots and on the horizontal visibility along the runway direction [Rtca04]. This research focuses on Category III LAAS that can provide guidance for automatic landing (note that precise definitions of three Categories are given in Chapter 2). Figure 1.5 shows a system overview of LAAS. As shown in this figure, a ground station consisting of multiple reference receivers (usually four) and a VHF data transmitter is sited at each airport. The reference station computes differential corrections based on ranges obtained by the reference receivers and broadcasts them to

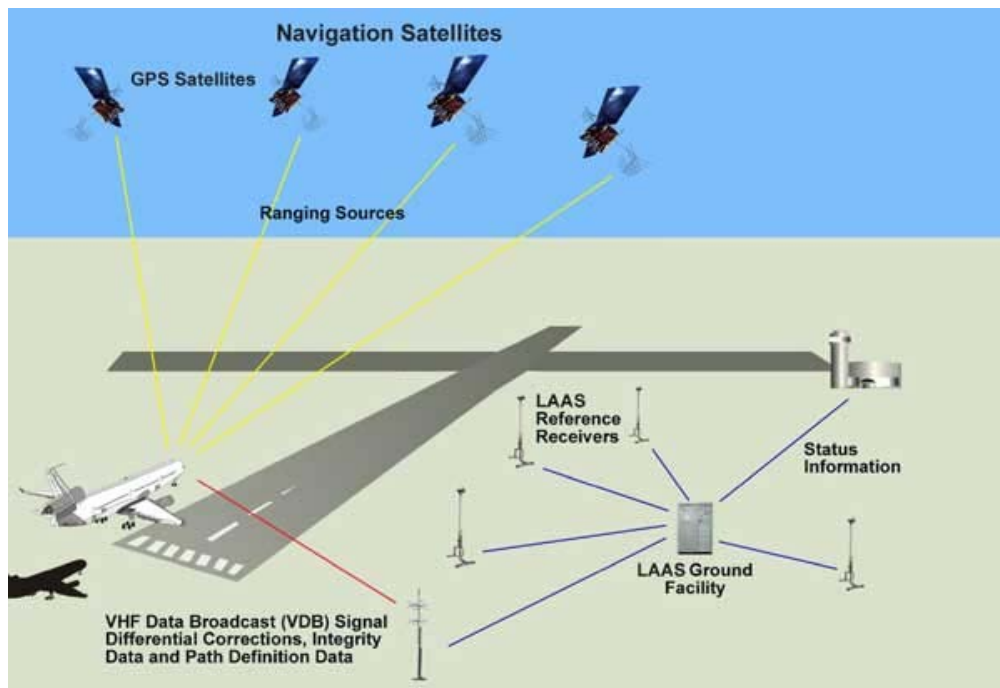


Figure 1.5: System Overview of LAAS (the original figure is found in [FAAwebsite])

the approaching aircraft using the VHF data broadcast (or VDB). Because of the proximity between the reference station and user aircraft (generally less than 45 km), user positioning accuracy is significantly improved; in fact, typical accuracy of LAAS-aided positioning is 2 – 2.5 meters in the vertical direction (95% performance). As will be explained further in Chapter 2, the accuracy requirement for Category III precision approaches is 2.9 meters (95%) in the vertical direction; hence, satisfying this requirement is not a significant challenge for LAAS.

Satisfying the accuracy requirement is important in its own right; however, compliance to the accuracy requirement is not sufficient to fulfill the most important performance characteristics—safety and reliability. The parameter that provides the basis of system safety and reliability is *integrity*, which is defined as “the ability of a system to provide timely warnings to users when the system should not be used for navigation.” To ensure integrity, the ground station monitors the quality of the differential corrections that it generates and broadcasts integrity-related information in addition to the corrections themselves. If it detects a sign of a deterioration in corrections or fundamental signal health due to some anomalous event, then either the affected corrections are no longer broadcast or one or more integrity-related parameters are adjusted such that this degradation does not pose a threat to users.

LAAS R&D efforts have identified several failure modes and anomalies that could pose a threat to LAAS-aided approaches. They include, for example, ranging signal deformation, faulty ephemeris data broadcasted by the satellite, intentional or accidental radio frequency interference, and anomalous ionosphere behavior. LAAS ground system integrity monitoring consists of various integrity algorithms, each of which is designed to detect anomalous conditions of one or multiple error sources and to mitigate the faulty conditions, most often by simply excluding the affected measurements from use. One way to satisfy stringent integrity requirements is to make these methods extremely sensitive to abnormal conditions. However, if they are overly sensitive, many “false alarms” will occur; consequently, the navigation service will be unnecessarily interrupted, and the system availability will significantly deteriorate. Hence, the

“sensitivity” of each detection algorithm has to be carefully tuned based on the physics and statistics of the faulty situation that the algorithm intends to mitigate.

Thanks to significant efforts devoted to the development of integrity algorithms, almost all faulty conditions that may threaten LAAS users can be mitigated by existing methods [Pullen02, Xie04, Lee05, Mitelman]. However, there is no method that mitigates errors induced by anomalous ionosphere behavior during strong solar storms to the degree required for Category II and III LAAS operations.

1.3.2 Ionosphere Anomalies: The Technical Challenge of this Research

The ionosphere is a region of ionized gases (free electrons and ions) extending between about 50 to 1000 km above the earth [Misra(Chapter 5), Klobuchar]. The ionization is caused by the sun’s radiation; thus, the state of the ionosphere is determined based primarily on the intensity of solar activity reaching the Earth. GPS ranging signals are delayed due to interactions with charged particles while traveling through the ionosphere, and this delay results in errors on the pseudorange measurements. Although ionosphere errors are highly variable and difficult to estimate precisely, they generally show very good spatial correlation. The nominal spatial gradient of ionosphere errors is at the range of 0.001 – 0.005 m/km (1σ); that is, the difference of the ionosphere errors on the ranges from a particular satellite to two users separated by 1 km is typically 0.001 – 0.005 meters [Misra(Chapter 5), Klobuchar, Lee06a]. Hence, LAAS users can almost completely cancel the ionosphere error using differential corrections. The residual error that remains is almost negligible for users nearing the end of their approaches (i.e., within 10 km of the LAAS ground station). Accordingly, ionosphere error was once considered to be an insignificant problem for LAAS.

This situation changed due to the discovery of extremely anomalous ionosphere behaviors. Datta-Barua *et al.* investigated ionosphere data on 6 – 7 April 2000 provided by the *Wide Area Augmentation System* (WAAS) and discovered an apparent ionosphere delay difference of 6 meters over a 19-kilometer separation, i.e. an ionosphere spatial

gradient of about 0.315 m/km, or about 100 times larger than the nominal one-sigma [Datta-Barua02]. Moreover, they showed evidence that this steep ionosphere gradient was moving with an average velocity (relative to the ground) of 110 m/s. Similar levels of moving ionosphere spatial gradients were also found on 29 – 30 October 2003 and on 20 November 2003 [Dehel, Ene, Komjathy04]. In addition, large near-stationary ionosphere gradients were discovered during the 29 – 30 October ionosphere storm [Datta-Barua05]. The abnormality of the ionosphere on November 20, 2003 is clearly shown in Figure 1.6, where the left figure is a snapshot of the ionosphere errors on GPS ranges over the Conterminous United States (CONUS) region on that day, while the right figure is a snapshot on a nominal day (October 28, 2003). It is evident that there are steep slopes of ionosphere errors between the blue region and the red region in the plot of the anomalous day.

In order to evaluate the potential impact of ionosphere anomalies, it became a crucial task to develop a quantitative model for anomalous ionosphere behavior. With this motivation, significant efforts have been devoted to analyze the ionosphere data during the anomalies noted above [Dehel, Ene, Komjathy04, Datta-Barua05]. Based on this

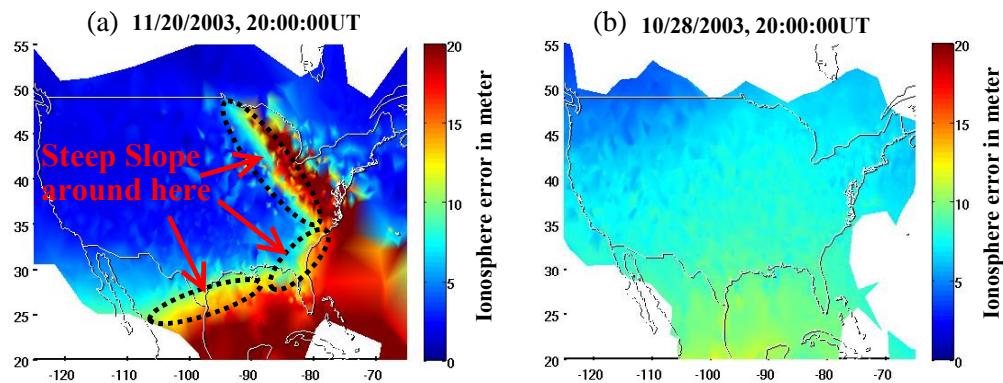


Figure 1.6: Vertical Ionosphere Error Distribution

(a) Anomalous day and (b) nominal day (Courtesy: Seebany Datta-Barua, Stanford University)

work, a so-called *ionosphere threat model* has been developed [Lee06b]. Based on several previous versions of this threat model, worst-case LAAS user impacts of ionosphere anomalies have been assessed by simulation [Luo02, Luo03, Luo04, Luo05]. Luo *et al.* showed that, if the most severe anomaly in the threat model affects a LAAS-equipped airport at the worst time, the user aircraft at the worst location could suffer residual ranging errors as large as 3 – 5 meters. If the satellite geometry for the user is poor, such a ranging error can result in a positioning error of larger than 10 meters, which is clearly hazardous for Category III precision approach—the class of approach that this research focuses on and which requires accurate and safe guidance all the way to touchdown on the runway.

Motivated by the results of these impact assessments, another research focus has been developing integrity methods to better mitigate ionosphere anomalies. However, these efforts have struggled with a fundamental problem, which is that the ionosphere error is difficult to estimate in real time by only using single frequency GPS signals. This problem is significant because, without estimating the ionosphere error, an integrity algorithm cannot directly observe the error source of interest—the difference in the ionosphere delay error between the ground station and the user. Existing methods, instead, detect anomalous ionosphere differences by observing another physical quantity such as ionosphere temporal gradients and transforming this quantity into the domain of the ionosphere difference with an appropriate mapping model. This “indirect” anomaly-detection approach generally includes uncertainties associated not only with the observation error but also with the mapping model. Due to this difficulty, no complete integrity method for Category III LAAS yet exists, and associated research fields are currently very active.

1.4 Related Research

This section introduces several important studies from two research fields closely related to this research: (1) the development of integrity algorithms using single-frequency

(current) GPS, and (2) the application of features of modernized GPS for mitigating ionosphere-related problems.

1.4.1 Integrity Methods using Single-Frequency GPS

The techniques introduced in this section are based on single-frequency (L1-only) GPS currently applied in LAAS. The first approach is to use an ionosphere-temporal-gradient monitor implemented in the ground station. Lee *et al.* introduced an integrity algorithm called *position-domain geometry screening* for Category I LAAS and confirmed with simulations for several airports that the method satisfied the integrity requirement with 99.9% system availability [Lee06b]. In fact, the FAA employs this algorithm for the Category I LAAS prototype system fielded at the Memphis airport. Because this method is sufficient for Category I LAAS, I personally asked Dr. Lee what availability would be obtained when applying this algorithm for Category III conditions. She kindly ran a simulation and estimated it at just 5%. Therefore, unfortunately, this method cannot be used for Category III LAAS without significant modifications.

Another approach is to use an airborne ionosphere-temporal-gradient monitor [Walter, Gratton05, Gratton06, Murphy06]. Murphy and Harris examined their airborne ionosphere monitor and showed with simulations that the monitor would detect almost all hazardous ionosphere conditions with high probability [Murphy06]. However, there still exist anomalous conditions that could be undetected with non-negligible probability of missed-detection, and it remains unclear if those undetected conditions are tolerable from the view-point of Category III user integrity.

As introduced above, research based on single-frequency GPS is very active and is searching for a solution to the ionosphere anomaly problem by combining currently-available technologies. However, many questions still remain unanswered, and no complete method has been demonstrated that can meet the integrity requirements of Category III LAAS. This research, in contrast, searches for a solution using a technology that will become available in a robust fashion in the near future—dual-frequency GPS.

1.4.2 Ionosphere Mitigation Techniques using Dual-Frequency Signals

Multi-frequency GPS techniques are known to be an effective means to reduce or remove ionosphere-induced errors. Among those techniques, of great interest to LAAS are *Divergence-Free Smoothing* and *Ionosphere-Free Smoothing* [Hwang, McGraw05]. Conceptually, these methods belong to the same family as *Single-Frequency Carrier Smoothing* employed in conventional LAAS to reduce multipath and receiver-noise errors. The main difference among these methods is the degree to which the ionosphere effect is removed from the output range measurements. Compared with Single-Frequency Carrier Smoothing, Divergence-Free Smoothing significantly reduces ionosphere errors especially under anomalous ionosphere conditions, but it is not perfect. In contrast, Ionosphere-Free Smoothing completely removes ionosphere errors under all ionosphere conditions. Ionosphere-Free Smoothing hence appears on the surface to be the best method for the ionosphere anomaly problem. However, its large noise level counteracts the benefit of ionosphere error elimination when ionosphere anomalies are not present.

Hwang *et al.* originally provided mathematical details of these two methods in [Hwang]. McGraw and Young then evaluated them from the view point of accuracy using simulation and recorded flight test data [McGraw05]. Stevens *et al.* evaluated these methods in the context of the Joint Precision Approach and Landing System (JPALS) which is a precision approach and landing aid for military aircraft and has a very similar system architecture to LAAS [Stevens], but they did not take account of the possibility of ionosphere anomalies.

Thus, several studies have addressed the benefit of Divergence-Free Smoothing and Ionosphere-Free Smoothing in the context of LAAS or LAAS-like systems. However, none of them has considered the problem of ionosphere anomalies. This research is the first attempt to apply these methods to the problem of mitigating ionosphere anomalies and to evaluate the resulting system from the view-point of overall system performance—accuracy, integrity, and availability.

1.5 Contributions

The objective of this research is to design and evaluate integrity methods to mitigate ionosphere anomalies, focusing on the Category III LAAS application. An acceptable method has to satisfy two mutually conflicting demands: (1) the method should be sufficiently sensitive to anomalous ionosphere behavior so as to satisfy the integrity requirements of Category III LAAS, but (2) it should avoid unnecessary interruptions of service continuity (to the degree possible) or a serious deterioration of system availability. This research utilized dual-frequency GPS methods—Divergence-Free Smoothing and Ionosphere-Free Smoothing—to achieve this goal, and the contributions summarized in the following bullets were made in the course of achieving that goal.

- **For each of Single-Frequency Carrier Smoothing, Divergence-Free Smoothing, and Ionosphere-Free Smoothing, this research evaluated worst-case LAAS user errors due to ionosphere anomalies (discussed in Chapter 4).** By adding an artificial amount of ionosphere error consistent with the most severe condition within the ionosphere threat model to empirical data taken by two closely-located receivers, it is possible to simulate a LAAS-aided operation during worst-case ionosphere conditions. This research conducted “failure tests” of this type for each of the three smoothing methods mentioned above and demonstrated that Divergence-Free and Ionosphere-Free Smoothing are much more robust against the severe ionosphere conditions than Single-Frequency Carrier Smoothing. Note that no anomaly detection method was applied in these failure tests.
- **This research designed and evaluated a system that implements Ionosphere-Free Smoothing (discussed in Chapter 5).** Ionosphere-Free Smoothing completely removes ionosphere errors from the GPS range measurements. Thus, by definition, the system using Ionosphere-Free Smoothing has no integrity risk associated with ionosphere anomalies. However, simulations showed that the system could not achieve reasonable availability due to the large receiver noise

remaining in the output of this smoothing method. Sensitivity analysis varying the receiver noise level revealed that, even under the most preferable conditions, such a system could only obtain 96% to 99.9% availability at best over a broad region of CONUS.

- **This research designed and evaluated a system that implements Divergence-Free Smoothing and an ionosphere monitoring method (discussed in Chapter 6).** Because Divergence-Free Smoothing does not mitigate all hazardous ionosphere conditions, an additional integrity monitoring algorithm is necessary for ensuring integrity. This research developed an ionosphere monitor that uses dual-frequency GPS signals and, combining this monitor with Divergence-Free Smoothing, introduced an algorithm that ensures integrity for Category III operations. Simulations showed that, under nominal ionosphere conditions, this system would achieve more than 99.9% availability over more than 70% of CONUS. However, under severe ionosphere conditions, this system cannot retain high availability because it will protect integrity at the expense of availability. Because of the rarity of ionosphere anomalies, this loss of availability is not a serious problem. Hence, this approach is definitely one solution for the ionosphere anomaly problem. This research, however, searched further for another solution to obtain better performance, which is the next contribution.
- **This research designed a system incorporating both Divergence-Free Smoothing and Ionosphere-Free Smoothing and switching between them based on the ionosphere conditions observed by the ionosphere monitor (discussed in Chapter 7).** One partial solution to avoiding availability loss under the severe ionosphere conditions is using Ionosphere-Free Smoothing. As shown in the second contribution, the system using Ionosphere-Free Smoothing achieves only 96% availability. However the good news is that the system is completely insensitive to the ionosphere condition; hence, it can obtain this 96% availability regardless of the ionosphere condition. Based on this benefit, this research

developed a “hybrid” system that implements both Divergence-Free Smoothing and Ionosphere-Free Smoothing. The system uses Divergence-Free Smoothing under nominal ionosphere conditions and switches to Ionosphere-Free Smoothing when anomalous ionosphere conditions are detected based on the best estimate of the current ionosphere state obtained by the ionosphere monitor. In particular, the optimal trigger condition at which the system switches from Divergence-Free to Ionosphere-Free smoothing was considered from the view point of overall system availability.

Among the four contributions summarized above, the last three contributions correspond to the design of three related integrity algorithms: the Ionosphere-Free-based algorithm, the Divergence-Free-based algorithm, and the hybrid algorithm. Figure 1.7 illustrates how these contributions fit within their related research fields. An important aspect of these algorithms is that, by using dual-frequency techniques, they all satisfy the integrity requirements of Category III LAAS. This is significant because, to date, no complete integrity method for Category III LAAS has been published. The difference among them is the expected system availability. By inheriting the advantages of both the Ionosphere-Free-based and the Divergence-Free-based algorithms, the hybrid algorithm achieves optimal availability, which is more than 99.9% availability over more than 70% of CONUS under nominal ionosphere conditions and more than 96% availability over 100% of CONUS under severe ionosphere conditions.

1.6 Reader’s Guide

Including this chapter that has provided an introduction to this research, this dissertation has eight chapters and three appendices, followed by a bibliography. Figure 1.8 shows the logical dependence among these chapters. Described in Chapters 2 through 4 is basically the existing work directly related to this research, although Chapter 4 also includes contributions made in this research. The contents of the next three chapters

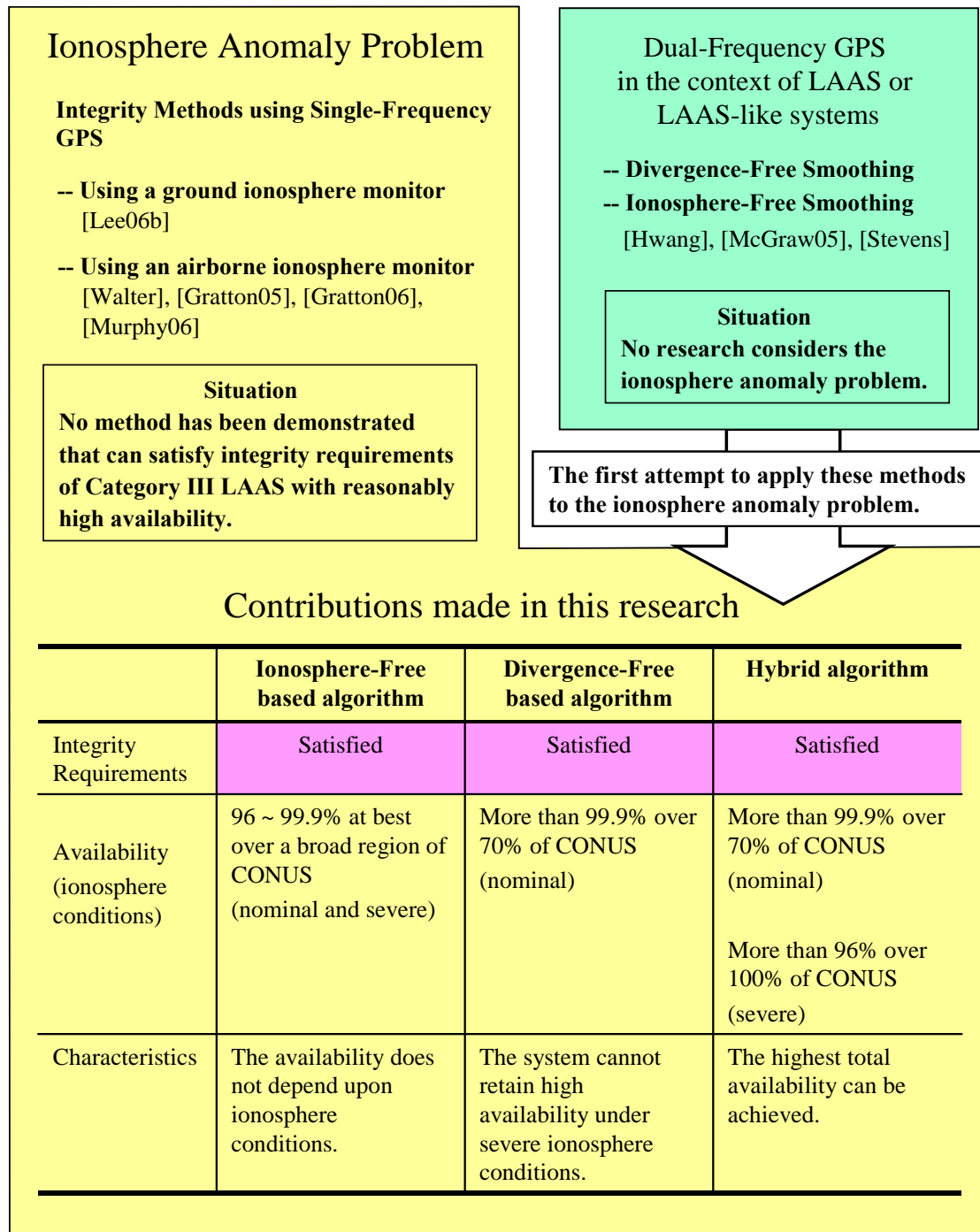


Figure 1.7: Contributions of this Dissertation and Related Research Areas

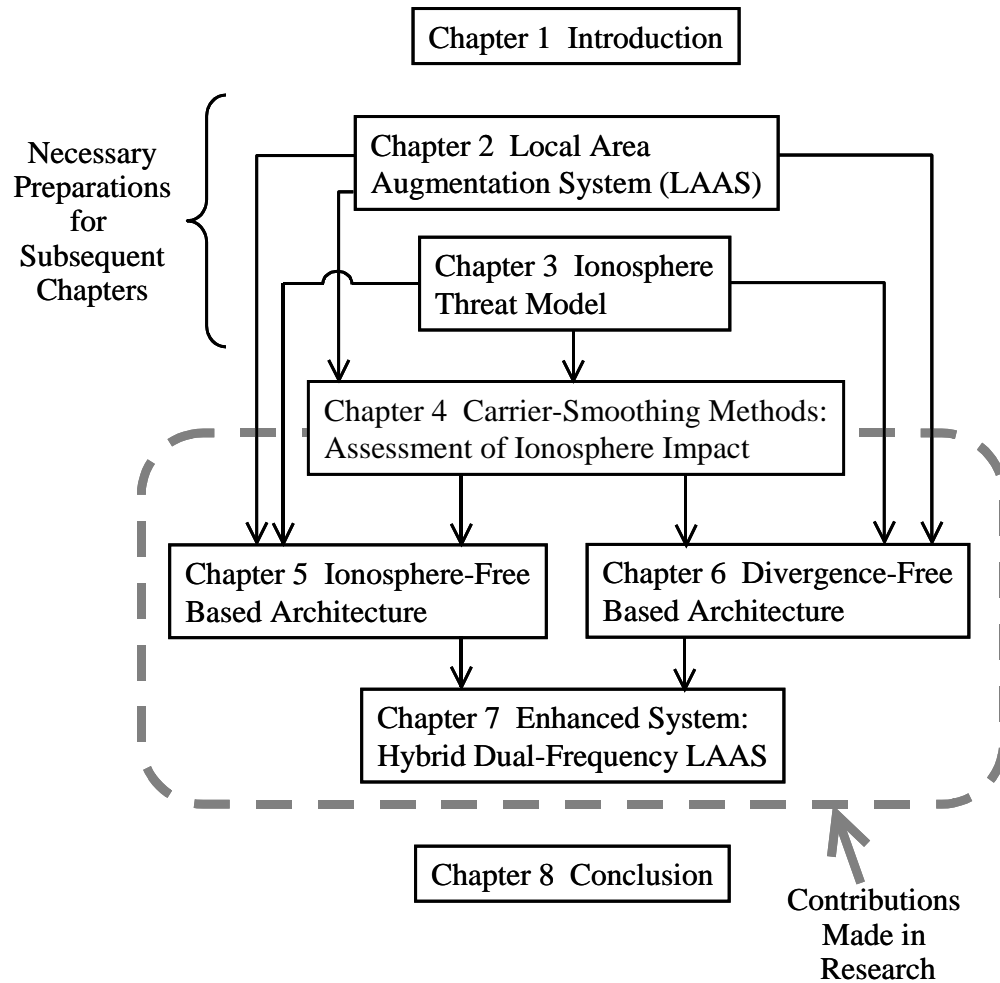


Figure 1.8: Organization of Dissertation

(Chapters 5, 6, and 7) focus on the contributions made in this research. Finally, Chapter 8 summarizes the results of this research and suggests new directions to explore. The following is a brief reference to each chapter.

Chapter 2 provides background information on LAAS that is relevant to this research. This chapter first specifies LAAS system requirements and then describes the LAAS accuracy model followed by the basic integrity methodology. In particular, ideas that are introduced in the integrity methodology shape the foundation for the methods

developed in this research. Thus, the discussions in this part of Chapter 2 are occasionally referred to in subsequent chapters.

Chapter 3 defines the ionosphere threat model that geometrically specifies anomalous ionosphere behavior targeted by this research. To define this model, this chapter briefly reviews previous work that analyzed the extreme ionosphere storms that occurred over the United States in October and November 2003.

Chapter 4 describes the Divergence-Free Smoothing and Ionosphere-Free Smoothing methods in detail—these two dual-frequency algorithms play major roles in this dissertation. Although these methods existed prior to the beginning of this research, the contribution in this chapter is to demonstrate, with failure tests, the superiority of those dual-frequency methods over the Single-Frequency Carrier Smoothing method employed in conventional LAAS under severe ionosphere anomaly conditions.

Chapter 5 proposes and evaluates a system architecture that implements Ionosphere-Free Smoothing. While, by definition, this smoothing method has perfect immunity against ionosphere anomalies, availability simulations show that this system cannot achieve acceptable availability due to the large receiver noise error remaining after smoothing. In addition to the results of this evaluation, this chapter describes in detail the algorithm for estimating LAAS system availability. The same algorithm is applied to evaluate a different system architecture in Chapter 6.

Chapter 6 proposes and evaluates an architecture that implements Divergence-Free Smoothing and an ionosphere anomaly detection algorithm. This system provides sufficient integrity against potential ionosphere anomalies and achieves acceptable availability under nominal ionosphere conditions. However, under severe ionosphere conditions, this system will protect integrity while sacrificing availability. Consequently, system availability under such conditions is poor.

Based on the outcomes of Chapters 5 and 6, Chapter 7 develops an architecture implementing both Divergence-Free Smoothing and Ionosphere-Free Smoothing and

optimizes the system operation to extract the highest possible system availability. This architecture, albeit complex, provides the optimal availability while still achieving the required integrity against ionosphere anomalies.

Finally, Chapter 8 summarizes the dissertation and suggests several technical topics that should be addressed by future research. Also discussed is the applicability of the proposed methods to more generic aircraft landing systems that would use other proposed GNSS, systems such as the European Galileo system.

CHAPTER 2

Local Area Augmentation System (LAAS)

LAAS developed out of several DGPS R&D efforts that started in the early 1990's. These efforts helped to specify system requirements, develop the basic system architecture, and introduce useful avenues for ensuring integrity against various fault modes. The main purpose of this chapter is to introduce the important outcomes of these efforts that form the basis for this research.

This chapter begins with system requirements. For LAAS, there exist well-studied system requirements which are documented in the *LAAS Minimum Aviation System Performance Standards* (MASPS) [Rtca04], a document that provides engineers with a useful framework to perform LAAS research. Referring to the MASPS, Section 2.1 gives an overview of the system requirements. Next, Section 2.2 derives an accuracy model that reflects expected performance under normal conditions, which is the first step to embark upon a study of safety issues. Finally, Section 2.3 introduces the basic integrity methodology for LAAS. The most important concept described in this section is the Protection Level (PL), which is a rare-event error bound that is calculated by user aircraft in real-time. This research develops a novel variation of the PL that works with Dual-Frequency GPS and mitigates unacceptable errors induced by ionosphere anomalies. Discussions of PL calculations in this chapter are, hence, occasionally referred to in subsequent chapters.

2.1 System Requirements

Traditionally, precision approaches and landings are classified into three categories based both on the altitude to which navigation systems provide guidance, known as *Decision Height* (DH), and on the required horizontal visibility on the runway called *Runway Visual Range* (RVR). The following details the specification of each category [Rtca04].

Category I (CAT I): Precision approaches with a DH higher than 60 meters and with an RVR of more than 550 meters.

Category II (CAT II): Precision approaches with a DH between 60 meters and 30 meters and with an RVR of more than 350 meters.

Category III (CAT III): While CAT III navigation systems are basically designed for automatic landing, there are three sub-classes based on the quality of ground equipments and the degree of fault tolerance of onboard guidance system via redundant avionics.

- **CAT IIIa:** Precision approaches with a DH lower than 30 meters or no DH and with an RVR of more than 200 meters.
- **CAT IIIb:** Precision approaches with a DH lower than 15 meters or no DH and with an RVR between 200 meters and 50 meters. CAT IIIb navigation systems can support automatic landing and rollout.
- **CAT IIIc:** Precision approaches with no DH and an RVR less than 50 meters. CAT IIIc navigation systems can support automatic landing, rollout, and taxi.

LAAS ground stations, which are to be sited at each airport provided with LAAS service, are designed to support one or more of these categories. For each category, the system is required to provide navigation to guide the aircraft into a specific “safe zone” that is

determined such that, if the *navigation system error* (NSE) for a given LAAS user (i.e., the difference between reported position and true position) goes outside this area, it could result in a hazardous condition. This safe zone is called the *Alert Limit* (AL) and is expressed by two parameters in two orthogonal dimensions: the *Lateral Alert Limit* (LAL), and the *Vertical Alert Limit* (VAL). Figure 2.1 illustrates a landing with the alert limits shown. For safe landings, LAAS has to provide navigation whose NSE is within the AL; moreover, if a positioning error should exceed the AL due to a failure or anomaly, the system has to warn the pilot (or autopilot) within a specific time (known as the *time-to-alert*). To design a system that accomplishes the needed performance, there are four fundamental parameters for which specific requirements are allocated [Enge99, Pervan96].

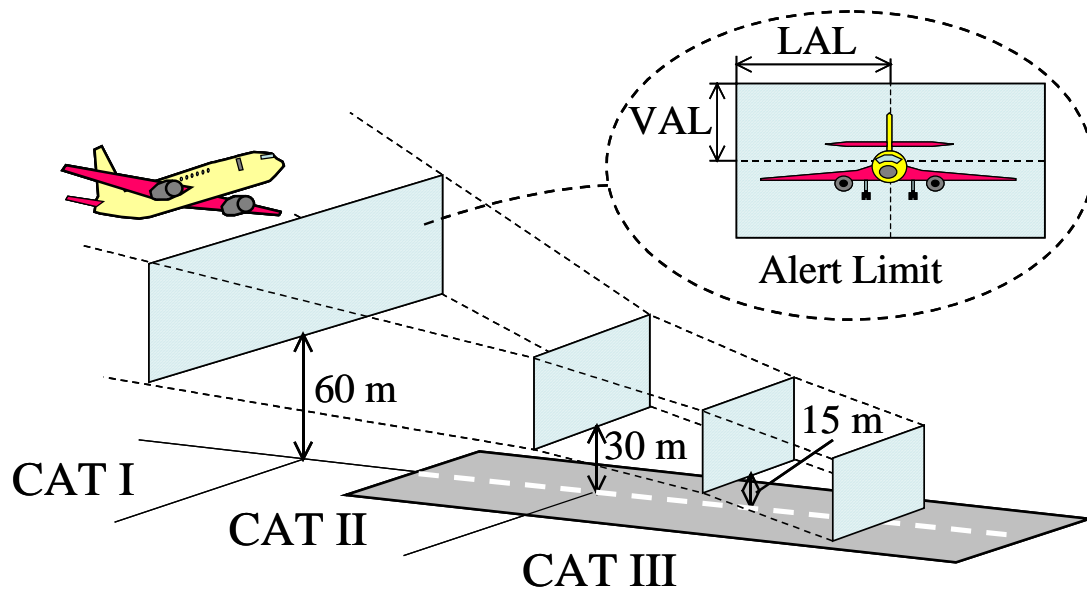


Figure 2.1: Approach and Landing with Alert Limits

Accuracy: Measure of the navigation output deviation from truth under fault-free conditions (often specified in terms of 95% performance).

Integrity: Ability of a system to provide timely alerts to users when the system should not be used for navigation. *Integrity risk* is the probability that no alert is issued while a positioning error exceeds the AL for a time longer than the required time-to-alert.

Continuity: Likelihood that the navigation system supports accuracy and integrity requirements for the duration of intended operation. *Continuity risk* is the probability of an alert requiring an approach to be aborted after it has been initiated.

Availability: Fraction of time that the navigation function is usable as determined by its compliance with the accuracy, integrity, and continuity requirements.

Table 2-1 shows the requirements for accuracy, integrity, and continuity for each category specified in MASPS [Rtca04]. Here, the requirements for integrity and continuity are specified in terms of a probability to be evaluated over the most critical period in an operation for each category (note that this interval may differ between the integrity and continuity requirements). For CAT IIb, the critical period for the lateral requirement is longer than that for the vertical requirement because CAT IIb LAAS supports operations beyond touchdown (extending through rollout) that require only lateral guidance. For availability, the MASPS [Rtca04] loosely specifies that “the service availability requirement shall be between 0.99 and 0.99999 for all categories” because the expected availability depends upon the operational need for each airport.

This research focuses on CAT IIb LAAS. As shown in Table 2-1, it must satisfy the very stringent integrity risk requirement of 10^{-9} per approach, which literally means that “we accept only one undetected navigation fault in a billion approaches.” This stringent requirement “once in a billion” motivates the need to mitigate risks that are extremely rare but can result in hazardous failure if unmitigated. Ionosphere anomalies are considered to be just such a risk.

Table 2-1: Requirements for Precision Approach and Landing

Category	Accuracy (95%)		Integrity				Continuity
	Lateral	Vertical	Integrity Probability	Time to Alert	LAL	VAL	Continuity Probability
CAT I	16.0 m	4.0 m	2×10^{-7} in any 150 sec	6 sec	40 m	10 m	8×10^{-6} in any 15 sec
CAT II / CAT IIIa	5.0 m	2.9 m	1×10^{-9} in any 15 sec	2 sec	17 m	10 m	4×10^{-6} in any 15 sec
CAT IIIb	5.0 m	2.9 m	1×10^{-9} in any 15 sec vertical, 30 sec lateral	2 sec	17 m	10 m	2×10^{-6} in any 15 sec vertical, 30 sec lateral

2.2 Accuracy

Before embarking on a discussion of integrity, it is first necessary to understand accuracy under nominal conditions. For that, this section begins by modeling GPS range measurements subjected to various error sources and then moves on to introducing the error-reduction methods employed in LAAS. Finally, the section derives statistical parameters representing the LAAS positioning accuracy that results from the error-reduced range measurements. These parameters play an important role in the LAAS integrity methodology discussed in the next section.

2.2.1 GPS Range Measurements

LAAS Positioning errors originate from GPS range errors. Hence, the discussion of accuracy should start by understanding GPS range measurements. The currently available civil signal—the L1 signal—consists of three components [Misra(Chapters 2 and 9)].

RF carrier: A Radio Frequency (RF) sinusoidal signal with the frequency of 1575.42 MHz. Its wavelength is approximately 19 cm.

Ranging code: A unique sequence of zeros and ones that is assigned to each satellite. In particular, the ranging code for the L1 signal is called the C/A code. Each C/A code consists of 1023 bits, or *chips*, and is repeated each millisecond. Accordingly, the duration of each chip is about $1\ \mu\text{s}$; thus, its wavelength is about 300 meters, and the chipping rate is 1.023 MHz. Each code is selected based on its auto- and cross-correlation properties to allow all satellites to transmit on RF carriers having the same frequency without significantly interfering with each other. In other words, GPS receivers can distinguish each satellite by taking the correlation between the incoming signal and a receiver-generated replica of the ranging code for each satellite and checking if there is a conspicuous peak in the correlation function.

Navigation data: A binary-coded message consisting of data concerning the satellite health states, ephemeris (orbit parameters), clock bias parameters, and an almanac (reduced-precision ephemeris data on all satellites in the constellation). The navigation data is generated in the *GPS Ground Segment* and uplinked to GPS satellites. Satellites then transmit this data at 50 bps, which is equivalent to a bit period of 20 milliseconds.

Each satellite generates its unique ranging code and combines it with navigation data with modulo-2 addition. The combined binary signal is then modulated upon the RF carrier with *Binary Phase Shift Keying* (BPSK): a bit of zero leaves the RF carrier unchanged, and a bit of one shifts the phase of the carrier by 180 degrees. Figure 2.2 is a schematic of this procedure. For details of the signal structure and of the signal generation methods, the interested reader is referenced to [Spilker96a, Spilker96b, Misra(Chapter 9)].

By processing the incoming signals, GPS receivers output two types of range measurements. One is the *code-phase measurement*, and the other is the *carrier-phase measurement*. The code-phase measurement is computed from the travel time of the

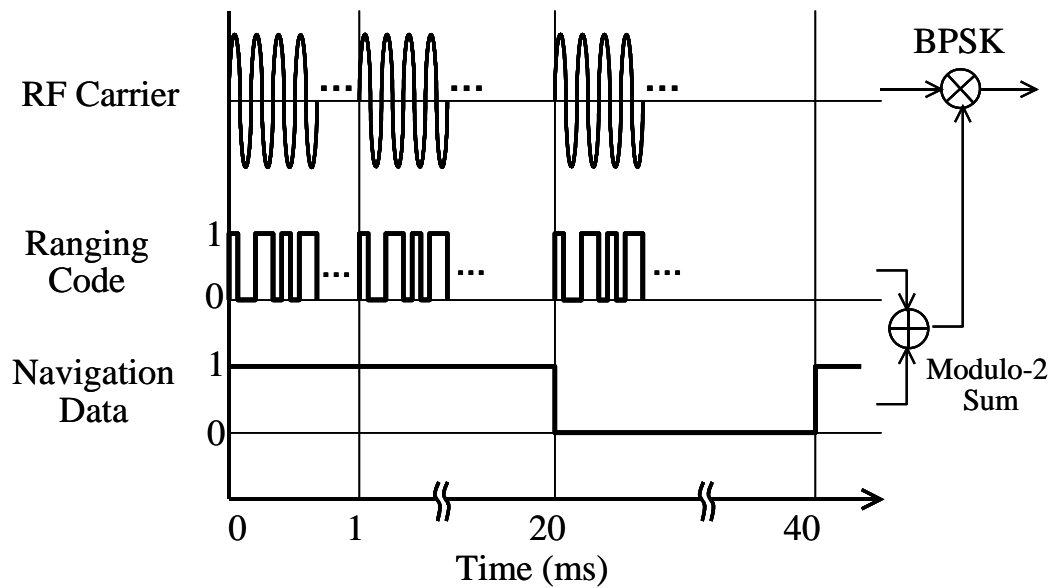


Figure 2.2: Schematic of L1 Signal Generation

ranging signals. For a given satellite, the GPS receiver generates a replica of the ranging code and searches for the correlation peak between the replica and the incoming signal by shifting the replica backward and forward in time. The time offset that maximizes the correlation corresponds to the best estimate of the travel time, although it remains corrupted by the receiver's own clock error. The code-phase measurement is determined by multiplying the travel time by the speed of light in vacuum.

In contrast, the carrier-phase measurement is computed from the difference between the phase of the receiver-generated carrier signal and the phase of the incoming signal. Because the phase difference is observed to within a cycle of the RF carrier, the receiver measures only a fraction of a cycle. Hence, the distance between the satellite and the receiver is the measured fraction plus an unknown number of whole cycles that is referred as the *integer ambiguity*. One needs to somehow determine this ambiguity to take full advantage of the carrier-phase measurement.

As discussed in Chapter 1, GPS range measurements are subject to various errors. Including these errors, the code- and carrier-phase measurements between a receiver, j , and a satellite, i , are modeled as follows.

$$\rho_j^i = r_j^i + cb_j - CB^i + E_j^i + T_j^i + I_j^i + MP_j^i + \nu_j^i \quad (2-1)$$

$$\phi_j^i = r_j^i + cb_j - CB^i + E_j^i + T_j^i - I_j^i + mp_j^i + \eta_j^i + N_j^i \quad (2-2)$$

where ρ is the measured code-phase measurement, ϕ is the measured carrier-phase measurement, r is the true distance between the satellite and the receiver antenna, cb is the error due to the receiver clock offset from GPS time, CB is the error due to the satellite clock offset from GPS time, E is the component of the ephemeris prediction error along the line of sight between the satellite and the receiver antenna, T is the troposphere error induced by the lower atmosphere, I is the ionosphere error induced by the upper atmosphere, MP and mp are multipath errors on code- and carrier-phase measurements, respectively, ν and η are the thermal noise errors in the receiver on code- and carrier-phase measurements, respectively, and N is the integer ambiguity multiplied by the carrier wavelength. Note that all terms are expressed in the length domain (in meters) after a proper transformation into units of length if necessary.

Table 2-2 presents a summary of typical errors on code- and carrier-phase measurements. It is in the same format as Table 1-1, which gives typical errors only on code-phase measurements. Among these errors, multipath, thermal noise, and ionosphere error are particularly interesting, because these errors do not have the same values between code- and carrier-phase measurements, while the other errors are the same. Moreover, the ionosphere error is the main focus of this research. Hence, it is worthwhile to discuss these errors in more detail.

Multipath and Thermal Noise

Although multipath and thermal noise affect both code- and carrier-phase measurements, these errors on carrier-phase measurements are significantly smaller than those on code-

Table 2-2: Summary of Errors in GPS Measurements, Including Those in Carrier-Phase Measurements

Source	Potential Error Size
Satellite clock model	Modeling error, $CB : 2$ m (rms)
Satellite ephemeris prediction	Component of the ephemeris error along the line of sight, $E : 2$ m (rms)
Ionosphere	<p>Error on the measurement, $I : 2 - 30$ m</p> <p>The error varies depending upon the elevation angle; the lower the elevation angle is, the larger the error is, because the propagation path length of a signal through the ionosphere decreases with the elevation angle.</p> <p>The error also depends upon the user geomagnetic latitude; the closer the user is to the geomagnetic equator, the larger the error is.</p> <p>The error also depends upon the time of the day (larger in day time) and the solar activity.</p>
Troposphere	<p>Error on the measurement, $T : 2 - 25$ m</p> <p>The error varies depending upon the elevation angle; the lower the elevation angle is, the larger the error is, because the propagation path length of a signal through the troposphere decreases with the elevation angle.</p> <p>The error also depends upon the user altitude; the higher the user is, the larger the error is.</p>
Multipath	<p>Code-Phase, $MP : 0.5 - 1$ m</p> <p>Carrier-Phase, $mp : 0.5 - 1$ cm (in a “clean” environment)</p>
Thermal noise	<p>Code-Phase, $\nu : 0.25 - 0.5$ m (rms)</p> <p>Carrier-Phase, $\eta : 1 - 2$ mm (rms)</p>

(The original data are found in [Misra] Table 5.4)

phase. Typical multipath plus thermal noise errors for carrier-phase measurements are about 1 cm in a clean environment, while those for code-phase measurements are about 1 meter (see Table 2-2). The magnitude of these errors mainly depends on the wavelength of the signal used for the measurement. In general, the longer the wavelength is, the larger the multipath and thermal noise errors are. Considering that the wavelength of the RF carrier—the primary signal for the carrier-phase measurement—is about 19 cm, and that the wavelength of the ranging code—a primary signal for the code-phase measurement—is about 300 meters, the significant difference in magnitude of these errors is understandable. In-depth discussions of these errors are found in [Misra(Chapters 5 and 10)].

Ionosphere Error

Equation (2-1) and (2-2) show that ionosphere errors on code- and carrier-phase measurements are the same in magnitude but opposite in sign. This comes from the following physics. The ionosphere is a frequency dispersive medium; that is, the refractive index is a function of the operating frequency [Klobuchar, Misra(Chapter 5)]. The major effects of the ionosphere upon GPS ranges are (1) group delay of the signal modulation, or absolute range error; and (2) carrier-phase advance as compared with the hypothetical carrier-phase that would be measured in the absence of the ionosphere, or relative range error. The ionosphere error on code-phase measurements corresponds to the group delay, while the ionosphere error on carrier-phase measurements corresponds to the phase advance. To evaluate the group delay (denoted by I_ρ) and the phase advance (denoted by I_ϕ), mathematical models based on the first-order approximation of the ionosphere refractive index for radio waves are widely used in the GPS community. The following equations give these models.

$$I_\rho = \frac{40.3 \cdot TEC}{f^2} \quad (2-3)$$

$$I_\phi = -\frac{40.3 \cdot TEC}{f^2} \quad (2-4)$$

where f is the carrier frequency, TEC (*Total Electron Content*) is the integrated number of electrons in a tube of 1 m^2 cross section extending from the receiver to the satellite, and “delay” is given as a positive value (“advance” has a negative value). Interestingly, as shown in (2-3) and (2-4), the magnitudes of the group delay and of the phase advance are the same (see [Klobuchar, Misra(Chapter 5)] for a detailed explanation of why this is the case). Hence, in equations (2-1) and (2-2), the ionosphere term (I) actually means the following.

$$I = I_\rho = -I_\phi = \frac{40.3 \cdot TEC}{f^2} \quad (2-5)$$

This frequency dependence of the ionosphere error is of great significance in the dual-frequency methods that will be discussed in Chapter 4.

For ionosphere error, another issue that should be noted here is the simplified geometrical model that is often used. As described above, the magnitude of ionosphere error is proportion to the total number of electrons existing along the signal path. Because the signal path length through the ionosphere is longer for a lower-elevation signal, the ionosphere error is generally larger for low-elevation satellites. In the simplified model, the ionosphere is considered to be a “thin shell” of infinitesimal thickness surrounding the earth. Based on this simplification of reality, the elevation-dependent ionosphere error ($I(El)$) is converted into an equivalent vertical ionosphere error (I_v) at the point of intersection of the line of sight with the thin shell (this point is called the *ionosphere pierce point*, or IPP). The conversion is done by the following equations.

$$I_v(h_I) = Oq(h_I, El) \cdot I(El) \quad (2-6)$$

$$Oq(h_I, El) = \sqrt{1 - \left(\frac{R_e \cos(El)}{R_e + h_I} \right)^2} \quad (2-7)$$

where $Oq(h_I, El)$ is called the *obliquity factor*, h_I is the height of the ionosphere shell (usually taken to be in the range of 350 – 450 km), R_e is the approximate radius of the Earth's ellipsoid (taken to be 6378.1363 km), and El is the elevation angle. Figure 2.3 illustrates this thin shell model.

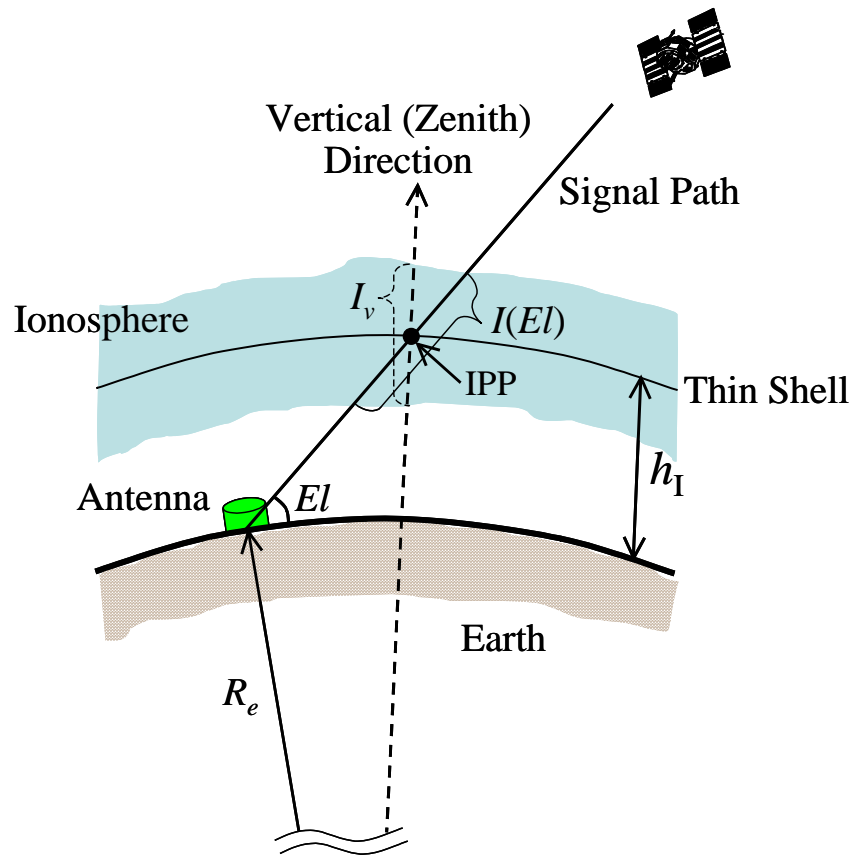


Figure 2.3: Thin-Shell Model and Geometrical Conversion from Slant Ionosphere Error to Vertical Ionosphere Error

The ionosphere “thin-shell” model assumes that electrons along a signal path in the vertical (zenith) direction concentrate on a spherical thin shell at a particular shell height (h_I). The point at which the signal path intersects with the thin shell is called the ionosphere pierce point (IPP). The vertical ionosphere error, I_v , at the IPP is governed by the number of concentrated electrons at that point. When the signal path is not in the vertical direction ($El \neq 90$ deg), the slant ionosphere error, $I(El)$, is related to the vertical ionosphere error at the IPP by means of the obliquity factor.

In fact, this research rarely uses the thin-shell model or the vertical ionosphere error (I_v). However, this model is traditionally used for various purposes, and the residual ionosphere error in the conventional LAAS accuracy model is expressed in terms of the vertical error and the obliquity factor, as discussed in the next section. In addition, this dissertation uses the concept of the ionosphere pierce point when modeling the movement of the ranging signal path through the ionosphere.

This section has described the signal structure and the measurement models for the L1 signal. Before moving forward to the accuracy improvement methods, here is a recapitulation of the key points about GPS range measurements.

- The GPS range signal consists of the RF carrier, ranging codes, and navigation data.
- There are two types of range measurements: code-phase measurements and carrier-phase measurements.
- Multipath and thermal noise errors on code-phase measurements are significantly larger than they are on carrier-phase measurements.
- Ionosphere errors on code- and carrier-phase measurements are the same in magnitude but opposite in sign.
- Ionosphere errors on the range measurement can be approximately converted into an equivalent vertical ionosphere error with the thin shell model and corresponding obliquity factor. In this thin-shell-model concept, the point at which the line of sight intersects with the thin shell is called the *ionosphere pierce point* or IPP.

The basic structure and the modeling techniques for the forthcoming civil signals—L2 and L5—are the same as those for the L1 signal and will be described in detail in Chapter 4.

2.2.2 Accuracy Improvement: Carrier Smoothing and DGPS

Code-phase measurements are the primary range measurements used in LAAS. As shown in the previous section, these measurements are subject to various errors. To reduce these errors, LAAS employs two classical methods: carrier smoothing, and DGPS. Carrier smoothing affects spatially-uncorrelated errors, namely multipath and thermal noise, while DGPS reduces spatially-correlated errors, namely satellite clock biases, ephemeris errors, ionosphere errors, and troposphere errors. Figure 2.4 shows a block diagram of this error-reduction process. First, both the ground station and the user

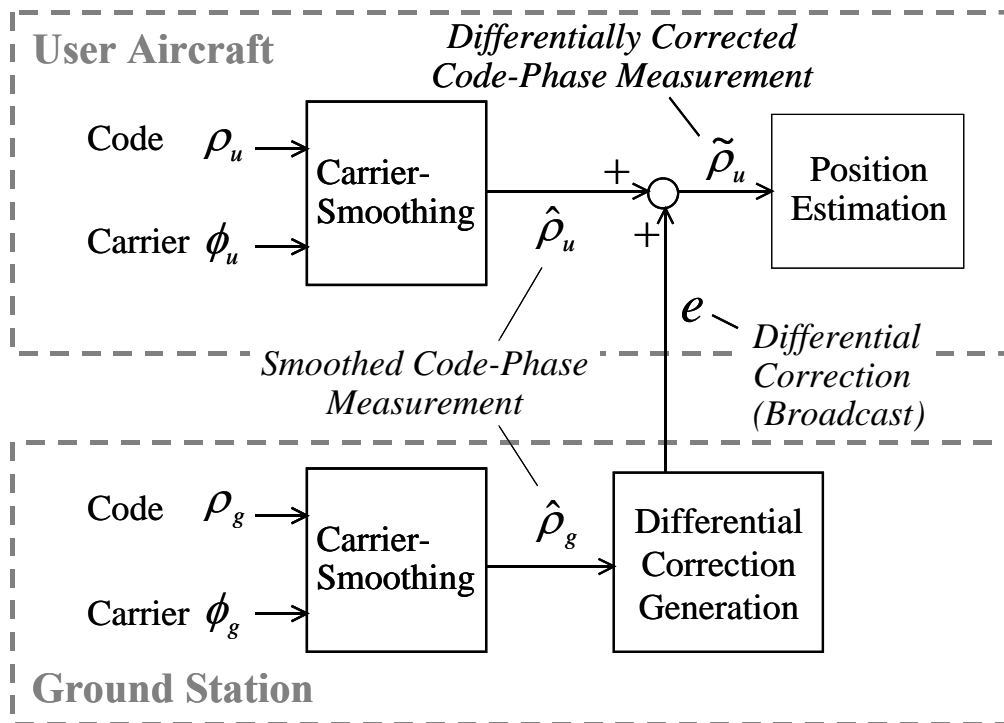


Figure 2.4: Block Diagram of Error Reduction Process in LAAS

The user aircraft and the ground station independently apply carrier smoothing to attenuate code-phase measurement errors. The ground station then generates differential corrections, e , based on its antenna location and broadcasts them. The user calibrates its smoothed measurements with the differential corrections and estimates its position.

aircraft execute carrier smoothing to reduce multipath and thermal-noise errors on their own measurements. The ground station then produces differential corrections for every satellite in view and broadcasts the corrections for satellites which pass all integrity tests (these integrity tests will be introduced in Section 2.3.3). The user calibrates the spatially-correlated errors using these corrections and estimates its position from the improved range estimates. Note that the ground station generally has two or more reference receivers located close to each other and generates a differential correction by averaging the corrections from all receivers tracking each satellite. Also note that, despite the proximity between the ground station and the user (less than 45 km), the satellites in view of the user are not always the same as those in view of the ground station. In such cases, the satellites common to both user and ground station are applied to user position estimation.

The remainder of this section gives a detailed introduction to carrier smoothing and DGPS.

Carrier Smoothing

The concept of carrier smoothing dates back to the early 1980's [Hatch]. Its primary goal is to suppress multipath and thermal-noise errors on code-phase measurements by using carrier-phase measurements. To explain the mechanism of carrier smoothing, simplified models for code- and carrier-phase measurements are used.

$$\rho_j^i = R_j^i + I_j^i + \varepsilon_j^i \quad (2-8)$$

$$\phi_j^i = R_j^i - I_j^i + N_j^i \quad (2-9)$$

$$R_j^i = r_j^i + cb_j - CB^i + E_j^i + T_j^i \quad (2-10)$$

Here, R includes all terms that are common between code- and carrier-phase measurements, and ε is a noise term in which the multipath and the thermal noise, MP and ν in equation (2-1), are aggregated. The multipath and the thermal noise on the

carrier-phase measurements, mp and η in equation (2-2), are neglected due to their being very small compared to those on the code-phase measurements.

Multipath and thermal-noise errors generally exhibit weak temporal correlations. The idea of carrier smoothing is to “average out” these errors by using much-less noisy carrier-phase measurements as aiding information. To accomplish it, this method uses the complementary filter illustrated in Figure 2.5. First, the code- and carrier-phase measurements are differenced to form the *Code-Minus-Carrier* (CMC) parameter, χ .

$$\chi = \rho - \phi = 2I - N + \varepsilon \quad (2-11)$$

The CMC parameter is then fed into a low-pass filter. Importantly, the CMC parameter does not contain the quantity of interest for the position estimation, namely, the range to the satellite. Hence, the low-pass filter operates only on the “out-of-interest” quantities (such as multipath and thermal-noise errors) without affecting the range to the satellite.

The low-pass filter is implemented as follows.

$$\hat{\chi}[t + \Delta T] = \frac{\tau - \Delta T}{\tau} \hat{\chi}[t] + \frac{\Delta T}{\tau} \chi[t + \Delta T] \quad (2-12)$$

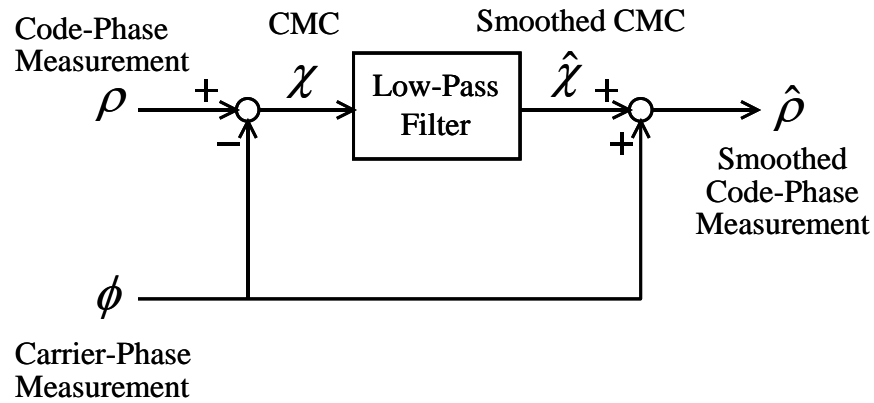


Figure 2.5: Filter Structure of Carrier-Smoothing

where $\hat{\chi}$ is the smoothed CMC, τ is the smoothing time constant and is conventionally set to 100 seconds in LAAS, and ΔT is the measurement update period, which is conventionally set to 0.5 seconds in LAAS. This low-pass filter can be approximated by a continuous-time filter expressed as follows in the Laplace-domain.

$$\hat{\chi}(s) = F(s)\chi(s) \quad (2-13)$$

$$F(s) = \frac{1}{\tau s + 1} \quad (2-14)$$

The derivation of this continuous-time model is shown in Appendix A. This approximation is appropriate whenever the smoothing time constant (τ) is significantly longer than the measurement update period (ΔT).

Finally, the smoothed CMC ($\hat{\chi}$) is combined with the carrier-phase measurement to restore the range to the satellite and to cancel out the integer ambiguity (N). The smoothed code-phase measurement ($\hat{\rho}$) is given in the Laplace-domain as

$$\hat{\rho}(s) = R(s) + (2F(s) - 1)I(s) + F(s)\varepsilon(s), \quad (2-15)$$

and is given in time domain as

$$\hat{\rho}(t) = R(t) + \hat{I}(t) + \hat{\varepsilon}(t), \quad (2-16)$$

where

$$\hat{I}(t) = \mathcal{L}^{-1}\{ (2F(s) - 1)I(s) \}, \quad (2-17)$$

$$\hat{\varepsilon}(t) = \mathcal{L}^{-1}\{ F(s)\varepsilon(s) \}. \quad (2-18)$$

As equation (2-15) shows, this carrier-smoothing filter attenuates the multipath and thermal noise (ε) without affecting the range to the satellite. However, at the same time,

the filter also influences the ionosphere error (I). Filtering the ionosphere error is not problematic in nominal ionosphere conditions (because the impact of this error remains negligible), but it introduces a nuisance effect under anomalous ionosphere conditions. This nuisance effect will be discussed in detail in Chapter 4, but here I continue a discussion of DGPS assuming that everything is normal.

Differential GPS (DGPS)

After executing carrier smoothing, the ground station produces differential corrections for each satellite in view. First, the ground station computes the geometric range to the satellite, i , from the reference receiver, g .

$$r_g^i = \|\mathbf{x}^i - \mathbf{x}_g\| \quad (2-19)$$

where \mathbf{x}^i is the satellite position obtained from the navigation message, and \mathbf{x}_g is the precisely-surveyed position of the reference antenna. The differential correction for the satellite (e_g^i) is computed as:

$$e^i = r_g^i - \hat{\rho}_g^i = -cb_g + CB^i - E_g^i - T_g^i - \hat{I}_g^i - \hat{\epsilon}_g^i \quad (2-20)$$

where $\hat{\rho}_g^i$ is the code-phase measurement adjusted by carrier smoothing. As mentioned above, the ground station consists of two or more reference receivers located near each other, each of which computes its own differential corrections. The corrections uplinked to the user are created by averaging the corrections from all receivers tracking each satellite.

The user aircraft applies the received corrections to its own smoothed code-phase measurements. The differentially-corrected code-phase measurement, $\tilde{\rho}_u^i$, is given as follows.

$$\begin{aligned}
\tilde{\rho}_u^i &= \hat{\rho}_u^i + e^i \\
&= r_u^i + cb_u - cb_g + (E_u^i - E_g^i) + (T_u^i - T_g^i) + (\hat{I}_u^i - \hat{I}_g^i) + \hat{\epsilon}_u^i - \hat{\epsilon}_g^i
\end{aligned} \tag{2-21}$$

Here, the second line of this equation is a precise model. However, because the difference of the ephemeris error between the ground station and the user ($E_u^i - E_g^i$) is negligible within the LAAS service range (45 km) absent faulty ephemeris data (which should be detected before corrections are broadcast), this term is generally ignored. Accordingly, the practical model is given as:

$$\tilde{\rho}_u^i = r_u^i + cb_{ug} + T_{ug}^i + \hat{I}_{ug}^i + \hat{\epsilon}_u^i - \hat{\epsilon}_g^i, \tag{2-22}$$

where the double-subscript notation denotes the difference between the ground station (g) and the user (u), i.e. $(\bullet)_{ug} = (\bullet)_u - (\bullet)_g$.

The user aircraft uses this differentially-corrected code-phase measurement for position estimation. Within this measurement, the receiver clock offset (cb_{ug}) is estimated along with position in three dimensions. Hence the measurement errors that affect position estimation are the residual troposphere error (T_{ug}), the residual ionosphere error (\hat{I}_{ug}), the smoothed multipath and thermal-noise error at the user ($\hat{\epsilon}_u$), and the smoothed multipath and thermal-noise error at the ground station ($\hat{\epsilon}_g$). The next section introduces statistical expressions for these errors and models the resulting positioning accuracy.

2.2.3 Model of Positioning Error

It is necessary to understand the process of position estimation in order to move forward to positioning accuracy because the errors on range measurements are projected into the position domain through this process. Receiver position and clock bias are estimated based on a linearized GPS measurement model. Let the true position (\mathbf{x}) and the true clock bias (cb) be represented as follows.

$$\mathbf{x} = \mathbf{x}_0 + \delta\mathbf{x}, \quad (2-23)$$

$$cb = cb_0 + \delta cb, \quad (2-24)$$

where \mathbf{x}_0 and cb_0 are the initial estimates for the position and the clock bias, and $\delta\mathbf{x}$ and δcb are the unknown corrections to be applied to these initial estimates. In LAAS, the position vector is defined in the coordination system shown in Figure 2.6, where the x-axis is along track positive forward in the local-level tangent plane, the y-axis is cross-track positive left in the plane, and the z-axis is positive up and orthogonal to the plane. When there are N satellites in view, the GPS measurement model is given as:

$$\hat{\mathbf{p}} - \mathbf{p}_0 = \delta\mathbf{p} = \mathbf{G} \begin{bmatrix} \delta\mathbf{x} \\ \delta cb \end{bmatrix} + \boldsymbol{\xi}, \quad (2-25)$$

where $\delta\mathbf{p}$ is an N -dimensional vector containing the differentially-corrected code-phase measurements ($\hat{\mathbf{p}}$) minus expected ranges (\mathbf{p}_0) that are computed based on the satellite positions (given by the ephemeris navigation data) and the estimated user position, and $\boldsymbol{\xi}$ is an N dimensional vector containing the residual errors of the differentially-corrected

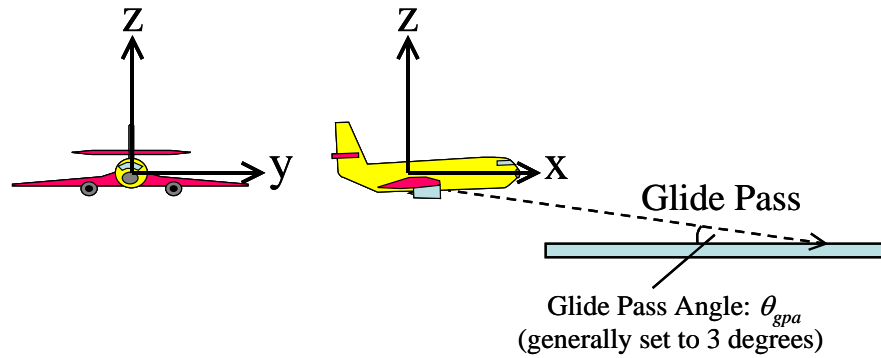


Figure 2.6: Coordination System for LAAS Position Estimation

code-phase measurements. \mathbf{G} is the *user-to-satellite geometry matrix* consisting of N rows, each of which is written in terms of the azimuth angle (Az) and the elevation angle (El) for the given satellite. Defining the azimuth angle as counterclockwise about the z -axis from the positive x -axis, and defining the positive elevation angle as upward from the x - y plane, the i^{th} row of \mathbf{G} is given as:

$$\mathbf{G}_i = [-\cos(El_i)\cos(Az_i) \quad -\cos(El_i)\sin(Az_i) \quad -\sin(El_i) \quad 1]. \quad (2-26)$$

In position estimation, $\delta\mathbf{x}$ and δcb in equation (2-25) are first solved by the weighted least-squares method, then the initial position and clock bias estimates are improved by substituting these solutions into equation (2-23) and (2-24). This process is iterated until the change in the estimates $\delta\mathbf{x}$ and δcb is sufficiently small. The weighted least-squares solution is given by:

$$\begin{bmatrix} \delta\mathbf{x} \\ \delta cb \end{bmatrix} = (\mathbf{G}^T \mathbf{W} \mathbf{G})^{-1} \mathbf{G}^T \mathbf{W} \delta\mathbf{p} = \mathbf{S} \delta\mathbf{p}, \quad (2-27)$$

$$\text{where } \mathbf{S} = (\mathbf{G}^T \mathbf{W} \mathbf{G})^{-1} \mathbf{G}^T \mathbf{W}. \quad (2-28)$$

The matrix \mathbf{S} projects the range-domain information into the position domain and is called the *weighted least-squares projection matrix*. \mathbf{W} is a covariance matrix of the measurements that accounts for unequal measurement quality, and its inverse is given as follows.

$$\mathbf{W}^{-1} = \begin{bmatrix} \sigma_{rm,1}^2 & 0 & \cdots & 0 \\ 0 & \sigma_{rm,2}^2 & \cdots & 0 \\ \vdots & \vdots & \ddots & \vdots \\ 0 & 0 & 0 & \sigma_{rm,N}^2 \end{bmatrix} \quad (2-29)$$

where σ_{rm} represents the standard deviation, or *sigma*, of the differentially-corrected range measurement. Here, it is usually assumed that the measurement errors are distributed based on zero-mean Gaussians, and that these errors are uncorrelated

between different satellites [Misra(Chapter 6)]. Based both on this assumption and on the linear projection from the rang domain to the position domain given in equation (2-27), the position error can be modeled as a zero-mean Gaussian distribution whose standard deviation is computed as follows.

$$\sigma_{vertical} = \sqrt{\sum_{i=1}^N S_{vert,i}^2 \sigma_{rm,i}^2} , \quad (2-30)$$

$$\sigma_{lateral} = \sqrt{\sum_{i=1}^N S_{2,i}^2 \sigma_{rm,i}^2} , \quad (2-31)$$

where $\sigma_{vertical}$ is the sigma of the vertical positioning error; $\sigma_{lateral}$ is the sigma of the lateral positioning error; $S_{2,i}$ is the $(2, i)$ component of the projection matrix \mathbf{S} , namely the projection onto the lateral component for the i^{th} satellite; and $S_{vert,i}$ is the projection onto the vertical component for the i^{th} satellite, which is given as:

$$S_{vert,i} = S_{3,i} + S_{1,i} \tan(\theta_{gpa}) \approx S_{3,i} \quad (2-32)$$

where θ_{gpa} is the glide path angle for the final approach and is usually 3 degrees. In equation (2-32), the term “ $S_{1,i} \tan(\theta_{gpa})$ ” accounts for the effect of uncertainty in the along-track position on the vertical positioning error. This research ignores this term both because $S_{1,i}$ is generally smaller than $S_{3,i}$ and because $\tan(\theta_{gpa})$, corresponding to the glide path angle of 3 degrees, is only about 0.05.

Due to the zero-mean Gaussian assumption, positioning accuracy can be fully evaluated by computing the standard deviations $\sigma_{vertical}$ and $\sigma_{lateral}$ from equation (2-30) and (2-31). To compute these sigmas, the standard deviation of each measurement (σ_{rm}) must be evaluated first. As discussed in the previous section, independent error sources affecting the differentially-corrected range measurements are airborne receiver noise, ground receiver noise, residual ionosphere error, and residual troposphere error. Hence, σ_{rm} for a specific satellite i is given as follows.

$$\sigma_{rm,i}^2 = \sigma_{air,i}^2 + \sigma_{gnd,i}^2 + \sigma_{iono,i}^2 + \sigma_{tropo,i}^2 \quad (2-33)$$

where σ_{air} , σ_{gnd} , σ_{iono} , and σ_{tropo} represent the standard deviations for the contributing errors listed above, respectively. These “primitive” sigmas are important because σ_{rm} —a value computed from these sigmas—is used not only for evaluating positioning accuracy ($\sigma_{vertical}$ and $\sigma_{lateral}$) but for estimating position itself through the weighting matrix, \mathbf{W} . In LAAS operations, the ground station has responsibility to provide users necessary information for computing σ_{gnd} , σ_{iono} , and σ_{tropo} . The remainder of this section introduces means to compute these “primitive” sigmas—methods that are widely used within the civil aviation community.

Model of Airborne Receiver Noise: σ_{air}

Residual airborne receiver noise after carrier smoothing consists of residual multipath and thermal noise. McGraw *et al.* [McGraw00] investigated empirical GPS range measurements taken by typical airborne receivers with a carrier smoothing in typical airborne environments and developed standard models called *Airborne Accuracy Designators* (AADs) that express σ_{air} (meters) as a function of the satellite elevation angle. They proposed two types of designators according to the available receiver technologies at that time: AAD-A that reflects the performance of “standard” receiver technologies with *wide-correlator sampling*, and AAD-B that reflects performance of “advanced” receiver technologies with *narrow-correlator sampling*. The following equations give these models.

$$\sigma_{air}(El) = \sqrt{\sigma_{mp}^2(El) + \sigma_n^2(El)} \quad (2-34)$$

$$\sigma_{mp}(El) = 0.13 + 0.53 \exp(-El/10) \quad (2-35)$$

$$\sigma_n(El) = a_0 + a_1 \exp(-El/\theta_c) \quad (2-36)$$

where σ_{mp} represents the residual multipath, σ_n represents the residual thermal noise, El represents the elevation angle given in degrees. Note that each designator has its own values for the parameters a_0 , a_1 , and θ_c as shown in Table 2-3. Figure 2.7 shows these models.

Table 2-3: Airborne Accuracy Designator Parameters

Accuracy Designator	a_0 (m)	a_1 (m)	θ_c (deg)
AAD-A	0.15	0.43	6.9
AAD-B	0.11	0.13	4.0

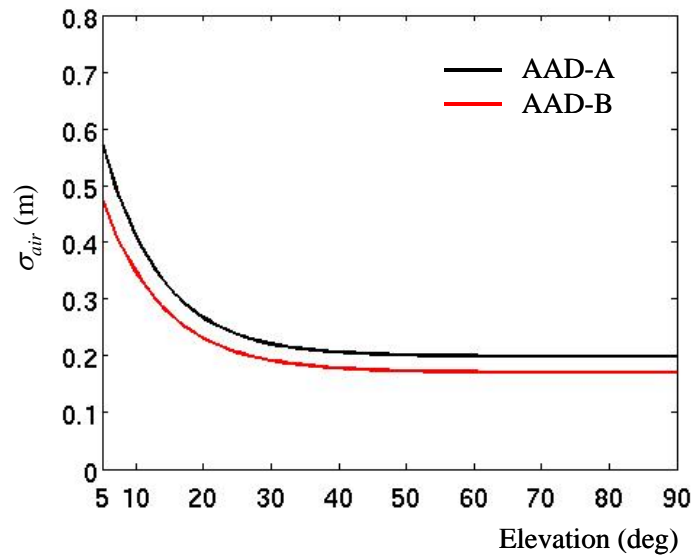


Figure 2.7: Airborne Accuracy Designators

These designators are now internationally authorized [Icao], and the MASPS [Rtca04] recommends that airborne users accomplish the receiver noise level no larger than at least one of these two designators. In practice, because these designators were developed based on empirical data collected on typical Boeing aircraft models (including all models from the 737 through the 777), and because these designators include some amount of margin on the empirical data, accomplishing the noise level of either of these designators is not troublesome [Murphy05]. In LAAS operations, the user aircraft evaluates σ_{air} for each satellite using the designator that the aircraft applies and uses these sigmas to construct the weighting matrix (**W**) and to evaluate the positioning accuracies ($\sigma_{vertical}$ and $\sigma_{lateral}$).

Model of Ground Receiver Noise: σ_{gnd}

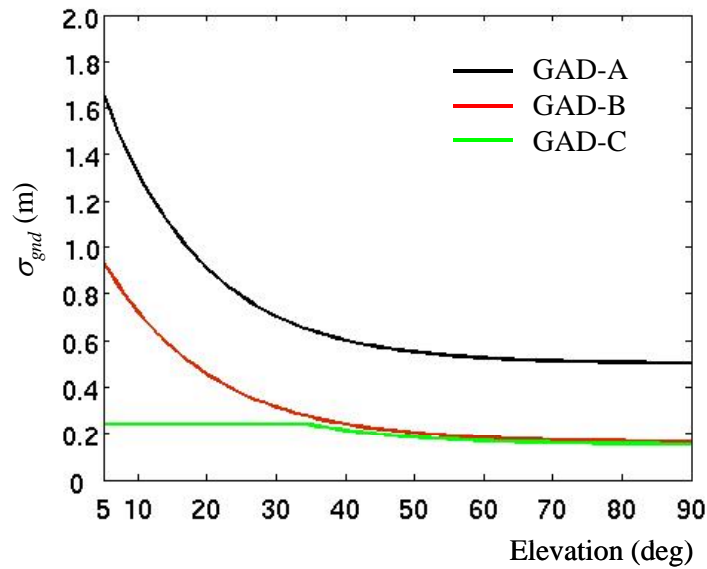
McGraw *et al.* also developed models for ground receiver noise, investigating empirical GPS measurements taken by typical ground receivers in typical ground station environments [McGraw00]. These models are called *Ground Accuracy Designators* (GADs) and define the σ_{gnd} (meters) as a function of elevation angle. They proposed three types of designators (GAD-A, -B, and -C) based on the available receiver and antenna technologies. The following equation gives these designators.

$$\sigma_{gnd}(El) = \begin{cases} \frac{1}{\sqrt{M}}(a_0 + a_1 \exp(-El / \theta_c)) & , El \geq 35 \text{ deg} \\ \frac{\sigma_{MAX}}{\sqrt{M}} & , El < 35 \text{ deg} \end{cases} \quad (2-37)$$

where M indicates the number of reference receivers used in the ground station, El is the satellite elevation angle in degrees, and each designator has its own parameters a_0 , a_1 , θ_c , and σ_{MAX} as shown in Table 2-4. Figure 2.8 shows these designators for $M = 1$.

Table 2-4: Ground Accuracy Designator Parameters

Accuracy Designator	a_0 (m)	a_1 (m)	θ_c (deg)	σ_{MAX} (m)
GAD-A	0.50	1.65	14.3	--
GAD-B	0.16	1.07	15.5	--
GAD-C	0.15	0.84	15.5	0.24

**Figure 2.8: Ground Accuracy Designators ($M = 1$)**

In practice, in a manner similar to the aircraft, each LAAS ground station must demonstrate that it meets a 95% receiver accuracy level no larger than at least one of these GAD curves. In addition, there is an important requirement for the ground station. In LAAS operation, the ground station is required to provide values of σ_{gnd} for each approved measurement that are used for ensuring integrity in the airborne system (the details of airborne integrity verification are described in the next section). Gaussian models for 95% accuracy are not generally applicable to 10^{-9} -level integrity analyses

because these models do not necessarily bound measurement errors corresponding to such small probabilities [Rife04]. Therefore, although each ground station has to achieve a level of accuracy whose 95% sigma is no larger than one of the GAD models, the broadcast σ_{gnd} , which represents 10^{-9} -level accuracy, is not necessarily bounded by the model. Ground stations may need to broadcast values of σ_{gnd} that exceed their GAD models based on the environments of their receiver and antenna sites.

Model of Residual Ionosphere Error: σ_{iono}

Residual ionosphere errors depend on the distance between the user and the ground station. The closer the user comes to the ground station, the smaller the residual error is. The standard deviation of residual ionosphere errors, σ_{iono} (meters), is modeled as follows [Rtca01].

$$\sigma_{iono} = \sigma_{vig} \cdot (d_{gu} + 2\tau v_{air}) \cdot Oq(h_I, El) \quad (2-38)$$

where σ_{vig} is the standard deviation of the nominal ionosphere spatial gradient (m/km) in the vertical (zenith) domain (the subscript “vig” stands for *vertical ionosphere gradient*), d_{gu} is the distance in kilometers between the ground station and the user, τ is the time constant of the carrier-smoothing filter and is conventionally set to 100 sec in LAAS, v_{air} is the horizontal speed of the aircraft (m/s), Oq is the obliquity factor (unitless) given by equation (2.7) and h_I (the thin-shell height) is set to 350 km [Rtca01].

The term “ $2\tau v_{air}$ ” in equation (2-38) represents the additional error due to ionosphere divergence that occurs when the user aircraft traverses the ionosphere gradient over one smoothing time constant (τ). The model of residual ionosphere error will be discussed again in Chapter 4 to examine the impact of the anomalous ionosphere on LAAS, and in this chapter, the theory behind the error model (2-38) will be described in detail.

In LAAS operation, the ground station broadcasts a bounding (conservative) value of σ_{vig} to users, which compute σ_{iono} using the received σ_{vig} and their own speed and

position. It is suggested that the appropriate value of σ_{vig} for CONUS be 0.004 m/km [Klobuchar, Lee06a].

Model of Residual Troposphere error: σ_{tropo}

Residual troposphere errors depend on the prevailing atmosphere conditions around the ground station and on the altitude of the approaching user. The lower the user altitude is, the smaller the residual error is. The standard deviation of the residual troposphere errors, σ_{tropo} (meters), is modeled as follows [Rtca01].

$$\sigma_{tropo} = \sigma_N h_0 \frac{10^{-6}}{\sqrt{0.002 + \sin^2(El)}} (1 - \exp(-\Delta h / h_0)) \quad (2-39)$$

where σ_N is the uncertainty of the refractivity index (unitless), h_0 is the troposphere scale height in meters, and Δh is the aircraft altitude in meters. Physical explanations about σ_N and h_0 are found in [Misra(Chapter 5), McGraw00], but an important point is that these parameters depends on the meteorological condition at each site and that the ground station has the responsibility to broadcast the parameters (σ_N and h_0) that are consistent with prevailing conditions at the site. In practice, the parameters may be set to constant values that cover the worst-case conditions determined in advance by a meteorological investigation of the site [McGraw00].

This section has described how to evaluate the LAAS user position errors $\sigma_{vertical}$ and $\sigma_{lateral}$. In fact, these sigmas are also used to compute *Protection Levels* (PLs) in both vertical and lateral axes. The PL is a very important parameter for integrity that measures the reliability of the position estimation. The next section provides an overview of the LAAS integrity methodology, including the PL concept.

2.3 Integrity Methodology

LAAS R&D efforts have proposed methods to ensure integrity against various faulty situations. The concept of the PL—a position-domain error bound computed by the user

aircraft—takes a central role in these integrity methods. In fact, the methods developed in this research also refer to this concept. This section surveys the LAAS system architecture from the integrity perspective and provides a basic understanding of how PLs are used in LAAS.

2.3.1 System Architecture from Integrity Perspective

As discussed in Section 2.1, integrity is the ability of the system to warn the pilot within a specific time if the aircraft's position error exceeds a pre-specified Alert Limit (AL). Because the concept of integrity is most relevant in the user's position domain, and because only the user knows which satellites from the set approved by the ground station are being applied to position calculations, the user aircraft should make the final determination of position-domain integrity during the landing operation. To this end, the user computes a real-time position error bound called the Protection Level (PL) and evaluates if the current positioning error is bounded within the AL or not. In order for users to properly determine this, the ground station has the responsibility to provide information about the quality of the GPS ranging signals. To do this, the ground station executes several integrity monitoring algorithms that detect and exclude faulty signals. To make clear the basic roles of the PL and the integrity algorithms, this section introduces what risk sources are currently identified and specifies which risks are mitigated by the integrity algorithms prior to the broadcast of differential corrections and which risks are mitigated by the user calculation of PLs after differential corrections are received during a given time epoch.

Recall that the allowable integrity risk for CAT IIb LAAS is 10^{-9} for any 15-second exposure time in the vertical dimension or any 30-second exposure time in the lateral dimension. Because LAAS will be exposed to more than one risk source that can induce a hazardous positioning error, this allowable risk must be interpreted as the sum of tolerances for these potential risk sources. LAAS R&D efforts have identified these risk sources and have allotted the total allowable risk to these sources based on their relative importance and severity. Figure 2.9 shows this integrity allocation tree [Rtca04].

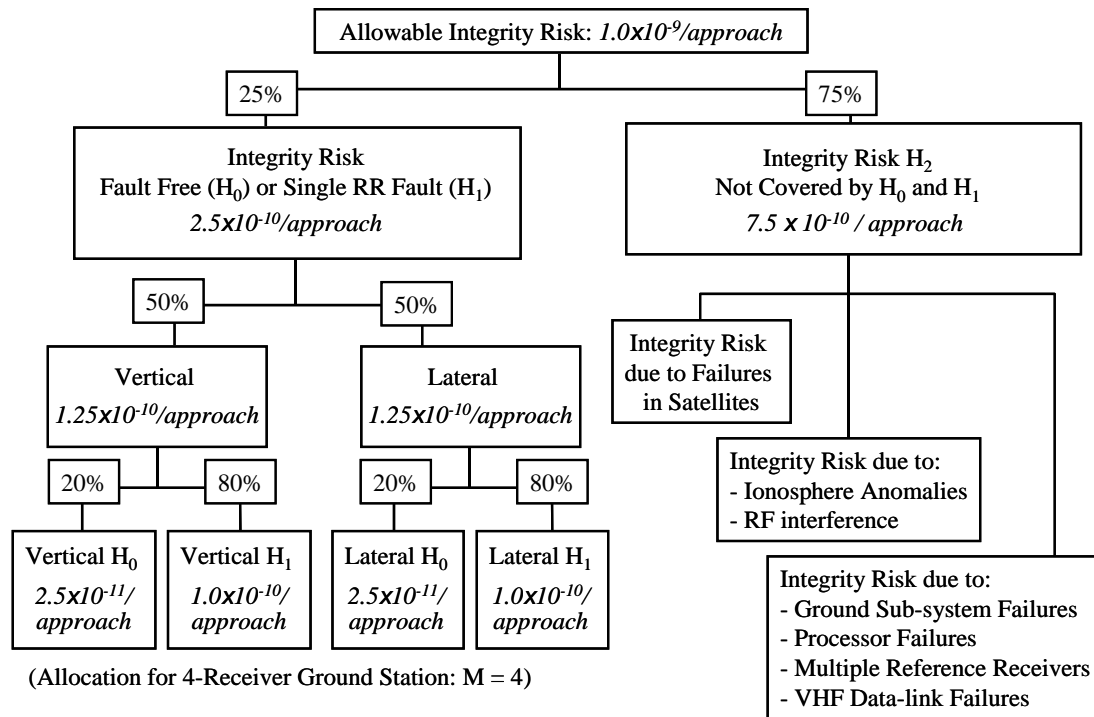


Figure 2.9: LAAS Integrity Allocation Tree

The total allowable integrity risk is divided into sub-allocations to various possible risks. The first risk category includes hazardous positioning errors under the fault free condition and those under the single reference receiver fault. The second category includes all risks not included in the first category; for example, risks due to satellite failures, ionosphere anomalies, and VHF data-link failures. The original figure is found in [Rtca04] Figure D-3.

As this figure shows, the risk sources are first divided into three categories: risk under fault-free conditions, which is called H_0 risk; risk under undetected single (not multiple) reference receiver failures, which is called H_1 risk; and all other risks not covered by the H_0 and H_1 risks, which are on the whole called H_2 risks and which include the ionosphere anomaly. The fault-free condition (H_0) is considered because “fault-free” does not mean “error-free.” Even under the fault-free condition, where the GPS satellites, the airborne and ground receivers, and the medium that GPS signals travel through all behave normally, it is impossible to bound the positioning error within a finite value with absolute confidence; in other words, there always exists a tiny chance that a position error exceeds the AL.

A quarter of the total allowable risk is allocated to the H_0 and H_1 risks. This allocation is further divided by half such that 50% is given to the vertical dimension and 50% is given to the lateral dimension. Then, each remaining sub-allocation is equally divided among the H_0 and H_1 risks in accordance with the number of reference receivers. For example, if there are 2 reference receivers (receivers A and B), the risk is divided into 3 cases: the fault-free case, the failure of receiver A, and the failure of receiver B. The example shown in Figure 2.9 is for the four-receiver ground station ($M = 4$).

The remaining three quarters of the total allowable risk is allocated among all H_2 risk categories. However, unlike the H_0 and H_1 risks, there is no required way for further sub-allocations for each of H_2 risks to be conducted—these sub-allocations are the responsibility of each LAAS ground system manufacturer.

The integrity associated with H_0 and H_1 risks is ensured by user PL calculations, and the integrity associated with the H_2 risks is ensured by integrity monitoring methods implemented in the ground station (the only exception is the integrity risk due to large ephemeris errors, for which a PL variation called PL_e has been introduced [Pullen01, Pervan05]). Figure 2.10 illustrates the LAAS system architecture from the integrity perspective. The main objective of the ground-based integrity methods is to detect satellites whose ranging signals are most probably affected by the risk sources classified in the H_2 risks and to exclude these satellites from user position estimation. This exclusion is generally done by broadcasting differential corrections and integrity information associated only with the remaining satellites that have been verified to be fault-free.

The integrity information consists of σ_{gnd} , parameters for σ_{iono} (specifically σ_{vig}), parameters for σ_{tropo} (specifically σ_N and h_0), and B-values, all of which are used to evaluate the PL (B-values are described in the next subsection). Because the measurements that remain after ground screening can be considered to be either those under the fault-free condition (H_0) or those under the undetected single reference receiver failure condition (H_1), the error bound computed from these measurements will

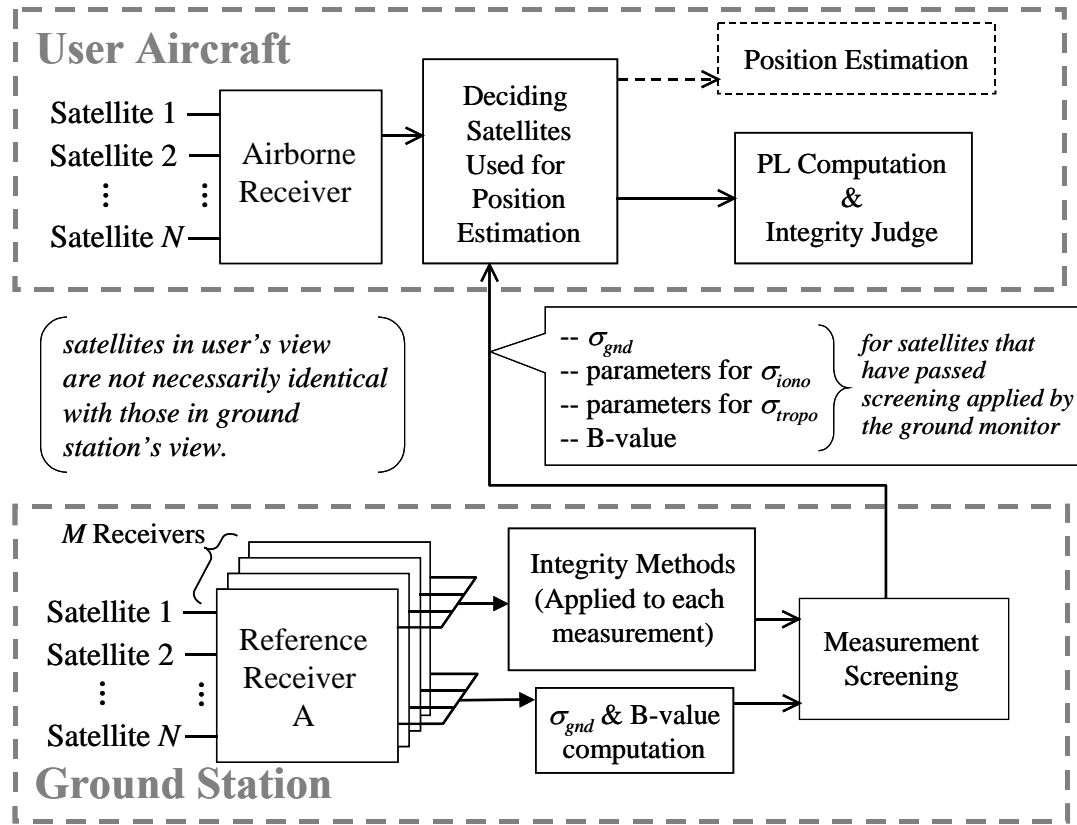


Figure 2.10: System Architecture from Integrity Perspective

Using various integrity algorithms targeted at different failure modes, the ground station detects anomalously erroneous range measurements and excludes them from the subsequent processes. For each remaining measurement, the ground station evaluates σ_{gnd} , σ_{iono} , σ_{tropo} , and B-values and broadcast them. The user aircraft evaluates its Protection Levels using information provided by the ground station and decides whether or not to complete the landing.

represent what the PL should be. Keep in mind that if the ground-based methods fail to detect faulty measurements, the resulting PL may fail to bound the actual positioning error; consequently, the landing is possibly exposed to a dangerous situation. To ensure that the risk of a hazard is acceptably low, the prior probability of this condition times the probability of missed-detection of the relevant ground-based algorithms must be small enough compared to the integrity risk sub-allocation associated with this condition.

2.3.2 Protection Level Concept

The PL is in fact a generic name for two parameters in LAAS: the *Vertical Protection Level* (VPL) for the vertical dimension, and the *Lateral Protection Level* (LPL) for the lateral dimension. System performance, such as availability, is typically dictated by the error bound in the vertical direction (namely the VPL) both because the Vertical Alert Limit (VAL) of 10 meters is much tighter than the Lateral Alert Limit (LAL) of 17 meters (see Table 2-1) and because the geometric diversity of the GPS satellite constellation is poorest in the vertical direction, typically causing larger vertical errors than horizontal errors when all else is equal. Therefore, the following discussion will consider the VPL only. The extension to the lateral direction (LPL) is straightforward and is nearly identical in form.

Let us think about the H_0 hypothesis. VPL_{H_0} is defined to satisfy the following equation.

$$\Pr(\text{vertical error} > VPL_{H_0} | H_0) \Pr(H_0) = \gamma_{H_0\text{-vertical}} \quad (2-40)$$

where $\Pr(H_0)$ is the *a priori* probability that the H_0 hypothesis is realized, and $\gamma_{H_0\text{-vertical}}$ is the allowable integrity risk for vertical H_0 integrity. If VPL_{H_0} is less than VAL, the probability that a vertical error exceeds VAL given the H_0 condition is theoretically less than the tolerance ($\gamma_{H_0\text{-vertical}}$). Conversely, if VPL_{H_0} is greater than VAL, it cannot be guaranteed that the probability of an error exceeding VAL is less than this tolerance. Therefore, in order to assure integrity under fault-free conditions, the airborne subsystem computes VPL_{H_0} in real time and warns the pilot as soon as the VPL_{H_0} exceeds VAL. Figure 2.11 illustrates this concept.

A closed-form equation to evaluate VPL_{H_0} is derived as follows. Manipulating equation (2-40) yields the following equation.

$$\Pr(\text{vertical error} > VPL_{H_0} | H_0) = \frac{\gamma_{H_0\text{-vertical}}}{\Pr(H_0)} = P_{ffmd} \quad (2-41)$$

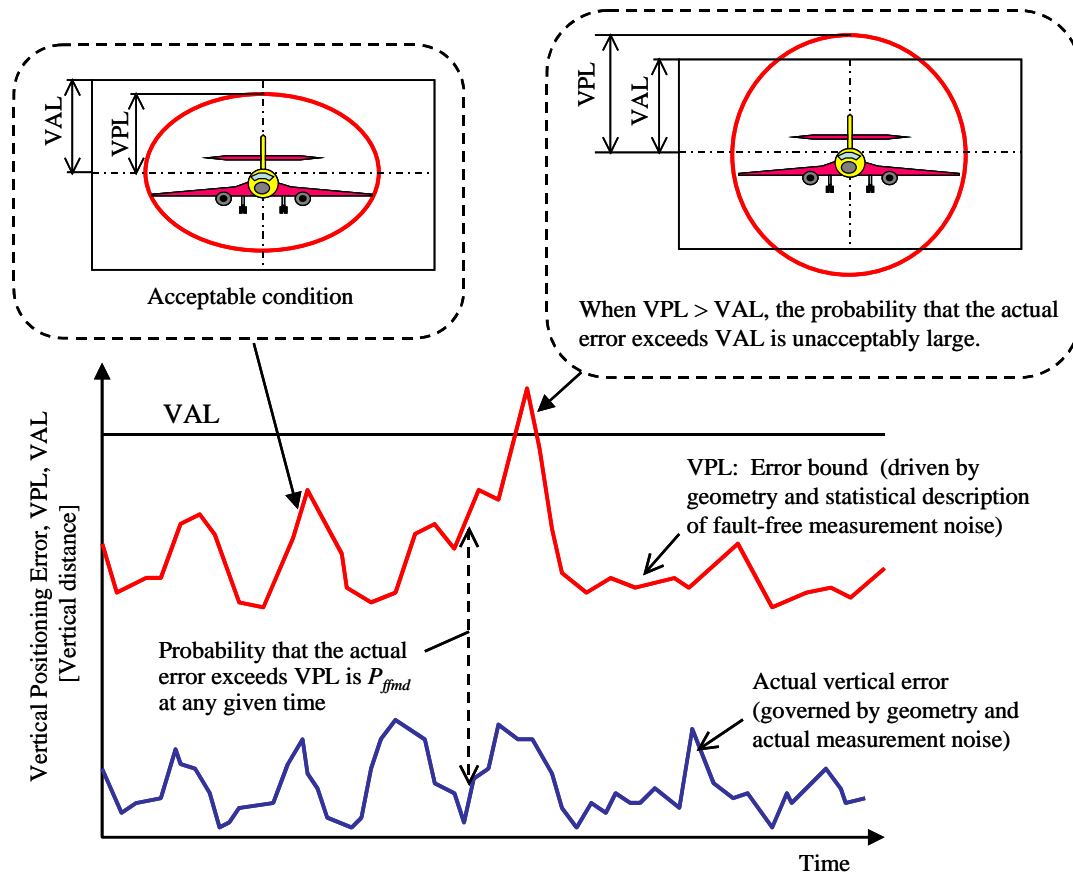


Figure 2.11: Integrity Determination Using Protection Level.

The true positioning error (blue curve) cannot be known; however, a theoretical confidence bound on the error can be established. For LAAS integrity, this bound in a given dimension is the PL (red curve). By definition, the probability that a true error exceeds the PL is no greater than the allowable integrity risk, P_{ffmd} . Therefore, if the airborne subsystem warns the pilot whenever the PL exceeds the AL, integrity is assured.

where P_{ffmd} can be interpreted as the maximum allowable risk that the vertical error exceeds the VPL_{H0} given the fault-free condition (the subscript “ffmd” stands for fault-free missed detection). As discussed in Section 2.2, under fault-free conditions, the distribution of vertical position errors is modeled as a zero-mean Gaussian with the standard deviation of $\sigma_{vertical}$ (see equation (2-30)). Hence, the value of VPL_{H0} can be determined by integrating this probability density up to P_{ffmd} .

$$\text{VPL}_{H_0} = -Q^{-1}\left(P_{\text{ffmd}}/2\right) \cdot \sigma_{\text{vertical}} \quad (2-42)$$

Figure 2.12 schematically expresses the relationship between VPL_{H_0} and the position-error distribution. The bell-shape curve shows the zero-mean Gaussian error distribution. The Q-function in equation (2-42) represents the cumulative probability in the negative-side tail of the Gaussian error distribution out-side VPL_{H_0} , which is the red-shaded area in the negative side of the plot.

As an example, let us derive the equation for VPL_{H_0} associated with a four-reference-receiver ground station. As shown in Figure 2.9, the tolerance for the vertical H_0 condition ($\gamma_{H_0\text{-vertical}}$) is 2.5×10^{-11} . The prior probability of the H_0 condition, $\text{Pr}(H_0)$, is generally (and conservatively) set to 1 because the system should work normally almost all the time. Accordingly, VPL_{H_0} for this configuration is given as follows.

$$\text{VPL}_{H_0} = -Q^{-1}\left(\frac{P_{\text{ffmd}}}{2}\right) \cdot \sigma_{\text{vertical}} = -Q^{-1}\left(\frac{\gamma_{H_0\text{-vertical}}}{2\text{Pr}(H_0)}\right) \cdot \sigma_{\text{vertical}} = 6.673\sigma_{\text{vertical}} \quad (2-43)$$

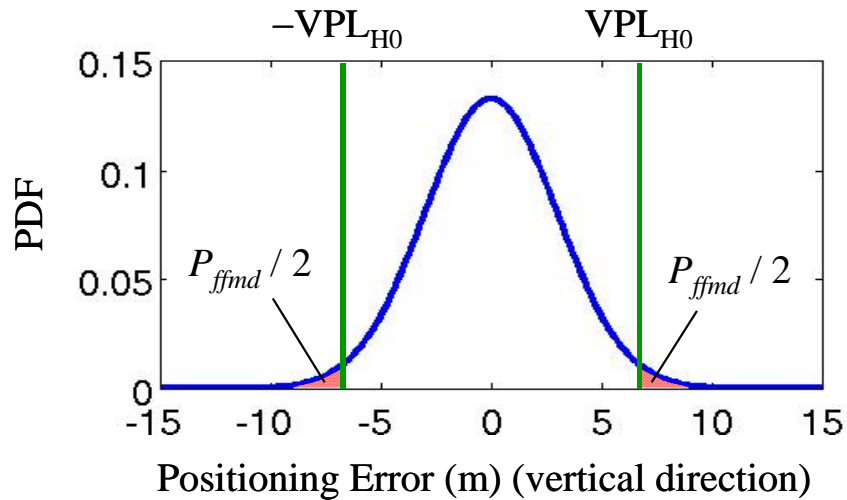


Figure 2.12: Position Error Distribution under Fault-Free Conditions and VPL_{H_0}

Recall that the computation of $\sigma_{vertical}$ requires four “primitive” sigmas— σ_{air} , σ_{gnd} , σ_{iono} , and σ_{tropo} (see equation (2-30) and (2-33)). The user evaluates σ_{air} by itself, and the necessary information to evaluate the other sigmas is provided by the ground station (see Figure 2.10). Therefore, the user can evaluate VPL_{H0} in real time and thus assure itself of sufficient integrity under fault-free conditions.

The VPL for the H_1 condition—undetected single reference receiver failure—can be derived based on the same framework as VPL_{H0} . An important difference between H_0 and H_1 conditions is the distribution of differential correction errors corresponding to each condition. The error distribution under the H_0 condition is a zero-mean Gaussian with a bounding standard deviation of σ_{gnd} . In contrast, the error distribution for the H_1 condition is modeled as a biased Gaussian whose bias is caused by an undetected reference-receiver malfunction. These biased-distributed differential corrections result in biased-distributed position errors; thus, the VPL_{H1} equation must take these biases into account. Figure 2.13 shows this concept. The left-hand figure shows the distribution of the differential corrections for a particular satellite which has a bias due to a reference-receiver malfunction, and the right-hand figure shows the resulting position-error distribution. The ground station estimates the bias for each differential correction and provides these estimates to the user, which computes VPL_{H1} using them. These bias estimates provided by the ground are called *B-values*, and the VPL_{H1} equation is given as follows.

$$VPL_{H1} = \max\{VPL_{H1,j}\} \quad \text{where } j \text{ represents a receiver } (j = 1, \dots, M) \quad (2-44)$$

$$VPL_{H1,j} = K_{md} \sqrt{\sum_{i=1}^N S_{vert,i}^2 \sigma_{H1,i}^2 + \left| \sum_{i=1}^N S_{vert,i} B_{i,j} \right|} \quad (2-45)$$

$$\sigma_{H1,i}^2 = \frac{M}{M-1} \sigma_{gnd,i}^2 + \sigma_{air,i}^2 + \sigma_{iono,i}^2 + \sigma_{tropo,i}^2 \quad (2-46)$$

For the four-reference-receiver ground station ($M = 4$), the inflation factor K_{md} (“*md*” stands for missed-detection) is given as 3.7 (unitless). Note that the ground station does

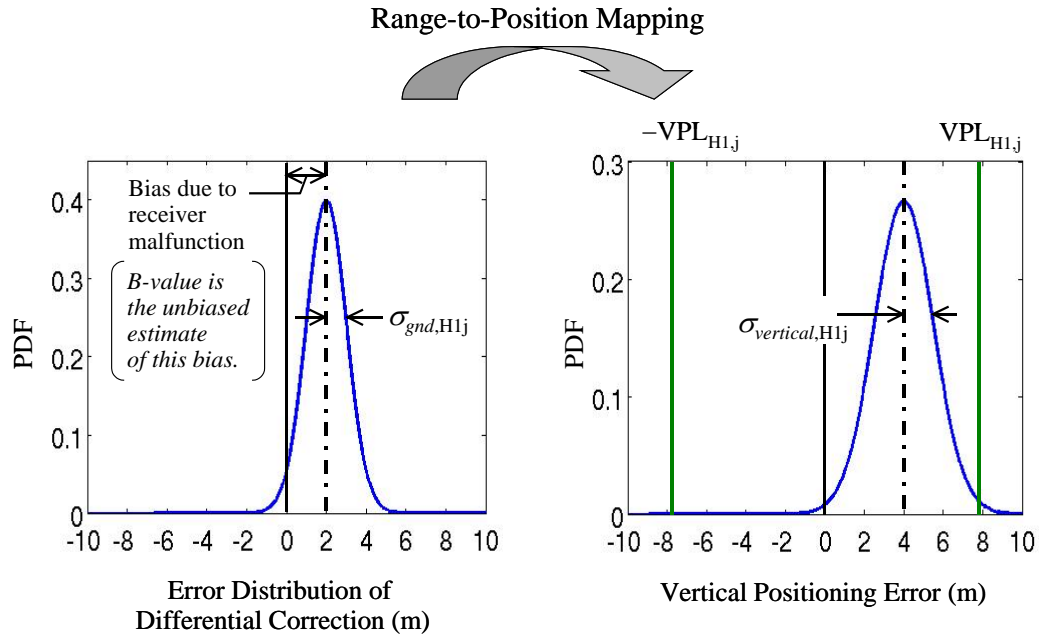


Figure 2.13: Biased-Distribution Due to Single Reference-Receiver Failure.

Because of the receiver failure, the error distribution of the differential correction is biased. Consequently, the distribution of the position estimation based on the faulty corrections is also biased.

not need to specify which receiver is faulted as it automatically computes B-values for all reference receivers under the hypothesis that each one is failed. The detailed logic behind equations (2-44), (2-45), and (2-46) is found in [Rtca04], and the method to compute B-values is described in Appendix B. As with VPL_{H0} , if VPL_{H1} is less than VAL, user integrity associated with the H_1 hypothesis is guaranteed.

Between VPL_{H0} and VPL_{H1} , the larger VPL actually dictates system availability. When all reference receivers are nominally functioning, VPL_{H0} tends to dominate over VPL_{H1} . In contrast, if a particular reference receiver fails, VPL_{H1} tends to be larger than VPL_{H0} .

2.3.3 Integrity Methods for H_2 Risks

Risk sources not covered by H_0 and H_1 conditions, namely H_2 risks, are generally taken care of by integrity monitoring algorithms implemented in the ground stations. LAAS

R&D efforts have developed a number of ground-based integrity methods. Among them is the *Signal Quality Monitor* (SQM) that takes care of the GPS ranging signal anomaly known as “signal deformation” [Mitelman, Phelts, Pullen02, Shively99, Zaugg, Rife06, Rtca04]. Signal deformation results from a failure of the signal-generating hardware onboard the GPS satellite and, if unmitigated, can induce unacceptably large measurement errors by significantly distorting the correlation function within the data tracking loop of the GPS receiver. To detect this anomalous signal behavior, SQM observes two types of metrics (*lambda test metric* and *rate test metric*) for each range measurement and compares them with a predetermined threshold derived based on a range-domain error bound called *Maximum-allowable Error in Range* (MERR), which is somewhat analogous to the PL in the position domain [Mitelman, Phelts, Pullen02]. If an unacceptable deformation is detected in the signal from a particular satellite, the satellite is then flagged and its measurements are excluded from position estimation.

Data Quality Monitoring (DQM) methods and *Measurement Quality Monitoring* (MQM) methods are other examples. DQM methods verify the reliability of navigation data broadcast by GPS satellites [Pullen01, Pervan05]. MQM methods detect sudden step errors and any other rapidly changing errors due to GPS clock anomalies and reference-receiver failures by verifying the consistency of both code and carrier measurements over the last few epochs [Xie01]. Existing range-domain monitoring methods like those above completely mitigate almost all fault modes introduced in Section 2.3.1 (more specifically Figure 2.9). However, it is worth to emphasize again that no existing method can mitigate unacceptable errors induced by anomalous ionosphere behavior to the degree required for CAT IIb LAAS.

2.4 Summary

This chapter has provided basic information related to LAAS system requirements, accuracy, and integrity that will be useful in subsequent chapters. The following bullets summarize the important points covered by this chapter.

- Section 2.1 designated three categories of precision approaches and landings and specified system requirements for Category IIb (CAT IIb) LAAS, the target of this research. In this section, four important parameters—Accuracy, Integrity, Continuity, and Availability—were defined.
- Section 2.2.1 modeled the various error sources that affect GPS ranging measurements. GPS receivers generally generate two types of range measurements: the code-phase measurement, and the carrier-phase measurement. Both of them were modeled, and their differences were highlighted.
- Section 2.2.2 introduced the concepts of carrier smoothing and DGPS and modeled the differentially corrected and smoothed code-phase measurement, which is the measurement finally used for position estimation. The mechanism of carrier smoothing described here will be referred to again in Chapter 4, where Dual-Frequency Carrier-Smoothing methods are discussed.
- Section 2.2.3 constructed an accuracy model consistent with nominal LAAS-aided positioning. To evaluate position accuracy, this model requires four “primitive” sigmas: the sigma representing the airborne receiver error, σ_{air} ; the sigma representing the ground station error, σ_{gnd} ; the sigma representing the residual ionosphere error, σ_{iono} ; and the sigma representing the residual troposphere error, σ_{tropo} . For each sigma, a widely-used model was introduced.
- Section 2.3.1 illustrated a basic LAAS system architecture from the integrity perspective and introduced two important building blocks forming the LAAS integrity strategy: the Protection Level (PL) and the combination of ground-based integrity algorithms. Currently-recognized integrity risk sources were introduced, and they were classified into risks mitigated by the PL and those mitigated by ground-based detection and measurement exclusion.
- Section 2.3.2 described the basic theory of the PL and demonstrated how to construct VPL_{H0} , a variation of the PL associated with fault-free conditions. The

basic PL concept and the VPL_{H0} derivation process will be referred to in Chapters 5 and 6, in which novel variations of the PL that mitigate errors induced by ionosphere anomalies are developed.

Now, this dissertation turns the attention to the details of threatening ionosphere anomalies. The next section briefly surveys previous efforts to model ionosphere anomalies and, based on this prior work, quantitatively specifies the anomalous conditions that this research must mitigate.

CHAPTER 3

Ionosphere Threat Model

The discovery of very unusual ionosphere behavior on April 6, 2000 [Datta-Barua02] is undoubtedly one of the most significant epochs in LAAS R&D. Datta-Barua *et al.* discovered this anomaly when analyzing ionosphere measurements known as WAAS *supertruth data* and published their results in 2002. Even before this discovery, it had been widely known that ionosphere behavior becomes anomalous and unpredictable during peaks of the eleven-year sunspot cycle [Klobuchar]. However, no one had suggested that, under intense solar conditions, ionosphere spatial gradients could increase by two orders of magnitude beyond typical levels. As the significance of such an ionosphere anomaly became known to the GPS community, two even more extreme ionosphere storms occurred in October and November of 2003. These two events further motivated the LAAS community to carefully examine the risk posed by ionosphere anomalies, and tremendous efforts have been devoted to analyzing these events [Dehel, Ene, Komjathy, Datta-Barua05].

Based on this data analysis, a geometric model that approximates anomalous ionosphere behavior with simple parameters has been developed. This model is called the *ionosphere anomaly threat model* and is relied on by most R&D efforts that tackle the ionosphere anomaly problem. This chapter describes the ionosphere threat model. First, the chapter defines the parameters that provide the basis for the model. Then, the

chapter offers a brief review of the work that contributed to determining the upper and lower bounds on these parameters based on analyzing the ionosphere storms in October and November 2003. Finally, the chapter defines a variation of the threat model that this research uses. Considering the potential expansion of the model due to the possible future discovery of more-severe ionosphere storms, this research uses a modified model that has wider parameter ranges than the current model.

3.1 Threat Model Parameter Definitions

Figure 3.1 shows a Matlab-generated visualization of the vertical ionosphere error over the eastern half of the Conterminous United States (CONUS) on November 20, 2003. A region of large ionosphere error spreads from southeast to northwest and changes its shape in a manner that is clearly nonlinear. As these snapshots imply, detailed behavior of this particular anomalous ionosphere example would be best modeled with nonlinear parameters, such as a wave front having a time-varying curved surface. However, it is impossible to generate a single nonlinear model that adequately represents all observed ionosphere anomalies. Thus, a simplified linear model was chosen as a best generalization of what has been observed in the anomaly database.

Considering a segment of anomalous ionosphere behavior as a linear semi-infinite wave front with constant propagation speed relative to the ground, the resulting ionosphere anomaly threat model expresses the specifics of the anomaly behavior with three parameters: the spatial gradient across the wave front in terms of slant (not vertical) ionosphere error, the forward propagation speed of the wave front, and the width of the wave front. Figure 3.2 illustrates this simplified wave front. Here, the spatial gradient of α (m/km) means that, for a given satellite, if the gradient affects both a user and a ground station that are separated by 1 km, their ionosphere errors differ by α meters regardless of the satellite's elevation angle.

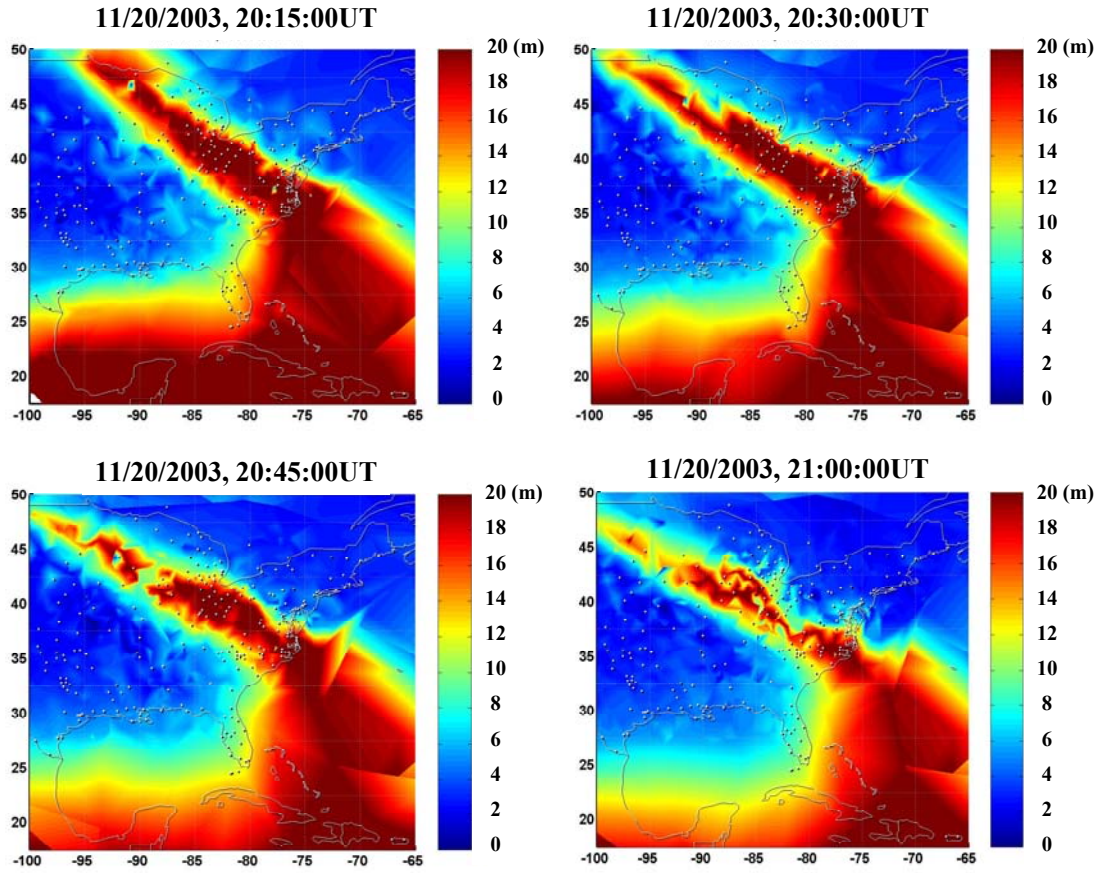


Figure 3.1: Matlab-Generated Visualization of Vertical Ionosphere Error Distribution

The subplots are “snapshots” of distribution of vertical ionosphere errors over the eastern part of the United States which are taken 15 minutes apart. It is clearly shown that a big belt-shaped feature exists over the northeastern part and gradually disappears. The original figure is found in [Luo04].

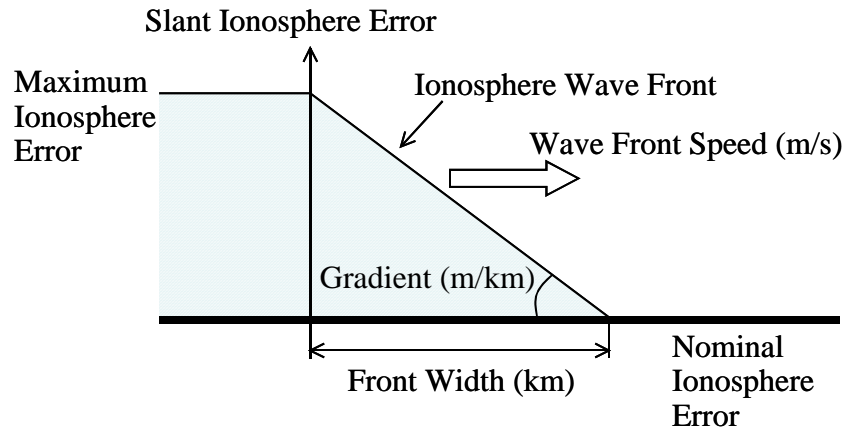


Figure 3.2: Simplified Model of Ionosphere Anomaly

It should be noted that the originally proposed threat model had a spatial-gradient parameter in the vertical (not slant) domain [Luo02, Luo03, Luo04]. When using this model, gradients in the slant domain were computed by applying obliquity factors (see equation (2-7)) corresponding to the elevation angles of the ranging signals in question. However, both because the vertical gradient includes uncertainty due to applicability of the ionosphere thin-shell model, and because ionosphere anomalies affect the LAAS user primarily through range measurements in the slant domain, the current model uses the slant-domain ionosphere gradient. As described in the next section, the maximum gradient of this model is a function of satellite elevation angle.

3.2 Ionosphere Anomaly Data Analysis

In brief, data analysis of the ionosphere anomalies in October and November 2003 had the purpose of “filling in” the parameter space of the threat model with actual anomalous ionosphere data. This section briefly reviews these efforts and describes currently authorized ranges on the threat model parameters that were determined based on outcomes of this data analysis.

Generally, two types of data have been used for the ionosphere data analysis: WAAS *supertruth data*, and data from the *National Geodetic Survey Continuously Operating Reference Stations* (CORS) network of receivers (in fact, Figure 3.1 shown in the previous section was generated by using CORS data). WAAS supertruth data comes from ionosphere measurements obtained from the WAAS network of 25 *Wide-area Reference Stations* (WRS's) [Enge96]. Figure 3.3 shows the locations of WRS's as of February 2006. Each WRS is equipped with three redundant L1/L2 dual-frequency receivers. Supertruth data is created by post-processing these dual-frequency GPS measurements and removing receiver and satellite biases to the extent possible. Details of this process are found for example in [Hansen, Shallberg]. Because supertruth data represents ionosphere errors measured by only the 25 WRS sites, it provides relatively sparse information at scattered points over the United States and nearby regions. Hence, supertruth data alone are not sufficient for investigating ionosphere behavior at the small separations relevant to LAAS operations.

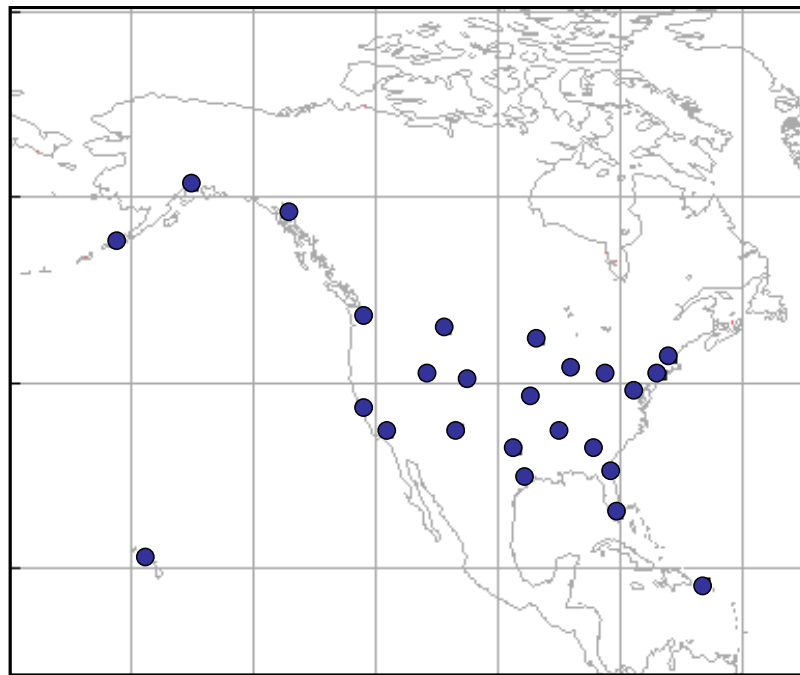


Figure 3.3: WRS Network

The CORS network is far denser than WAAS and has hundreds of dual-frequency receiver-equipped stations in the United States (see Figure 3.4). The Jet Propulsion Laboratory (JPL) has been estimating ionosphere errors by post-processing the dual-frequency CORS measurements using essentially the same methods used for WAAS supertruth data [Komjathy]. These ionosphere estimates do not have the same accuracy and reliability as WAAS supertruth data, because each CORS station has only one receiver, and this receiver is just based on *Commercial Off-The-Shelf* (COTS) equipment, unlike the certified receiver triads used in each WRS. However, the density of the data points is a significant benefit. In particular, the circled regions in Figure 3.4 have dense networks of stations whose baselines are in the range of 25 – 75 km and thus provide useful data for small-area-based data analysis. Hence, most of the data analysis was conducted inside these regions, combining sparse WAAS supertruth data with much-denser CORS data [Dehel, Ene, Komjathy, Datta-Barua05].

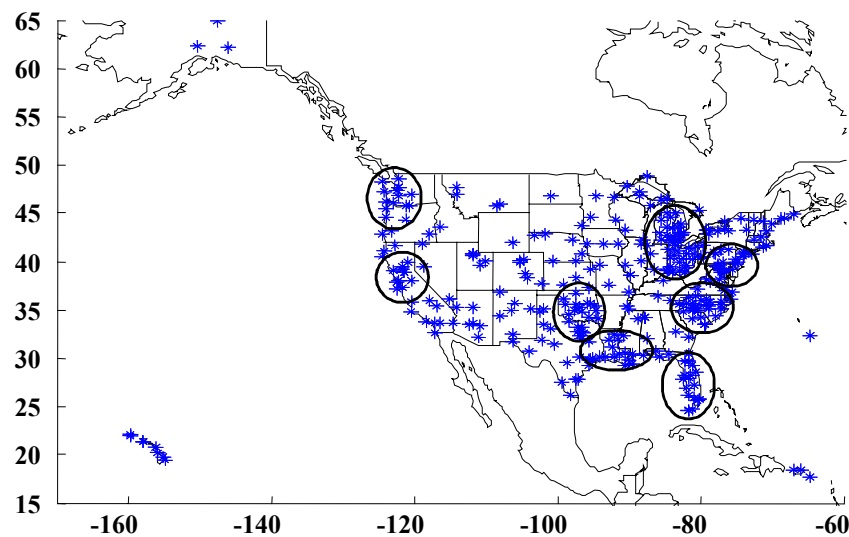


Figure 3.4: CORS Network and Selected Clusters

For data analyses, stations in the circled regions are used because these regions have dense networks of stations whose baselines are in the range of 25 – 75 km. The original figure is found in [Luo04].

Figure 3.5 shows an example of ionosphere errors observed by several CORS stations located in the Ohio/Michigan region on 20 November 2003 [Pullen06]. As shown in this figure, seven CORS stations almost simultaneously observed a very unusual change in the ionosphere error where the errors first steeply rise, then vary up and down at a rapid rate, and suddenly fall back towards zero. Data sets showing this kind of eccentricity were analyzed in the context of the threat model geometry, and approximate information regarding the threat model parameters—spatial gradient, wave front speed, and front width—was extracted. For example, in the particular data set shown in Figure 3.5, the maximum spatial gradient of 0.35 m/km was found in the sharp falling edge

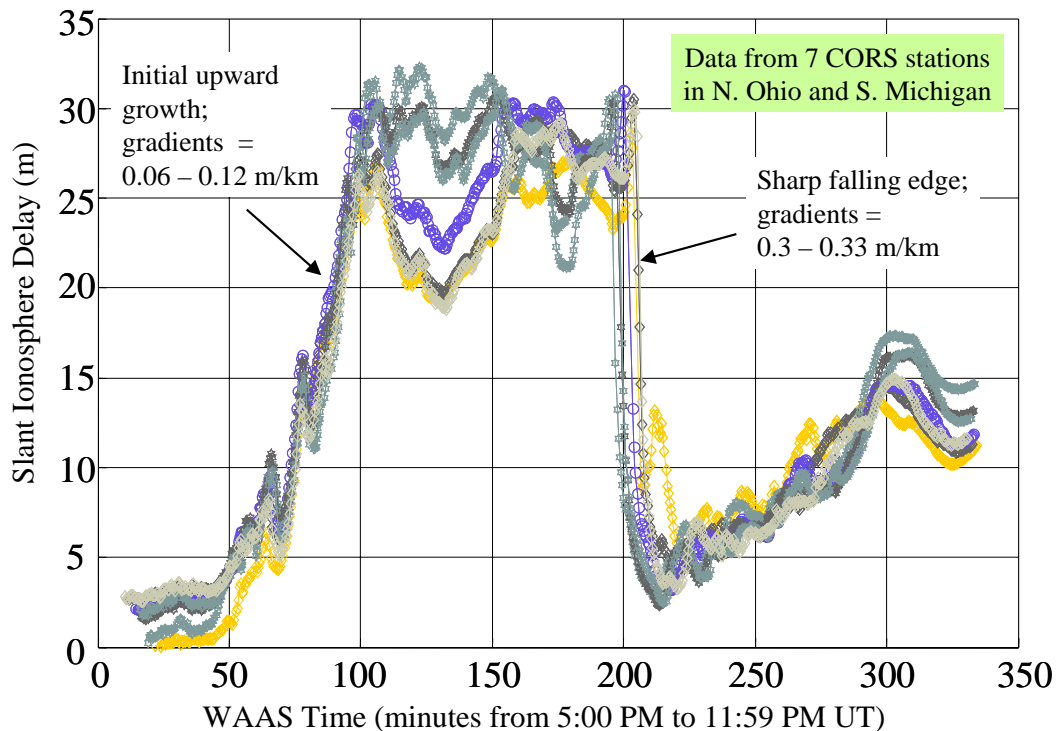


Figure 3.5: Ionosphere Error Evolution during 11/20/03 Ionosphere Storm in Northern Ohio and Southern Michigan

Within the steep upward growth of ionosphere errors from 5 meters to 30 meters within about 50 minutes, ionosphere spatial gradients of 0.06 to 0.12 m/km were found. Within the sharp falling edge from 30 meters to 5 meters within about 20 minutes, spatial gradients of 0.3 to 0.33 m/km were found. The original figure is found in [Luo05].

between the stations named GARF and GAST. Details of the data analysis methods are found in [Ene].

This data analysis revealed that there were clear correlations between spatial gradients and satellite elevation angles and between spatial gradients and wave front speed. In general, anomalous spatial gradients on lower-elevation satellites are somewhat smaller than those on higher-elevation satellites. Moreover, wave fronts having extremely large gradients, such as more than 0.2 m/km, generally had higher speeds. Although these features are purely data-derived and there is no theoretical explanation for them, in order to avoid unnecessary conservatism, the threat model parameter ranges were based on these data points.

Table 3-1 shows the currently confirmed ranges of the threat model parameters [Lee06b]. As shown in this table, ranges are first classified into two groups based on the elevation angle with a threshold of 12 degrees; then, each group is divided again into two groups based on the wave front speed with a threshold of 90 m/s. As noted above, wave fronts having the maximum gradient belong to the high-elevation/high-speed category. This threat model is deemed as the final version in the CAT I LAAS development [Lee06b].

Table 3-1: Currently Confirmed Ranges of Threat Model Parameters

Elevation	Speed (m/s)	Width (km)	Gradient (m/km)
Low: <12 deg	High: 90 – 750	25 – 200	0.030 – 0.150
	Low: 0 – 90	25 – 200	0.030 – 0.125
High: ≥12 deg	High: 90 – 750	25 – 200	0.030 – 0.330
	Low: 0 – 90	25 – 200	0.030 – 0.125

3.3 Threat Model Used in This Research

As discussed in the previous section, the current parameter ranges are determined based on actual ionosphere anomaly data. This implies that, if an extreme ionosphere behavior that does not lie inside these ranges is discovered in existing ionosphere data sets or occurs in the future, the model should be expanded so as to cover the newly discovered data point. To design an integrity method robust against such potential expansion, this research includes extra margin in the gradient magnitude. Moreover, because the current parameter ranges are set for supporting CAT I LAAS that has much less stringent integrity requirements, it is reasonable to consider extra margin when targeting CAT III LAAS.

Table 3-2 shows the parameter ranges chosen to include margin. As shown in this table, the new model is not only larger but simpler than the current model. While the current model has multiple gradient ranges depending upon front speed and satellite elevation, the new model has a single gradient range independent of speed and the elevation. The remainder of this dissertation uses this expanded and simpler threat model.

Table 3-2: Threat Model Parameters Used in This Research

Elevation	Speed (m/s)	Width (km)	Gradient (m/km)
All Elevations	0 – 750	25 – 200	0.00 – 0.40

CHAPTER 4

Carrier-Smoothing Methods: Assessment of Ionosphere Impact

The risk of ionosphere anomalies to LAAS users comes from residual ionosphere errors (after DGPS corrections are applied) that are induced by large ionosphere spatial gradients affecting LAAS operations. As discussed in Chapter 2, error reduction by DGPS relies on the fact that ionosphere errors on airborne and ground station range measurements are almost identical within the LAAS service area (45 km), as shown in Figure 4.1 (a). However, once an extreme ionosphere gradient affects a LAAS-aided landing, dissimilar ionosphere errors on the airborne and the ground measurements could induce a large residual error on the differentially corrected measurement (see Figure 4.1 (b)), causing a potentially-hazardous position error.

Based on the linear-wave-front model described in the previous chapter, the instantaneous difference between airborne and ground ionosphere delays can be computed as a product of the ionosphere spatial gradient (α) and the distance between the user and the ground station (d_{gu}), assuming both of them are included within the linearly-changing component of the wave front. Hence, at first glance, the residual ionosphere error after the DGPS correction seems to be equal to this product ($\alpha \cdot d_{gu}$). However, things are not so simple. The airborne and ground ionosphere errors also

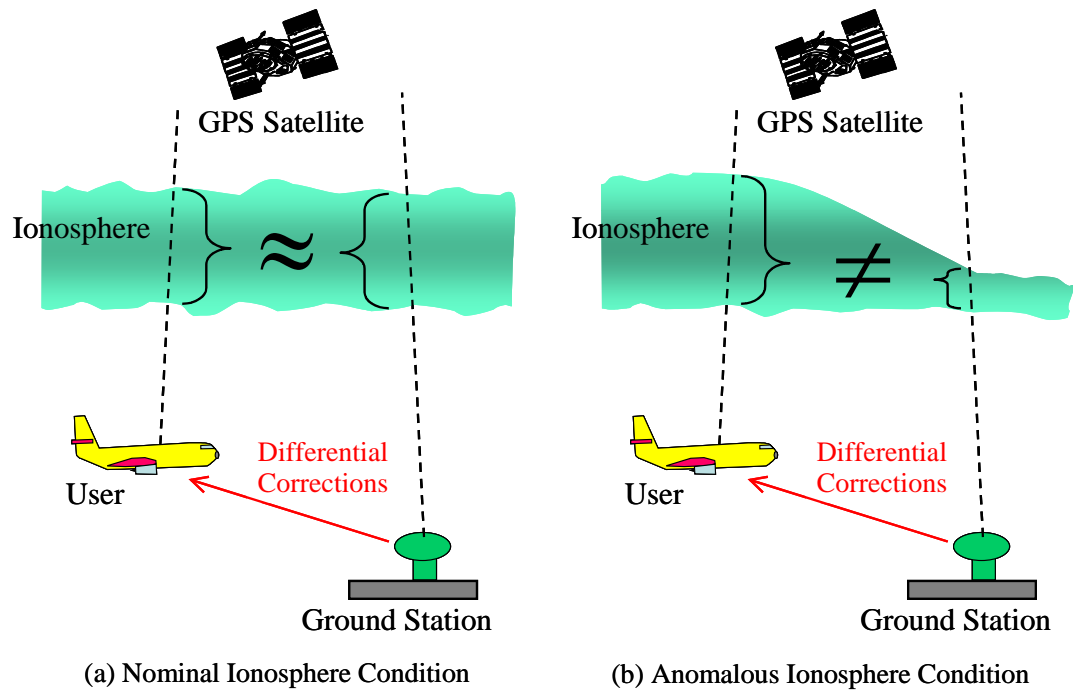


Figure 4.1: Ionosphere Effect on LAAS-aided Landing

(a) Under nominal ionosphere conditions, ionosphere errors on airborne and ground measurements correlate very well with each other. (b) Under anomalous conditions, in contrast, airborne and ground ionosphere errors are decorrelated even within the short baseline of the LAAS service area due to the large ionosphere spatial gradient between them.

change over time due to the relative motion between the ionosphere and the range signal paths. These time-varying ionosphere errors are fed into the carrier-smoothing filter that is intended to reduce multipath and thermal noise errors, inducing additional errors in the airborne and the ground receivers. Thus, two factors cause residual ionosphere errors under anomalous conditions: (1) the large spatial gradient that affects the airborne and the ground measurements, and (2) the induced temporal gradient of the ionosphere error on each measurement.

Divergence-Free Smoothing (denoted in the remainder of this dissertation as “DFree”) and Ionosphere-Free Smoothing (denoted in the remainder of this dissertation as “IFree”) operate upon these two factors and reduce or remove the ionosphere impact

within LAAS-corrected range measurements. In order to demonstrate the benefit of these methods, this chapter evaluates and compares the effect of the worst ionosphere anomaly (using the linear-wave-front model) on future LAAS architectures that use dual-frequency DFree or IFree in place of today's Single-Frequency Carrier Smoothing (denoted in the remainder of this dissertation as SFCS). First, Section 4.1 specifies the geometry of the front-affected landing, which serves as the “baseline” geometry for anomalous-ionosphere situations. Based on this geometry, Section 4.2 theoretically assesses the impact of the ionosphere wave front when using SFCS. Section 4.3 introduces the theories of DFree and IFree and evaluates ionosphere effects upon them. Section 4.4, in contrast to the theoretical analysis, evaluates the ionosphere impact using empirical data. By injecting simulated ionosphere errors into the empirical data taken by two closely-located receivers, the section simulates anomaly-affected landings and evaluates user errors for each method. Finally, Section 4.5 summarizes this chapter.

4.1 Geometrical Specification of LAAS Operation Affected by Ionosphere Wave Front

This section geometrically models the condition where an ionosphere wave front is affecting a ground station and a user aircraft that is conducting a CAT III landing. Also described are several basic models that dictate relationships between airborne and ground ionosphere behavior.

Figure 4.2 depicts this baseline geometry. As shown in the figure, this research assumes that the *decision point*—a point on the ground corresponding to the decision height—is 5 km from the ground station; and that the user aircraft passes this point with a velocity of 0.07 km/s, which is a typical landing velocity for jet aircraft. Note that, because a ground station has multiple reference receivers, the location representing the ground station, which is called *reference point*, is usually given at the centroid of the reference receiver locations. In an ideal case, the ground station (reference point) would be sited at the decision point such that the ionosphere error would be completely canceled at the point through the DGPS correction. In fact, it is the optimal location for single-runway

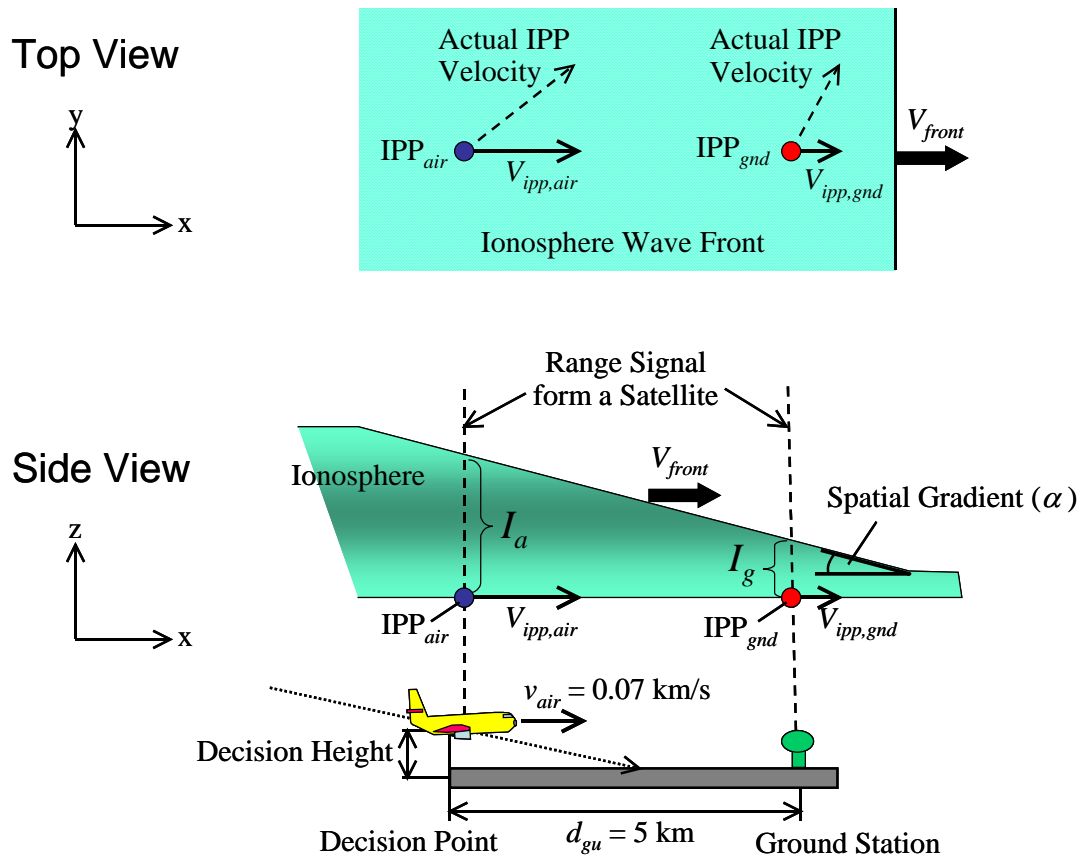


Figure 4.2: Baseline Geometry of LAAS-aided Landing under Ionosphere Anomaly

The decision point is assumed to be located 5 km from the ground station, and the user aircraft passes this point with a velocity of 0.07 km/s. Only ionosphere wave fronts that move along the x-axis are considered. Movement of a signal path is represented by the velocity of the IPP relative to the path.

airports. However, LAAS has the major benefit that only one ground station can serve all runways and approaches at the airport, and the same quality of service is expected for all supported approaches. Hence, for multiple-runway airports, the ground station would ideally be located such that the distances from it to all approach decision points are close to the same. Considering a typical large multiple-runway airport in CONUS, the 5 km separation is reasonable except for perhaps the very largest airports (Denver and Houston/IAH, where two LAAS ground stations each may be needed to cover all runways).

In Figure 4.2, an ionosphere wave front that has a constant (in time) gradient of α m/km is affecting the range measurements from one particular satellite to the user aircraft and the ground station. I_a and I_g in Figure 4.2 represent the instantaneous ionosphere errors on the airborne and ground measurements, respectively. The difference of these errors is given as the product of the gradient (α) and the distance between the user and the ground station (d_{gu}).

$$I_a - I_g = \alpha \cdot d_{gu} \quad (4-1)$$

Note that d_{gu} is 5 km at the decision point, as specified above.

In addition to the instantaneous geometry shown in Figure 4.2, the dynamics of the geometry are also an important issue for analyzing ionosphere effects. In particular, there are three essential velocities: the velocity of the ionosphere wave front, which is denoted by V_{front} (m/s); and the velocities of the signal paths from the satellite to the airborne and the ground receivers, which are denoted by $V_{ipp,air}$ and $V_{ipp,gnd}$ respectively. Although, in practice, the wave front can move in an arbitrary direction in the horizontal plane, this dissertation considers only the wave fronts moving along the x-axis (the horizontal axis along the approach glide-path) because such wave fronts induce the worst-case error given an anomalous spatial gradient. This point is clearly illustrated in Figure 4.3. The airborne and ground signals from a particular satellite always align parallel to the x-axis direction during the final approach. Hence, if an ionosphere wave front with a gradient of α has an angle of θ with respect to the x-axis, the ionosphere difference between the airborne and ground signals is given as $\alpha d_{gu} \cos(\theta)$, which is maximized when the angle θ is zero. This dissertation considers only this worst-case direction; i.e. the direction of V_{front} is assumed to be parallel to the x-axis.

The velocity of the signal path movement in the ionosphere can be approximately represented by the horizontal velocity of the ionosphere pierce point (IPP), a point where the signal path intersects the hypothetical thin-shell ionosphere model described in Section 2.2.1. As shown in Figure 4.2, $V_{ipp,air}$ is the x-component of the airborne IPP

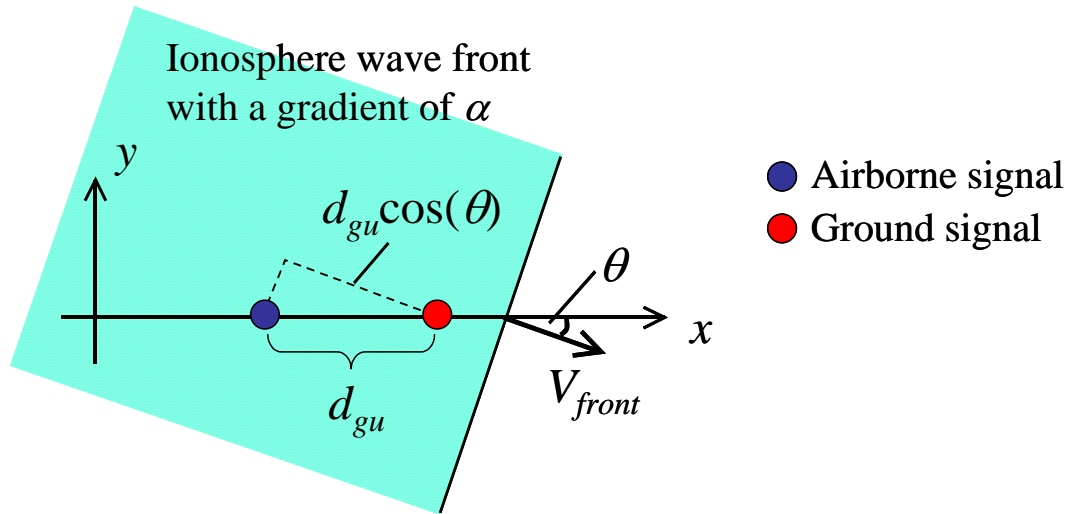


Figure 4.3: Moving direction of ionosphere wave front and ionosphere delay difference between airborne and ground signals

An airborne signal and its associated ground signal align parallel to the direction of x -axis. If an ionosphere anomaly wave front moves toward a direction forming an angle θ with respect to the x -axis, the difference in ionosphere delay between the airborne and the ground signals is given as “ $\alpha d_{gu} \cos(\theta)$ ” where α is the gradient of the wave front, and d_{gu} is the distance between the airborne and the ground signals.

velocity, and $V_{ipp,gnd}$ is the x -component of the ground station IPP velocity. The IPP velocity depends upon the assumed thin shell height, and this dissertation assumes that height to be 350 km.

The relative motion between the ionosphere wave front and the range signal path creates a change of the ionosphere error in time. Inspecting Figure 4.2, and noting that α is modeled as constant over time, one can easily show that the ionosphere change rate is given as follows.

$$\frac{dI_a}{dt} \equiv \dot{I}_a = \alpha \cdot (V_{front} - V_{ipp,air}) = \alpha \cdot dV_{front / ipp,air} \quad (4-2)$$

$$\frac{dI_g}{dt} \equiv \dot{I}_g = \alpha \cdot (V_{front} - V_{ipp,gnd}) = \alpha \cdot dV_{front / ipp,gnd} \quad (4-3)$$

where \dot{I}_a and \dot{I}_g are the temporal gradients of the airborne and the ground ionosphere errors, and $dV_{front/ipp,air}$ and $dV_{front/ipp,gnd}$ are the relative velocities between the wave front and the airborne and the ground IPPs.

Because distances from aircraft or ground stations to corresponding IPPs (the order of hundreds of kilometers) are sufficiently smaller than distances to GPS satellites (more than 20,000 kilometers), difference between the airborne and the ground IPP velocities is approximately equal to the aircraft velocity (v_{air}) yielding the following relationship.

$$\dot{I}_a - \dot{I}_g = \alpha \cdot (V_{front} - V_{ipp,air}) - \alpha \cdot (V_{front} - V_{ipp,gnd}) = -\alpha \cdot v_{air} \quad (4-4)$$

The geometry depicted in Figure 4.2 is considered to be the “baseline” geometry for the remainder of this dissertation, and the geometrical relationships discussed above (including equations (4-1) through (4-4)) provide important models for evaluating ionosphere front effects. Note that, in practice, an ionosphere wave front can affect range signals from multiple satellites at the same time, as shown in Figure 4.4. Even so, the situation for each satellite can be analyzed by means of the baseline geometry. Also

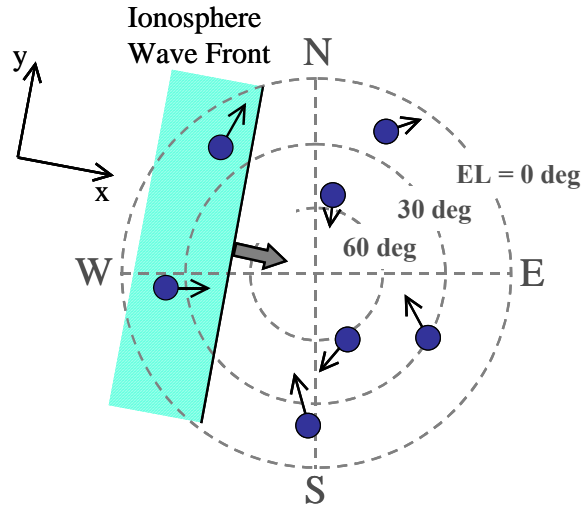


Figure 4.4: Two-Satellite Affected Case

note that the ground station has multiple reference receivers; hence, there should be multiple signal paths to the ground station. However, for simplicity, these paths are represented by the single signal path in Figure 4.2, and this simplification does not affect the accuracy of the assessment.

4.2 Theoretical Impact Assessment for Single-Frequency Carrier Smoothing

This section theoretically assesses the impact of the ionosphere wave front on the existing LAAS architecture, which employs Single-Frequency Carrier-Smoothing (SFCS) to reduce multipath and thermal-noise errors. The basics of SFCS were described in Section 2.2.2, but this section studies the method from the view-point of the ionosphere impact. Recall that SFCS is given by a block diagram shown in Figure 4.5. The filter inputs are the L1 code- and carrier-phase measurements (ρ_{L1} and ϕ_{L1}), which are modeled in the Laplace-domain as:

$$\rho_{L1}(s) = R(s) + I_{L1}(s) + \varepsilon_{L1}(s) \quad (4-5)$$

$$\phi_{L1}(s) = R(s) - I_{L1}(s) + N_{L1}(s) \quad (4-6)$$

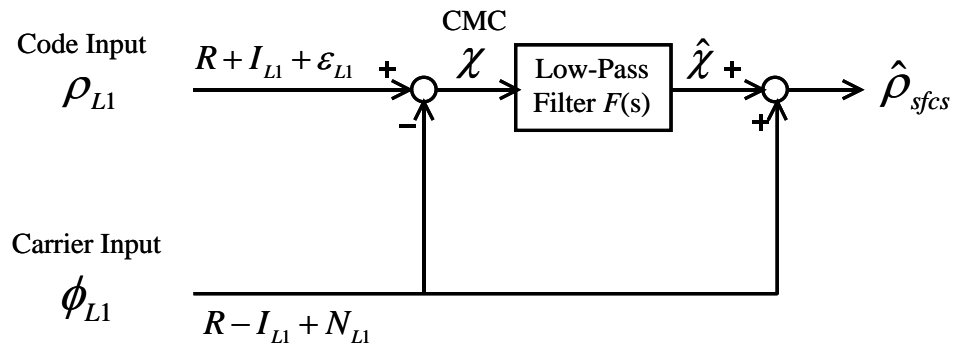


Figure 4.5: Block Diagram of SFCS

where R represents the true geometric range plus range errors common to both code- and carrier-phase measurements, such as satellite and receiver clock offsets, ephemeris error, and troposphere error; I is the ionosphere error; ε is the multipath plus thermal-noise error; and N is the carrier-phase integer ambiguity. The signal-subscript (“L1”, “L2”, or “L5”) is specified in the remainder of this dissertation if necessary. Note that the term “ R ” is not subscripted by “L1”, because this value does not depend upon the signal frequency. In other words, if a receiver simultaneously measures ranges using multiple signals on different frequencies, say L1 and L2, the values corresponding to “ R ” are identical for these measurements (i.e. $R_{L1} = R_{L2}$).

The transfer function of the low-pass filter in this block diagram is given as:

$$F(s) = \frac{1}{\tau s + 1} \quad (4-7)$$

where τ is the smoothing time constant, which is conventionally set to 100 seconds for LAAS.

The Code-Minus-Carrier (CMC) observable—a measurement fed into the low-pass filter and denoted by χ in Figure 4.5—is given as follows.

$$\chi_{SFCS}(s) = 2I_{L1}(s) - N_{L1}(s) + \varepsilon_{L1}(s) \quad (4-8)$$

As with the signal-subscript (“L1”, “L2”, or “L5”), the remainder of this dissertation specifies the smoothing method as a subscript (“SFCS”, “DFree”, or “IFree”) if necessary.

In the CMC equation (4-8), the ionosphere term “ $2I$ ” is often called *code-carrier divergence* because it results from the fact that the ionosphere causes the code- and carrier-phase measurements to diverge from each other by affecting them differently, namely by delaying code phase while advancing carrier phase by the same amount. Fed

into the low-pass filter, this code-carrier divergence induces a nuisance effect which is described shortly.

In SFCS, the smoothed CMC, $\hat{\chi}$, is combined with the carrier-phase measurement to generate the smoothed code-phase measurement, $\hat{\rho}$, which is modeled as follows.

$$\hat{\rho}_{sfcs}(s) = R(s) + (2F(s) - 1)I_{L1}(s) + F(s)\varepsilon_{L1}(s) \quad (4-9)$$

Of particular interest here is the ionosphere error. Let \hat{I} denote the ionosphere error on the smoothed code-phase measurement.

$$\hat{I}(s) = (2F(s) - 1)I(s) \quad (4-10)$$

$$\hat{I}(t) = \mathcal{L}^{-1}\{ (2F(s) - 1)I(s) \} \quad (4-11)$$

If the ionosphere error on the raw code-phase measurement, I , is constant, the SFCS filter has no effect on the error, i.e. $\hat{I} = I$. However, if the raw-code ionosphere error changes with time, the filter influences the error. From equations (4-7) and (4-10), the difference between the raw-code and the smoothed ionosphere errors is given by:

$$\delta I(s) = \hat{I}(s) - I(s) = (2F(s) - 2)I(s) = -\frac{2\tau s}{\tau s + 1}I(s). \quad (4-12)$$

Suppose that the raw-code ionosphere error has the form of a bias plus a ramp, that is:

$$I(t) = I_0 + \dot{I} t \quad (4-13)$$

or in the Laplace-domain:

$$I(s) = \frac{I_0}{s} + \frac{\dot{I}}{s^2} \quad (4-14)$$

The steady-state behavior of δI can be determined by substituting equation (4-14) into equation (4-12) and applying the *final-value theorem* of the Laplace transform.

$$\delta I_{ss} = \lim_{s \rightarrow 0} s \cdot \left[-\frac{2\tau s}{\tau s + 1} \left(\frac{I_0}{s} + \frac{\dot{I}}{s^2} \right) \right] = -2\tau \dot{I} \quad (4-15)$$

This result shows that the SFCS filter introduces an additional error or “delay” as a time-varying ionosphere error ($\dot{I} \neq 0$) passes through the filter, which is exactly the case of the baseline geometry defined in the previous section.

Recall that, in the baseline geometry, the user aircraft and the ground station are both suffering from time-varying anomalous ionosphere errors. Based on the discussions above, as this type of ionosphere error passes through the SFCS filter, the output ionosphere error is given as follows.

$$\hat{I}_a(t) = I_a(t) - 2\tau \dot{I}_a(t) \quad \text{for airborne measurements} \quad (4-16)$$

$$\hat{I}_g(t) = I_g(t) - 2\tau \dot{I}_g(t) \quad \text{for ground measurements} \quad (4-17)$$

Here, I_a and I_g are instantaneous ionosphere errors on the airborne and ground measurements, and \dot{I}_a and \dot{I}_g are their temporal gradients (see Figure 4.2). After applying DGPS, the residual ionosphere error ($\Delta \hat{I}$) is given as follows.

$$\Delta \hat{I}_{SFCS} = \hat{I}_a - \hat{I}_g = (I_a - I_g) - 2\tau (\dot{I}_a - \dot{I}_g) \quad (4-18)$$

This equation shows that the residual error is caused not only by the ionosphere spatial gradient, which is fairly intuitive, but also by the ionosphere temporal gradient, which is also significant.

When evaluating the residual ionosphere error using equation (4-18), the temporal gradients (\dot{I}_a and \dot{I}_g) are troublesome to compute, because they are a function of both

IPP velocity and ionosphere wave front velocity (see equations (4-2) and (4-3)). However, the geometrical relationships discussed in the previous section provide a much more simple way to evaluate the residual error. Substituting equations (4-1) and (4-4) into equation (4-18) yields the following relationship.

$$\Delta \hat{I}_{SFCS} = \alpha \cdot (d_{gu} + 2\tau v_{air}) \quad (4-19)$$

Now the evaluation of the residual error becomes much simpler; the necessary parameters are the ionosphere spatial gradient, the distance between the user and the ground station, and the velocity of the user.

Using this model, let us evaluate the worst-case error of the ionosphere-front-affected landing. As discussed in Chapter 3, the maximum gradient (α) considered in this research is 0.4 m/km. The aircraft velocity (v_{air}) and the distance (d_{gu}) at the decision point are 0.07 km/s and 5 km as described in the previous section, and the smoothing time constant (τ) is 100 seconds. Substituting these values into equation (4-19), the maximum residual ionosphere error in the range domain is evaluated as:

$$\max(\Delta \hat{I}_{SFCS}) = 0.4 \text{ (m/km)} \cdot [5 \text{ (km)} + 2 \cdot 100 \text{ (sec)} \cdot 0.07 \text{ (km/s)}] = 7.6 \text{ (m)}. \quad (4-20)$$

This error is for one satellite. If multiple satellites are affected by the front, or if only one satellite is affected by the front, but its geometry is very bad, the 7.6-meter ranging error could result in a hazardous positioning error.

This section has evaluated the effects of an ionosphere wave front on the existing SFCS-based LAAS architecture. Before moving on to Dual-Frequency Carrier-Smoothing methods, here is a recap of the key points about SFCS.

- When an ionosphere wave front affects a LAAS-aided landing, the instantaneous ionosphere difference between airborne and ground raw-code measurements remains as a residual error in the differentially-corrected measurements.

- In addition to the actual ionosphere difference, delay effects that appear in the SFCS filter outputs when time-varying ionosphere errors are fed into the filter induce additional errors.
- The theoretical worst-case residual ranging error is 7.6 meters, based on the assumed maximum spatial gradient of 0.4 m/km.

The next section discusses Dual-Frequency Carrier-Smoothing methods, which significantly mitigate the impacts of anomalous ionosphere wave fronts.

4.3 Theoretical Impact Assessment for Dual-Frequency Carrier Smoothing

As discussed in the previous section, during ionosphere anomalies, two different factors cause large residual errors on differentially corrected measurements. One is the large ionosphere spatial gradient affecting the user and the ground station, and the other is the ionosphere temporal gradient on each measurement that results from the relative motion between the ionosphere wave front and the signal path through the ionosphere. Divergence-Free Smoothing (DFree) and Ionosphere-Free Smoothing (IFree) operate upon these factors and significantly reduce the residual ionosphere errors. This section introduces the theories of DFree and IFree and evaluates the ionosphere effects on these methods.

4.3.1 Overview of New Civil Signals

First, let us overview the forthcoming civil signals. As introduced in Chapter 1, in the near future (probably within the next ten years), GPS will provide three civil signals: the L1 (currently available) signal, the L2 signal, and the L5 signal. Their carrier frequencies are 1575.42 MHz, 1227.60 MHz, and 1176.45 MHz, respectively. Figure 4.6 shows the signal spectra for these three signals. Note that a second civil signal in the L1 band, or “L1C”, will be introduced in the future [Hein06b, Stansell], but the

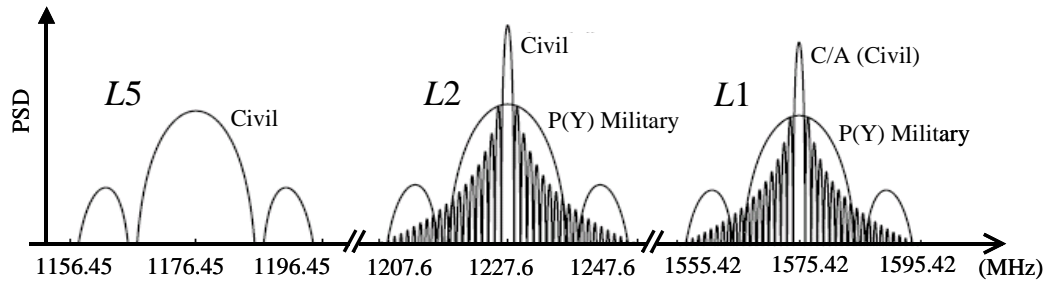


Figure 4.6: Signal Power Spectra of Three Civil Signals

In the future, a second civil signal in L1 band called “L1C” signal will be introduced. The spectrum of this signal is not included in this figure. Original plots are found in [Misra] Figure 9.20.

definition of this signal has not been formally approved, and its spectrum is not shown in Figure 4.6.

DFree and IFree require range measurements on two frequencies, which allows three possible combinations: L1/L2, L2/L5, and L1/L5. From the aviation view point, however, the L1/L5 combination is preferable because these two signals, unlike the L2 signal, reside in Aeronautical Radio Navigation Service bands. Therefore, this dissertation focuses only on the L1/L5 combination, although all the methods developed in this research are applicable for all three possible combinations.

While the new L5 civil signal uses a modernized wider-band structure than that of L1 C/A-code [Enge03], it basically has the same signal elements as the L1 signal: an RF carrier, ranging code, and navigation data. Moreover, the signal is subject to the same error sources as the L1 signal, allowing one to use the same measurement models.

$$\rho_{L5} = R + I_{L5} + \varepsilon_{L5} \quad (4-21)$$

$$\phi_{L5} = R - I_{L5} + N_{L5} \quad (4-22)$$

The primary differences between the L1 and L5 signals are the signal power and the chipping rate of the ranging codes. The radiated power of the L5 signal will be approximately four times greater than that of the L1 signal, and its chipping rate will be 10.23 MHz, which is ten times faster than the L1 chipping rate. These factors contribute to improve L5 signal acquisition and tracking performance; consequently, multipath and thermal noise errors on L5 measurements (ε_{L5}) are expected to be significantly smaller than those on L1 measurements (ε_{L1}) [Enge03].

Another difference between L1 and L5 lies in the ionosphere error. As described in Section 2.2.1, the ionosphere is a frequency dispersive medium and induces measurement errors that depend upon the RF carrier frequency. In terms of the *Total Electron Content* (*TEC*) along the signal path, the L5 ionosphere error is modeled (to first order) as follows.

$$I_{L5} = \frac{40.3 \cdot TEC}{f_{L5}^2} \quad (4-23)$$

where f_{L5} is the L5 carrier frequency (1176.45 MHz). Because *TEC* is common between L1 and L5 signals, their ionosphere errors are related to each other by:

$$I_{L5} = \frac{f_{L1}^2}{f_{L5}^2} I_{L1} \approx 1.79 I_{L1}. \quad (4-24)$$

Note that these ionosphere models (equations (4-23) and (4-24)) are based on the first-order approximation of the ionosphere refractive index for radio waves (see Section 2.2.1). However, because this approximation is sufficiently accurate [Datta-Barua06], this dissertation uses these models to derive dual-frequency carrier-smoothing models.

Although there are many other interesting characteristics regarding the forthcoming civil signals (including the modernized L2 civil signal), having shown the most relevant characteristics to this research, the focus is now turned to DFree and IFree. For more

details regarding the new civil signals, interested readers are referenced to the open literature such as [Enge03, Julien, Kaplan(Chapter 4)].

4.3.2 Divergence-Free Smoothing

Divergence-Free Smoothing (DFree) corrects for the effect of the ionosphere temporal gradient—the $2\tau\dot{I}$ delay effect that appears in the SFCS filter output when a time-varying ionosphere error is fed into the filter (see equations (4-16) and (4-17)). As described in Section 4.2, the delay effect is caused by code-carrier divergence ($2I$) being fed into the low-pass filter. The basic idea of DFree is to cancel out code-carrier divergence before the signals pass through the low-pass filter (hence the name “Divergence-Free”). Figure 4.7 illustrates the block diagram of DFree. As shown in this figure, the basic filter structure is the same as SFCS (see Figure 4.5); however, the filter inputs are different and are given as follows.

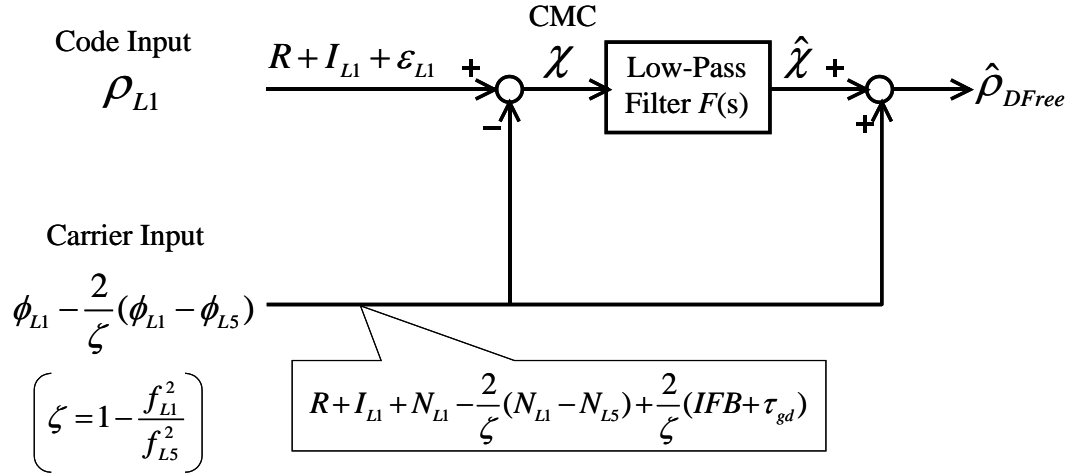
$$\text{Code input: } \rho_{L1} \quad (4-25)$$

$$\text{Carrier input: } \phi_{L1} - \frac{2}{\zeta}(\phi_{L1} - \phi_{L5}) \quad \text{where} \quad \zeta = 1 - \frac{f_{L1}^2}{f_{L5}^2} \quad (4-26)$$

Using the basic range measurement models (equations (4.6), (4.22), and (4.24)), the carrier input is modeled as:

$$\phi_{L1} - \frac{2}{\zeta}(\phi_{L1} - \phi_{L5}) = R + I_{L1} + N_{L1} - \frac{2}{\zeta}(N_{L1} - N_{L5}) + \frac{2}{\zeta}(IFB + \tau_{gd}). \quad (4-27)$$

Here, IFB is the receiver *interfrequency bias* that is caused by hardware differences between L1 and L5 signal paths and appears when combining L1 and L5 measurements made by the receiver, and τ_{gd} is the interfrequency bias of the satellite transmitter that is also caused by L1/L5 satellite hardware differences [Hansen, Wilson]. Because these values are cancelled within the filter along with carrier-phase integer ambiguities, they have no effect on smoothed measurements. The key point of this carrier input is, in fact,

**Figure 4.7: Block Diagram of DFree**

the positive ionosphere error, which was negative in SFCS due to the use of L1 carrier-phase measurements as the carrier input. Accordingly, differencing DFree code and carrier inputs generates “ionosphere-free” CMC.

$$\chi_{DFree} = \varepsilon_{L1} - N_{L1} + \frac{2}{\zeta}(N_{L1} - N_{L5}) - \frac{2}{\zeta}(IFB + \tau_{gd}) \quad (4-28)$$

This CMC is fed into the low-pass filter and then combined with the carrier input to restore the original range information. The filter output is the smoothed code-phase measurement, which is modeled as follows.

$$\hat{\rho}_{DFree}(s) = R(s) + I_{L1}(s) + F(s)\varepsilon_{L1}(s) \quad (4-29)$$

Note that there is no filtering effect on the raw-code ionosphere error as there is with SFCS; hence, the output ionosphere error does not suffer from the $2\tau\dot{I}$ delay when exposed to a ramp ionosphere input. Moreover, the random noise, $F(s)\varepsilon_{L1}(s)$, is the same as that of SFCS (see equation (4-9)).

Due to the absence of filtering effects, the residual ionosphere error after DGPS correction becomes equivalent to the absolute difference of the instantaneous ionosphere errors on the airborne and the ground measurements, which is given as follows.

$$\Delta \hat{I}_{DFree} = I_a - I_g = \alpha \cdot d_{gu} \quad (4-30)$$

This equation provides the worst-case residual error at the decision point.

$$\max(\Delta \hat{I}_{DFree}) = 0.4 \text{ (m/km)} \cdot 5 \text{ (km)} = 2 \text{ (m)} \quad (4-31)$$

Recall that the worst residual error for SFCS was determined to be 7.6 meters (see equation (4-20)). DFree significantly reduces the effect of the worst ionosphere wave front while, as noted above, keeping the noise error level the same as SFCS.

So far, this section has examined DFree based on L1 code-phase measurements. It is also possible to implement a variation of DFree that uses L5 code-phase measurements by swapping the L1 and L5 signals within the filter inputs. The output of this L5-based DFree variant is given as:

$$\hat{\rho}_{DFree,L5}(s) = R(s) + I_{L5}(s) + F(s)\varepsilon_{L5}(s). \quad (4-32)$$

L5-based DFree has an advantage and a disadvantage compared with L1-based DFree. The advantage is that, because L5 code-phase measurements are expected to be much less noisy than L1 measurements, the output noise level, $F(s)\varepsilon_{L5}(s)$, should be smaller than that of L1-based DFree, $F(s)\varepsilon_{L1}(s)$. The disadvantage is that, as shown in equation (4-24), the ionosphere error on the L5 measurement is about 1.79 times larger than that on the L1 measurement. Because the ionosphere threat model is defined in terms of L1-based ionosphere errors, when using L5-based DFree, the maximum gradient becomes 0.72 m/km ($\approx 1.79 \times 0.4 \text{ (m/km)}$). Consequently, the maximum residual ionosphere error becomes:

$$\max(\Delta \hat{I}_{DFree,L5}) = 0.72 \text{ (m/km)} \cdot 5 \text{ (km)} = 3.6 \text{ (m)}. \quad (4-33)$$

This advantage and disadvantage pose a trade-off when designing DFree-based integrity methods in Chapter 6.

4.3.3 Ionosphere-Free Smoothing

Ionosphere-Free Smoothing (IFree) is a smoothing method that completely removes all ionosphere-related errors. Figure 4.8 shows the IFree block diagram. As shown in this figure, the basic filter structure is the same as DFree and SFCS. The inputs are given as follows.

$$\text{Code input: } \rho_{L1} - \frac{1}{\zeta}(\rho_{L1} - \rho_{L5}) \quad (4-34)$$

$$\text{Carrier input: } \phi_{L1} - \frac{1}{\zeta}(\phi_{L1} - \phi_{L5}) \quad (4-35)$$

Based on the range measurement models (equations (4.5), (4.6), (4.21), (4.22) and (4.24)), it can be shown that these linear combinations of dual-frequency measurements generate “ionosphere-free” signals.

$$\rho_{L1} - \frac{1}{\zeta}(\rho_{L1} - \rho_{L5}) = R + \varepsilon_{L1} - \frac{1}{\zeta}(\varepsilon_{L1} - \varepsilon_{L5}) + \frac{1}{\zeta}(IFB + \tau_{gd}) \quad (4-36)$$

$$\phi_{L1} - \frac{1}{\zeta}(\phi_{L1} - \phi_{L5}) = R + N_{L1} - \frac{1}{\zeta}(N_{L1} - N_{L5}) + \frac{1}{\zeta}(IFB + \tau_{gd}) \quad (4-37)$$

The output of IFree is given as:

$$\hat{\rho}_{IFree}(s) = R(s) + F(s) \left(\varepsilon_{L1}(s) - \frac{1}{\zeta}(\varepsilon_{L1}(s) - \varepsilon_{L5}(s)) \right) + \frac{1}{\zeta}(IFB + \tau_{gd}). \quad (4-38)$$

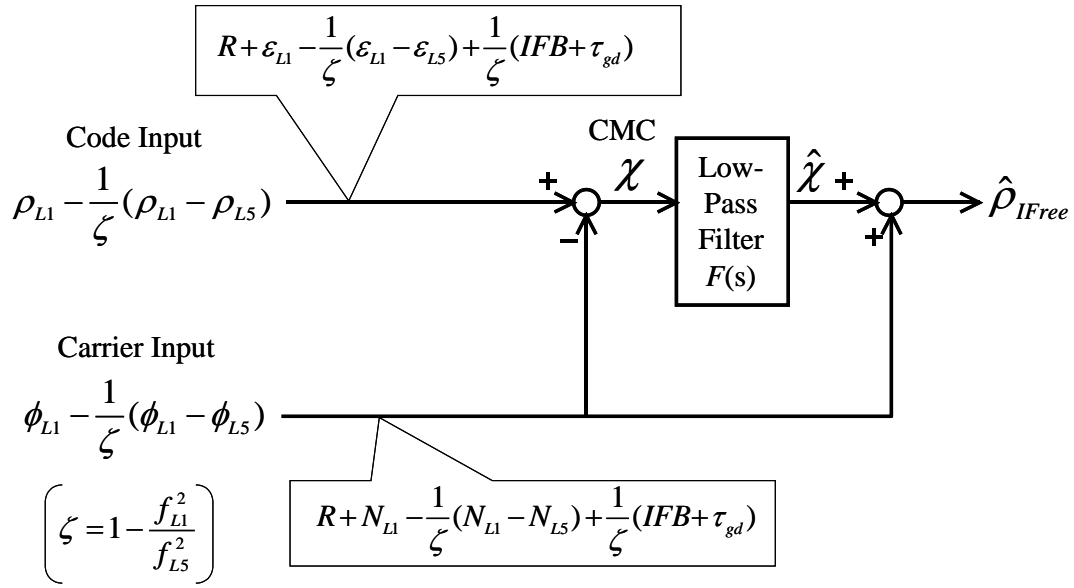


Figure 4.8: Block Diagram of IFree

The ionosphere-free inputs yield ionosphere-free output; consequently, the residual ionosphere error after the DGPS correction is zero, regardless of ionosphere conditions.

$$\Delta \hat{I}_{IFree} = 0 \quad (4-39)$$

Here, it is necessary to address the effect of interfrequency biases. Unlike DFree, the receiver and satellite interfrequency bias terms (IFB and τ_{gd}) remain in the filter output. The satellite bias (τ_{gd}) is cancelled through application of DGPS corrections because both ground station and users experience the same bias. On the other hand, the receiver bias value (IFB) is unique to each receiver and is not cancelled through DGPS corrections. However, just like the receiver clock offset, this bias affects all measurements by the same amount; hence, it is estimated within the clock offset as part of position estimation. Accordingly, IFB poses no negative effects on position estimation.

As shown above, IFree is immune to ionosphere-related problems; hence, it appears on the surface to be the best of the three smoothing methods described in this dissertation.

However, a critical drawback of IFree is the large noise error on the output signals. Due to the use of dual-frequency code-phase measurements, outputs of IFree are influenced by code errors on two frequencies and are hence much noisier than those of DFree and SFCS both of which use only single-frequency code-phase measurements as the code input. This large noise level has a negative effect on the integrity method, preventing IFree from being used as the primary filter in LAAS. This trade-off is discussed in detail in Chapter 5.

4.4 Empirical Demonstration of Ionosphere Impact

Sections 4.2 and 4.3 analytically evaluated ionosphere anomaly effects on the three smoothing methods. This section examines whether or not these assessments agree with the behavior of actual measurements. Simulated ionosphere errors are artificially injected onto empirical measurements taken by closely-located dual-frequency GPS receivers under nominal ionosphere conditions, and residual user errors during LAAS-aided landing under the worst ionosphere condition are evaluated.

One concern about this experiment is that DFree and IFree based on the L1/L5 combination cannot be implemented due to the absence of the L5 signal in current GPS satellites. This experiment, instead, uses semi-codeless L1/L2 dual-frequency receivers that generate L2 code- and carrier-phase measurements from the existing (encrypted) L2 signals by using a technique called *semi-codeless tracking* [Keegan, Lawrence, Lennen]. Compared with the L2 measurements taken by these receivers, coded L5 measurements in the future should be less noisy due to the enhanced characteristics of the L5 signal (see Section 4.3). However, in these ionosphere anomaly tests, measurement noise is overwhelmed by the injected ionosphere errors; consequently, the difference in measurement noise between the L2 and the L5 signals does not affect the results significantly. In fact, all simulation results are consistent with the theoretical evaluations given above.

4.4.1 Experimental Setup

Empirical measurements were taken by two dual-frequency antenna/receiver systems that the Stanford GPS laboratory had developed in previous work related to LAAS and WAAS. One antenna is sited on the rooftop of the Stanford Durand building, and the other is sited on the Stanford HEPL (Hansen Experimental Physics Laboratory) rooftop that is separated from the Durand rooftop by approximately 145 meters. The relative position of these antennas is illustrated in Figure 4.9. Both antennas are NovAtel Pinwheel (survey grade) antennas, and each of them is connected to a NovAtel OEM-4 semi-codeless L1/L2 dual-frequency receiver.

The Durand and the HEPL systems are assumed to be the airborne and the ground systems, respectively. Raw measurements taken by the HEPL system are first smoothed by a selected carrier-smoothing filter; then, differential corrections are computed using precise knowledge of the HEPL antenna location. Meanwhile, raw measurements from

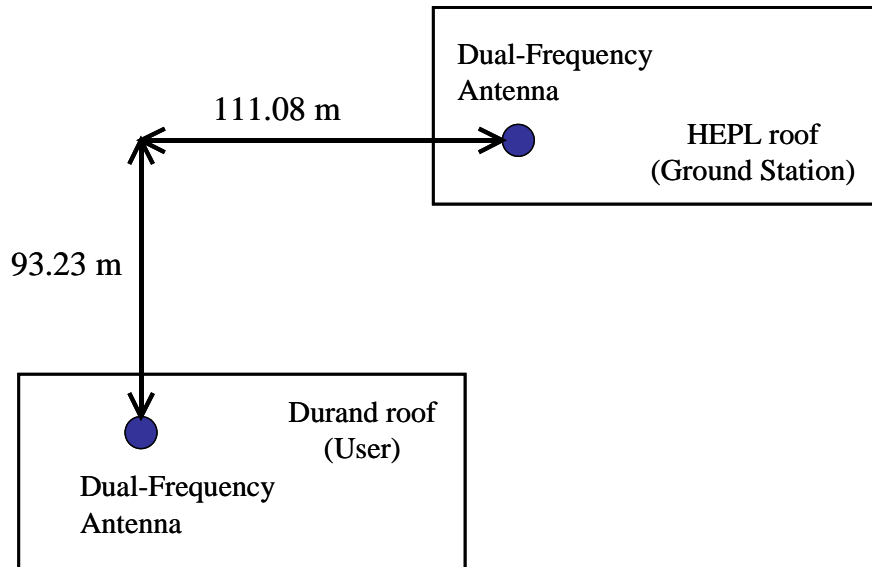


Figure 4.9: Experimental Antenna Locations

the Durand system are also smoothed by the same smoothing filter; then, these smoothed measurements are corrected by the differential corrections generated by the HEPL system, providing differentially-corrected measurements for an “airborne user” represented by the Durand system.

To emulate landing operations under the worst ionosphere condition, controlled ionosphere errors are injected into pre-existing collections of nominal data. Considered here is the period of the last 200 seconds before the aircraft reaches the decision point. Figure 4.10 illustrates this situation. As shown in this figure, an ionosphere wave front with a spatial gradient of 0.4 m/km (the maximum gradient) is affecting range signals from a particular satellite to the airborne and ground receivers. With respect to the relative motion between the wave front and the range signal path, it is assumed that the wave front is moving with the IPP of the ground measurement, namely:

$$dV_{front / ipp, gnd} = V_{front} - V_{ipp, gnd} = 0 \text{ (km/s)}. \quad (4-40)$$

This assumption allows us to keep the ground (HEPL) datasets unchanged, because the temporal gradient on the ground ionosphere error that would be induced by the wave front becomes zero.

$$\dot{I}_g = \alpha \cdot dV_{front / ipp, gnd} = 0 \quad (4-41)$$

On the other hand, the airborne signal path has a relative motion with respect to the wave front, which is approximately equal to the aircraft velocity. In other words, the relative velocity between the ground IPP (which has the same velocity as the front) and the airborne IPP approximates the aircraft velocity (which is set here to 0.07 km/s).

$$dV_{front / ipp, air} = V_{front} - V_{ipp, air} = -0.07 \text{ (km/s)} \quad (4-42)$$

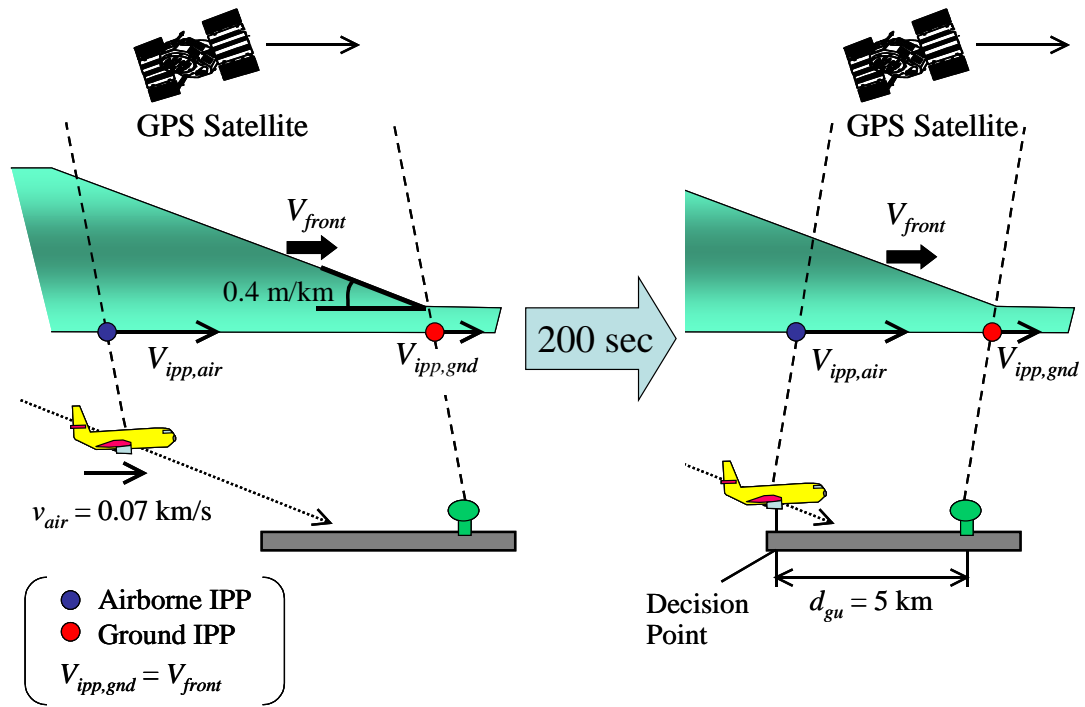


Figure 4.10: Simulated Landing Situation

The simulation case was set up to represent the last 200 seconds before the aircraft reaches the decision point. The ionosphere wave front affecting the landing has the maximum gradient (0.4 m/km) and moves with a velocity identical to that of the ground IPP.

Consequently, the airborne (Durand) measurement suffers a negative ramp ionosphere error whose temporal gradient is given as:

$$\dot{I}_a = \alpha \cdot dV_{front / ipp,air} = -0.028 \text{ (m/s)}. \quad (4-43)$$

As noted above, the aircraft reaches the decision point after 200 seconds, and at this point, the absolute ionosphere difference between the airborne and the ground measurements would be 2 meters—a product of the ionosphere spatial gradient (0.4 m/km) multiplied by the distance from the ground station to the decision point (5 km). This boundary condition and the ionosphere temporal gradient given by equation (4-43)

determine the ionosphere error injected into the airborne (Durand) L1 measurements. This error is shown as a solid line in Figure 4.11.

As discussed several times, ionosphere errors are a function of the RF carrier frequency. Ionosphere errors on the L1 (1575.42 MHz) and L2 (1227.60 MHz) measurements are related to each other as:

$$I_{L2} = \frac{f_{L1}^2}{f_{L2}^2} I_{L1} \approx 1.65 I_{L1} \quad (4-44)$$

The ionosphere error injected into the L2 measurements is generated by inflating the L1 ionosphere error by a factor of 1.65. This error is shown as a dashed line in Figure 4.11.

In this failure test, I simulated both nominal case and anomalous case for comparison. The complete procedure is given below.

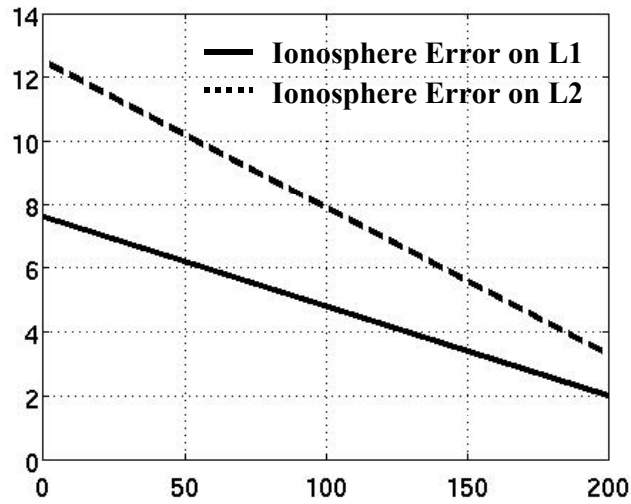


Figure 4.11: Injected Ionosphere Error

Nominal Condition Case

- (1) Select one smoothing filter type from three choices: SFCS, DFree, or IFree.
- (2) Apply the selected filter to the raw measurements taken by the two antenna sites (Durand and HEPL).
- (3) Using the smoothed measurements of the HEPL site, generate differential corrections.
- (4) Generate differentially-corrected pseudoranges by applying the corrections made in step (3) to the smoothed measurements of the Durand site. Each corrected pseudorange is the summation of the theoretical range from the Durand antenna to the satellite, residual ranging errors after DGPS correction, and the difference of the Durand and HEPL receiver clock biases (this parameter is modeled by equation (2-21)).
- (5) Perform position estimation at the Durand site using the corrected pseudoranges. In addition to the three-axis position solution, the fourth estimate corresponds to the difference of the Durand and HEPL receiver clock biases (the term " $cb_u - cb_g$ " in equation (2-21)).
- (6) Subtract the theoretical ranges to the satellite and the estimated clock biases from the corrected pseudoranges. The resulting values represent the residual ranging errors after DGPS corrections under nominal conditions.
- (7) Repeat steps (1) through (6) for all three smoothing filters (SFCS, DFree, and IFree) to allow comparisons among the three methods.

Anomalous Condition Case

- (1) Select one particular satellite in view and add the artificial ionosphere errors to the nominal raw measurements from the satellite.

- (2) Select one smoothing filter type from three choices: SFCS, DFree, or IFree.
- (3) To generate differentially-corrected pseudoranges for the anomalous condition, perform same steps as steps (2), (3), and (4) in the nominal-condition case described above.
- (4) Subtract the theoretical ranges to the satellite and the estimated clock biases from the corrected pseudoranges. Here, the clock biases are those estimated in the nominal condition case (i.e., the output of step (5) in the nominal case). The resulting values represent residual ranging errors after DGPS corrections for the particular anomalous condition added to the raw measurements.
- (5) Repeat steps (2) through (4) for all three smoothing filters (SFCS, DFree, and IFree) to allow comparisons among the three methods.

4.4.2 Impact Evaluation Results

I selected two 200-second time slots (or epochs) from a data set taken on February 22, 2007, as shown in Table 4-1. Of these time slots, the first slot was selected such that the satellite geometry was the poorest—the lowest number of satellites—within the day, while the second was selected arbitrarily.

Table 4-1: Experimental Time Slots (Date: February 22, 2007)

Time Slot (UTC)	Note
11:15:25 – 11:18:45	Selected because of the poorest satellite geometry
12:25:14 – 12:28:34	Selected arbitrarily

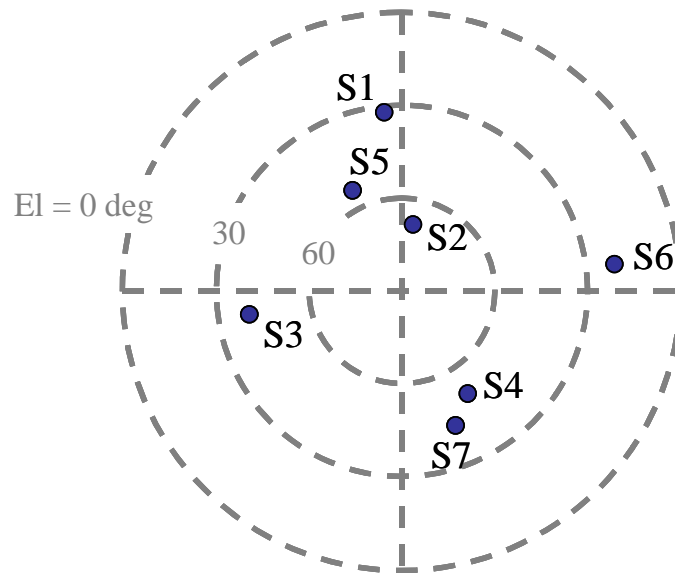


Figure 4.12: Satellite Geometry of Time Slot #1

Figure 4.12 shows the satellite geometry at the beginning of the first time slot. Figure 4.13 depicts residual ranging errors after DPGS corrections for all satellites for the case where no artificial ionosphere error was added. The blue, red, and green curves represent the errors when using SFCS, DFree, and IFree, respectively. Due to the close proximity of the two antennas (145 meters), the residual troposphere and ionosphere errors are virtually zero; hence, residual multipath and thermal noise dominate the errors in Figure 4.13. As shown in this figure, residual errors for DFree and SFCS are almost identical, and those for IFree are larger than the others for all satellites, a result consistent with the theory described in Section 4.2 and 4.3.

Figure 4.14 shows the vertical position errors for the three methods. Again the blue, red, and green curves correspond to SFCS, DFree, and IFree, respectively. Because of the large measurement noise, the IFree position error is more than twice of magnitude of the others. Generalized, this result implies the inferiority of IFree to DFree and SFCS under nominal ionosphere conditions. Recall that the dual-frequency receivers used in this

experiment measure L2 code-phase using semi-codeless tracking. This process could induce additional errors that will not appear the future dual-frequency receivers that will measure L2 and L5 ranges in the same manner as current L1 ranging. Even considering this issue, the result in Figure 4.14 demonstrates the disadvantage of IFree.

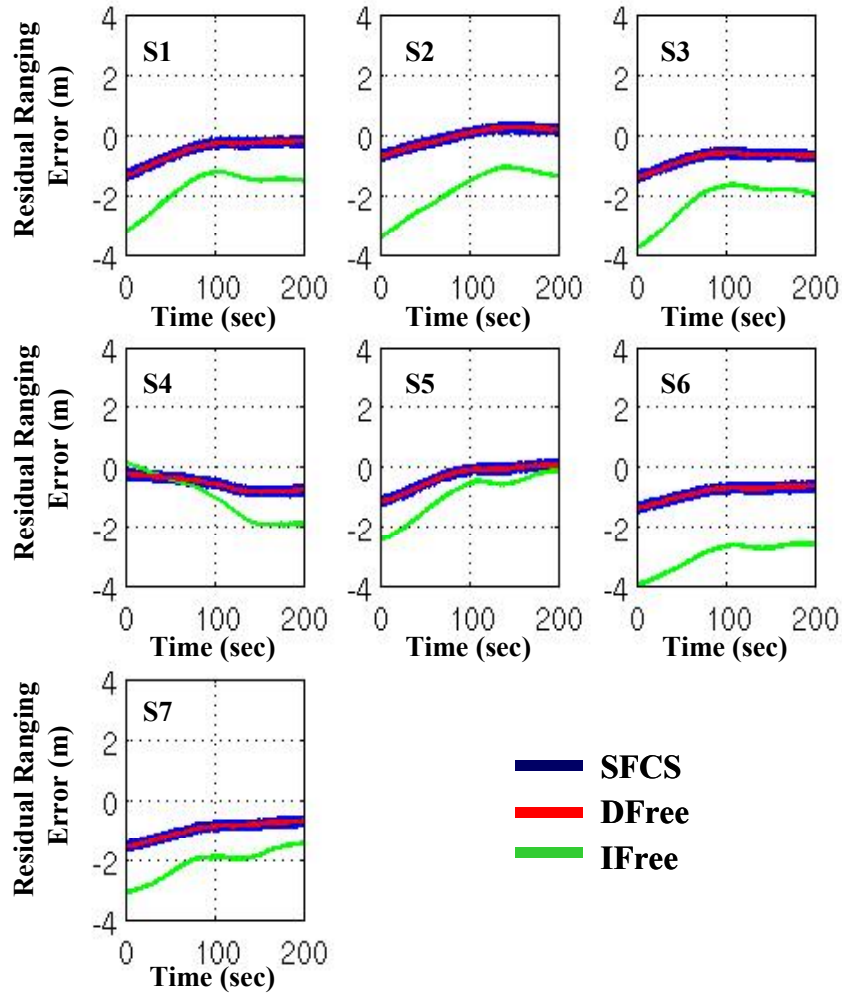


Figure 4.13: Residual Ranging Error for Time Slot #1 (nominal case)

The residual errors from SFCS and DFree are almost indistinguishable and are generally smaller than that of IFree. Note that the 200-second point corresponds to the decision point.

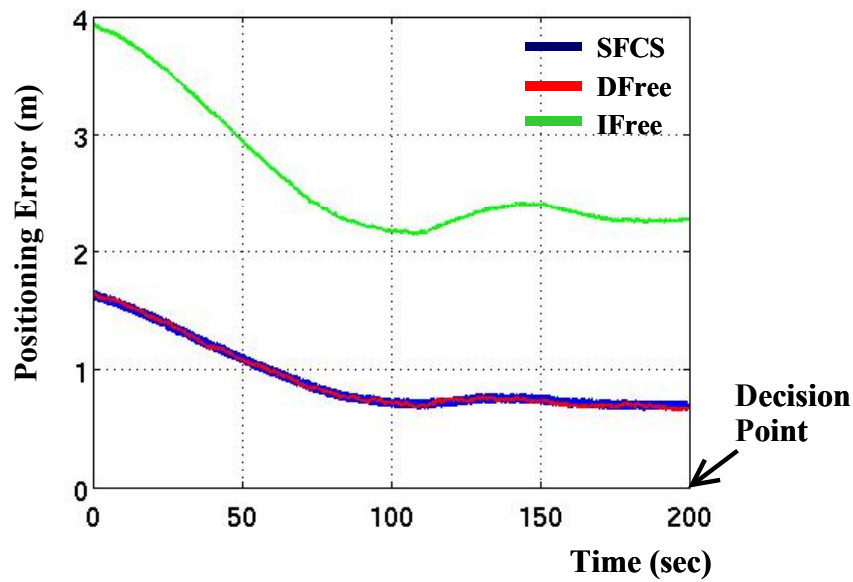


Figure 4.14: Vertical Position Error during Time Slot #1 (nominal case)

The vertical position errors of SFCS and DFree are almost indistinguishable and are much smaller than that of IFree.

Next, it was assumed that an ionosphere anomaly wave front affected the lowest-elevation satellite (S6), as shown in Figure 4.15, and the artificial ionosphere errors shown in Figure 4.11 were injected into the L1/L2 measurements of this satellite. Note that the measurements for all other satellites remained as they were for the nominal case. Figure 4.16 provides the residual ranging errors for S6 after the injection. By definition, the residual error for IFree does not change from that of the nominal case, as the additional ionosphere errors on S6 are completely removed by IFree. In contrast, the residual errors for DFree and SFCS show significant changes due to the injected ionosphere error. The black dashed line in the figure represents the injected ionosphere error, which is equivalent to the ionosphere difference between the user and the ground station. The residual error of DFree matches this ionosphere difference, which is consistent with the theory discussed in Section 4.3.2—the residual ionosphere error of DFree is equal to the absolute ionosphere difference between the airborne and the ground measurements. On the other hand, the residual error of SFCS is much larger than the actual ionosphere difference. This is also consistent with the theory discussed

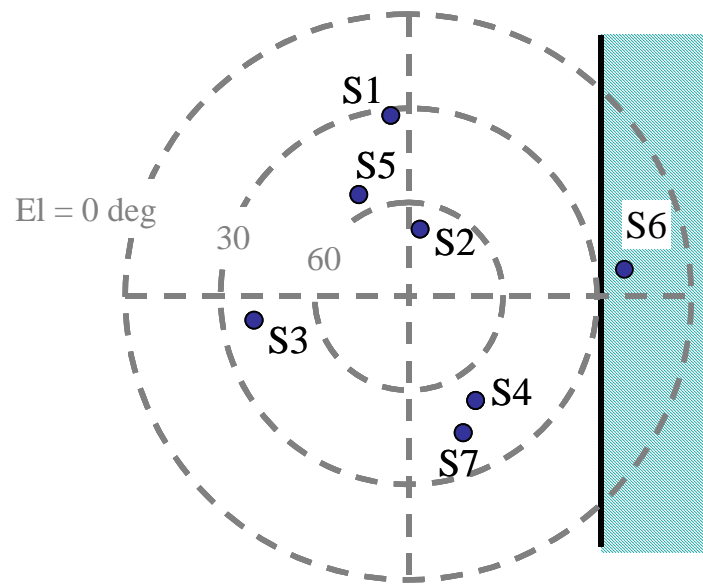


Figure 4.15: Lowest-Elevation Satellite is Affected by an Ionosphere Wave Front

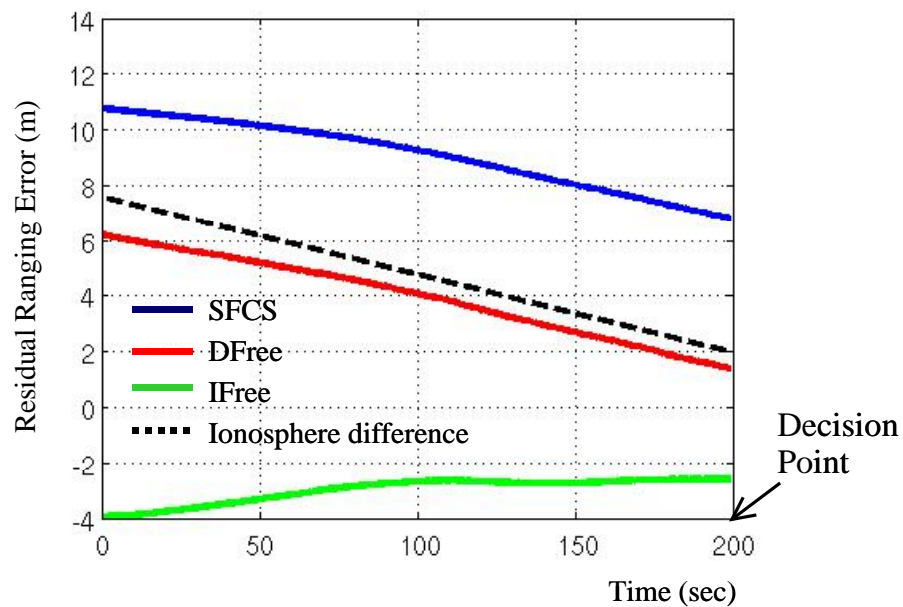


Figure 4.16: Residual Ranging Error after Injecting Artificial Ionosphere Error (Time Slot #1)

The residual error from IFree does not change from the nominal case. The error from DFree is inflated from the nominal case due to the ionosphere spatial gradient. The error of SFCS is significantly inflated due to effects of both the ionosphere spatial gradient and the temporal gradient.

in Section 4.2—the residual ionosphere error of SFCS is dictated not only by the ionosphere spatial gradient but also by the temporal gradient. The error at the decision point (the 200-second point) is close to the theoretically-estimated value of 7.6 meters (see equation (4.20)).

Figure 4.17 shows the vertical position errors for the anomalous case. The superiority of the methods is completely overturned from the nominal case. IFree provides accurate positioning notwithstanding the severe ionosphere condition, whereas the accuracies of DFree and SFCS significantly deteriorate. In particular, the vertical position error of SFCS is hazardous, exceeding 10 meters at the decision point—a value that corresponds to VAL for CAT III LAAS (see Table 2-1).

Figure 4.18 shows the satellite geometry at the beginning of the second time slot, and Figure 4.19 shows residual ranging errors for all satellites under nominal conditions. Errors for IFree are generally larger in magnitude than those for DFree and SFCS, but

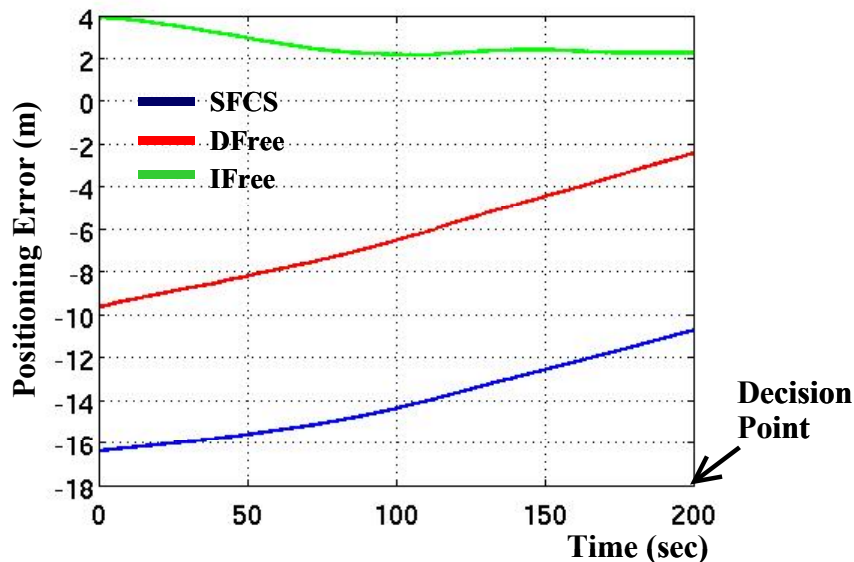


Figure 4.17: Vertical Position Error after Injecting Artificial Ionosphere Error (Time Slot #1)

The IFree vertical position error exceeds the 10-meter CAT III VAL at the decision point due to the inflated ranging error and the relatively poor satellite geometry (7 satellites in view).

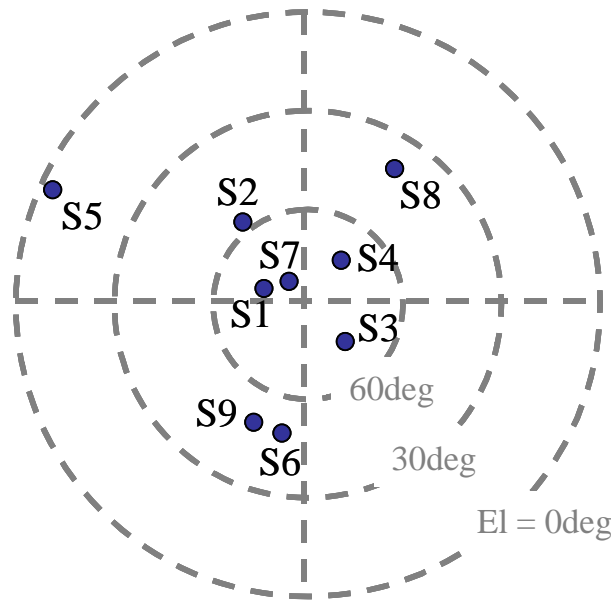


Figure 4.18: Satellite Geometry of Time Slot #2

some exceptions can be seen such as for satellites S2 and S5. Figure 4.20 presents the vertical position errors for each of the three methods. In this figure, the error for IFree is smaller than those for DFree and SFCS, which is a result that is inconsistent with theory. However, this smaller IFree error most likely occurs by chance. To confirm this point, I expanded the time slot forward and backward by 400 seconds each and estimated the position errors. Figure 4.21 shows this result. As shown in this figure, the IFree error exceeds the DFree and SFCS errors outside the original time slot. Hence, although the IFree error is smaller in the original time slot, it appears to vary more widely than those of DFree and SFCS.

Similarly to the first time slot, I injected the additional ionosphere error into the lowest-elevation satellite (S5). Figure 4.22 shows the resulting residual errors. Again these results are consistent with theory. The error for IFree has no change from the nominal case, the error for DFree lies in the vicinity of the actual ionosphere difference between the user and the ground station (the black dashed line), and the error for SFCS is significantly larger than the actual ionosphere difference due to the effect of ionosphere

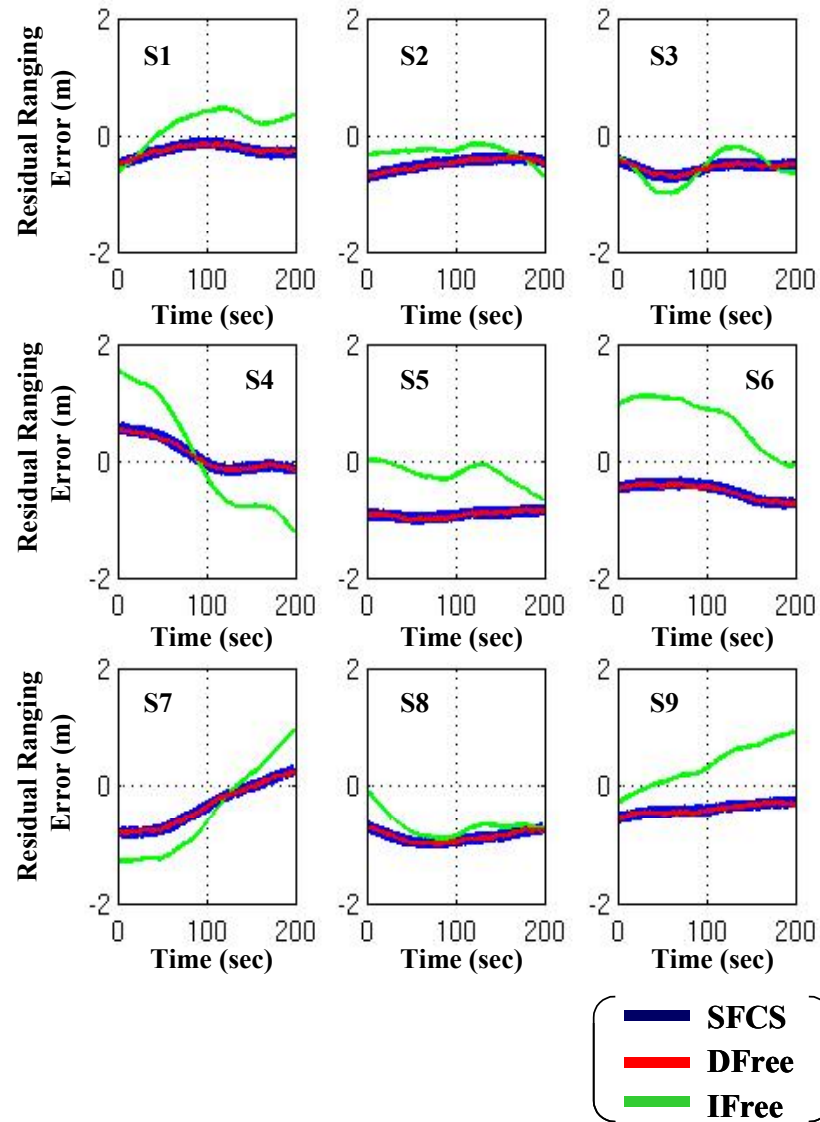


Figure 4.19: Residual Ranging Error for Time Slot #2 (nominal case)

As with the first time slot (Figure 4.12), the residual errors for SFCS and DFree are almost indistinguishable and are smaller than that of IFree most of the time.

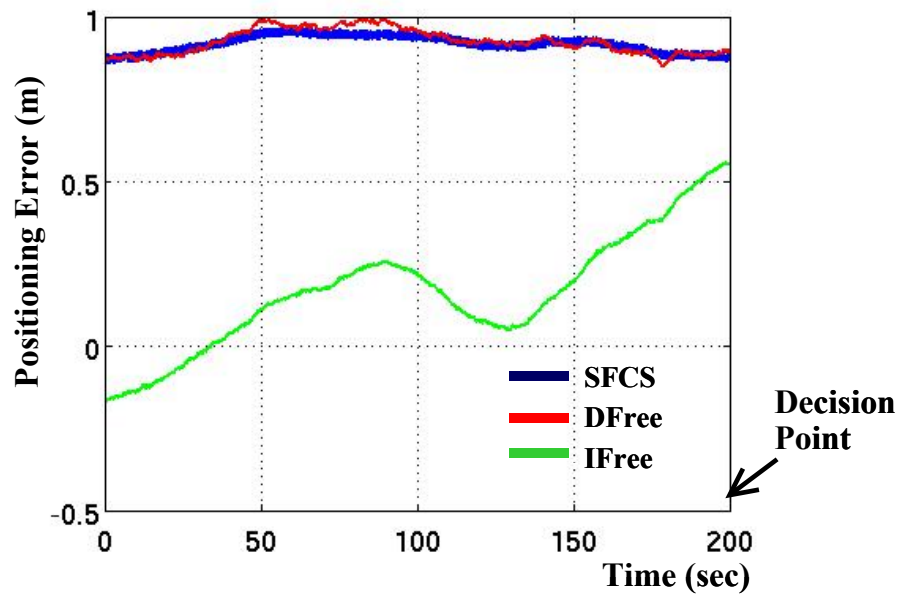


Figure 4.20: Positioning Error during Time Slot #2 (nominal case)

The positioning error of IFree is smaller than those of SFCS and DFree, which is inconsistent with theory. This result occurs most likely by chance because, as shown in Figure 4.21, the IFree error mostly exceeds the errors of the other smoothing methods outside the examined time window.

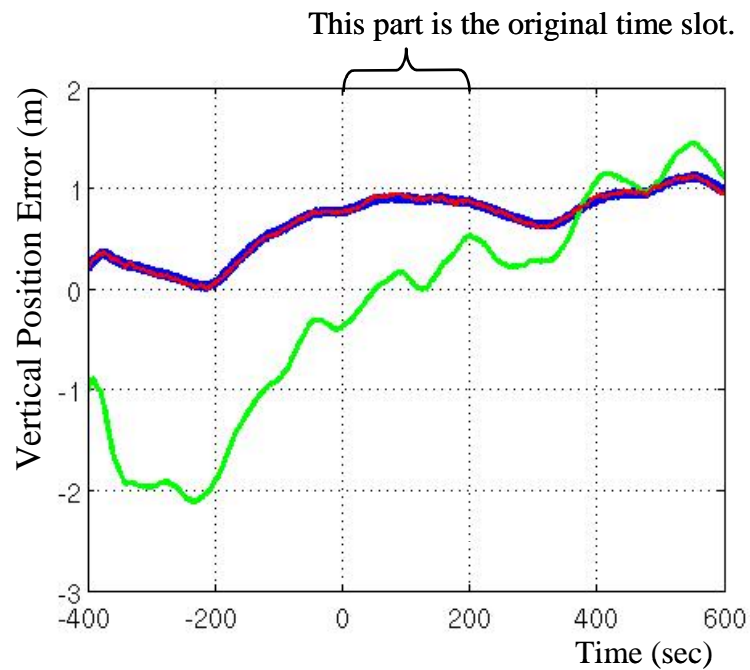


Figure 4.21: Vertical Position Error for Expanded Time Slot (nominal case)

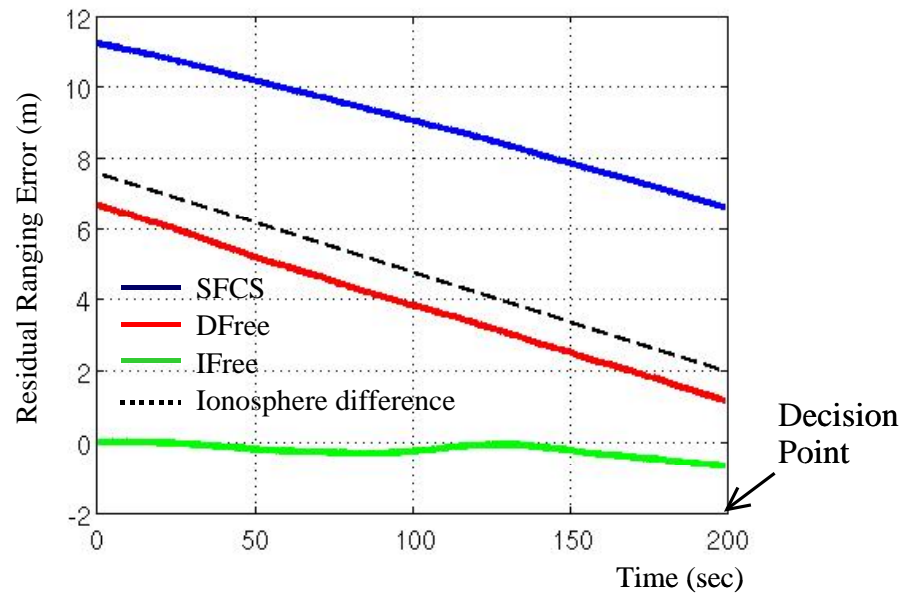


Figure 4.22: Residual Ranging Error after Injecting Artificial Ionosphere Error (Time Slot #2)

temporal gradients. The vertical position errors presented in Figure 4.23, as with those in Figure 4.17, demonstrate the vulnerability of SFCS and the immunity of IFree against anomalous ionosphere wave fronts.

The experimental results shown above support theoretical assessments shown in the previous sections. One thing that should be addressed is the dissimilarity between the experimental setup and the actual landing operation. This experiment equates the static Durand antenna with a moving airborne antenna. However, this inconsistency has no significant effect on the credibility of this experiment because what was evaluated was the residual errors, and they were computed based on the actual antenna location. Hence, if one could know the true location of the airborne antenna at every moment in an approach operation, similar error profiles would be obtained.

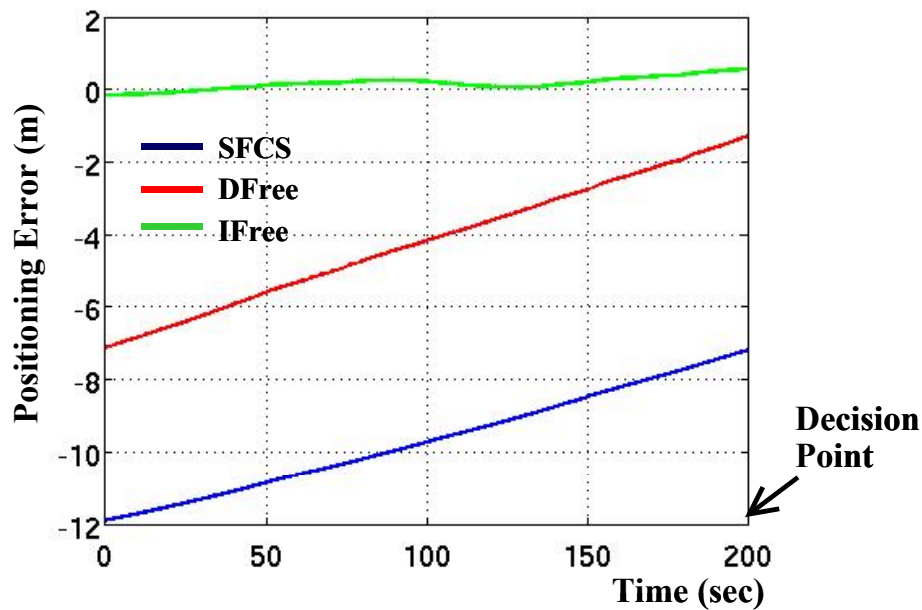


Figure 4.23: Positioning Error after Injecting Artificial Ionosphere Error (Time Slot #2)

As with the first time slot (see Figure 4.17), the SFCS error is quite large. However, this time, the error at the decision point does not exceed the 10-meter CAT III VAL. This is because the satellite geometry of this time slot (9 satellites in view) is better than that of the first time slot (7 satellites in view).

4.5 Summary

This chapter has quantitatively assessed the effect of a severe ionosphere anomaly wave front on LAAS architectures employing SFCS, DFree, and IFree smoothing methods. Theoretical assessments were mostly supported by experimental results. The following bullets summarize key characteristics of the three smoothing methods that were addressed in this chapter.

- Under nominal ionosphere conditions, SFCS and DFree have roughly the same level of output noise, whereas IFree usually has a larger output noise level. Consequently, navigation using IFree-based LAAS in nominal ionosphere conditions is generally less accurate than that of SFCS or DFree-based LAAS.

- Under anomalous ionosphere conditions, SFCS-based LAAS may suffer two error-inducing factors: large ionosphere spatial gradients affecting the user and ground station, and large ionosphere temporal gradients due to relative motion between the ionosphere wave front and the range signal path. The temporal gradients induce delay effects, resulting in significantly larger residual ranging errors compared with the actual ionosphere difference between the user and ground station.
- The DFree filter corrects for the effect of the ionosphere temporal gradient, generating much smaller residual ranging errors under anomalous conditions, when compared with SFCS. In theory, this residual ranging error is equivalent to the ionosphere difference between the user and the ground station.
- The IFree filter eliminates all ionosphere-related effects, enabling a LAAS architecture that is completely insensitive to ionosphere conditions but rather more sensitive to noise under any conditions.

Table 4-2 summarizes the worst-case residual ionosphere errors at the decision point for the three methods.

Table 4-2: Summary of Worst Residual Ionosphere Error at Decision Point

Method	Worst Residual Ionosphere Error (m)	Note
SFCS	7.6	
DFree	2.0	The noise level is the same as SFCS.
IFree	0.0	The noise level is much larger than SFCS and DFree.

Now, this dissertation turns to describing integrity methods that work with IFree and DFree. The next chapter develops an integrity method that can be used in an IFree-based LAAS architecture and evaluates this approach from the view point of system availability.

CHAPTER 5

Ionosphere-Free Based Architecture

As explained in Chapter 4, Ionosphere-Free Smoothing (IFree) eliminates the ionosphere error from each range measurement, enabling a LAAS architecture that is completely immune to differential range errors due to ionosphere anomalies. Of concern for IFree is the large noise level of the resulting smoothed measurements due to the use of dual-frequency code-phase measurements in the filter. This chapter develops an integrity method for IFree-based LAAS that accounts for these characteristics and evaluates the performance of the resulting system from the viewpoint of system availability.

The chapter begins by developing a user VPL equation associated with IFree (Section 5.1). This equation has no ionosphere-related term, but the receiver noise error terms are set larger than those in conventional VPL equations. Next, Section 5.2 describes a simulation method that estimates system availability based on the VPL equations used in the system. This research employs the simplest simulation method among those introduced by previous studies [Shively04, Rife05]. Section 5.3 conducts simulations in which certain key model inputs, such as the satellite constellation and the receiver noise model, are modified. Finally, Section 5.4 summarizes this chapter.

5.1 VPL Equation for IFree-Based LAAS

Because IFree removes the ionosphere error from each range measurement, the integrity risk related to ionosphere spatial gradients becomes irrelevant. Hence, the integrity risk allocation tree for the IFree-based architecture has no branch for ionosphere anomalies, unlike the risk tree for conventional LAAS that has a non-negligible branch for these anomalies (see Figure 5.1). However, a side effect of the complete removal of ionosphere errors is the large noise error level of the smoothed measurements. These larger nominal errors negatively affect VPL_{H0} and VPL_{H1} , which are the positioning error bounds that limit integrity risk due to fault-free user errors and due to undetected single-reference-receiver failures. This section modifies those VPLs such that they are consistent with noisy IFree measurements.

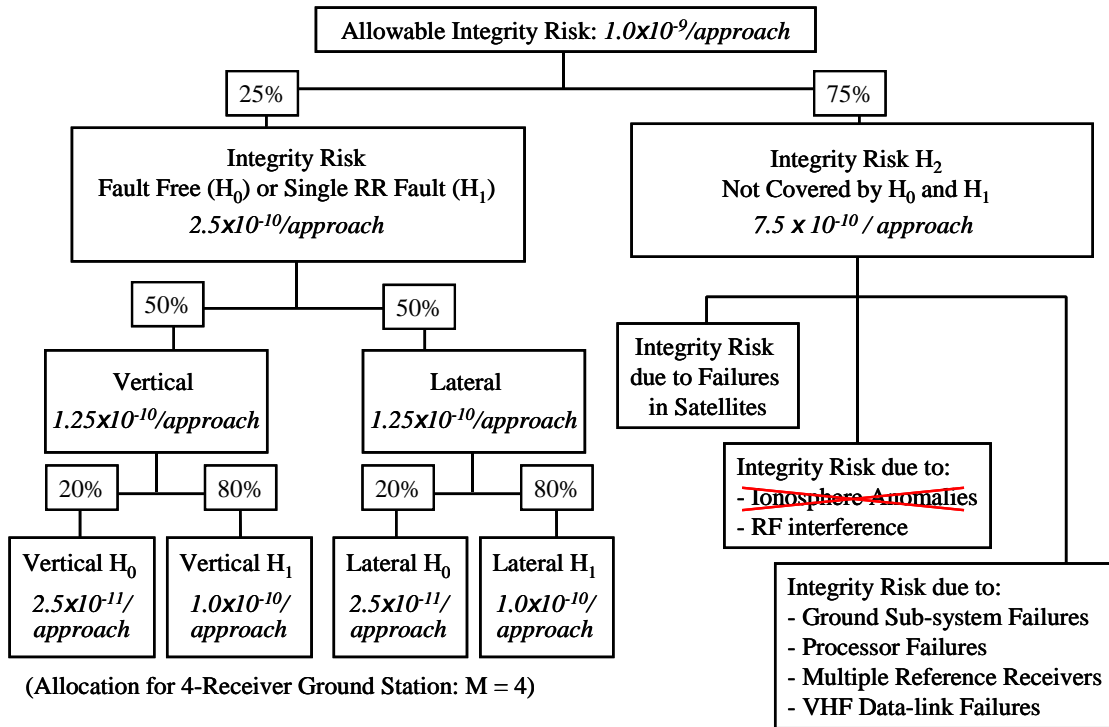


Figure 5.1: IFree-Based LAAS Integrity Allocation Tree

The integrity risk associated with ionosphere spatial-gradient anomalies, which is significant in conventional LAAS, becomes irrelevant for IFree-based LAAS.

Because the basic concept of VPL does not change for IFree, the VPL_{H0} and VPL_{H1} equations for IFree-based LAAS (denoted as VPL_{IFH0} , and VPL_{IFH1}) have the same form as those for conventional LAAS (see Section 2.3.2).

$$VPL_{IFH0} = K_{ffmd} \sqrt{\sum_{i=1}^N S_{vert,i}^2 \sigma_{rm,i}^2} \quad (5-1)$$

$$VPL_{IFH1,j} = K_{md} \sqrt{\sum_{i=1}^N S_{vert,i}^2 \sigma_{H1,i}^2} + \left| \sum_{i=1}^N S_{vert,i} B_{i,j} \right| \quad (5-2)$$

(where j represents the j th receiver failure)

For the four-receiver ground station configuration, the inflation factors K_{ffmd} and K_{md} are set to 6.673 and 3.7, respectively [Rtca04]. In these equations, the sigma terms $\sigma_{rm,i}$ and $\sigma_{H1,i}$ must be revised from those of conventional LAAS, while the calculation of B-values does not change (see Appendix B). Given that no ionosphere-related term is needed, these sigmas are modeled as follows.

$$\sigma_{rm,i}^2 = \sigma_{IFgnd,i}^2 + \sigma_{IFair,i}^2 + \sigma_{tropo,i}^2 \quad (5-3)$$

$$\sigma_{H1,i}^2 = \frac{M}{M-1} \sigma_{IFgnd,i}^2 + \sigma_{IFair,i}^2 + \sigma_{tropo,i}^2 \quad (5-4)$$

where σ_{IFgnd} and σ_{IFair} are the standard deviations of ground and airborne IFree-based receiver noise errors, σ_{tropo} is the standard deviation of residual troposphere errors given by equation (2.39), and M is the number of healthy reference receivers used by the ground station. Strictly speaking, to develop IFree-receiver noise models (σ_{IFgnd} and σ_{IFair}) that reflect actual receiver performance, one needs to analyze actual IFree measurements based on the L5 signal and L5-capable receivers, just as McGraw *et al.* did in developing the Accuracy Designators (AADs and GADs) for current single-frequency (L1) receivers [McGraw00]. However, since the L5 civil signal on GPS has not been fielded yet, such an analysis is not yet possible. Instead, for the purpose of this

simulation-based analysis, it is possible to construct purely theoretical models for σ_{IFgnd} and σ_{IFair} .

Recall the model of IFree filter outputs from Section 4.3.3.

$$\hat{\rho}_{IFree}(s) = R(s) + F(s) \left(\varepsilon_{L1}(s) - \frac{1}{\zeta} (\varepsilon_{L1}(s) - \varepsilon_{L5}(s)) \right) + \frac{1}{\zeta} (IFB + \tau_{gd})$$

(5-5)

where $\zeta = 1 - \frac{f_{L1}^2}{f_{L5}^2}$

The second term represents residual noise error on smoothed measurements. Assuming that errors on L1 and L5 code-phase measurements are independent (which is a conservative assumption), the standard deviation of the residual noise (σ_{IF}) is modeled as:

$$\sigma_{IF} = \sqrt{\left(1 - \frac{1}{\zeta}\right)^2 \sigma_{L1}^2 + \frac{1}{\zeta^2} \sigma_{L5}^2}$$

(5-6)

where σ_{L1} denotes the standard deviation of the residual noise error on smoothed L1 code measurements, and σ_{L5} denotes the same thing for smoothed L5 code measurements. As discussed in Section 4.3.1, the L5 noise error level (σ_{L5}) is expected to be significantly smaller than the L1 noise level (σ_{L1}) due to the higher power and faster chipping rate of the L5 signal, although at present it is unclear how much smaller. To account for the uncertain advantage, the following parameterization is useful.

$$\sigma_{L5} = \kappa_{L15} \cdot \sigma_{L1} \quad (0 < \kappa_{L15} \leq 1)$$

(5-7)

Using the parameter κ_{L15} , IFree noise error is modeled in terms of the noise on smoothed L1 measurements (σ_{L1}).

$$\sigma_{IF} = \sqrt{\left(1 - \frac{1}{\zeta}\right)^2 + \frac{\kappa_{L15}^2}{\zeta^2}} \sigma_{L1}$$

(5-8)

Figure 5.2 plots the ratio of σ_{IF} to σ_{L1} as a function of κ_{L15} . As this plot shows, even with a κ_{L15} of 0.5, which means that the noise error standard deviation of the L5 signal is half that of the L1 signal, the noise error level of IFree is about 2.35 times larger than that of SFCS.

Equation (5-8) models σ_{IF} in terms of σ_{L1} , enabling the use of the Accuracy Designators (AADs and GADs) to determine the airborne and the ground IFree receiver models (σ_{IFair} and σ_{IFgnd}). Substituting AAD-B and GAD-C4 for σ_{L1} in equation (5-8), the IFree receiver models are given as follows.

$$\sigma_{IFair} = \sqrt{\left(1 - \frac{1}{\zeta}\right)^2 + \frac{\kappa_{L15}^2}{\zeta^2}} \text{ AAD-B} \quad (5-9)$$

$$\sigma_{IFgnd} = \sqrt{\left(1 - \frac{1}{\zeta}\right)^2 + \frac{\kappa_{L15}^2}{\zeta^2}} \text{ GAD-C4} \quad (5-10)$$

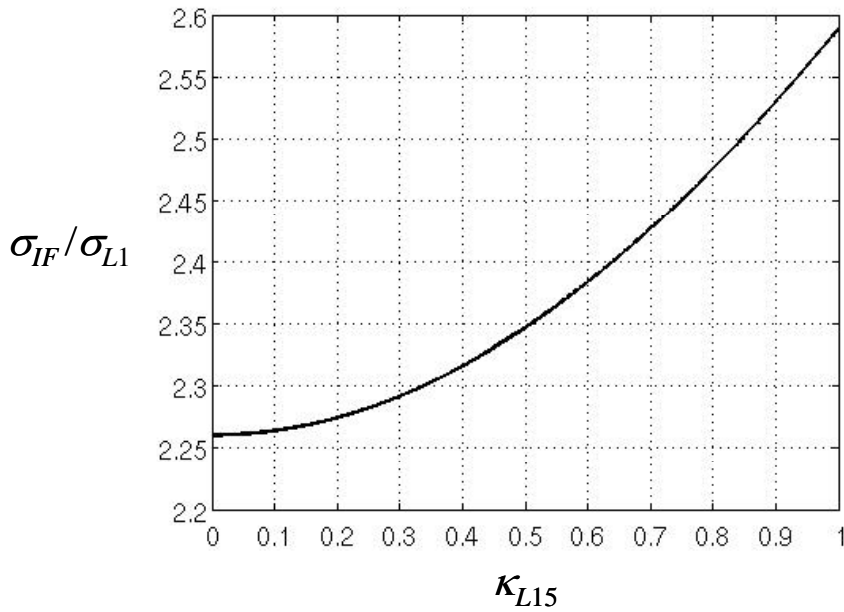


Figure 5.2: Ratio of σ_{IF} to σ_{L1} as a Function of κ_{L15}

By specifying a value for the parameter κ_{L15} , the airborne and ground IFree receiver models are set; consequently, VPL_{IFH0} and VPL_{IFH1} can be computed from these models.

The next section describes a simulation method that estimates anticipated system availability using these VPL equations.

5.2 Availability Simulation Method

As described in Section 2.1, system availability has conventionally been characterized by “long-term” availability, which is the fraction of time that the LAAS system ensures that the accuracy, continuity, and integrity requirements are met. Previous studies have proposed several methods to evaluate long-term availability using VPL equations [Shively04, Rife05]. Among these methods, this research employs a straightforward method in which integrity checks are done by using only VPLs that can be computed given a satellite geometry. Among the VPL equations developed in the previous section, VPL_{IFH1} is not determined even given a satellite geometry because it incorporates B-values which are random variables that are independent of geometry. Accordingly, the simulation method cannot account for the VPL_{IFH1} integrity check. However, this limitation does not significantly deteriorate the quality of the resulting availability evaluation because, when all reference receivers are properly working, their B-values tend to be small, resulting in VPL_{IFH1} consistently below VPL_{IFH0} . In other words, in the typical condition that no reference receiver has failed, VPL_{IFH0} is generally the dominant VPL, and it dictates system availability. Therefore, even without checking VPL_{IFH1} , it is acceptable to estimate availability based only on VPL_{IFH0} (indeed, this is the standard approach taken in LAAS research).

For a given airport location, satellite geometries are repeated for each sidereal day whose mean period is 23 hours, 56 minutes, 4 seconds [Misra(Chapter 4)]. Hence, “long-term” system availability is defined as the average “instantaneous” availability over one sidereal day of repeatable GPS satellite geometries. Instantaneous availability ($P_{avail}[t_l]$) for a particular sample epoch (t_l) is a weighted average of availability assessments for all

possible satellite geometries that the airport could experience at the epoch and is computed by the following equation.

$$P_{avail}[t_l] = \sum_U \sum_{m=1}^{\mathcal{G}(U)} \frac{P_{SVout}(U)}{\mathcal{G}(U)} P_{avail-idc}(\lambda_m(t_l, U)) \quad (5-11)$$

Here, $P_{avail-idc}(\lambda_m(t_l, U))$ is an availability indicator variable for a given satellite geometry that is denoted by $\lambda_m(t_l, U)$, where U indicates the number of satellites that are experiencing scheduled or unscheduled downtime during the sample epoch; $\mathcal{G}(U)$ is the number of satellite combinations that occur for the U -satellite-out condition, i.e. $\mathcal{G}(U)$ is “ N choose U ” for a constellation of N satellites; the variable “ m ” is a satellite combination index; and $P_{SVout}(U)$ is the probability that any U satellites from the constellation are unavailable.

The indicator variable ($P_{avail-idc}(\lambda_m(t_l, U))$) takes a value of 1 if the system is available for the geometry in question, otherwise it takes a value of 0. For IFree-based LAAS, the decision rule for this indicator is given as follows.

$$P_{avail-idc}(\lambda_m) = \begin{cases} 1 & \text{if } VAL \geq VPL_{IFH0}(\lambda_m) \\ 0 & \text{otherwise} \end{cases} \quad (5-12)$$

Note that VPL_{IFH0} in this decision rule is for the IFree-based LAAS architecture introduced in this chapter, but equation (5-12) is more general. Any VPL that can be computed based on satellite geometry is usable in general.

As equation (5-11) shows, for each epoch, all possible satellite geometries including those associated with constellation states having unusable satellites are considered to evaluate instantaneous availability ($P_{avail}[t_l]$). For each possible geometry $\lambda_m(t_l, U)$, the availability indicator ($P_{avail-idc}(\lambda_m(t_l, U))$) is evaluated based on the criterion given by equation (5-12), and a weighted average is taken based on the probability of occurrence of this particular geometry (the term “ $P_{SVout}(U) / \mathcal{G}(U)$ ” in equation (5-11)).

The following simplified example explains this process more clearly. Suppose that there are only three GPS satellites (S1, S2, and S3), and that two of them (S1 and S2) are visible from a particular airport at a given epoch. Figure 5.3 illustrates this situation. In this case, there are eight possible constellation states: one state for all-three-satellites-healthy, three states for one-of-three-satellites-unhealthy, three for two-of-three-satellites-unhealthy, and one for all-three-satellites-unhealthy. For all of these eight states, the availability indicators are evaluated and averaged with the corresponding weights, which depend on the state probability of a given satellite being healthy or unhealthy.

Table 5-1 summarizes the necessary parameters to compute the instantaneous availability for this particular situation. In the all-satellite-healthy state (state #1), the satellite geometry $\lambda_1(t_l, 0)$ consists of satellites S1 and S2, and the probability of occurrence of this geometry is given as $P_{S_{Vout}}(0)/1$ where the denominator of 1 comes

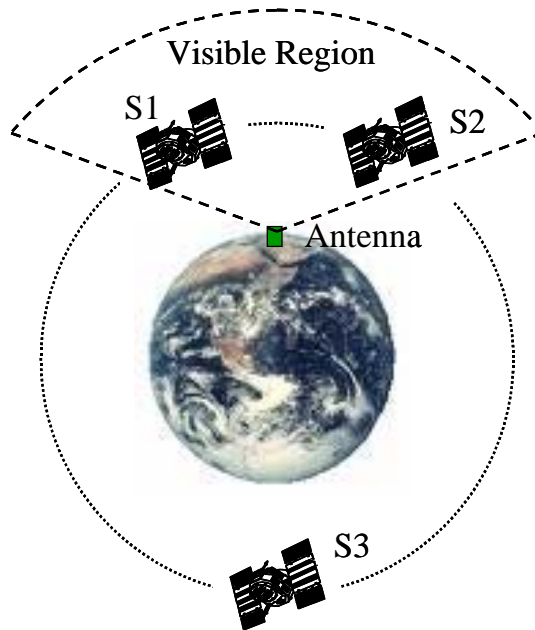


Figure 5.3: Hypothetical Constellation and Satellite Geometry

Table 5-1: Summary of Eight Possible Constellation States

State #	Number of Unavailable Satellites (U)	$\mathcal{G}(U)$	Unavailable Satellites	Visible Satellites $\lambda_m(t_l, U)$	Weighting Probability
1	0	$\mathcal{G}(0) = 1$ (3 choose 0)	--	$\lambda_1(t_l, 0) = [S1, S2]$	$P_{SVout}(0)/1$
2	1	$\mathcal{G}(1) = 3$ (3 choose 1)	S1	$\lambda_1(t_l, 1) = [S2]$	$P_{SVout}(1)/3$
3			S2	$\lambda_2(t_l, 1) = [S1]$	
4			S3	$\lambda_3(t_l, 1) = [S1, S2]$	
5	2	$\mathcal{G}(2) = 3$ (3 choose 2)	S1, S2	$\lambda_1(t_l, 2) = []$	$P_{SVout}(2)/3$
6			S2, S3	$\lambda_2(t_l, 2) = [S1]$	
7			S3, S1	$\lambda_3(t_l, 2) = [S2]$	
8	3	$\mathcal{G}(3) = 0$ (3 choose 3)	S1, S2, S3	$\lambda_1(t_l, 3) = []$	$P_{SVout}(3)/1$

from the fact that there is only one satellite combination for the all-satellite-available case ($\mathcal{G}(0) = 1$), and the numerator of $P_{SVout}(0)$ is the probability that no satellite is unavailable at this epoch. In state #3, the satellite geometry $\lambda_2(t_l, 1)$ includes only satellite S2 because of the outage on S1, and the weighting probability is given as $P_{SVout}(1)/3$ where the denominator of 3 comes from the fact that there are three satellite combinations for one-satellite-unhealthy (S1 out, S2 out, and S3 out), and the numerator of $P_{SVout}(1)$ is the probability that any one satellite from the constellation is unavailable at the epoch. Note that some geometries can be realized in multiple constellation states. For example, the geometry consisting of satellite S1 only is realized in states #3 and #6.

The instantaneous availabilities computed by equation (5-11) are uniformly averaged for all sample epochs (t_l : $l = 1, \dots, L$), providing the long-term availability estimate.

$$P_{avail} = \sum_{l=1}^L \frac{1}{L} \left[\sum_U \sum_{m=1}^{g(U)} \frac{P_{SVout}(U)}{g(U)} P_{avail-idc}(\lambda_m(t_l, U)) \right] \quad (5-13)$$

This research sets the sampling period to 5 minutes; hence, there are 288 epochs through a 24-hour day ($L = 288$). This sampling period is reasonable because satellite geometry does not change drastically over a 5-minute interval.

5.3 Simulation: Settings, Results, and Discussions

Using the simulation method introduced in the previous section, this section evaluates the availability of IFree-based LAAS whose VPL is given as VPL_{IFH0} constructed in Section 5.1. Six simulation cases are examined by varying the satellite constellation and the parameters used in the VPL_{IFH0} equation. Section 5.3.1 specifies these simulation cases and explains their motivations, while Section 5.3.2 shows the simulation results and discusses them.

5.3.1 Simulation Settings

To conduct an availability simulation, one needs to specify the satellite constellation, the probabilities of satellite outages that are consistent with the selected constellation, and the parameters that form the VPL_{IFH0} equation such as κ_{L15} (see equation (5-7)). This research examines two different GPS satellite constellations and two different values of κ_{L15} .

Satellite Constellations

A natural choice of the GPS satellite constellation is the 24-satellite constellation that the GPS Joint Program Office is currently charged to maintain. Table 5-2 presents the orbital parameters of this constellation that are specified in [Dod]. This constellation was originally designed to provide the best coverage if a single satellite becomes inoperative, although it is not optimal from the viewpoint of full-constellation satellite visibility [Massatt, Spilker96c]. Moreover, several spare satellites are appropriately

Table 5-2: Orbital Parameters of Current 24-Satellite Constellation [Dod]

Epoch		July 1, 1993 18:36:14.4 (UTC)			
Semi-Major Axis (km)		26,559.7			
Eccentricity		0.00			
Inclination (deg)		55			
Slot	RAAN (deg)	Argument of Latitude (deg)	Slot	RAAN (deg)	Argument of Latitude (deg)
A1	272.847	268.126	D1	92.847	135.226
A2		161.786	D2		265.446
A3		11.676	D3		35.156
A4		41.806	D4		167.356
B1	332.847	80.956	E1	152.847	197.046
B2		173.336	E2		302.596
B3		309.976	E3		66.066
B4		204.376	E4		333.686
C1	32.847	111.876	F1	212.847	238.886
C2		11.796	F2		345.226
C3		339.666	F3		105.206
C4		241.556	F4		135.346

RAAN: Right Ascension of Ascending Node

located within the six orbit planes of this constellation to replace future satellite failures, including multiple failures [Massatt]. Overall, the 24-satellite constellation has been maintained very well. Table 5-3 lists the probabilities of satellite outages that were estimated based on historical observations of the constellation states [Dod]. As this table shows, the probability that all 24 satellites in primary (as opposed to spare) orbit slots are healthy is very high ($P_{SVout}(0) = 0.983$). This combination of the 24-satellite constellation and the corresponding probabilities of satellite outages is the baseline condition for availability simulations in this dissertation because it represents the most likely (and most conservative) situation at the near-term completion of GPS modernization.

Also of interest are constellations having more than 24 satellites in “primary” slots. In response to increasing civilian demands, several constellations with larger numbers of satellites have been studied [Massatt]. This research examines a 30-satellite six-plane constellation introduced in [Massatt] that can be implemented with the addition of 6 satellites (one to each of the existing 6 orbit planes) and minor repositioning of the current primary orbit slots. Table 5-4 presents the orbital parameters of this 30-satellite constellation. There are two problems for the use of this constellation in availability

Table 5-3: Historical Probabilities of Satellite Outages [Dod]

Number of Operation Satellites	Number of Unavailable Satellites (U)	Probability: $P_{SVout}(U)$
24	0	0.983
23	1	0.006
22	2	0.010.
21	3	0.001
20-	4+	0

Table 5-4: Orbital Parameters of Current 30-Satellite Constellation [Massatt]

Epoch		Not specified in [Massatt]			
Semi-Major Axis (km)		26,610.0			
Eccentricity		0.00			
Inclination (deg)		55			
Slot	RAAN (deg)	Argument of Latitude (deg)	Slot	RAAN (deg)	Argument of Latitude (deg)
A1	272.85	270.63	D1	92.85	138.633
A2		161.88	D2		255.93
A3		20.15	D3		37.33
A4		44.88	D4		167.88
A5		134.35	D5		283.68
B1	332.85	71.93	E1	152.85	193.93
B2		182.53	E2		307.43
B3		318.43	E3		51.48
B4		214.38	E4		331.81
B5		294.05	E5		83.33
C1	32.85	97.98	F1	212.85	245.71
C2		9.93	F2		355.23
C3		342.18	F3		103.98
C4		228.53	F4		131.41
C5		127.23	F5		220.98

RAAN: Right Ascension of Ascending Node

simulations. One is that there is no probability set for satellite outages based on actual observations of the constellation states. With regard to this issue, this research assumes that this improved constellation will be managed with the same or superior level of effort as the current constellation and that the probabilities of one or more satellite outages are the same as those of current 24-satellite constellation (see Table 5-5).

The other problem is that no epoch is specified for this constellation in [Massatt]. Without specifying an epoch, satellite locations with respect to points on the earth cannot be determined because the epoch determines the relative rotation angle between the *Earth-Centered Earth-Fixed* (ECEF) coordinate system on which antenna locations are expressed and the *Conventional Inertial Reference System* (CIRS) on which satellite locations and velocities are expressed [Misra(Chapter 4)]. Figure 5.4 illustrates this point clearly. The left-hand figure shows a geometry for which an arbitrary epoch is set, and the right-hand figure shows a geometry for which a different arbitrary epoch is set. The satellite positions are the same in CIRS for both cases; however, the antenna location in CIRS is different due to the difference of the specified epochs, although the location in ECEF is identical for both epochs. Consequently, the relative locations of

Table 5-5: Assumed Probabilities of Satellite Outages for 30-Satellite Constellation

Number of Operation Satellites	Number of Unavailable Satellites (U)	Probability: $P_{SVout}(U)$
30	0	0.983
29	1	0.006
28	2	0.010.
27	3	0.001
26-	4+	0

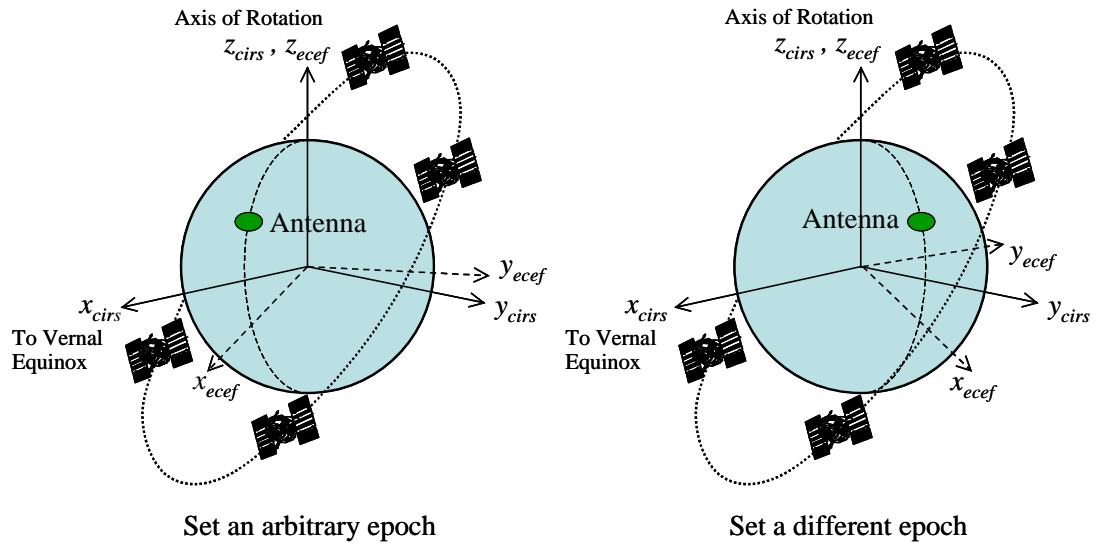


Figure 5.4: Difference of Relative Position of Satellites with Respect to Antenna When Assuming Two Different Epochs

satellites with respect to the antenna are different for these epochs. Because there is no obvious way to determine the epoch for the 30-satellite constellation, this research arbitrarily sets two epochs to 00:00:00 (UTC) and 10:00:00 (UTC) on March 12, 2007 and compares the results to investigate the sensitivity of availability to two epochs that are 10 hours apart.

Finally, it is important to remember that the assumption of a 30-satellite constellation with the probabilities of satellite outages the same as the current constellation is fairly optimistic. As noted above, this constellation is completed by adding 6 new satellites, one for each of the 6 existing orbital planes. Moreover, several spare satellites have to be deployed to keep this constellation available with satellite health probabilities as high as those of the current constellation. As such, completing and maintaining a 30-satellite constellation will require vast expenditures of money. In fact, as of the time of writing this dissertation, there is no authorized plan for such a constellation improvement, although much discussion of its desirability is taking place.

Parameters for VPL_{IFH0} Equation

The standard deviation of troposphere errors (σ_{tropo}) and the parameter κ_{L15} that controls the IFree receiver model have to be determined to conduct availability simulations. Strictly speaking, σ_{tropo} depends upon the difference in altitude between the user aircraft and the ground station and upon meteorological conditions at each airport (see Section 2.2.3). However, because the availability analysis point is set at the CAT IIIb decision height which is less than 15 meters, σ_{tropo} is negligible in compared with the other error sources. Hence, for simplicity, it is set to zero.

$$\sigma_{tropo} = 0 \quad (5-14)$$

With regard to the parameter κ_{L15} , this research examines two values: 1 and 0.5. A value of 1 for κ_{L15} means that the noise error standard deviation of the L5 signal is the same as that of the L1 signal, which is an extremely pessimistic assumption; while a value of 0.5 for κ_{L15} means that the noise error standard deviation of the L5 signal is half that of the L1 signal, which is a moderate assumption. Figure 5.5 plots the resulting airborne and ground IFree receiver models (σ_{IFair} and σ_{IFgnd}) for these two values of κ_{L15} .

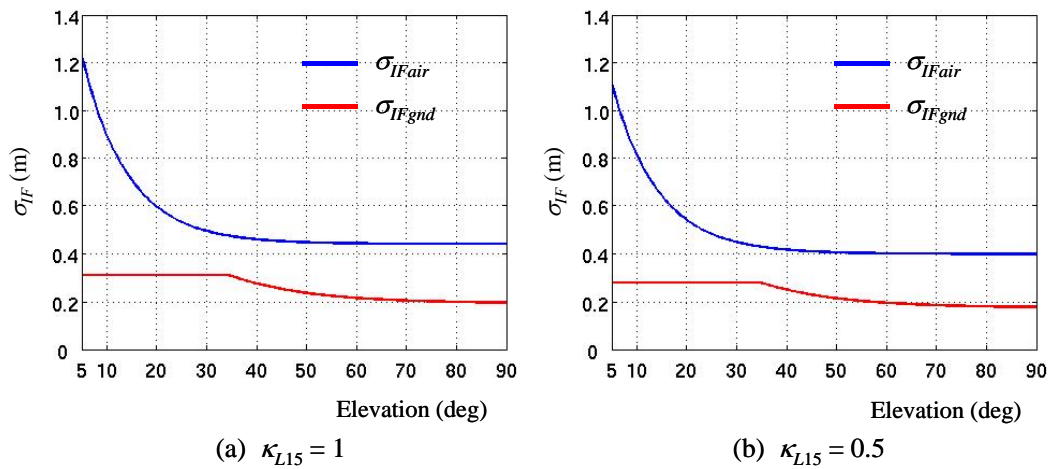


Figure 5.5: IFree-Receiver Models Used in Simulations

Summary of Simulation Settings

Table 5-6 summarizes the simulation cases that have been run. For each of these cases, system availabilities are estimated for each point within a grid of locations in CONUS separated by 2 degrees of latitude and longitude. As discussed above, the current 24-satellite constellation is the most likely constellation at the completion of GPS modernization. Cases #1 and #2 correspond to this constellation. For Case #1, the receiver error model is set based on an extremely pessimistic assumption ($\kappa_{L15} = 1$), while Case #2 uses an error model based on a moderate assumption ($\kappa_{L15} = 0.5$). The actual availability will, therefore, likely exist somewhere between the results of these two cases. Cases #3 to #6 simulate the 30-satellite constellation with the two different epoch times proposed above.

Table 5-6: Summary of Simulation Conditions

Case #	Constellation	κ_{L15}	Note
1	24-Satellite	1	Actual availability will be between the results of Case #1 and Case #2
2		0.5	
3	30-Satellite (Epoch 00:00:00)	1	The 30-satellite constellation will be realized only if the political and economical situations permit.
4		0.5	
5	30-Satellite (Epoch 10:00:00)	1	Because no epoch is specified in the original ephemeris data, two epochs are assumed to see the sensitivity to epochs.
6		0.5	

5.3.2 Results and Discussions

Figures 5.6 and 5.7 show the results for Cases #1 and #2, which are two cases that use the current 24-satellite constellation. As Figure 5.7 shows, even with the optimistic assumption for the receiver model ($\kappa_{L15} = 0.5$), the estimated availability is less than 99.9% for more than 50% of CONUS. This result indicates that, although IFree-based LAAS possesses perfect robustness against anomalous ionosphere gradients, the price in terms of reduced availability due to noisy measurements is prohibitive. Unless receiver noise is drastically reduced, IFree-based LAAS will not be considered as a practical approach for CAT IIb landing.

If the satellite constellation is improved, however, the situation will change. Figures 5.8 and 5.9 show the results for Cases #3 and #4, which assume a 30-satellite constellation with a starting epoch of 00:00:00 (UTC) on 03/12/07. As Figure 5.8 shows, if this particular 30-satellite constellation is realized, more than 99.99% availability can be achieved over a very wide region in CONUS, even with the pessimistic assumption of L5 signal accuracy ($\kappa_{L15} = 1$). One concern regarding this result is the effect of the ambiguity in the epoch for the examined constellation. Figures 5.10 and 5.11 show the results for a starting epoch of 10:00:00 on 03/12/07 (Cases #5 and #6). The difference in results between the two epochs suggests that the availability pattern in the region below 40-degree North latitude may change considerably depending upon the assumed starting epoch. In particular, the regions where availability is less than 99% completely differ between these two cases. However, from a global point of view, these results suggest that IFree-based LAAS could achieve more than 99.9% availability over a wide region in CONUS with this 30-satellite constellation.

Finally, an important point that should be emphasized again is the insensitivity of IFree-based LAAS to anomalous ionosphere conditions. The simulation results above actually represent availability under nominal ionosphere conditions: no ionosphere anomaly was considered in estimating availability. However, by definition, IFree-based LAAS will obtain almost the same availability even under ionosphere anomalies (note that the

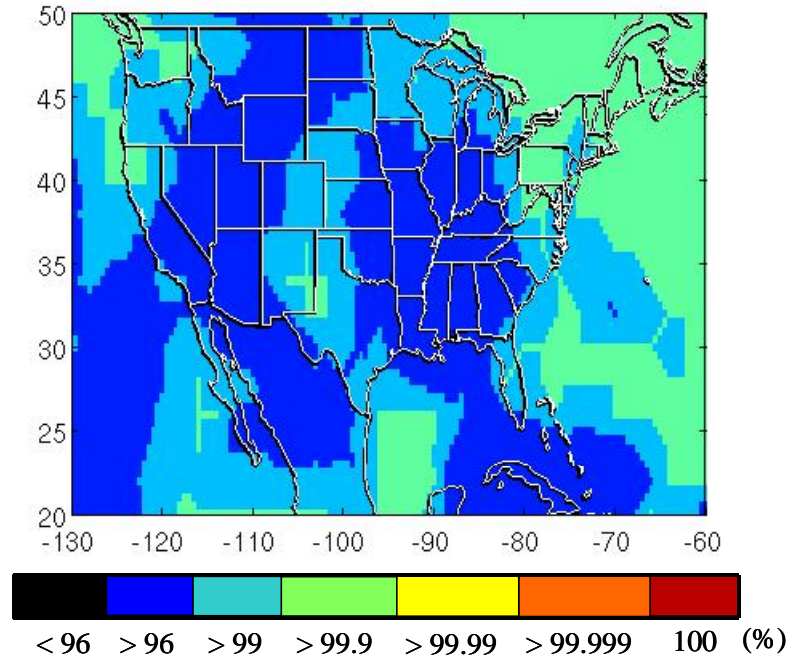


Figure 5.6: Simulation Result for Case #1

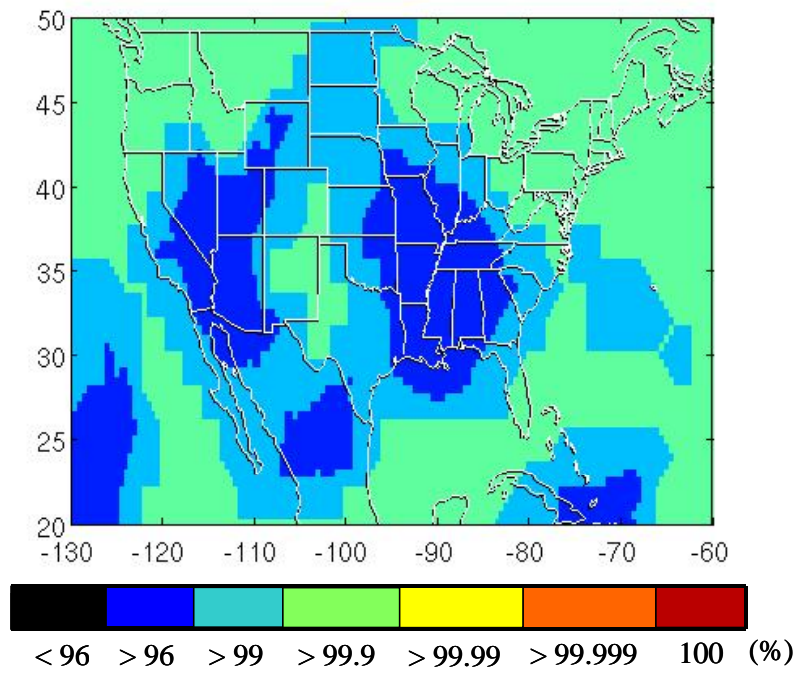
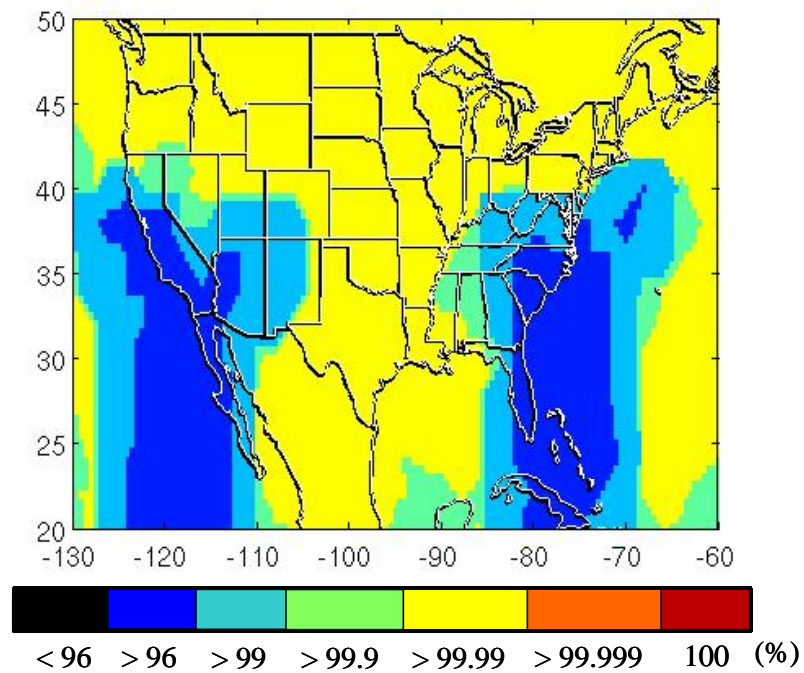
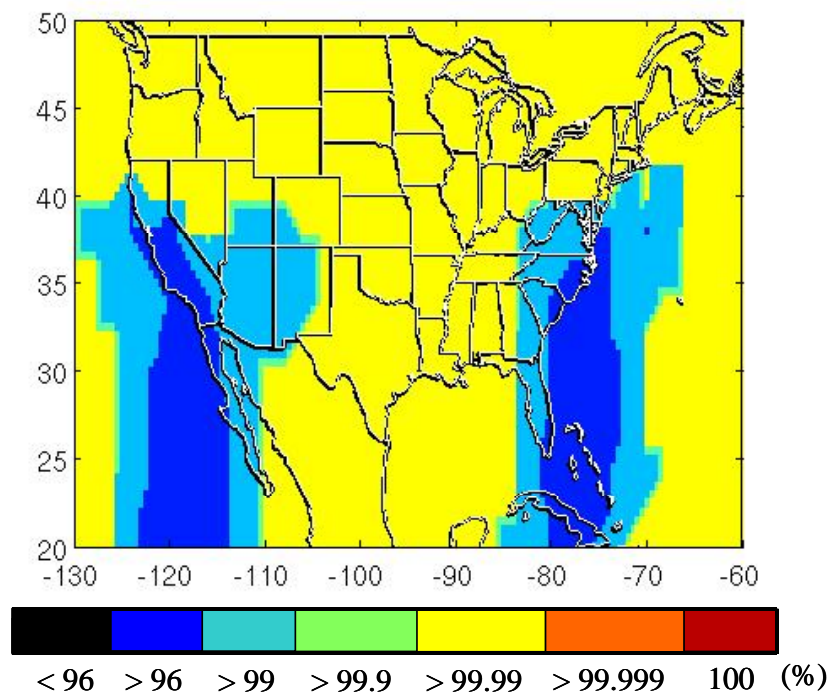


Figure 5.7: Simulation Result for Case #2

**Figure 5.8: Simulation Result for Case #3****Figure 5.9: Simulation Result for Case #4**

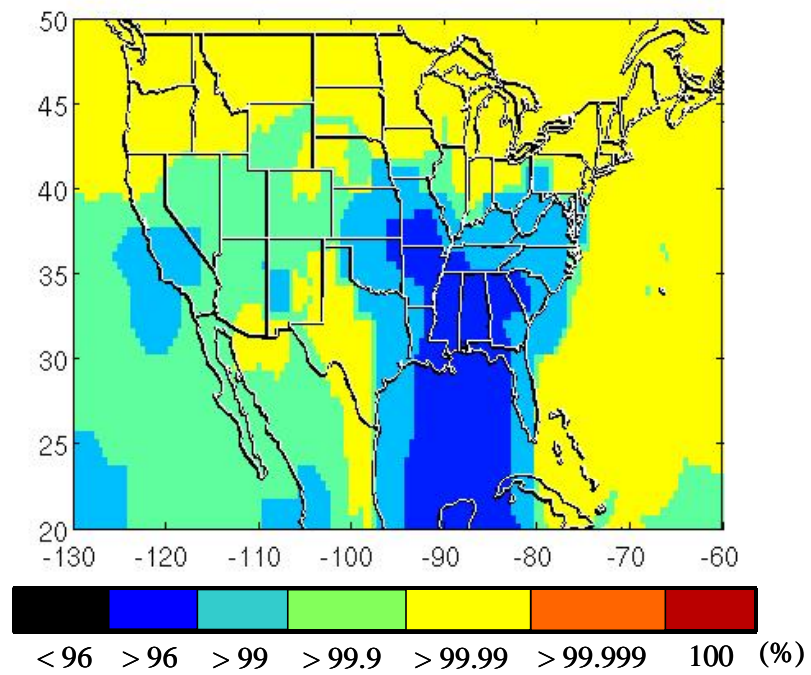


Figure 5.10: Simulation Result for Case #5

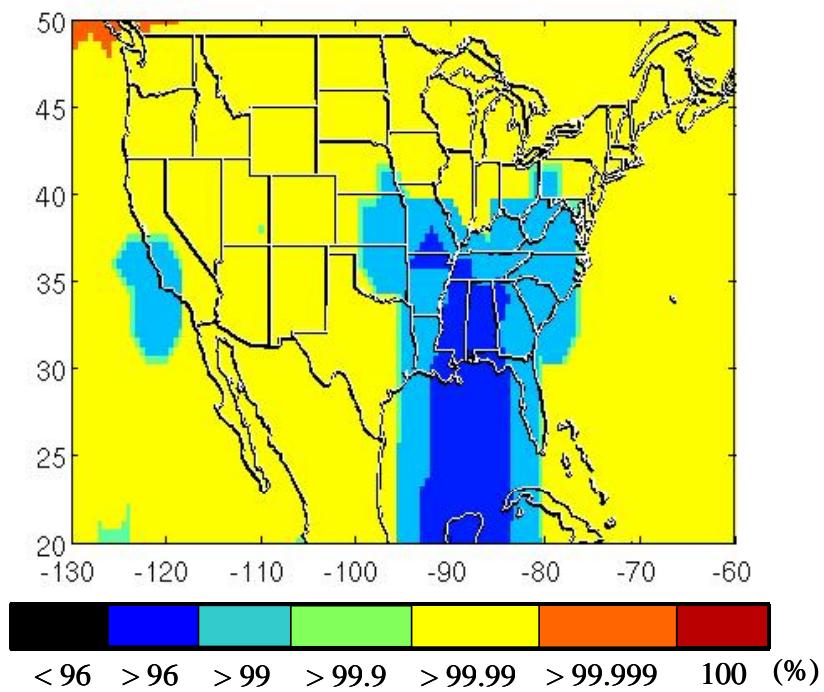


Figure 5.11: Simulation Result for Case #6

potential loss of satellite tracking due to scintillation under ionosphere anomalies could slightly reduce availability [Dehel]). Although the availability between 96% and 99.9% shown in Cases #1 and #2 (Figures 5.6 and 5.7) is unacceptable as the availability under nominal ionosphere conditions, it may be attractive as the availability under anomalous ionosphere conditions. Because of this advantage, IFree plays an important role in the enhanced “hybrid” system discussed in Chapter 7.

5.4 Summary

This chapter has developed an integrity method for dual-frequency LAAS that implements IFree as its carrier-smoothing filter. The resulting system was evaluated by availability simulations. The following bullets summarize important points discussed in this chapter.

- The integrity risk associated with ionosphere spatial gradients becomes completely irrelevant for IFree-based LAAS. Instead, the large noise error level of smoothed range measurements becomes the primary concern. Considering these characteristics, this chapter developed VPL_{IFH0} and VPL_{IFH1} equations that ensure the integrity of IFree-based LAAS for nominal (H_0) and single-reference-receiver failure (H_1) conditions, respectively.
- A simulation method that estimates availability based on these VPL equations was introduced. This method considers VPLs that can be computed if a satellite geometry is specified. In addition, this method takes account of not only the constellation state where all satellites are normally functioning but also constellation states where one or more satellites are experiencing scheduled or unscheduled outages.
- Availability simulations were conducted by varying the nominal GPS satellite constellation and the IFree error models of the airborne and the ground receivers. The constellations examined are the current 24-satellite constellation and the 30-satellite constellation introduced in [Massatt]. The 24-satellite constellation is the

most likely constellation to result from modernized GPS. The 30-satellite constellation is, in contrast, an improved constellation that might be realized if political and economic conditions permit. For the IFree receiver models, two extreme cases were examined. One is a pessimistic case where the L5 measurement noise error sigma is assumed to be the same as that of the L1 measurement noise. The other is a moderate case where the L5 noise error sigma is assumed to be half that of the L1 noise.

- Simulation results for the 24-satellite constellation revealed that IFree-based LAAS would achieve availabilities between 96% and 99.9% under nominal ionosphere conditions, which is not sufficient for actual operations. However, a key benefit of IFree-based LAAS is that the system will achieve almost the same availability even under anomalous ionosphere conditions. More than 96% availability under anomalous conditions may be attractive.
- Simulation results for the 30-satellite constellation showed that IFree-based LAAS would provide much better availability than it would for the 24-satellite constellation, and the resulting level of availability (99.9% or better) would likely be sufficient for efficient CAT IIb operations. However, it should be kept in mind that the 30-satellite constellation is a fairly optimistic assumption.

Recall that the goal of this research is to design an integrity method for ionosphere anomalies that satisfies the integrity requirements of CAT IIb LAAS without degrading system availability. Unfortunately, the IFree-based architecture proved not to be a satisfactory solution for this challenge unless the GPS satellite constellation is enhanced. The next chapter discusses another approach that uses DFree.

CHAPTER 6

Divergence-Free Based Architecture

This chapter discusses a LAAS architecture that employs Divergence-Free Smoothing (DFree) as its carrier-smoothing filter. When compared to IFree, DFree has one major advantage and one major disadvantage. The advantage is that its output noise level is much smaller than that of IFree because, unlike IFree, DFree uses only single-frequency code-phase measurements as its code input (see Section 4.3). This advantage is attractive because the low availability of IFree-based LAAS is caused by the large noise error on IFree outputs. The disadvantage is that DFree-based LAAS still suffers from residual ionosphere errors on differentially-corrected measurements under ionosphere spatial-gradient anomalies, whereas IFree completely liberates LAAS from any problems induced by ionosphere gradients. Section 4.3 showed that the residual ionosphere error for DFree is equivalent to the difference in ionosphere errors between airborne and ground measurements. The worst-case residual error at the decision point is, thus, approximately 2 meters, which is the product of the maximum spatial gradient of 0.4 m/km and the user-to-station separation of 5 km at the decision point. If this 2-meter error is not mitigated, it can result in unacceptable integrity risk. Therefore, the DFree-based architecture requires an integrity monitoring method that excludes range measurements whose ionosphere differences are hazardously large.

A straightforward approach to detecting large ionosphere differences is to separately estimate ionosphere errors in both airborne and ground systems and compare the estimated errors. This approach is theoretically feasible because the ionosphere error can be estimated by using dual-frequency measurements (ionosphere error estimation methods using dual-frequency measurements are described in detail for example in [Hansen, Hwang]). However, the estimated ionosphere errors are generally very noisy and offset by interfrequency biases due to the use of dual-frequency measurements. I have actually developed an ionosphere monitor involving ionosphere estimation, but it was ineffective for these reasons [Konno06].

This dissertation instead introduces another approach in which the airborne and ground monitors independently observe instantaneous rates of change of ionosphere errors to detect “signs” of anomalous ionosphere conditions. A benefit of this approach is that ionosphere change rates can be estimated easily and precisely, in contrast to ionosphere errors themselves. In fact, research on conventional single-frequency LAAS has proposed ionosphere monitoring methods in which ionosphere change rates are estimated using L1 Code-Minus-Carrier (CMC) measurements [Simili, Lee06b, Xie04]. This research, in contrast, develops a method that uses dual-frequency carrier-phase measurements to estimate the ionosphere change rates. Using only “clean” carrier-phase measurements and avoiding “noisy” code-phase measurements, this method quickly estimates very precise ionosphere change rates, making the monitor very sensitive in detecting ionosphere anomalies.

Although this monitor is capable of detecting almost all ionosphere anomalies, there exists a particular condition to which the monitor is theoretically insensitive. This problem is common among all methods that use ionosphere rate estimates to detect anomalies. In simple terms, this insensitivity is caused by the fact that the monitor observes ionosphere temporal gradients rather than spatial gradients or (better yet) absolute differences in ionosphere errors between the user and the ground station. Analyzing this undetectable condition, this research determines the worst-case condition for the ionosphere-rate monitoring method and develops a variation of VPL that

overbounds vertical position errors induced by that worst-case scenario. This VPL is called VPL_{iono} . The CAT IIb integrity requirement is met by using the ionosphere monitor and VPL_{iono} together. Availability simulations show that the resulting system will achieve more than 99.9% availability over more than 70% of CONUS and more than 99% availability over more than 85% of CONUS.

To explain DFree-based LAAS, this chapter begins by providing an overview of the system architecture from the integrity perspective (Section 6.1). Given the big picture of the integrity method, Section 6.2 describes the ionosphere monitoring method. After this, Section 6.3 analyzes conditions of ionosphere wave fronts to which the monitor is insensitive and specifies the worst-case condition for the monitor. Based on this worst-case condition, Section 6.4 develops the VPL_{iono} equation that protects the integrity of DFree-based LAAS. For the resulting system, Section 6.5 conducts availability simulations. Finally, Section 6.6 summarizes the key results discussed in this chapter.

Note that, as discussed in Section 4.3, two types of DFree can be implemented by using L1 and L5 measurements: one using L1 code-phase measurements as its code input (denoted here as “L1-based DFree”) and one using L5 code-phase measurements as its code input (denoted here as “L5-based DFree”). Figure 6.1 shows their block diagrams. In this chapter, integrity methods are first developed based on L1-based DFree and then are modified for L5-based DFree.

6.1 Overview of Integrity Method for DFree-Based LAAS

In the system introduced in this chapter, airborne and ground ionosphere monitors independently detect ranging signals that are most probably affected by anomalous ionosphere and exclude these signals. The ground station broadcasts its screening results to the user, and the user estimates its position excluding the faulted signals identified by the combined results of ground and airborne monitoring. At the same time, the user computes VPL_{DFH0} , VPL_{DFH1} , and VPL_{iono} based on accuracy information for the remaining signals. Comparing the maximum of these VPLs with VAL, the user

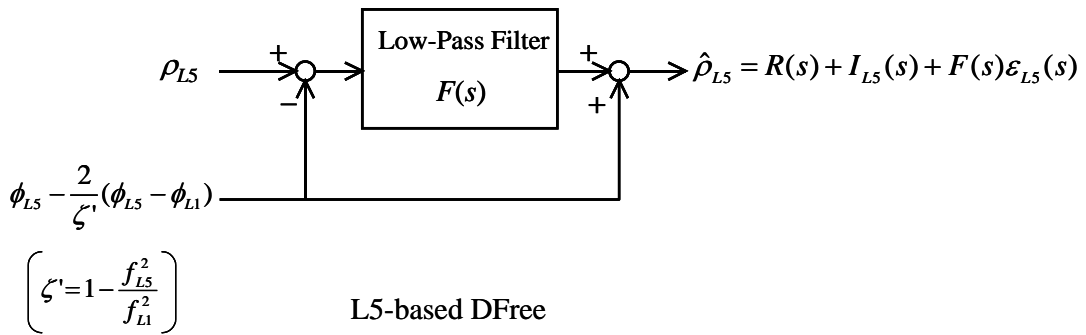
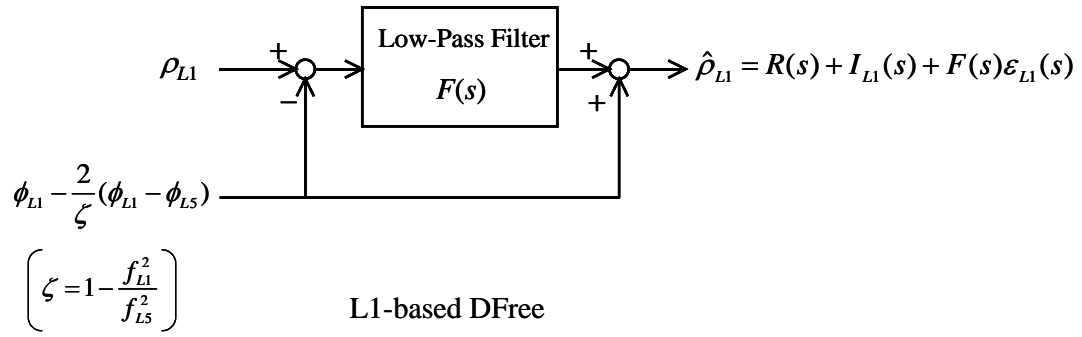


Figure 6.1: Two Types of Divergence-Free (DFree) Filters

decides whether or not to complete the landing operation. Figure 6.2 illustrates the block diagram of this integrity method.

Among these three VPLs, the equations for VPL_{DFH0} and VPL_{DFH1} are almost identical to the equations for VPL_{H0} and VPL_{H1} for conventional LAAS [Rtca04]. They are given as:

$$VPL_{DFH0} = K_{ffmd} \sqrt{\sum_{i=1}^N S_{vert,i}^2 \sigma_{rm,i}^2} \quad (6-1)$$

$$VPL_{DFH1,j} = K_{md} \sqrt{\sum_{i=1}^N S_{vert,i}^2 \sigma_{H1,i}^2} + \left| \sum_{i=1}^N S_{vert,i} B_{i,j} \right| \quad (6-2)$$

(j represents the j th receiver failure)

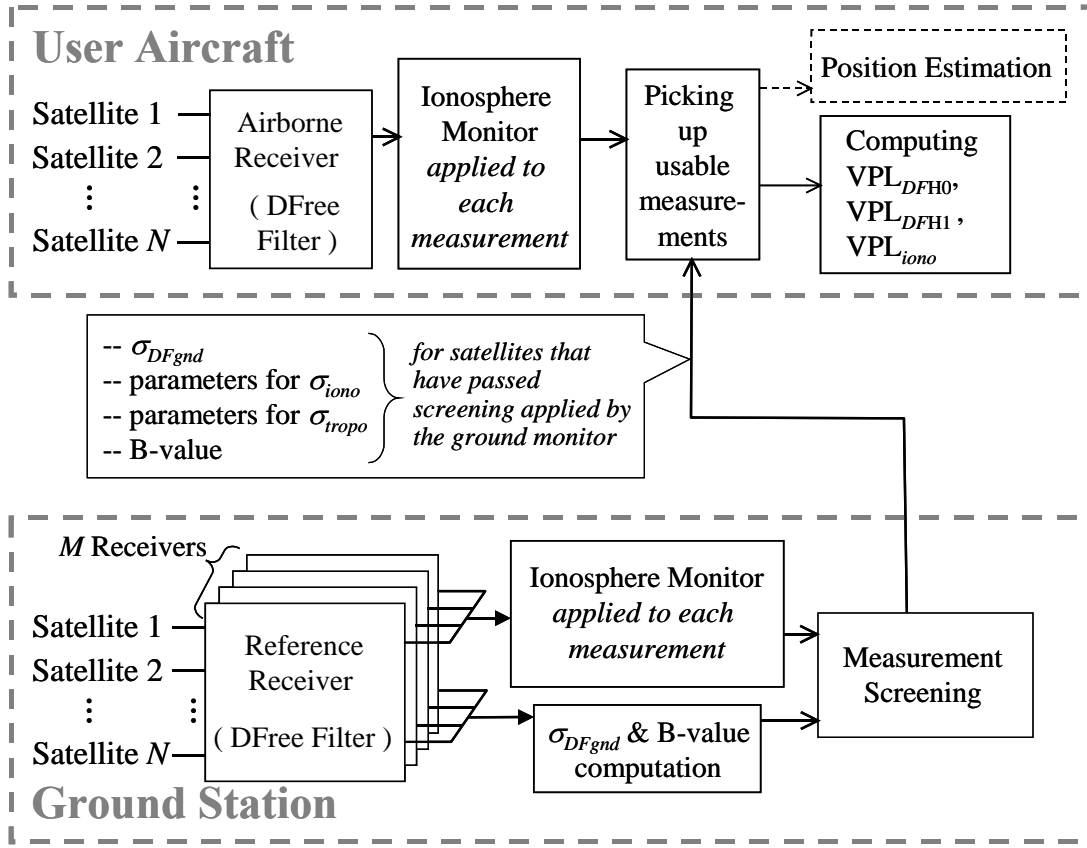


Figure 6.2: Block Diagram of Integrity Method

where the inflation factors K_{ffmd} and K_{md} are set to 6.673 and 3.7 for the four-receiver ground station configuration [Rtca04], the method for computing ground station B-values is described in Appendix B, and equations for $\sigma_{rm,i}$ and $\sigma_{H1,i}$ are given as follows.

$$\sigma_{rm,i}^2 = \sigma_{DFgnd,i}^2 + \sigma_{DFair,i}^2 + \sigma_{tropo,i}^2 + \sigma_{DFiono,i}^2 \quad (6-3)$$

$$\sigma_{H1,i}^2 = \frac{M}{M-1} \sigma_{DFgnd,i}^2 + \sigma_{DFair,i}^2 + \sigma_{tropo,i}^2 + \sigma_{DFiono,i}^2 \quad (6-4)$$

(M : Number of active reference receivers in the ground station)

where σ_{DFgnd} and σ_{DFair} are the standard deviations of the ground and the airborne DFree-receiver noise errors, σ_{tropo} is the sigma of residual troposphere errors given by

equation (2.39), and σ_{DFiono} is the sigma of residual ionosphere errors under nominal ionosphere conditions.

Because the noise level of L1-based DFree is identical with that of SFCS (see Section 4.3), the airborne and the ground receiver noise models (σ_{DFair} and σ_{DFgnd}) are the same as those for conventional LAAS. As a consequence, the LAAS accuracy designators (AADs and GADs) become reasonable choices for these models. Among these designators, this research uses AAD-B and GAD-C4 for the L1-based DFree airborne and ground receiver noise models, respectively. Note that, as discussed in Section 2.2.3, ground sigma values obtained from the GAD model may need to be inflated in accordance with the environment of the receiver site in order for σ_{DFgnd} to bound measurement errors out to a probability corresponding to the integrity requirement (10^{-9}). However, this research uses GAD-C4 without inflation to compute σ_{DFgnd} , assuming that this model is conservative enough to bound ground measurement errors out to a probability of less than 10^{-9} .

The form of sigma associated with residual ionosphere errors is slightly different between DFree-based LAAS and conventional LAAS because the ionosphere effects on DFree are different from those on SFCS (see Section 4.3). The σ_{DFiono} equation is given as:

$$\sigma_{DFiono} = \sigma_{vig} \cdot d_{gu} \cdot Oq(El) \quad (6-5)$$

where σ_{vig} is the standard deviation of nominal ionosphere spatial gradients in the vertical (zenith) domain and is set to 0.004 (m/km) in CONUS [Lee06a], d_{gu} is the distance in kilometers between the ground station and the user, and Oq is the obliquity factor corresponding to the elevation angle of the signal in question (see equation (2-7)).

With regard to L5-based DFree, the only difference in the VPL_{DFH0} and VPL_{DFH1} equations is the receiver noise model. As discussed in Section 4.3, the output noise level of L5-based DFree is expected to be smaller than that of L1-based DFree due to the

improved characteristics of the L5 signal (i.e., the higher signal power and the faster chipping rate compared to the L1 C/A-code signal). This research uses 0.5·AAD-B and 0.5·GAD-C4 for σ_{DFair} and σ_{DFgnd} of L5-based DFree. In other words, it assumes that the standard deviation of L5 signal errors is half that of L1 errors. This assumption is equivalent to the moderate assumption used in the availability simulations for IFree-based LAAS (see Section 5.3.1).

6.2 Ionosphere Change Rate Monitor

As described in the previous section, the airborne and the ground ionosphere monitors independently exclude ranging signals that are most probably affected by anomalous ionosphere. This section explains how the monitor detects faulty signals. Note that this ionosphere monitor needs no modification regardless of whether it is used with L1-based DFree or L5-based DFree.

To detect faulty signals, the ionosphere monitor observes ionosphere change rates that are estimated by using L1 and L5 carrier-phase measurements (ϕ_{L1} and ϕ_{L5}). First, the ionosphere error plus integer ambiguity is computed by the following equation.

$$\begin{aligned} \tilde{I}_{L1}[k] &= \frac{1}{\zeta}(\phi_{L5}[k] - \phi_{L1}[k]) = I_{L1}[k] + \frac{1}{\zeta}(N_{15}[k] + IFB + \tau_{gd}) + \frac{1}{\zeta}\varepsilon_{\phi15}[k] \\ &\left(\zeta = 1 - \frac{f_{L1}^2}{f_{L5}^2} \quad , \quad N_{15} = N_{L5} - N_{L1} \quad , \quad \varepsilon_{\phi15} = \varepsilon_{\phi L5} - \varepsilon_{\phi L1} \right) \end{aligned} \quad (6-6)$$

where ε_{ϕ} represents the multipath plus thermal noise error on the carrier-phase measurements. Assuming that no cycle slip is detected (and that none occurs, so that the differential integer ambiguities cancel out), instantaneous ionosphere change rates are computed as:

$$\tilde{I}_{L1,raw}[k] = \frac{1}{qT_{im}}(\tilde{I}_{L1}[k] - \tilde{I}_{L1}[k - q]) = \dot{I}_{L1}[k] + \dot{\varepsilon}_{\phi15}[k] \quad (6-7)$$

where T_{im} is the sampling period of the carrier-phase measurements, which is set to 0.5 seconds for LAAS, and q is an arbitrary integer that is set to 2 (by setting it to 2, the monitor looks at measurements 1 second backward in time). The raw ionosphere rates from (6-7) are then fed into a low-pass filter to reduce the noise.

$$\hat{I}_{L1}[k] = \frac{\tau_{im} - 1}{\tau_{im}} \hat{I}_{L1}[k-1] + \frac{1}{\tau_{im}} \tilde{I}_{L1,raw}[k] \quad (6-8)$$

where τ_{im} is the time constant for the low-pass filter, which is herein set to 20 seconds.

The estimated change rates \hat{I}_{L1} from (6-8) are the test statistics of this ionosphere monitor. They are compared with a fixed threshold to detect range signals that are most probably affected by anomalous ionosphere. A proper threshold is thus necessary to detect the faulted signals correctly. To determine this threshold, it is necessary to analyze statistical properties of nominal ionosphere change rates that are actually estimated by the process above. However, this analysis is currently impossible because the L5 signal has not been implemented in space yet. As the next-best option, this research determines a preliminary threshold based on the analysis of empirical data collected by an L1/L2 dual-frequency receiver. I collected L1/L2 carrier-phase measurements for six non-consecutive days (see Table 6-1) with the antenna/receiver system sited on the Durand building at Stanford University and statistically analyzed the ionosphere change rates computed from these measurements (modifying the change rate

Table 6-1: Dates for Data Taking on Durand Rooftop

Year	Date
2006	3/14, 4/12, 5/19, 7/27, 12/13
2007	2/22

estimation process to use L1/L2 measurements instead of L1/L5 measurements is straightforward).

Figure 6.3 presents all of the empirical change rates resulting from this experiment. This figure clearly shows that the gradient magnitude depends on the satellite elevation angle. Sample means and standard deviations are computed from the collected data in nine elevation bins of 10 degrees each. The results from each bin are then interpolated with fourth-order polynomials, creating continuous functions that represent the mean and the standard deviation of the empirical data. These functions— $\mathcal{M}_{ig_data}(El)$ for the mean, and $\sigma_{ig_ata}(El)$ for the standard deviation—are given as follows.

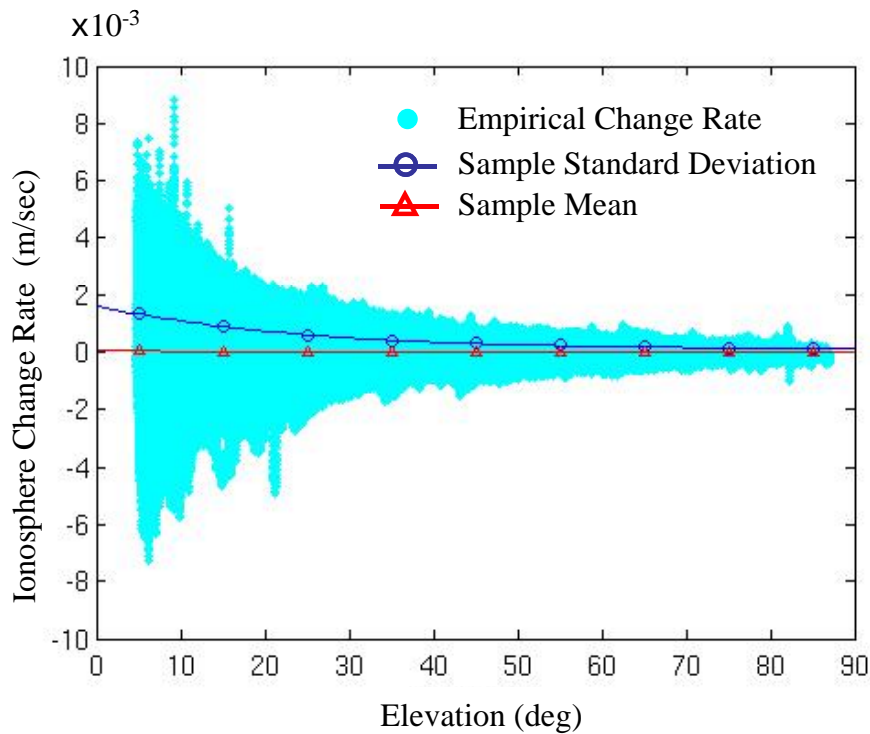


Figure 6.3: Ionosphere Change Rate Estimated from Empirical Data

$$\begin{aligned} \mathcal{M}_{ig_data}(El) = & 2.94 \times 10^{-11} El^4 - 5.98 \times 10^{-9} El^3 + \\ & 4.10 \times 10^{-7} El^2 - 1.10 \times 10^{-5} El + 9.31 \times 10^{-5} \quad (\text{m/s}) \end{aligned} \quad (6-9)$$

$$\begin{aligned} \sigma_{ig_data}(El) = & 2.00 \times 10^{-11} El^4 - 7.29 \times 10^{-9} El^3 + \\ & 9.75 \times 10^{-7} El^2 - 5.99 \times 10^{-5} El + 1.59 \times 10^{-3} \quad (\text{m/s}) \end{aligned} \quad (6-10)$$

where El is given in degrees. These functions are plotted in Figure 6.3.

By normalizing the empirical change rates with these functions, change rates independent of elevation angles are obtained. Figure 6.4 depicts the cumulative distribution function (CDF) of the normalized change rates. Ideally, the normalized change rates should be distributed according to a zero-mean Gaussian distribution with a standard deviation of 1, which is drawn as the red line in Figure 6.4. The plot clearly indicates that this ideal Gaussian distribution does not overbound the tails of the empirical data. Using a parameter search, it was found that, if the standard deviation is

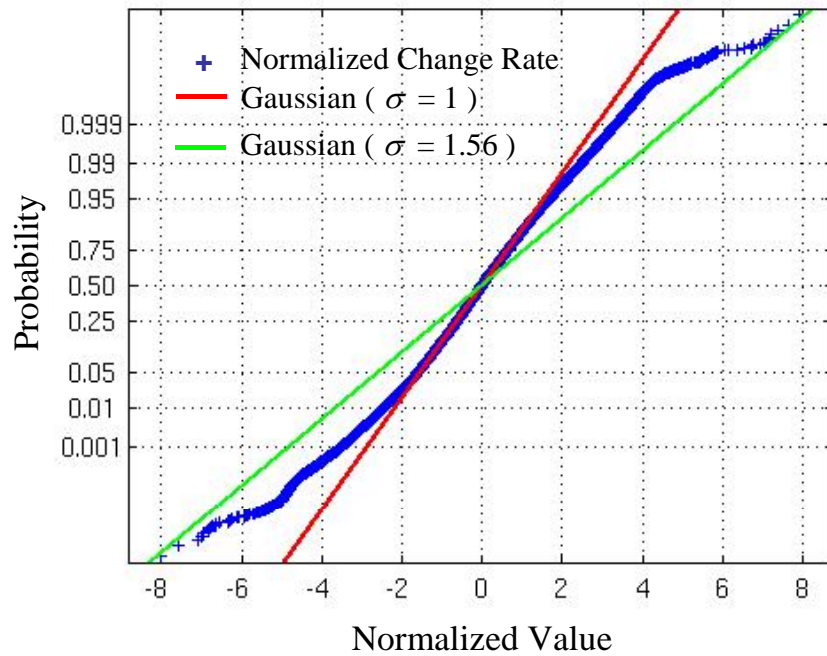


Figure 6.4: Cumulative Distribution Function of Normalized Change Rate

inflated by a factor of 1.56, the inflated Gaussian (the green line in Figure 6.4) overbounds the empirical data. The nominal ionosphere change rates in the archived data are therefore bounded by a zero-mean Gaussian distribution whose sigma (σ_{ig_bound}) is determined by the following equation.

$$\sigma_{ig_bound}(El) = 1.56 \cdot \sigma_{ig_data}(El) \quad (\text{m/s}) \quad (6-11)$$

Note that, in the logic above, the distribution bias (\mathcal{M}_{ig_data}) is neglected due to it being small compared to σ_{ig_data} .

Finally, the elevation-dependent threshold is set as:

$$\begin{aligned} Th_{ig}(El) &= \pm K_{ffd_ig} \cdot \sigma_{ig_bound}(El) \quad (\text{m/s}) \\ K_{ffd_ig} &= 6 \end{aligned} \quad (6-12)$$

Figure 6.5 plots this threshold (only for the positive side). The multiplier K_{ffd_ig} is set to 6 based on continuity considerations. As discussed above, in nominal (or fault-free) condition, ionosphere change rates are bounded by a zero-mean Gaussian distribution with the sigma of σ_{ig_bound} (m/s). By setting the threshold to six sigma, the theoretical probability of fault-free detection becomes less than 1.98×10^{-9} , where a fault-free detection is conservatively considered to always result in loss of continuity (meaning that the aircraft must abort its landing operation). Because the overall continuity requirement for CAT IIb LAAS is 2×10^{-6} (see Table 2-1), the probability of 1.98×10^{-9} corresponds to about 0.1% of the total allowed probability of continuity loss. Although there is no authorized allocation to continuity risk due to fault-free alerts by the ionosphere monitor, it should be sufficient to allot 0.1% of the total requirement to this particular risk.

This section determined the threshold based on the L1/L2 measurements, although the monitor is designed for the use of L1/L5 measurements. When it becomes possible, it makes sense to repeat the same data analysis procedure using L1/L5 measurements to determine the threshold for the actual monitor. However, the only difference that should

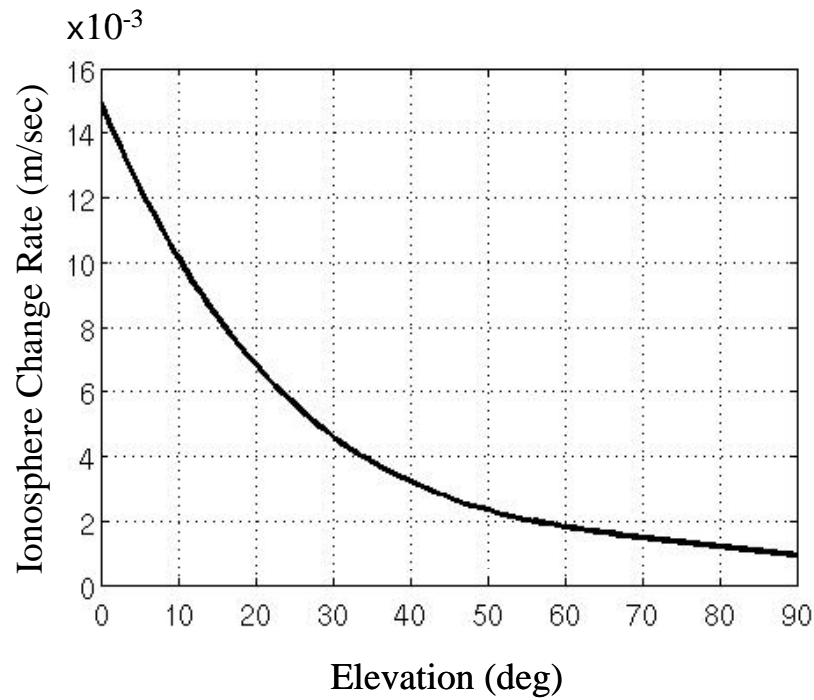


Figure 6.5: Threshold of Ionosphere Monitor

appear between the L1/L2 and L1/L5 data analyses is the effect of carrier-phase noise. The ionosphere change rates in the archived data in this research are contaminated by L1 and L2 carrier noise, while the change rates estimated in the future L1/L5 data analysis will be contaminated by L1 and L5 carrier noise. This difference should be very small; therefore, the threshold based on L1/L5 data should be very similar to that shown in this section (Figure 6.5) given similar receiver design, antennas, and siting conditions.

Finally, because the carrier-phase noise error is small to begin with, this monitor can generate very precise test statistics by setting the time constant in the low-pass filter (τ_{im}) as short as 20 seconds. Consequently, this monitor is quick and very sensitive in detecting most ionosphere anomalies. Figure 6.6 depicts the step response of this filter. Note that the 90% settling time is about 23 seconds. This 23-second settling time is much shorter than those of existing L1 Code-Minus-Carrier based ionosphere-rate monitors [Simili, Xie04]. For example, the *code-carrier divergence monitor* introduced in [Simili] has a settling time of about 150 seconds. Because an approach is nominally

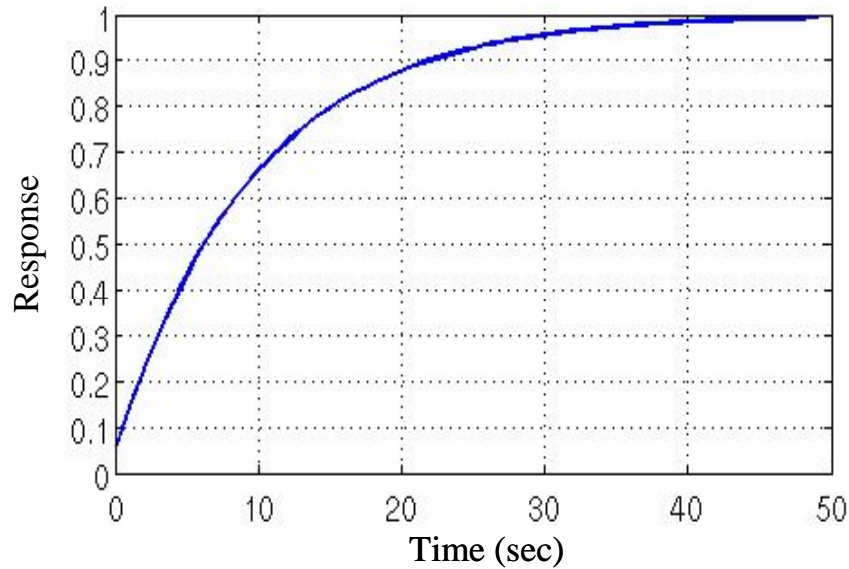


Figure 6.6: Step Response of Ionosphere Monitor

150 seconds long, the short response time means that the monitor will detect the onset of an unacceptable ionosphere effect within the time to complete the approach.

6.3 Undetectable Ionosphere Wave Fronts and the Worst-Case Condition for the Monitor

Although the dual-frequency ionosphere rate monitor introduced in the previous section can detect almost all ionosphere anomalies, there exists a particular condition to which the monitor is theoretically insensitive. This section describes this undetectable condition. A fundamental problem of this monitoring method is that it observes temporal gradients rather than spatial gradients or (better yet) absolute differences of ionosphere errors between the user and ground station. If an ionosphere wave front looks stationary from the point of view of the monitor, it is very difficult to detect.

Let us think about the simplest situation where an ionosphere wave front is affecting the airborne and the ground signals from a satellite in view, as illustrated in Figure 6.7. As discussed in Section 4.1, the ionosphere change rates on the airborne and the ground

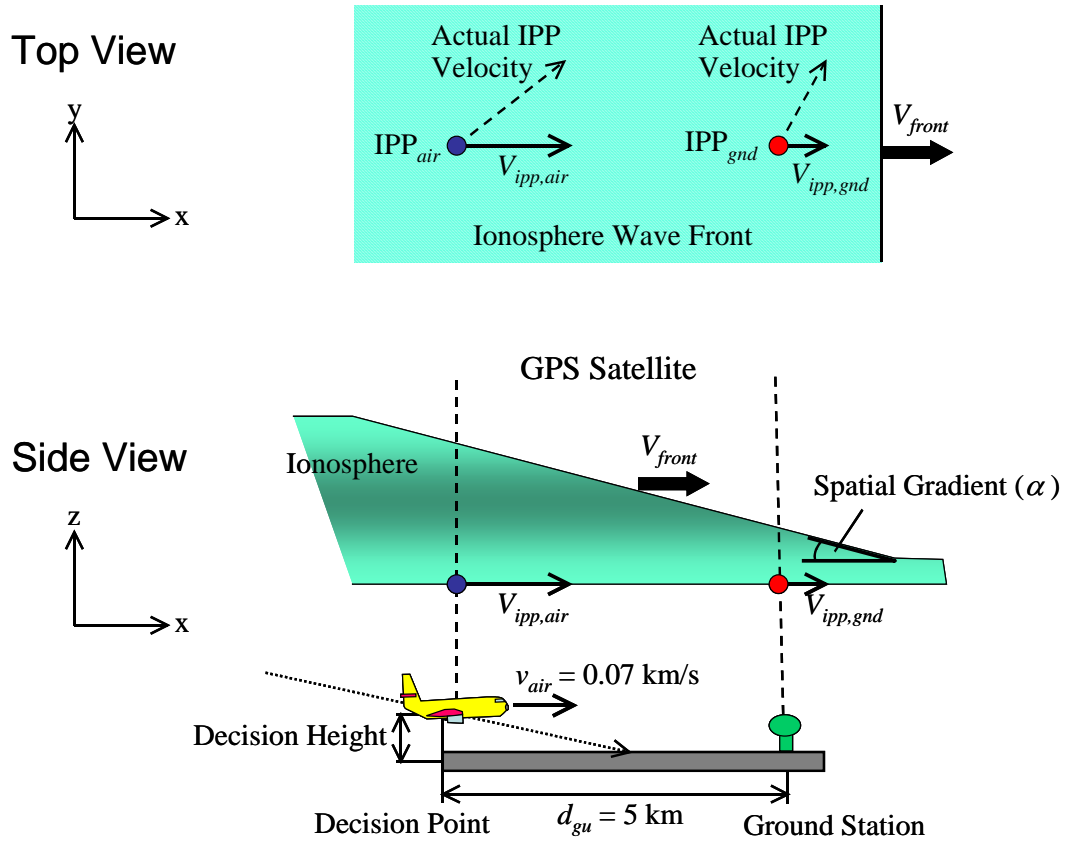


Figure 6.7: LAAS Operation Affected by Ionosphere Wave Front

Signals from a satellite to both airborne and the ground receivers are affected by an ionosphere wave front. The ionosphere change rate on each signal is dictated by the difference between the wave front velocity, V_{front} , and the IPP velocity, V_{ipp} .

measurements (\dot{I}_a and \dot{I}_g) are related to the spatial gradient of the ionosphere wave front (α) by the following equations.

$$\dot{I}_a = \alpha \cdot (V_{front} - V_{ipp,air}) = \alpha \cdot dV_{front / ipp,air} \quad (6-13)$$

$$\dot{I}_g = \alpha \cdot (V_{front} - V_{ipp,gnd}) = \alpha \cdot dV_{front / ipp,gnd} \quad (6-14)$$

From this model, it is obvious that, if the ionosphere front moves with the IPP (i.e. $dV_{front/ipp} = 0$), the observed ionosphere change rate becomes zero, making the monitor

insensitive to the front. Thus, ionosphere fronts that move with IPPs are very difficult for the monitor to detect.

Implementing the monitor in both user and ground station partially compensates for this weakness against the potential synchronized movement of fronts and IPPs. Because the user is approaching the ground station at a typical velocity of 0.07 km/s at the decision point, the airborne IPP has a different velocity from the associated ground IPP. Hence, if an ionosphere front moves with the airborne IPP, it must have a relative velocity of about 0.07 km/s with respect to the ground IPP, and vice versa. This relative velocity is actually large enough for the ground monitor to detect most threatening fronts. To make this point clear, let us transform the detection threshold on ionosphere change rates shown in Figure 6.5 into a threshold in the domain of ionosphere spatial gradients, using the linear model above (equation (6-13) or (6-14)) with $dV_{front/ipp,gnd} = 0.07$ km/s. Figure 6.8 depicts the resulting threshold for the ionosphere spatial gradient as a function of the elevation angle. As this figure indicates, if the relative velocity of the front with respect

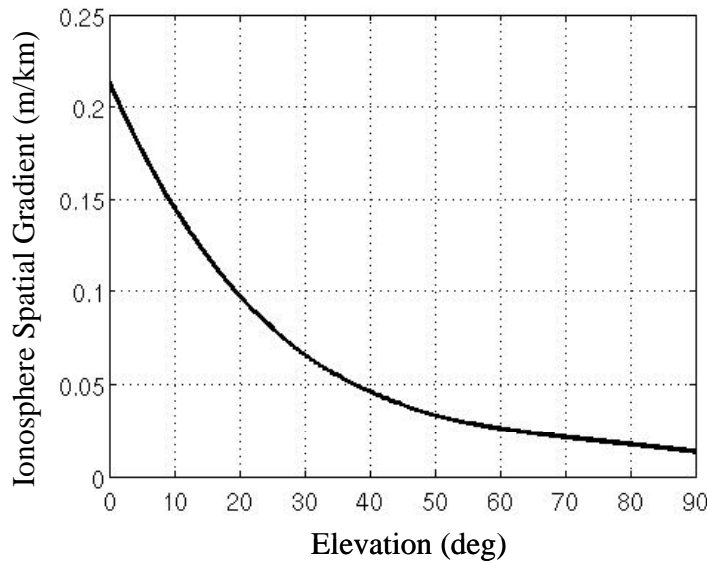


Figure 6.8: Monitor Threshold in Terms of Ionosphere Spatial Gradient

Given $dV_{front/ipp} = 0.07$ km/sec, the linear model of equation (6-13) (or (6-14)) transforms the threshold for the ionosphere change rate (Figure 6.5) into a threshold on the ionosphere spatial gradient. When $dV_{front/ipp}$ is 0.07 km/sec, the ionosphere monitor will detect fronts whose gradients are larger than this threshold.

to the IPP is 0.07 km/s, most threatening fronts—more specifically fronts steeper than 0.2 m/km—can be detected by the monitor, as they are located above the threshold throughout the entire range of possible elevation angles. Therefore, ionosphere fronts that affect both airborne and ground measurements, such as the one shown in Figure 6.7, will be detected by either the airborne or the ground monitor, if not both monitors.

Despite this constraint, a small set of undetectable fronts remains: fronts that move with the airborne IPP (or the ground IPP) and hit the ground IPP (or the airborne IPP) just as the airborne user passes over the decision point. Figure 6.9 illustrates this condition. An ionosphere wave front affects an airborne signal. The IPP on this signal is located 5 km from the leading edge of the front and is moving with the front, i.e. $dV_{front/ipp,air}$ is zero. Due to this synchronized movement, the airborne monitor cannot detect the front. The associated ground signal, on the other hand, is located more than 5 km from the airborne

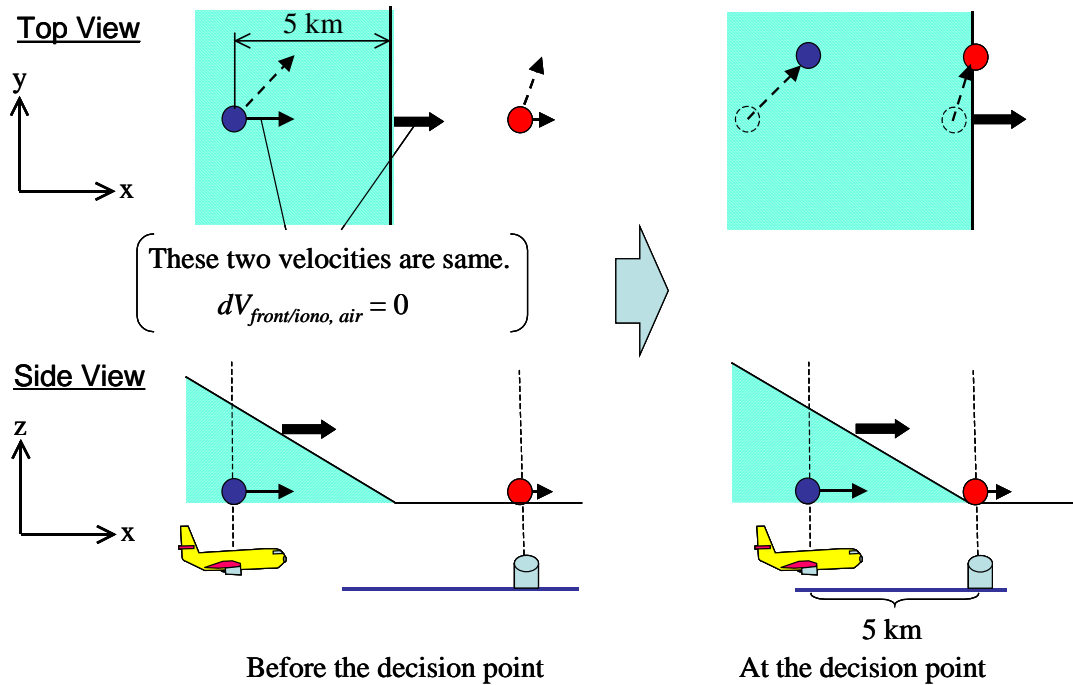


Figure 6.9: Undetectable Condition

An airborne signal is affected by an ionosphere wave front. The IPP on the signal is located 5 km from the leading edge of the front and moves with the front ($dV_{front,ipp} = 0$).

signal before the user passes over the decision point, meaning that the ground signal is not affected by the front before the decision point. Consequently, the ground monitor has no chance to detect the front during the approach of this particular airborne user. Note that this example shows the case where an airborne IPP is affected by a front, but a similar undetectable condition is also realized when an ionosphere front moves with an ground signal and hits the associated airborne signal when the user passes over the decision point.

This undetectable condition described above can also be applied to the case where a front affects ranging signals from more than one satellite. Figure 6.10 illustrates the undetectable condition for two satellites. Airborne signals from two satellites (i and j) are affected by an ionosphere front. The IPPs of these signals align on a line that is parallel to the leading edge of the front and is located 5 km from the edge. Moreover,

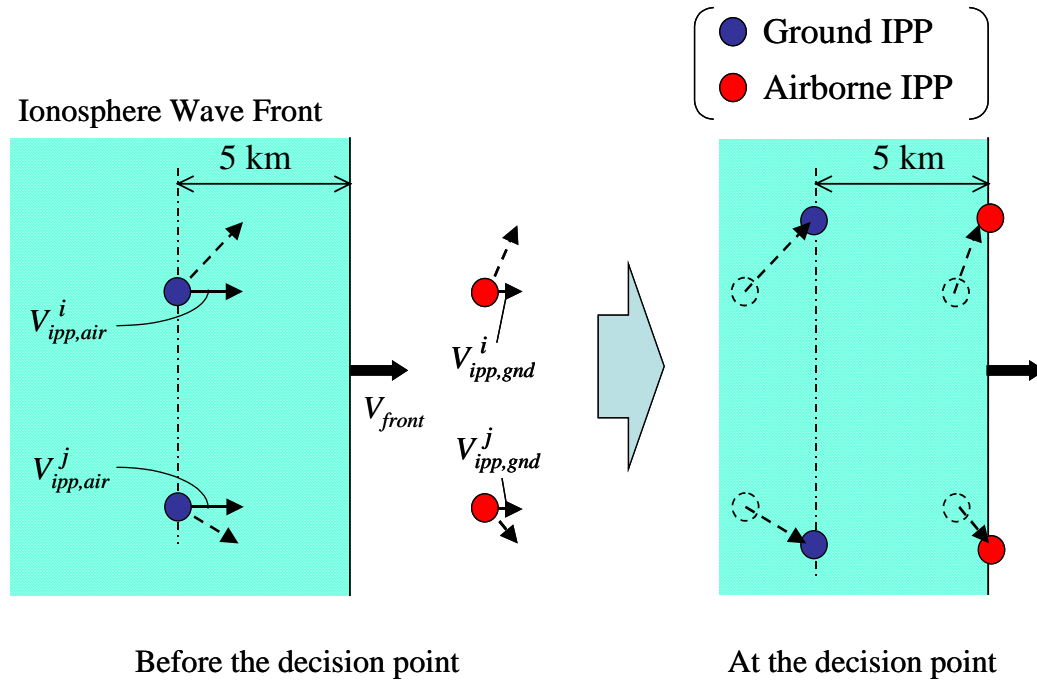


Figure 6.10: Undetectable Condition for Two Satellites (Top View)

Airborne signals from satellites i and j are affected by an ionosphere wave front. The IPPs of these signals align on a line that is parallel to the leading edge of the front and is located 5 km from the edge. The front velocity, V_{front} is equal to the velocities of these IPPs, $V_{ipp,air}$.

these IPPs move with the front, preventing the airborne monitor from detecting the front. On the other hand, the associated ground signals are not affected by the front before the user passes over the decision point, meaning that the ground monitor cannot detect the front during the approach of this particular user. Expanding this geometrical condition, one can easily construct a related undetectable condition for fronts that affect ranging signals from three satellites. Figure 6.11 illustrates this condition. Under this condition, both airborne and ground monitors will miss detecting the front for the same reason as the two-satellite case.

As shown above, it is easy to construct theoretical conditions for undetectable fronts that affect multiple ranging signals. However, being able to construct theoretical conditions does not mean that such situations can actually occur. Figures 6.10 and 6.11 imply that

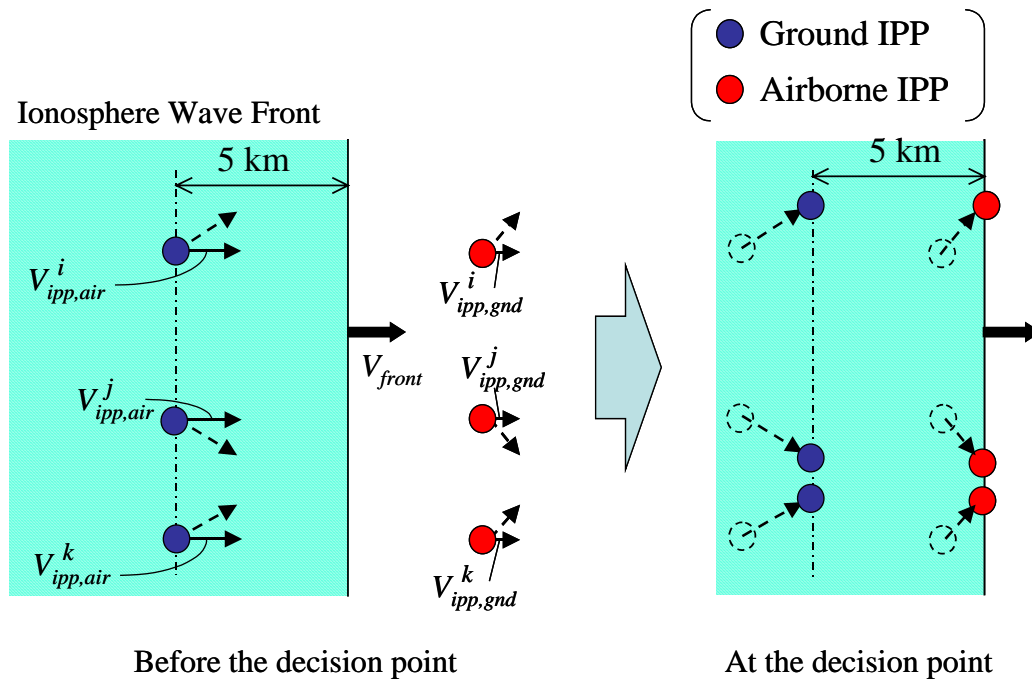


Figure 6.11: Undetectable Condition for Three Satellites (Top View)

Airborne signals from satellites i , j , and k are affected by an ionosphere wave front. The IPPs of these signals align on a line that is parallel to the leading edge of the front and is located 5 km from the edge. The front velocity, V_{front} is equal to the velocities of these IPPs, $V_{ipp,air}$.

the geometries of IPPs that could suffer from undetectable fronts very rarely occur, because it is highly improbable that multiple IPPs align on a line and move in the same direction. To confirm if such a unique condition would occur in practice, I investigated actual GPS satellite geometries for three airports: Memphis International Airport, Los Angeles International Airport, and John F. Kennedy International Airport (New York). The details of this investigation are described in Appendix C, but here, I show the outline of the investigation and its results.

This investigation first searched for satellite geometries in which two IPPs aligned on a single line and moved with velocities whose components orthogonal to the baseline were the same (see Figure 6.12). Signal pairs that satisfy this geometrical condition have the potential to be affected by undetectable fronts. Satellite geometries over the three airports above were generated with 10-minute time interval based on the standard 24-satellite GPS constellation [Dod], and for each geometry, IPP pairs that satisfy the geometrical condition described above were searched for by examining instantaneous IPP locations and velocities. This search found several IPP pairs meeting the condition, suggesting that one cannot neglect the threat of a front that simultaneously affects signals from two satellites without being detected by the ionosphere monitor. The investigation next searched for satellite geometries where three IPPs aligned on a single line and moved with velocities whose components orthogonal to the baseline were the same (see Figure 6.13). This time, the search found no IPP triplets that satisfied such a condition. This result means that, at least for the three airports searched in depth, there are no geometries that experience the condition where the ionosphere monitor can miss detecting fronts affecting signals from three or more satellites.

Based on the results of this investigation, I conclude that the ionosphere monitoring method may miss detecting fronts simultaneously affecting signals from two satellites, but that the method always detects fronts if they simultaneously affect signals from three or more satellites. Consequently, the worst-case condition for DFree-based LAAS that implements this ionosphere monitor is defined as follows.

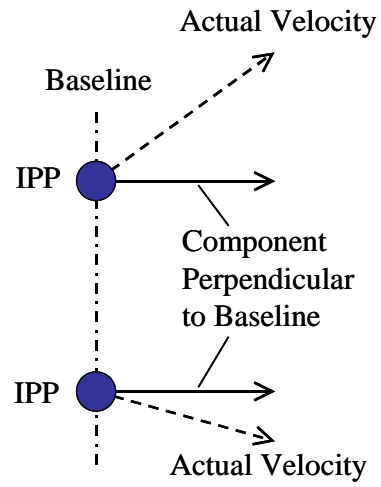


Figure 6.12: IPP Geometry the Investigation Searched for (Two-Satellite Case)

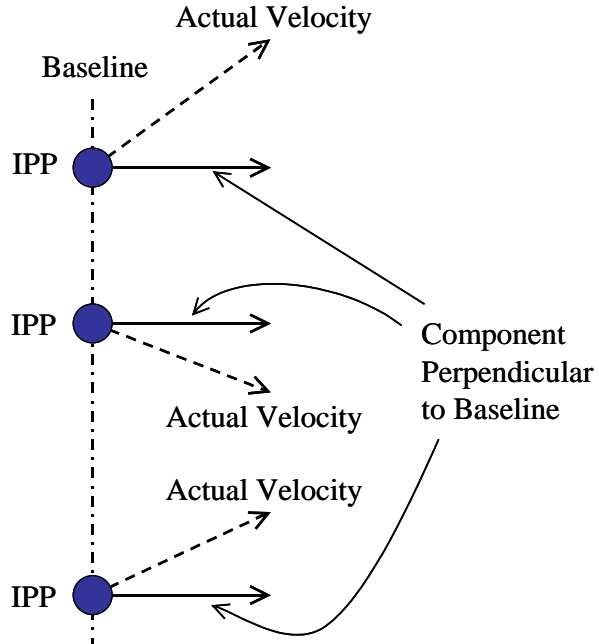


Figure 6.13: IPP Geometry the Investigation Searched for (Three-Satellite Case)

Worst-Case Condition: *A situation where an ionosphere anomaly wave front with the maximum gradient (0.4 m/km) affects signals from two satellites without being detected by either the airborne or ground ionosphere monitor.*

Here, it is important to note that the logic used to derive the worst-case condition does not constitute a formal proof. Two opposite assertions would be possible for this condition. One is to claim that a search that covers only three airports is not enough to eliminate the possibility that the monitor misses detecting ionosphere fronts affecting more than two satellites. IPP triplets that satisfy the undetectable condition might be discovered in analyzing geometries of other airports, making the risk of missed-detection of fronts affecting more than two satellites non-negligible.

The opposite claim would be that it is too conservative to conclude that the monitor could fail to detect fronts affecting two satellites. I analyzed instantaneous locations and velocities of IPPs based on snapshots of GPS satellite geometries and found IPP pairs whose instantaneous states satisfied the undetectable condition. However, I did not consider how these IPP pairs would transition to and from the undetectable state. In reality, all IPPs continuously change their locations and velocities and will not typically be in the undetectable state for very long before moving out of the state. As a result, through continuous monitoring, the ionosphere monitor is likely to detect faulty signals even if they are in the undetectable condition during a short period.

My personal opinion is closer to this second claim. Considering both the movements of IPPs and the very improbable nature of the undetectable condition, the ionosphere monitor should have a good chance to detect faulty signals. In fact, no previous study has considered an undetectable condition as severe as the one in this research. Some studies have discussed the possibility that an anomalous ionosphere wave front moves with one particular satellite such that the ionosphere-rate monitor could fail to detect it [Gratton05, Lee06b, Murphy06], but only this research considers the situation where two IPPs are moving with an ionosphere wave front. Thus, although further work will be needed to verify this worst-case condition, this research presumes that the worst-case

condition defined here is sufficiently conservative and derives an error bound (VPL_{iono}) on the basis of it.

6.4 Derivation of VPL_{iono}

VPL_{iono} represents a conservative bound on the theoretical vertical positioning error (E_{iono}) induced by the undetected ionosphere wave front. This positioning error is modeled as the sum of the random error associated with nominal range measurements and the bias error caused by the undetected front. The probability distribution of this error is hence given as:

$$p(E_{iono}) = \mathcal{N}(Bias, \sigma_v^2) \quad (6-15)$$

where $Bias$ represents the bias error due to the undetected front, and σ_v is the standard deviation of the random positioning error, which is given as:

$$\sigma_v = \sqrt{\sum_{i=1}^N S_{vert,i}^2 (\sigma_{DFair,i}^2 + \sigma_{DFgnd,i}^2 + \sigma_{DFiono,i}^2 + \sigma_{tropo,i}^2)}. \quad (6-16)$$

As discussed in Section 6.1, the appropriate models for σ_{DFair} and σ_{DFgnd} are AAD and GAD. The standard deviation of residual ionosphere errors (σ_{DFiono}) is given as equation (6-5), and the sigma of residual troposphere errors (σ_{tropo}) is given as equation (2-39).

VPL_{iono} is determined such that the probability of loss of integrity due to ionosphere anomalies does not exceed the allowable integrity risk for this fault mode. Loss of integrity involves three events: first, a threatening ionosphere anomaly occurs and affects a particular LAAS facility; second, the ionosphere monitor fails to exclude range signals affected by the anomaly; and finally, VPL_{iono} fails to bound the fault-induced positioning error. Each of these events has a probability: P_{iono} , the prior probability of threatening ionosphere anomalies; P_{md} , the conditional probability of missed detection by the ionosphere monitor given the existence of the anomaly affecting a given LAAS site; and P_{pl} , the conditional probability that the positioning error exceeds the error

bound given that an anomaly exists and that missed detection occurs. To meet integrity, the product of these three probabilities must not exceed the allowable integrity risk associated with ionosphere anomalies (P_a).

$$P_a > P_{pl} P_{md} P_{iono} \quad (6-17)$$

From this constraint, the maximum allowable risk (P_{pl}^*) that the positioning error exceeds the error bound given that the monitor has failed to detect signals affected by the anomaly is expressed as:

$$P_{pl}^* = \frac{P_a}{P_{md} P_{iono}} \quad (6-18)$$

VPL_{iono} is determined such that the risk of a vertical positioning error exceeding it does not surpass the maximum allowable risk given by (6-18) while the ionosphere behavior is monitored by the ionosphere monitor. Hence, given the distribution of vertical positioning error from equation (6-15), the value of VPL_{iono} can be determined by integrating this probability density up to the point that the probability of the error exceeding VPL_{iono} becomes the allowable risk P_{pl}^* from equation (6-18).

$$VPL_{iono} = -Q^{-1}\left(\frac{P_a}{P_{md} P_{iono}}\right)\sigma_v + Bias \quad (6-19)$$

Figure 6.14 schematically expresses the relationship between VPL_{iono} and the positioning error distribution. The bell-shaped curve represents the error distribution given range signals affected by an ionosphere wave front which the monitor has failed to detect (i.e., the Gaussian distribution given by equation (6-15)). The Q-function in equation (6-19) corresponds to the cumulative probability in the tail of the Gaussian error distribution outside VPL_{iono} (i.e., the shaded region in Figure 6.14). Strictly, the tails on both sides of the distribution should be taken into account. However, because the total probability in one side is negligible compared with the probability in the other,

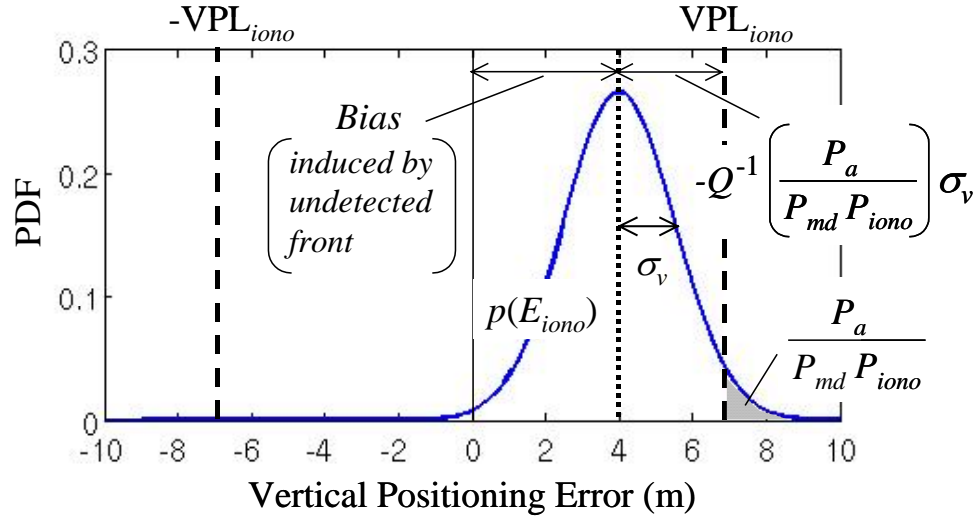


Figure 6.14: Relationship between VPL_{iono} and Vertical Position Error Distribution

only one tail is considered in equation (6-19), and the allowable risk (P_{pl}^*) is assigned to this tail.

Equation (6-19) gives the general form of VPL_{iono} . The remainder of this section specifies the term *Bias* and the three probabilities (P_a , P_{md} , and P_{iono}) considering the worst-case condition defined in the previous section.

Maximum Bias of Error Distribution: $Bias_{max}$

Recall that the worst-case condition for DFree-based LAAS that implements the ionosphere monitor described in this chapter is that an ionosphere front with the maximum gradient simultaneously affects range signals from two satellites without being detected by the monitor. The maximum bias in the positioning error induced by this condition occurs when the undetected front affects the two most “sensitive” satellites, meaning the two satellites for which a given range error magnitude translates

into the largest vertical position error magnitude. Accordingly, the maximum bias is given by the following equation.

$$Bias_{\max} = \max \left(\max_i \left(|S_{\text{vert},i}| \cdot \Delta \hat{I}_{\max} \right) , \max_{i,j} \left(|S_{\text{vert},i} + S_{\text{vert},j}| \cdot \Delta \hat{I}_{\max} \right) \right) \quad (6-20)$$

where $\Delta \hat{I}_{\max}$ is the maximum residual ionosphere error on the differentially-corrected measurement which is induced by the front. As discussed in Section 4.3, the residual ionosphere error for DFree-based LAAS is equivalent to the absolute difference of the instantaneous ionosphere errors on the airborne and the ground measurements (see equation (4-30)). Hence, $\Delta \hat{I}_{\max}$ is given as follows.

$$\Delta \hat{I}_{\max} = \alpha_{\max} \cdot d_{gu} \quad (6-21)$$

$$\alpha_{\max} = 0.4 \text{ (m/km)}$$

where α_{\max} is the maximum ionosphere spatial gradient, and d_{gu} is the distance between the user and the ground station. The maximum ionosphere error at the decision point, therefore, becomes 2 meters (recall that the user-to-station separation at the decision point is assumed to be 5 km).

In most cases, the maximum error occurs when the two most sensitive satellites are affected by the front—the second argument of the outer $\max(\bullet)$ in equation (6-20). However, on rare occasions, the error created by a front affecting the most sensitive single satellite is larger than the error created by the same front affecting the most sensitive two satellites. For example, if a satellite geometry has an $S_{\text{vert},i}$ row vector ($i = 1, \dots, 5$) given as $[-2.12, 0.67, 0.54, 0.03, 0.88]$, the maximum bias for the two-satellite-affected situation is 4.18 meters ($2 \times |-2.12 + 0.03|$), which is smaller than the maximum bias for the one-satellite-affected situation of 4.24 meters ($2 \times |-2.12|$).

Integrity Risk Allocated to Ionosphere Fault: P_a

The integrity risk allocated to ionosphere faults (P_a) is a sub-allocation from the overall system integrity requirement (10^{-9} /approach). As described in Section 2.3, ionosphere anomalies are categorized as H_2 risks. Three quarters of the total allowable integrity risk is allocated to the H_2 integrity risk category, but there is no authorized allocation to each of the individual H_2 risks. This research allots 10% of the total integrity requirement to ionosphere faults, setting P_a to 10^{-10} .

Probability of Missed-Detection of Ionosphere-Affected Signals: P_{md}

Under the worst-case condition, the probability of missed detection (P_{md}) is the probability that the ionosphere monitor fails to detect an ionosphere wave front that affects signals from two satellites in view. As discussed in Section 6.3, front “detectability” depends upon the relative velocity of the front with respect to the IPP ($dV_{front/ipp}$), which is a quantity that the monitor cannot observe. Hence, P_{md} cannot be explicitly determined. In other words, it is impossible to estimate in real time how often an ionosphere front is synchronized with a pair of IPPs. Although P_{md} is likely to be very small because this synchronization appears to be extremely rare, this research conservatively sets it to 1.

By setting the probability of missed detection to 1, it may appear that the monitor does not contribute to the mitigation of ionosphere risk. However, the monitor has already contributed significantly by reducing the set of ionosphere threats to cases in which the number of ranging signals that are affected by an ionosphere front without being detected by the monitor is two or fewer. In other words, in an anomalous condition, the monitor should exclude almost all the ranging signals affected by the anomaly, and after the exclusion, the number of signals that still have potential to be affected by the anomaly is limited to two or fewer.

Prior Probability of Ionosphere Anomaly: P_{iono}

The prior probability of an ionosphere anomaly (P_{iono}) is a controversial parameter in the LAAS community. To set this parameter, this research refers to work by Pullen *et al* [Pullen06]. They estimated the fraction of days in which spatial gradients enough to threaten LAAS might occur by investigating databases of ionosphere events. Applying some mitigating conditions to this baseline probability, they proposed P_{iono} of 10^{-6} as a sufficiently conservative value. This research adds extra conservatism to their estimate, setting P_{iono} to 10^{-5} for any given airport.

Table 6-2 summarizes the parameters necessary to complete the VPL_{iono} equation. Substituting these parameters into equation (6-19), the final VPL_{iono} equation is given as follows.

$$\begin{aligned}
 VPL_{iono} &= -Q^{-1}\left(\frac{10^{-10}}{1 \times 10^{-5}}\right) \cdot \sigma_v + Bias_{\max} \\
 &= 4.265 \cdot \sigma_v + \\
 &\quad \max\left(\max_i(|S_{vert,i}| \cdot \alpha_{\max} \cdot d_{gu}), \max_{i,j}(|S_{vert,i} + S_{vert,j}| \cdot \alpha_{\max} \cdot d_{gu})\right)
 \end{aligned} \tag{6-22}$$

Table 6-2: Summary of Input Parameters for VPL_{iono}

Parameter	Value or Equation
$Bias_{\max}$	$\max\left(\max_i(S_{vert,i} \cdot \alpha_{\max} \cdot d_{gu}), \max_{i,j}(S_{vert,i} + S_{vert,j} \cdot \alpha_{\max} \cdot d_{gu})\right)$
P_a	10^{-10} (10% of the total integrity requirement)
P_{md}	1
P_{iono}	10^{-5}

With regard to L5-based DFree, interesting differences emerge in this VPL_{iono} equation. As discussed in Section 4.3, L5-based DFree has an advantage and a disadvantage when compared to L1-based DFree. The advantage is that the output noise level of L5-based DFree is expected to be much smaller than that of L1-based DFree. Therefore, to compute σ_v in equation (6-22), better receiver noise models should be used. In the same manner as VPL_{DFH0} and VPL_{DFH1} , this research uses moderate models of 0.5·AAD-B and 0.5·GAD-C4 in the VPL_{iono} equation for L5-based DFree. The disadvantage of L5-based DFree is that the ionosphere error on the L5 measurement is about 1.8 times larger than the error on the L1 measurement (see Section 4.3). Due to this disadvantage, the maximum ionosphere spatial gradient to compute the bias term, α_{max} in equation (6-22), is inflated from 0.4 m/km to 0.72 m/km (i.e., by a factor of 1.8).

As the integrity method of DFree-based LAAS, three VPL definitions (VPL_{DFH0} , VPL_{DFH1} , and VPL_{iono}) have been described. Table 6-3 summarizes these VPL equations. For VPL_{iono} , it was noted in the previous section that further work would be needed to verify the two-satellite worst-case condition for the ionosphere monitor. If the worst-case condition were altered, modifying the VPL_{iono} equation is straightforward—only the “ $Bias_{max}$ ” term in equation (6-22) would be modified based on the revised number of undetected signals.

Table 6-3: Summary of VPL Equations (4 Reference-Receiver Configuration)

VPL _{DFH0}	$6.673 \sqrt{\sum_{i=1}^N S_{vert,i}^2 \sigma_{rm,i}^2}$ $(\sigma_{rm,i}^2 = \sigma_{DFgnd,i}^2 + \sigma_{DFair,i}^2 + \sigma_{tropo,i}^2 + \sigma_{DFiono,i}^2)$		
VPL _{DFH1,j}	$3.7 \sqrt{\sum_{i=1}^N S_{vert,i}^2 \sigma_{H1,i}^2} + \left \sum_{i=1}^N S_{vert,i} B_{i,j} \right $ $\left(\sigma_{H1,i}^2 = \frac{4}{3} \sigma_{DFgnd,i}^2 + \sigma_{DFair,i}^2 + \sigma_{tropo,i}^2 + \sigma_{DFiono,i}^2 \right)$		
VPL _{iono}	$4.265 \sqrt{\sum_{i=1}^N S_{vert,i}^2 \sigma_{rm,i}^2} +$ $\max \left(\max_i (S_{vert,i} \cdot \alpha_{\max} \cdot d_{gu}), \max_{i,j} (S_{vert,i} + S_{vert,j} \cdot \alpha_{\max} \cdot d_{gu}) \right)$		
L1-based DFree		L5-based DFree	
$\sigma_{DFair} : \text{AAD-B}$		$\sigma_{DFair} : 0.5 \cdot \text{AAD-B}$	
$\sigma_{DFgnd} : \text{GAD-C4}$		$\sigma_{DFgnd} : 0.5 \cdot \text{GAD-C4}$	
$\sigma_{DFiono} = 0.004 \cdot d_{gu} \cdot Oq(El)$		$\sigma_{DFiono} = 0.0072 \cdot d_{gu} \cdot Oq(El)$	
$\alpha_{\max} = 0.4 \text{ (m/km)}$		$\alpha_{\max} = 0.72 \text{ (m/km)}$	

6.5 Availability Simulations: Results and Discussions

This section evaluates the availability of the proposed DFree-based system, using the same simulation method introduced in Section 5.2. Because the integrity methodology is different between DFree-based LAAS and IFree-based LAAS, the decision rule for the availability indicator must be modified. For the DFree system, the decision rule is given in terms of VPL_{DFH0} and VPL_{iono} as shown below.

$$P_{avail-idc}(\lambda_m) = \begin{cases} 1 & \text{if } VAL \geq VPL_{DFree} \\ 0 & \text{otherwise} \end{cases} \quad (6-23)$$

$$VPL_{DFree} = \max(VPL_{DFH0}(\lambda_m), VPL_{iono}(\lambda_m))$$

All other processes in the availability simulation are the same.

For DFree, availability was first compared between systems using L1-based DFree and L5-based DFree assuming the 24-satellite constellation with the historical probabilities of satellite outages (see Tables 5-2 and 5-3). Figures 6.15 and 6.16 present the results for these two systems. As shown in Figure 6.16, the availability of the L5-based system is unacceptably low all over CONUS. This result implies that the disadvantage of larger ionosphere errors on L5 measurements overwhelms the advantage associated with lower receiver noise. Because of the significant inferiority of L5-based DFree, the remainder of this dissertation addresses only the system using L1-based DFree and calls it “DFree-based LAAS.”

As shown in Figure 6.15, DFree-based LAAS achieves more than 99.9% availability in the western and the northeastern regions of CONUS. Compared with the result for IFree-based LAAS shown by Figure 5.7, availability is clearly improved in the western region. However, as with IFree-based LAAS, there is a region in the southeast where availability is less than 99%. This common trend of low availability shown by two different approaches (IFree-based and DFree-based) strongly suggests that this region of CONUS has poor satellite geometry compared to other regions. Note that the typical

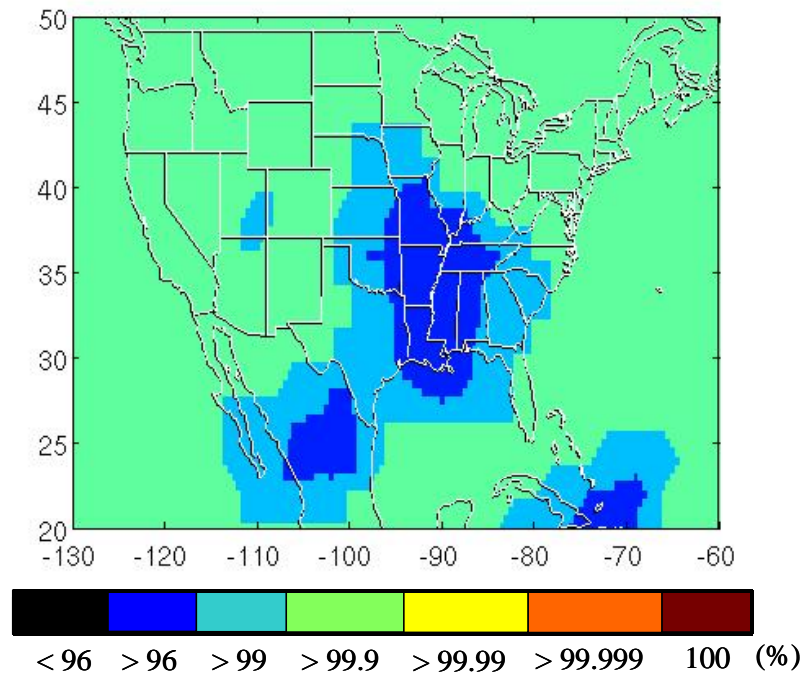


Figure 6.15: Simulation Result for L1-Based DFree (24-SV Constellation)

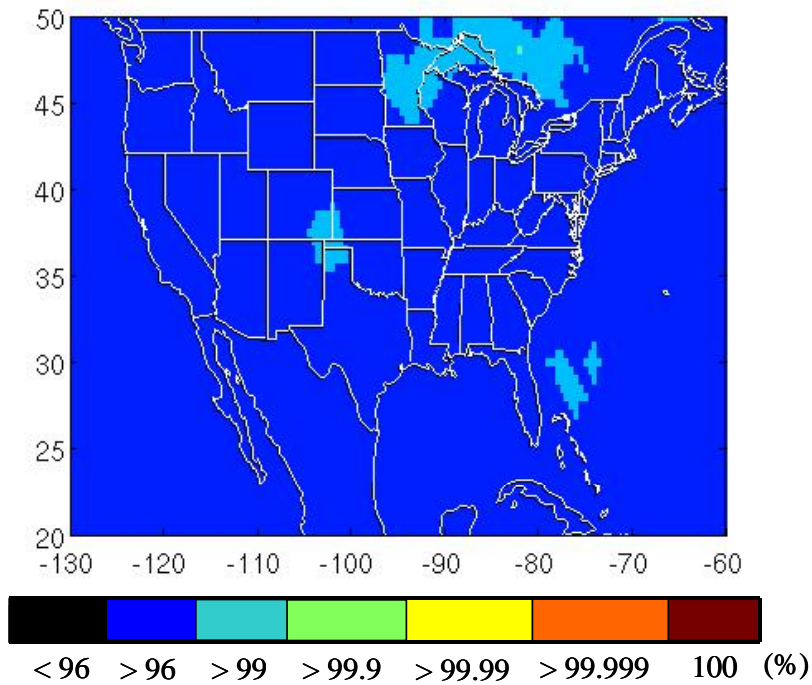


Figure 6.16: Simulation Result for L5-Based DFree (24-SV Constellation)

availability in this low-availability region is about 98%. In contrast, availability is quite good outside of this region.

Simulations for the 30-satellite constellation—optimistic case studies—were also conducted. As noted in the previous chapter, this constellation does not have a specific epoch defined for it. Hence, two cases were simulated with the epoch set to 00:00:00 and 10:00:00 (UTC) on March 12, 2007. Figure 6.17 shows the result for 00:00:00, and Figure 6.18 shows the result for 10:00:00. As these figures show, the local availability profile varies depending upon the assumed epoch. However, these results suggest that DFree-based LAAS will provide high availability over a very broad region of CONUS with the 30-satellite constellation.

Finally, it is also important to understand that the availability results above are for nominal ionosphere conditions. This simulation method is incapable of considering situations in which ionosphere wave fronts affect LAAS operations. If an ionosphere anomaly were to occur, the ionosphere monitor would almost certainly exclude signals affected by the ionosphere front, unless the very rare undetectable condition described in Section 6.3 were realized. The resulting deterioration of usable satellite geometry inflates VPL and, at some point, makes the system unavailable. Consequently, under ionosphere anomalies, DFree-based LAAS cannot retain the high availability shown in this section. Let us look at an example. Figure 6.19 (a) shows the satellite geometry at San Francisco International Airport (SFO) at 04:34:00 (UTC) on July 1, 1993, which has been generated from the ephemeris of the 24-satellite constellation (see Table 5-2). Azimuths and elevations of the visible satellites are listed in Table 6-4. VPL_{DFree} for this geometry is computed as 9.12 meters and is smaller than the 10-meter VAL at the decision point, meaning that LAAS is available. Suppose that an ionosphere front appears in the southeast corner of the sky and affects the signal from satellite 2 (see Figure 6.19 (b)) and that the ionosphere monitor excludes this signal. In this case, VPL_{DFree} for the remaining signals becomes 10.27 meters, which exceeds the 10-meter VAL at the decision point. If a user aircraft were on its final approach at this time in this particular condition, it would not be able to use LAAS. As demonstrated by this

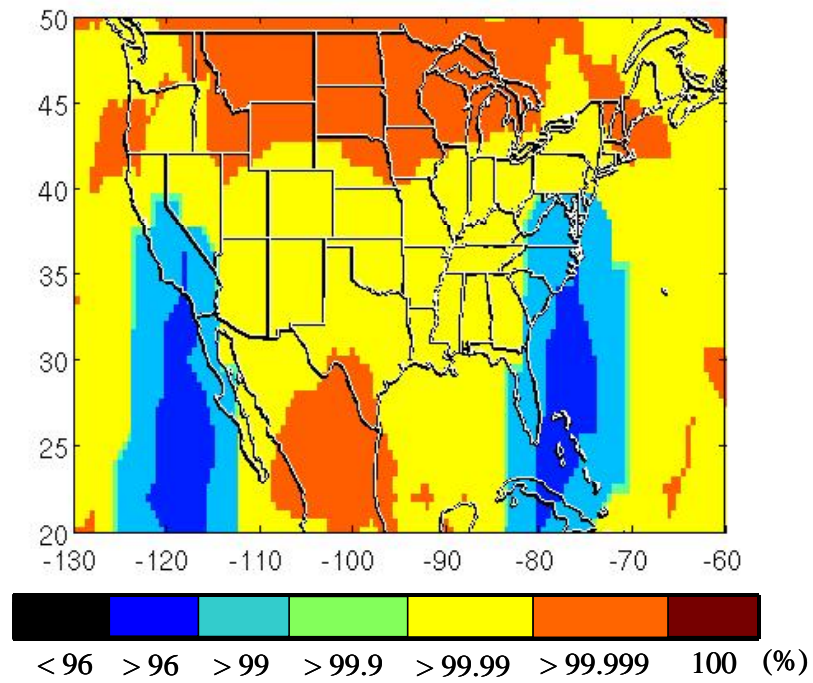


Figure 6.17: Simulation Result for 30-SV Constellation (00:00:00)

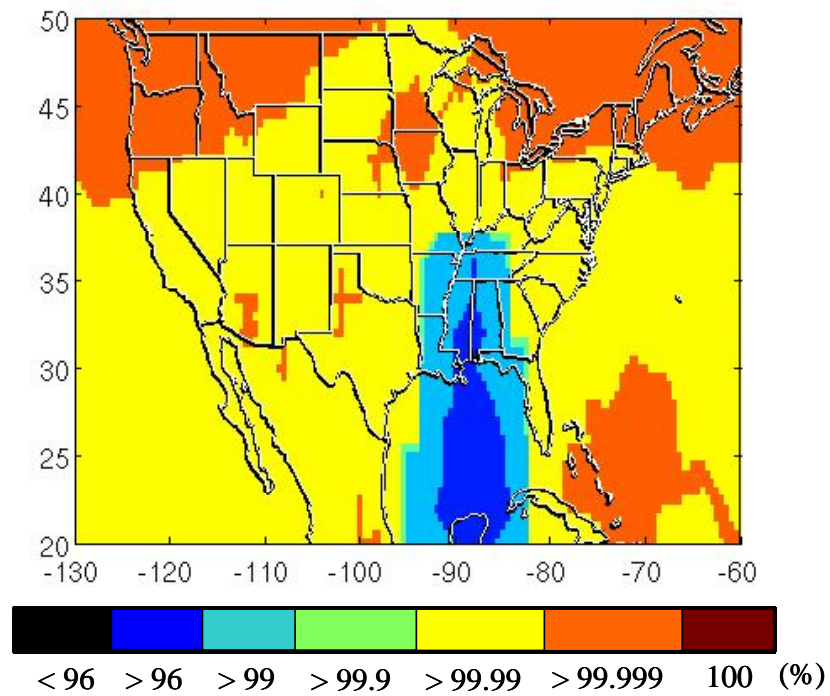


Figure 6.18: Simulation Result for 30-SV Constellation (10:00:00)

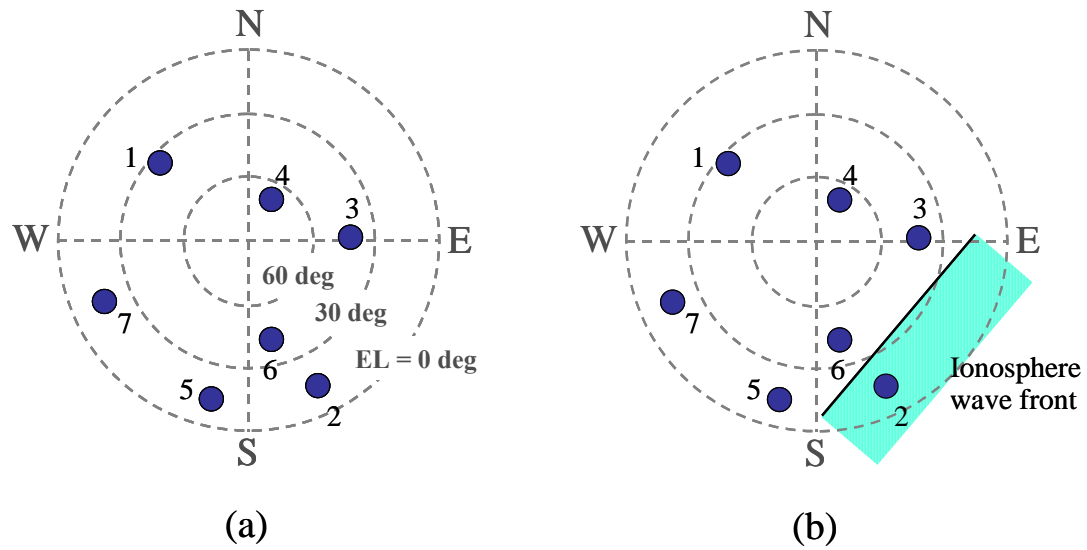


Figure 6.19: Sample Satellite Geometry over SFO (04:34:00 UTC on July 1, 1993)

(a) nominal condition, (b) an anomalous condition in which an ionosphere wave front appears at the southeast corner of the sky and affects signals from satellite 2.

Table 6-4: Location of Each Satellite in Sample Geometry

SV #	Az (deg)	El (deg)	SV #	Az (deg)	El (deg)
1	311.67	33.00	5	192.02	12.46
2	156.00	15.14	6	167.23	41.90
3	89.19	42.37	7	246.75	15.70
4	26.11	67.93	--	--	--

example, DFree-based LAAS could become unavailable under anomalous ionosphere conditions.

Although DFree-based LAAS has the potential to lose availability under ionosphere anomalies, this vulnerability does not overshadow the total quality of the system due to the rarity of ionosphere anomalies. As discussed in Section 6.4, the probability of the occurrence of an ionosphere anomaly is very conservatively estimated to be 10^{-5} per approach. Losing availability on such rare occasions is not a problem as long as the system provides integrity during these events, which is guaranteed by the proposed integrity algorithm. Therefore, given the simulation result of high availability over a broad region of CONUS under nominal conditions, the system architecture proposed in this chapter can be considered to be a satisfactory solution for the research goal—designing an integrity method for ionosphere anomalies that satisfies the integrity requirements of CAT IIb LAAS without negatively affecting system availability.

6.6 Summary

This chapter introduced a LAAS architecture that implements DFree with an ionosphere monitor. The availability of the resulting system was evaluated using the same method introduced in Chapter 5. The following bullets summarize key characteristics of the introduced methods and key results of the availability simulations.

- Unlike IFree, DFree does not mitigate all hazardous ionosphere conditions; hence, an integrity algorithm for ionosphere anomalies is required to meet the CAT IIb integrity requirement. This chapter introduced an integrity strategy that uses an ionosphere monitoring method along with a novel variation of VPL called VPL_{iono} .
- By observing instantaneous ionosphere change rates, the ionosphere monitor detects and excludes ranging signals that are most probably affected by anomalous ionosphere. By using only carrier-phase measurements to estimate the ionosphere change rates, this monitor can detect almost all faulted signals with

high sensitivity. However, it has the potential to fail to detect ionosphere wave fronts that move with IPPs.

- This chapter analyzed the geometrical conditions in which the monitor becomes insensitive to ionosphere fronts and defined the worst-case condition for the system using this monitor. This is a situation where an ionosphere wave front with the maximum gradient affects signals from two satellites without being detected by the ionosphere monitor.
- VPL_{iono} was designed to overbound the maximum vertical position error induced by the worst-case condition. Using VPL_{iono} and the ionosphere monitor together, the CAT IIIb integrity requirement is met.
- Availability simulations showed that, under nominal ionosphere conditions, the proposed system would achieve more than 99.9% availability over a broad region of CONUS except the southeast region where the estimated availability is less than 99% (typical availability in this region is about 98%).
- Although this nominal simulation result is promising, a limitation of this system is that it cannot retain high availability under anomalous ionosphere conditions. However, considering the rarity of ionosphere anomalies, losing availability during such rare events does not significantly reduce the overall availability of the system.

Because of the high availability shown by simulations, the approach introduced in this chapter can be considered to be a solution for the research goal of designing an integrity method for ionosphere anomalies that satisfies the integrity requirements of CAT IIIb LAAS without harming system availability.

A drawback of this system is the potential to lose availability under ionosphere anomalies. To address this vulnerability, the next section enhances the system with

IFree. This enhanced system uses IFree as a backup to DFree under anomalous ionosphere conditions where the DFree-based method may not be available.

CHAPTER 7

Enhanced System: Hybrid Dual-Frequency LAAS

The idea of the enhanced system is simple. Chapter 6 demonstrated that DFree-based LAAS provides sufficiently high availability while guaranteeing integrity (see Figure 6.15). However, it has the potential to lose availability during ionosphere anomalies by protecting integrity at the expense of availability. Chapter 5 showed that IFree-based LAAS cannot achieve sufficiently high availability under nominal ionosphere conditions. However, its advantage is that the expected availability does not change depending upon the ionosphere condition; in other words, the system can achieve higher than 96% availability even under severe ionosphere conditions (see Figure 5.7). The enhanced system enjoys the advantages of both architectures by implementing both DFree and IFree and switching between them based on ionosphere conditions. This architecture is more complex, but it provides optimal availability while still achieving the required integrity against ionosphere anomalies.

Section 7.1 introduces a simple system architecture that implements both DFree and IFree. For this “hybrid” system, it is important to specify observable and viable conditions under which the system switches from DFree to IFree such that the system

can fully obtain the advantages of IFree. Section 7.2 discusses this issue from the viewpoints of simplicity and availability. Finally, Section 7.3 summarizes this chapter.

7.1 Hybrid Dual-Frequency System Architecture

In order to switch between DFree and IFree without interrupting navigation, users and ground stations must execute both DFree and IFree methods simultaneously and in parallel. Figure 7.1 shows a simple architecture that carries out this task. As shown in this figure, the ground station produces differential corrections associated with each of DFree and IFree (e_{DFree} and e_{IFree}). At the same time, the ionosphere monitor described in Chapter 6 detects signals that are most probably affected by anomalous ionosphere. Then, the corrections (e_{DFree} and e_{IFree}) and sigmas (σ_{DFgnd} and σ_{IFgnd}) as well as B-values

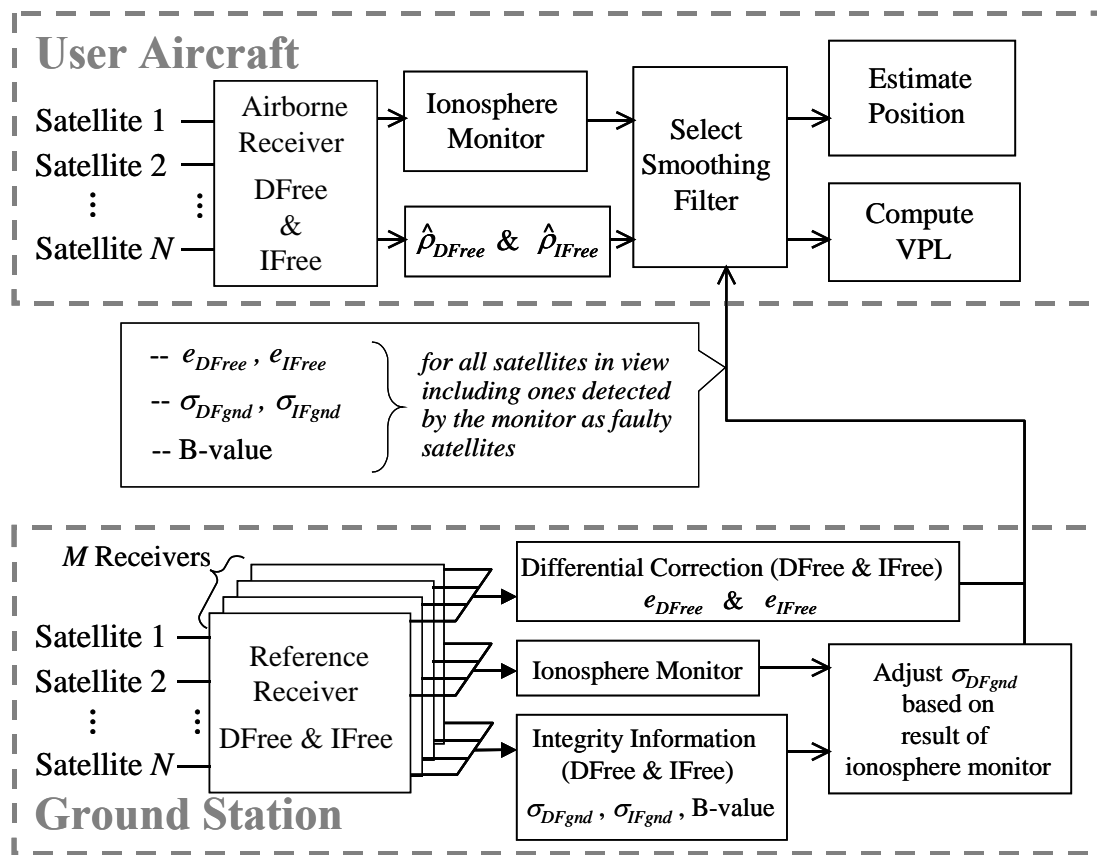


Figure 7.1: Hybrid Dual-Frequency System Architecture

are broadcast. Note that the ground station should broadcast corrections and sigmas for all satellites in view even if there are satellites detected by the ionosphere monitor as ones being affected by anomalous ionosphere, because such satellites can be used for position estimation if the user selects IFree. The result of monitoring should be passed to the user by adjusting the corresponding σ_{DFgnd} to a predetermined fixed value (such as 100.0) so that the user can exclude affected satellites when DFree is selected.

The user aircraft, on the other hand, also executes both DFree and IFree and applies differential corrections provided by the ground station, generating differentially-corrected measurements associated with each of these two methods. After that, range measurements for position estimation are selected between DFree-based and IFree-based measurements based on the selection strategy, which is the main topic of the next section. Finally, the user estimates its position by using the selected measurements and evaluates the VPLs associated with the selected method.

It is important to note that this hybrid approach does not actually require aircraft to implement both DFree and IFree. Even if user aircraft do not have the IFree filter, they are still compatible with the hybrid ground station. These users should apply DFree corrections while discarding the other information. The necessary integrity is guaranteed even for DFree-only users; in other words, the benefit obtained from the hybrid system is additional availability under ionosphere anomalies, not integrity. This flexibility would be attractive when deploying actual systems.

7.2 Switching Strategy between DFree and IFree

The main objective of switching from DFree to IFree is to obtain the highest possible availability during ionosphere anomalies while still meeting all integrity requirements. This section examines three types of switching strategies that balance simplicity and availability. In the first strategy, the system changes the smoothing method only for signals that the ionosphere monitor detects as those affected by anomalous ionosphere. Theoretically, this strategy will provide optimal availability but, unfortunately, would be impractical. The second strategy is computing VPLs associated with both DFree-based

and IFree-based architectures and selecting the smoothing method whose VPL is smaller. In this strategy, smoothing filters for all signals in view are changed simultaneously once the switch is triggered. The third strategy also switches the smoothing method for all signals in view simultaneously. In contrast to the second strategy, the switch is triggered whenever the ionosphere monitor detects one or more faulty signals. This strategy does not achieve optimal availability but is simpler because it does not require computing VPLs associated with the two architectures.

7.2.1 Switching Strategy I

In the DFree-based LAAS architecture introduced in Chapter 6, when the ionosphere monitor detects signals that may be affected by anomalous ionosphere, the system discards these signals, resulting in a deterioration of the satellite geometry. If, however, the smoothing filter for these signals is changed to IFree, these signals can be reintroduced for position estimation because the IFree filter “erases” the effect of the ionosphere anomaly. With regard to other signals that are not affected by the ionosphere anomaly, the system should keep using DFree, because IFree increases the signal noise level. Therefore, the strategy that switches the smoothing filter only for faulty ranging signals appears to be optimal from the viewpoints of both the satellite geometry and the signal noise level.

This strategy, however, has a critical problem that is caused by interfrequency biases. Recall that the outputs of DFree and IFree are modeled as follows.

$$\hat{\rho}_{DFree}(s) = R(s) + I_{L1}(s) + F(s)\varepsilon_{L1}(s) \quad (7-1)$$

$$\hat{\rho}_{IFree}(s) = R(s) + F(s)\left(\varepsilon_{L1}(s) - \frac{1}{\zeta}(\varepsilon_{L1}(s) - \varepsilon_{L5}(s))\right) + \frac{1}{\zeta}(IFB + \tau_{gd}) \quad (7-2)$$

As these equations show, the IFree output includes interfrequency biases (IFB and τ_{gd}), while the DFree output does not. If the system uses IFree for all signals in view, the interfrequency biases are estimated within the clock offset, posing no problem for

position-fixing. However, if the system mixes DFree and IFree together, these biases become additional error sources. Therefore, in order for this strategy to work, the airborne and the ground system must know the interfrequency biases for their receivers and (almost perfectly) calibrate these biases out of their measurements. This onerous requirement makes this strategy impractical.

7.2.2 Switching Strategy II

This section introduces a switching strategy that changes the smoothing filter for all ranging signals in view based on a VPL comparison between DFree-based and IFree-based architectures. Because all signals are simultaneously switched from one smoothing method to the other, the interfrequency-bias problem addressed in the previous section does not occur. Moreover, because VPL directly dictates system availability, within the constraint that all signals are simultaneously switched, this switching strategy will provide optimal availability.

To formalize this, let VPL_{DFree} be the maximum between VPL_{DFH0} and VPL_{iono} , and let VPL_{IFree} be VPL_{IFH0} . Under nominal conditions (namely, no satellite exclusion), VPL_{DFree} is usually smaller than VPL_{IFree} . However, once an ionosphere anomaly occurs and the ionosphere monitor excludes satellites affected by the anomaly, VPL_{DFree} increases due to the deterioration of the usable satellite geometry. If the system switches to IFree, the excluded satellites can be reintroduced into the position estimation. Comparing VPL_{DFree} after the exclusion and VPL_{IFree} for the original geometry and then selecting the method having the smaller VPL, the system will be able to achieve maximum availability while always protecting integrity (since the VPL equations do so by definition).

A drawback of this strategy is that the system needs to evaluate both VPL_{DFree} and VPL_{IFree} at every epoch. However, as discussed in Section 7.1, the system needs to execute DFree and IFree in parallel to avoid an interruption of navigation by switching, the additional cost to compute both VPLs is limited.

7.2.3 Switching Strategy III

This section discusses a switching strategy that changes the smoothing filter for all signals when the ionosphere monitor detects one or more faulty signal. This strategy is simple, but it could result in loss of availability compared to the previous switching strategy. Suppose that one signal in view is excluded by the ionosphere monitor. If VPL_{DFree} for the remaining signals is less than VAL , and if VPL_{IFree} for the original geometry (including the excluded signal) exceeds VAL , then the system loses availability by switching to IFree, while it would have been available otherwise. If such losses occur frequently, this strategy is not worth the simplification gained.

To analyze how much loss will be suffered by this strategy, this research defines *advantaged sub-geometries* and *disadvantaged sub-geometries*. Here, the phrase “sub-geometry” is used to represent the geometry comprised by the remaining signals after the exclusion of one signal. An advantaged sub-geometry is one that satisfies the following conditions.

- The sub-geometry is unavailable with DFree, namely $VPL_{DFree} > VAL$.
- The system becomes available if all signals are switched to IFree, namely $VPL_{IFree} \leq VAL$ (here, VPL_{IFree} is the one for the original geometry, with no signal exclusion).

A disadvantaged sub-geometry is opposite and is defined as follows.

- The sub-geometry is available with DFree, namely $VPL_{DFree} \leq VAL$.
- The system becomes unavailable if all signals are switched to IFree, namely $VPL_{IFree} > VAL$.

For example, consider again the satellite geometry over SFO that was used in Section 6.5. Figure 7.2 shows this satellite geometry, and Table 7-1 lists the azimuths

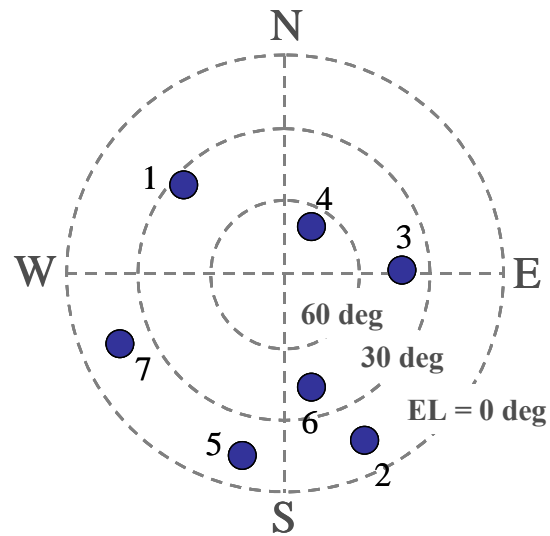


Figure 7.2: Example Satellite Geometry over SFO

Table 7-1: Location of Each Satellite in Example Geometry

SV #	Az (deg)	El (deg)	SV #	Az (deg)	El (deg)
1	311.67	33.00	5	192.02	12.46
2	156.00	15.14	6	167.23	41.90
3	89.19	42.37	7	246.75	15.70
4	26.11	67.93	--	--	--

and elevations of each of the satellites in view (this figure and table are identical to Figure 6.19 and Table 6-4, respectively). VPL_{DFree} and VPL_{IFree} for this geometry are computed as 9.12 meters and 9.09 meters, respectively (note that this geometry is a very rare geometry that has VPL_{DFree} larger than VPL_{IFree}). For this geometry, there are 7 possible sub-geometries whose values of VPL_{DFree} are listed in Table 7-2. The sub-geometry without satellite 2 and the one without satellite 6 are advantaged sub-geometries because the values of VPL_{DFree} for these sub-geometries exceed the VAL of 10 meters while VPL_{IFree} for the original geometry is less than 10 meters. The others are neither advantaged nor disadvantaged because the availability of the system is not changed by switching.

By counting the advantaged and disadvantaged sub-geometries for all original geometries over 24 hours, it can be estimated how much availability gain or loss will occur due to this switching strategy. I generated satellite geometries every 5 minutes from the standard 24-satellite constellation [Dod], assuming that all 24 satellites were healthy and counted these sub-geometries. Figures 7.3 and 7.4 show the counts of advantaged and disadvantaged sub-geometries, respectively, and Figure 7.5 presents their difference, i.e. advantaged minus disadvantaged (note that the color assignments of

Table 7-2: VPL_{DFree} for Each Sub-Geometry

Excluded SV #	VPL_{DFree} (m)	Excluded SV #	VPL_{DFree} (m)
1	9.50	5	9.13
2	10.27	6	11.98
3	9.17	7	9.09
4	9.31	--	--

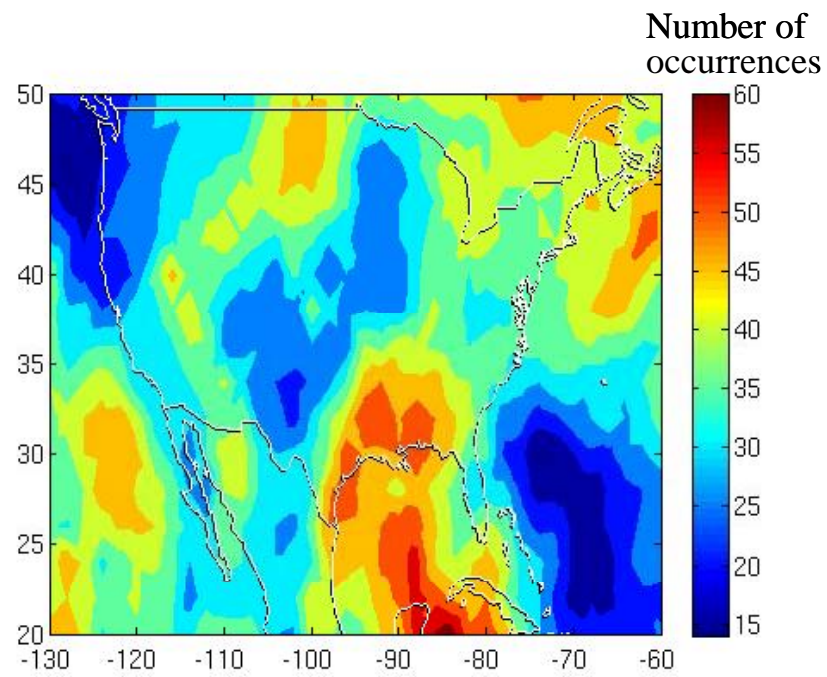


Figure 7.3: Count of Advantaged Sub-Geometries

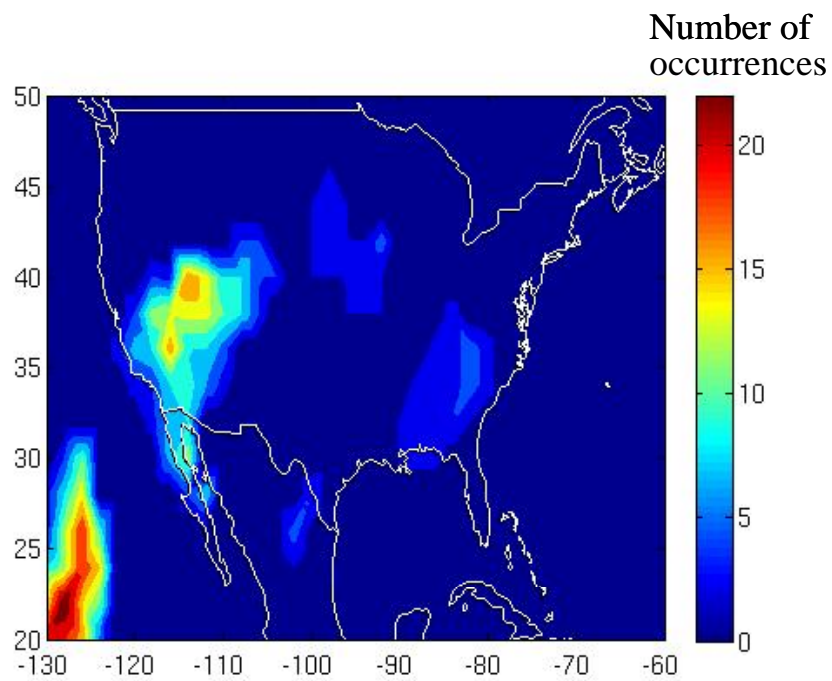


Figure 7.4: Count of Disadvantaged Sub-Geometries

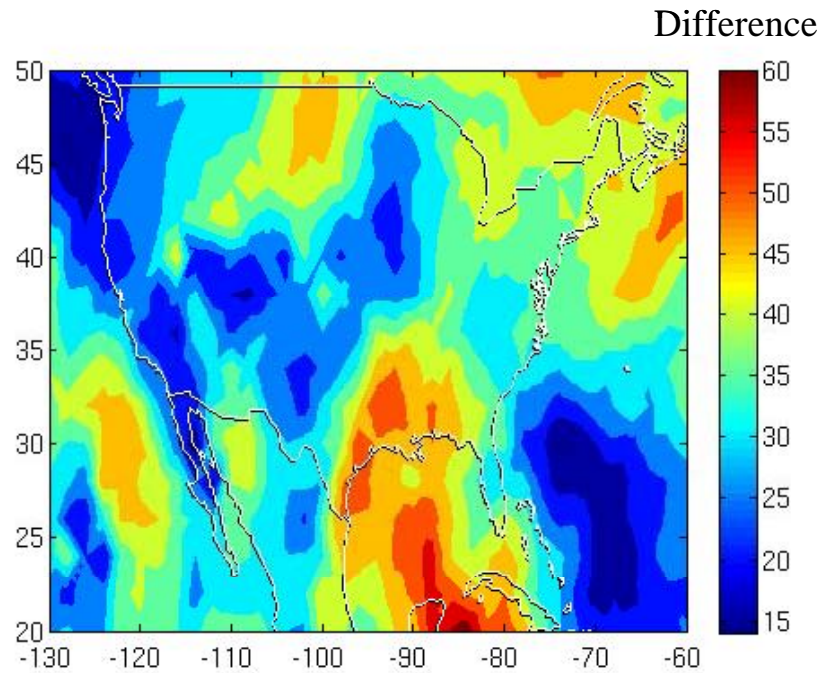


Figure 7.5: Difference of Advantaged minus Disadvantaged Sub-Geometries

these figures are different). Figure 7.3 indicates that there are many advantaged sub-geometries. Recall that the definition of advantaged sub-geometries includes the condition that DFree is unavailable for that sub-geometry. Hence, the result in Figure 7.3 implies that DFree-based LAAS will lose availability fairly often when a single satellite is excluded due to anomalous ionosphere. In contrast, Figure 7.4 indicates that few disadvantaged sub-geometries exist (and only in limited regions). This means that switching to IFree based on the “one-satellite-exclusion” rule will cause almost no loss of availability. Furthermore, Figure 7.5 shows that the number of advantaged cases surpasses that of disadvantaged all over CONUS, meaning that the switching strategy introduced in this section is statistically beneficial everywhere in CONUS.

7.3 Summary

This chapter introduced a system architecture that implements both DFree and IFree. In this architecture, IFree is used as a backup to DFree in situations where DFree loses

availability due to severe ionosphere anomalies. Although IFree is a backup method, the system must always execute both smoothing filters in parallel to switch between them without interrupting navigation.

An important issue in this chapter is under what conditions the system should switch from DFree to IFree. The optimal switching strategy is the one in which the system evaluates VPL_{DFree} and VPL_{IFree} in parallel and selects the method with the smaller VPL. Other than this optimal strategy, this chapter showed that a very simple strategy also works effectively. In this simpler approach, the system switches from DFree to IFree whenever the ionosphere monitor detects one or more faulty signals.

The resulting hybrid system, while being more complex than DFree or IFree alone, provides more than 96% availability even under severe ionosphere anomalies, which is probably impossible for DFree-only LAAS.

CHAPTER 8

Conclusion

Severe ionosphere anomalies are currently regarded as the most threatening fault mode for LAAS. This research has focused on developing new integrity methods that mitigate ionosphere anomalies to the degree required for future CAT IIIb LAAS operations. This chapter summarizes the key achievements of this research and proposes several suggestions for future research.

8.1 Core Research Contributions

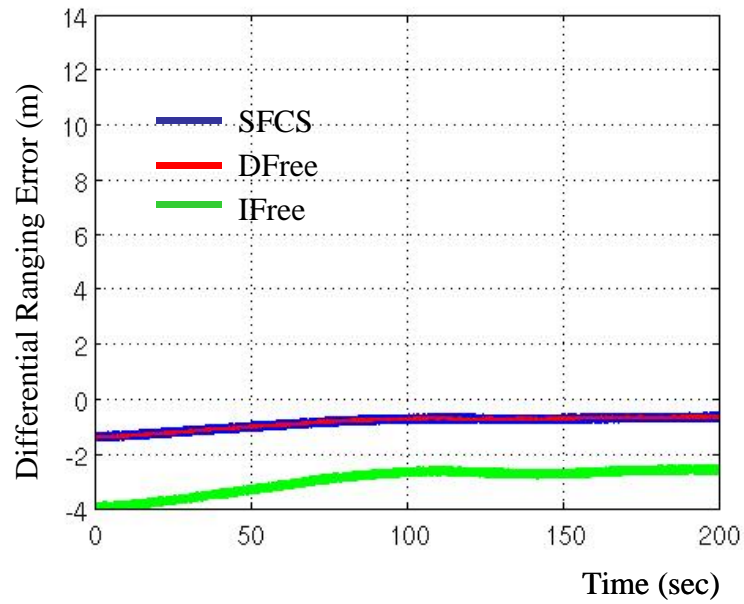
The goal of this research is to design and evaluate methods that satisfy two mutually conflicting demands: (1) the method should be sufficiently sensitive to anomalous ionosphere behavior so as to satisfy the integrity requirements of CAT IIIb LAAS, but (2) it should also provide acceptable system availability. To accomplish this goal, this research uses two types of dual-frequency carrier-smoothing filters—Divergence-Free Smoothing (DFree) and Ionosphere-Free Smoothing (IFree). These filters existed prior to the beginning of this research, but their accuracy and integrity performance had not been evaluated in the presence of ionosphere spatial-gradient anomalies. This research is the first to develop system architectures that apply these filters as the central part of integrity methods for ionosphere anomaly mitigation and evaluate the resulting systems

from the viewpoint of overall system availability. The key contributions made during this research are summarized below.

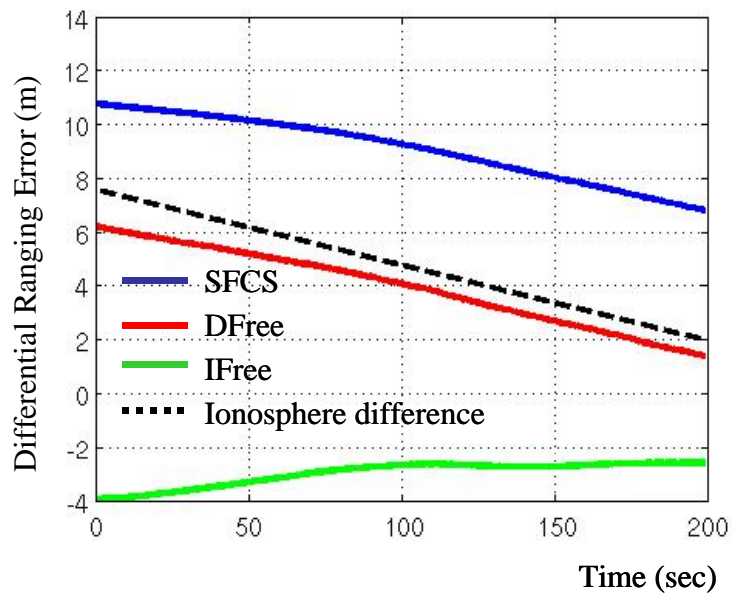
8.1.1 Evaluation of DFree and IFree Considering Ionosphere Anomalies

The major contributions of this research involve quantitative evaluation of DFree and IFree from the viewpoint of both robustness against ionosphere anomalies and residual receiver noise errors. Chapter 4 analytically derived the maximum differential ranging error—the error on the differentially-corrected measurement—for each of DFree, IFree, and conventional Single-Frequency Carrier-Smoothing (SFCS) under the most severe ionosphere condition. In addition, this chapter verified these theoretical values with “failure tests,” which are semi-empirical-data-based simulations in which an artificial amount of ionosphere error consistent with the most severe anomaly condition is added to empirical data taken under nominal ionosphere conditions.

Figure 8.1 shows key results of these failure tests. Figure 8.1 (a) depicts differential ranging errors under a nominal ionosphere condition for each of DFree, IFree, and SFCS (this plot is identical to the plot for satellite S6 in Figure 4.13 except the y-axis range). As shown in this figure, the residual error for IFree is noticeably larger than the other two, which have almost identical residual errors. This result reflects the fact that IFree has larger receiver noise errors in its outputs compared to the other two methods. Figure 8.1 (b) plots differential ranging errors under the most severe ionosphere condition (this plot is identical to Figure 4.16). In contrast to the nominal case, IFree shows its superiority to the other two methods and demonstrates its insensitivity to ionosphere conditions. The DFree error is noticeably larger than the error of IFree, but it is much smaller than the SFCS error, implying that DFree is much more robust against ionosphere anomalies than SFCS. Moreover, the DFree error is located in the vicinity of the ionosphere difference between the user and the ground station (the black dashed line in the figure) which is induced by the artificially injected ionosphere error. This result is consistent with the theory that the residual ionosphere error of DFree is equivalent to the ionosphere difference between user and ground station.



(a) Nominal Condition



(b) Anomalous Condition

Figure 8.1: Failure Test Results from Injecting a Simulated Ionosphere Anomaly into Nominal Test Data

8.1.2 IFree-based LAAS

As described in Chapter 5, this research designed and evaluated a LAAS system architecture that implements IFree as its smoothing filter. Because IFree completely eliminates ionosphere delay errors from GPS range measurements, there is no integrity risk associated with ionosphere anomalies for the IFree-based system. Instead, the major concern is large receiver noise errors remaining in smoothed measurements. Considering these characteristics, this research developed equations for VPL_{IFH0} and VPL_{IFH1} that limit integrity risks associated with fault-free user errors (H_0) and undetected single reference-receiver failures (H_1).

Availability simulations showed that this IFree-based approach would achieve an availability of between 96 and 99.9% over a broad region of CONUS (see Figure 8.2, which is identical to Figure 5.7). Although IFree-based LAAS liberates users from any ionosphere-spatial-gradient-related problems, this level of availability is not acceptable

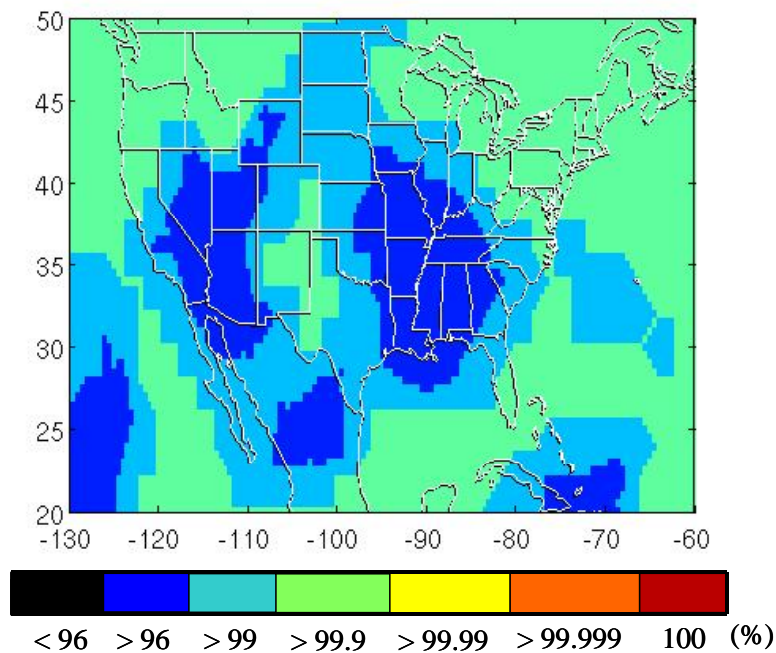


Figure 8.2: Availability of IFree-Based LAAS

for the practical use. An advantage of this architecture, however, is that the system achieves the same availability regardless of the ionosphere-spatial-gradient condition. More than 96% availability under severe ionosphere conditions is attractive.

8.1.3 DFree-based LAAS

A system architecture that uses DFree as its smoothing filter was also designed and evaluated in Chapter 6. Because DFree does not mitigate all hazardous ionosphere conditions, an ionosphere monitoring algorithm is necessary for this architecture to meet the CAT IIb integrity requirement.

This research introduced an ionosphere monitoring algorithm used by both ground and airborne receivers that detects and excludes signals that are probably affected by anomalous ionosphere by observing ionosphere change rates. Using dual-frequency carrier-phase measurements to estimate the ionosphere change rates, this algorithm detects faulty signals quickly and sensitively. However, faulty signals that move with ionosphere wave fronts from the perspective of the observing receiver are very difficult for this monitor to detect. Analyzing potential geometrical conditions in which the monitor becomes ineffective, the worst-case condition for the monitoring algorithm was defined. To ensure integrity under the worst-case condition, this research developed a VPL_{iono} equation that bounds vertical position errors induced under this condition. Using this VPL_{iono} together with the ionosphere monitoring algorithm, the CAT IIb integrity requirement is met.

Availability simulations for the resulting system showed that this approach can achieve more than 99.9% availability over more than 70% of CONUS (see Figure 8.3, which is identical to Figure 6.15). One drawback of this approach is that the system may lose availability under severe ionosphere conditions by protecting integrity at the expense of availability. However, due to the rarity of ionosphere anomalies, losing availability during such rare events does not overshadow the attractiveness of the proposed system.

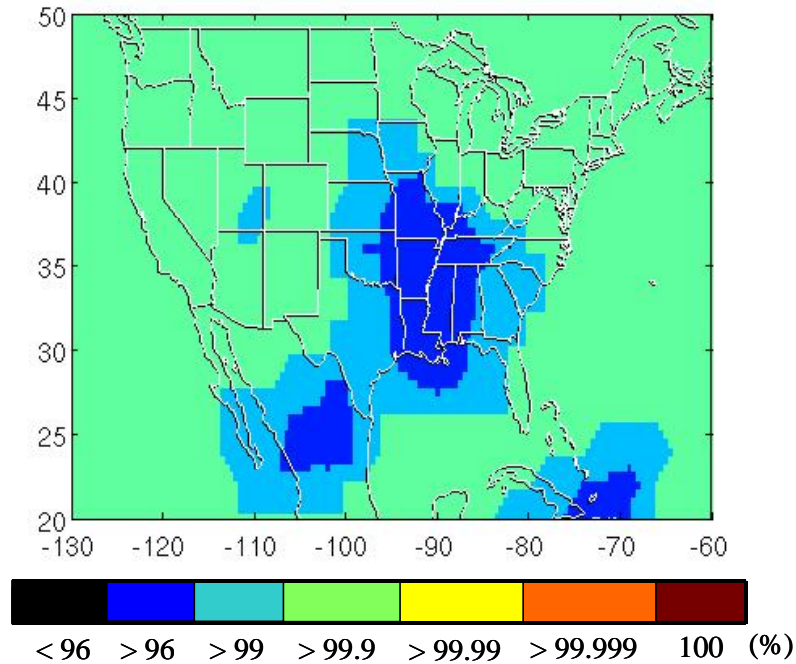


Figure 8.3: Availability of DFree-Based LAAS

8.1.4 Enhanced System: Hybrid Dual-Frequency LAAS

A drawback of DFree-based LAAS is its potential to lose availability under severe ionosphere anomalies. One partial solution to avoiding this availability loss is using IFree as a “backup” smoothing method. IFree can provide more than 96% availability regardless of the ionosphere spatial-gradient condition. Thus, by executing DFree and IFree in parallel and selecting the proper method in real time depending upon the ionosphere condition, optimal availability can be obtained under both nominal and anomalous conditions. This research introduced a system architecture that implements both DFree and IFree. To utilize this hybrid system in practice, it is important to determine under what condition the system should change the smoothing filter between DFree and IFree. This research showed that the optimal switching strategy is the one in which the system evaluates VPL_{DFree} and VPL_{IFree} in parallel and selects the method with the smaller VPL.

8.2 Suggestions for Future Work

Demand for all-weather navigation aids for aircraft precision approach and landing is widespread. It is almost certain that the use of satellite-based positioning systems like LAAS will be the central concept for such navigation systems. Currently, satellite-based positioning systems are under development in several countries such as Russia, China, Japan, and European Union (EU) [Misra(Chapters 1 and 3), Kogure, Bartenev, Grohe]. These systems along with the existing GPS are generally called Global Navigation Satellite Systems (GNSS). Among these GNSS systems, the European Galileo system is designed to be both independent and interoperable with GPS [Misra(Chapter 3), Julien, Hein06a] and will hopefully be a reliable partner of GPS. The interoperability strategy includes the signal design strategy, in which specific ranging signals to be broadcast by Galileo are allocated in the same frequency bands as GPS. In particular, the Galileo L1 and E5a signals have the same center frequencies and similar band-widths as the GPS L1 and L5 signals, respectively. Due to the expected interoperability of GPS and Galileo, the methods introduced in this dissertation are basically applicable for the use of Galileo. This section provides suggestions to expand the work of this dissertation to general GNSS-based aircraft landing systems.

8.2.1 Research on Ionosphere Anomalies

The VPL_{iono} equation in Chapter 6 includes a parameter corresponding to the maximum ionosphere spatial gradient in the ionosphere threat model, which means that the integrity of DFree-based LAAS depends upon the reliability of this threat model. As described in Chapter 3, the threat model used in this research is the result of tremendous efforts devoted to analyzing ionosphere anomalies observed over CONUS, and this model is now being used to certify LAAS in support of CAT I operations. However, this does not mean that the model will never change. In several years (around 2011), the next solar maximum period will come. There is at least an outside chance that severe ionosphere anomalies not bounded by the current threat model will occur. In such a case, the threat model should be modified, and if that happened, the appropriate parameter in

the VPL_{iono} equation should be modified. Hence, careful observations of ionosphere behavior must be continued.

When developing LAAS-like systems (known as Ground Based Augmentation Systems, or GBAS) in regions other than CONUS, the regionally-dependent of ionosphere behavior should be considered. Ionosphere behavior is much more irregular in regions near the geomagnetic equator compared to mid-latitude regions such as CONUS [Walter, Dehel]. The threat model for equatorial regions, hence, could be more severe than the one used in this research. Therefore, it is important to investigate ionosphere behavior over non-CONUS regions before deploying GBAS systems. In fact, in several other countries affected by equatorial ionosphere, such as Japan and Brazil, anomalous ionosphere behavior is an active research area [Sakai, Yoshihara, Saito, Konno05, Rajagopal, Komjathy02].

Another issue associated with ionosphere anomalies that affects the methods proposed in this dissertation is the prior probability of ionosphere anomalies. The VPL_{iono} equation directly depends upon this probability (see Section 6.4). I selected the value of 10^{-5} per approach referencing [Pullen06]. In fact, to set this value, I added extra conservatism to the value proposed in [Pullen06], which is 10^{-6} per approach, because I thought that the value of 10^{-6} was estimated based on limited observations of ionosphere anomalies and that it would be reasonable to add extra margin to it, considering the stringent CAT IIIB integrity requirement. However, if further research verifies the prior probability of 10^{-5} per approach or proposes a lower probability, this margin can be removed, making the resulting VPL_{iono} smaller. Consequently, better availability would be obtained by DFree-based GBAS.

8.2.2 Effects of Adding Extra Satellites

A major benefit of using Galileo in addition to GPS is obtaining ranging signals from additional satellites. With regard to the DFree-based architecture, the low availability in the southeast region of CONUS is caused by poor satellite geometries compared with other regions (see Section 6.5). Under these circumstances, improving satellite

geometry is fundamental to improving availability. Hence, it would be interesting to evaluate availability using the combined GPS and Galileo constellations while keeping all the other methods the same. There, however, is a caveat to applying a better constellation to the DFree-based architecture. When deriving the VPL_{iono} equation, this research defined the worst-case condition for the ionosphere monitoring algorithm by neglecting the situation where an ionosphere wave front affects signals from more than two satellites in view without being detected by the monitor (see Section 6.3). However, if a significant number of extra satellites are added in view, the likelihood of situations where the monitor fails to detect a front affecting more than two satellites could be non-negligible. Hence, further work would be needed to verify (or alter) the worst-case condition when applying an improved constellation to DFree-based GBAS.

The IFree-based architecture should be considered as another option for the GPS-plus-Galileo constellation. As demonstrated in Section 5.3, IFree-based LAAS achieves acceptable availability with a 30-GPS-satellite constellation. Because the GPS-plus-Galileo constellation will include a total of 50 satellites or more (Galileo system is planned to have 30 “primary” satellites), the IFree-based architecture will most probably achieve good availability with this constellation. If sufficient availability is obtained, this architecture will be the best option for CAT IIb GBAS, because the ionosphere-spatial-gradient problem—the biggest problem for GBAS—is completely solved. Thus, availability assessment for the IFree-based architecture using the GPS-plus-Galileo constellation (and other future GNSS constellations) is an important research topic.

8.3 Summary

This research has examined in detail two types of dual-frequency carrier-smoothing techniques, putting them at the center of the ionosphere integrity methodology for CAT IIb LAAS. Simulation results indicate that these techniques have the potential to serve as the primary carrier-smoothing filters for future GBAS landing systems and are productive avenues for further research. I hope this research acts as a springboard for

new research on more generic aircraft landing systems using additional satellite-based positioning systems—going beyond GPS to the future GNSS.

APPENDIX A

Continuous Approximation of Smoothing Filter

As described in Section 2.2, the low-pass filter within the carrier-smoothing filter is implemented as follows.

$$\hat{\chi}[t + \Delta T] = \frac{\tau - \Delta T}{\tau} \hat{\chi}[t] + \frac{\Delta T}{\tau} \chi[t + \Delta T] \quad (\text{A-1})$$

where χ is the Code-Minus-Carrier (CMC) parameter; $\hat{\chi}$ is the smoothed CMC; ΔT is the sampling period of the signal, which is set to 0.5 seconds in LAAS; and τ is the time constant, which is set to 100 seconds in LAAS. Manipulating equation (A-1) yields the following.

$$\frac{\hat{\chi}[t + \Delta T] - \hat{\chi}[t]}{\Delta T} + \frac{\hat{\chi}[t]}{\tau} = \frac{\chi[t]}{\tau} \quad (\text{A-2})$$

If the time constant is significantly larger than the sampling period ($\Delta T \ll \tau$), the following approximation is appropriate.

$$\lim_{\Delta T \rightarrow 0} \left[\frac{\hat{\chi}[t + \Delta T] - \hat{\chi}[t]}{\Delta T} + \frac{\hat{\chi}[t]}{\tau} \right] = \lim_{\Delta T \rightarrow 0} \left[\frac{\chi[t]}{\tau} \right] \quad (\text{A-3})$$

$$\dot{\hat{\chi}}(t) + \frac{1}{\tau} \hat{\chi}(t) = \frac{1}{\tau} \chi(t)$$

Taking the Laplace transform of equation (A-3), the transfer function of the low-pass filter is obtained.

$$s\hat{\chi}(s) + \frac{1}{\tau} \hat{\chi}(s) = \frac{1}{\tau} \chi(s) \quad (\text{A-4})$$

$$\hat{\chi}(s) = \frac{1}{\tau s + 1} \chi(s)$$

APPENDIX B

Method to Compute B-values

Assuming only one LAAS ground system reference receiver fails at a time, for a given satellite, the best estimate of the impact of the hypothetical failure on the pseudorange correction is the difference between the average of the corrections for the satellite over all receivers and the average of the corrections excluding the hypothetical faulted receiver. If a receiver actually fails, the corresponding estimate would be large. However, in this logic, the receiver clock bias becomes a problem. Corrections from different receivers involve different clock biases, and the error due to receiver failure is not distinguishable from the differences of these clock biases. Therefore, before taking averages across receivers, these biases must be eliminated.

Suppose that there are M operating and healthy reference receivers and that there are N satellites in view that are observed by all of these receivers. Let e_j^i denote the correction for satellite i computed by receiver j . As noted above, all corrections generated by a given receiver include the clock bias of that receiver. One method for mitigating this bias is to remove an estimate of the bias. This estimate is computed by taking the average of corrections over the N commonly-observed satellites for the given receiver. Hence, the correction for satellite i by receiver j (\tilde{e}_j^i) after removing the clock bias estimate is given as:

$$\tilde{e}_j^i = e_j^i - \frac{1}{N} \sum_{n=1}^N e_j^n \quad (\text{B-1})$$

Using these “bias-free” corrections, the B-value for satellite i and receiver j ($B_{i,j}$) is computed as follows.

$$B_{i,j} = \frac{1}{M} \sum_{m=1}^M \tilde{e}_m^i - \frac{1}{M-1} \sum_{\substack{m=1, \\ m \neq j}}^M \tilde{e}_m^i \quad (\text{B-2})$$

If all receivers are normally working, B-values represent random measurement noise, namely thermal noise plus multipath errors. If one particular receiver is actually faulted, B-values associated with this receiver would represent measurement biases induced by this failure and would be larger than the nominal values.

APPENDIX C

Verification of Undetectable Conditions

This appendix investigates actual satellite geometries over three randomly selected airports to verify if the undetectable conditions of the ionosphere monitoring algorithm introduced in Section 6.3 can be realized in practice.

C.1 Undetectable Condition for Two Satellites

Suppose that signals from satellites i and j are affected by an ionosphere wave front. There are four ionosphere pierce points (IPPs) associated with this event: two IPPs for the user and two IPPs for the ground station. Let us use IPP_{air}^i , IPP_{air}^j , IPP_{gnd}^i , and IPP_{gnd}^j to distinguish these four IPPs, where the superscript specifies the satellite, and the subscript specifies airborne IPP or ground IPP. The undetectable condition for the two-satellite case consists of the following two sub-conditions.

- (1) Both IPP_{air}^i and IPP_{air}^j are moving with the ionosphere wave front.
- (2) Both IPP_{air}^i and IPP_{air}^j are within 5 km of the leading edge of the front. Here, 5 km corresponds to the assumed separation between the user and the ground station at the decision point.

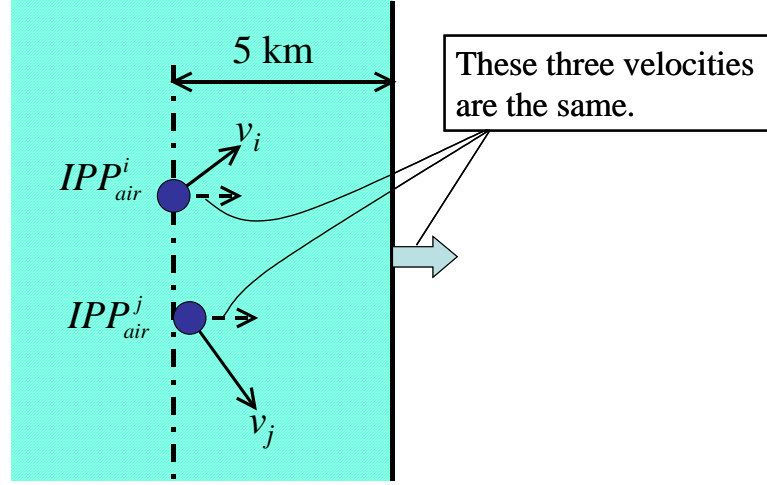


Figure C.1: Undetectable Condition for Two Satellites

Figure C.1 illustrates an IPP pair that satisfies these sub-conditions. Because of sub-condition (1), the airborne monitor cannot detect the front. In addition, sub-condition (2) dictates that the front does not affect the ground IPPs (IPP_{gnd}^i and IPP_{gnd}^j) before the user passes over the decision point, preventing the ground monitor from detecting the front during the landing operation. Note that this condition is for cases where an ionosphere front first affects airborne signals, then later affects the associated ground signals. Although this appendix discusses only these cases, a similar discussion is applicable for cases where a front affects ground signals first and then affects airborne signals.

In regard to sub-condition (1), given any two IPPs, one can always find an ionosphere front that moves with these IPPs. Let v_i and v_j be the velocities of arbitrary two IPPs, and let $v_{i,j}$ be the velocity of the front that moves with these IPPs. The velocity $v_{i,j}$ can be obtained by solving the following four equations.

$$e_{i,j} \in \text{span}(v_i, v_j) \quad (\text{C-1})$$

$$\langle e_{i,j} \cdot (v_i - v_j) \rangle = 0 \quad (\text{C-2})$$

$$\langle e_{i,j} \cdot v_i \rangle \geq 0 \quad (\text{C-3})$$

$$v_{i,j} = \langle e_{i,j} \cdot v_i \rangle e_{i,j} \quad (\text{C-4})$$

where $e_{i,j}$ is the unit vector of $v_{i,j}$. Equations (C-1) and (C-2) dictate the direction of $v_{i,j}$, and equation (C-3) gives the sign of it. Equation (C-4) determines the length of the vector. Figure C.2 provides a diagram of the relationships among v_i , v_j , and $v_{i,j}$. Note that, in the equations above, the velocities are given in Cartesian coordinates. Actual movements of ionosphere fronts on a large scale may be modeled more precisely in spherical coordinates. However, equations (C-1) to (C-4) are accurate enough for the purpose of this investigation while avoiding undue complexity.

As discussed above, an ionosphere front that satisfies sub-condition (1) can be found for any IPP pairs. The problem is sub-condition (2). In order to verify if there are IPP pairs that can be affected by a front satisfying both sub-conditions, I investigated actual satellite geometries over three airports: Memphis International Airport, Los Angeles International Airport, and John F. Kennedy International Airport (New York).

Simulation Procedure

Satellite geometries were generated for each 10-minute time step over 24 hours using the

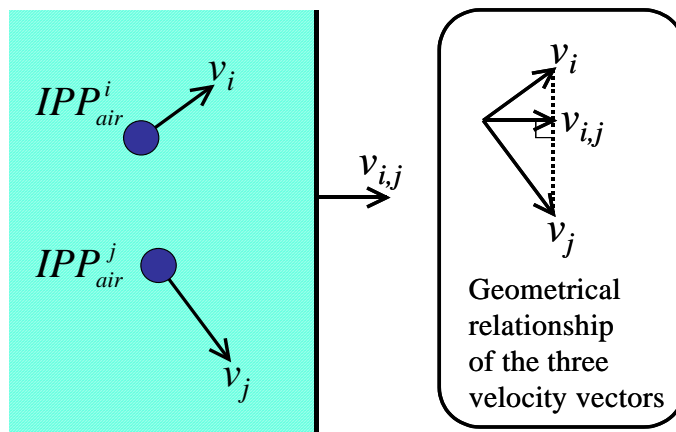


Figure C.2: Velocity of an Ionosphere Wave Front That Moves with Two IPPs

standard 24-satellite constellation [Dod] for these three airports. Thus, there are 144 sample geometries for each airport. For each geometry, the following process was conducted.

- (1) Select an arbitrary IPP pair from the geometry and compute the velocity of the front that moves with these two IPPs using equations (C-1) to (C-4).
- (2) Place the leading edge of a hypothetical ionosphere front that moves with the velocity obtained in (1) on one of these IPPs and measure the distance (d) from this edge to the other IPP. Figure C.3 illustrates this step.
- (3) Perform steps (1) and (2) for all IPP pairs in the geometry.

IPP pairs whose values of d are less than 5 km have the potential to be affected by a front that satisfies the undetectable condition.

Investigation Result

Overall, 48 IPP pairs with d values less than 5 km were found in geometries at the three airports examined. Figure C.4 depicts d values for Memphis, where the x axis represents the epoch index (there are 144 epochs), and the y axis indicates the value of d in kilometers. For each epoch, there are multiple data points whose number corresponds to

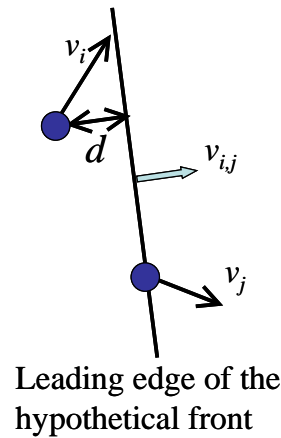


Figure C.3: Schematic of Process (2) (Computing d)

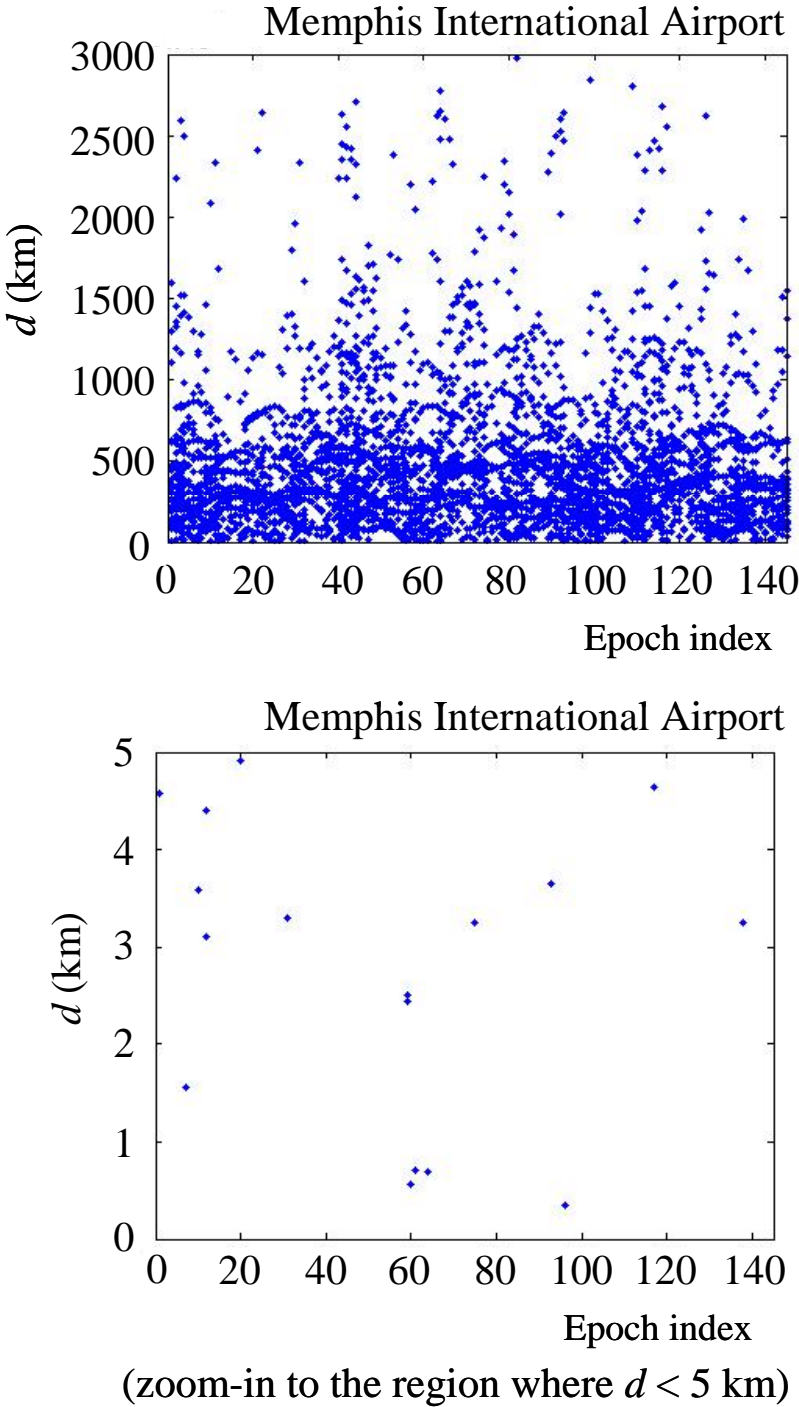


Figure C.4: Investigation Result for Memphis

the number of independent IPP pairs in the given geometry. It is clear that there are many IPP pairs that have d values less than 5 km. Table C-1 summarizes the number of such IPP pairs for each airport. As shown in this table, vulnerable IPP pairs are found in similar numbers at these three airports.

The discovery of vulnerable IPP pairs in actual satellite geometries suggests that the probability of the undetectable ionosphere anomaly condition for the two-satellite-impacted case should not be neglected.

C.2 Undetectable Condition for Three Satellites

Suppose that signals from three satellites (i, j , and k) are affected by an ionosphere wave front. Using the same notation for an IPP as used in the previous section, the undetectable condition for the three-satellite case is given as follows.

- (1) All three of IPP_{air}^i , IPP_{air}^j , and IPP_{air}^k are moving with the ionosphere wave front.
- (2) All three IPPs are within 5 km of the leading edge of the front.

Figure C.5 illustrates an IPP triplet that satisfies these sub-conditions. Again, this undetectable condition is for the situation where a front first affects airborne signals, then later affects the associated ground signals. The undetectable condition for the opposite case can be defined in a similar manner.

Table C-1: Summary of Investigation Results

Airport	Number of IPP pairs that have d values less than 5 km
Memphis International Airport	17
JFK International Airport (New York)	14
Los Angeles International Airport	17

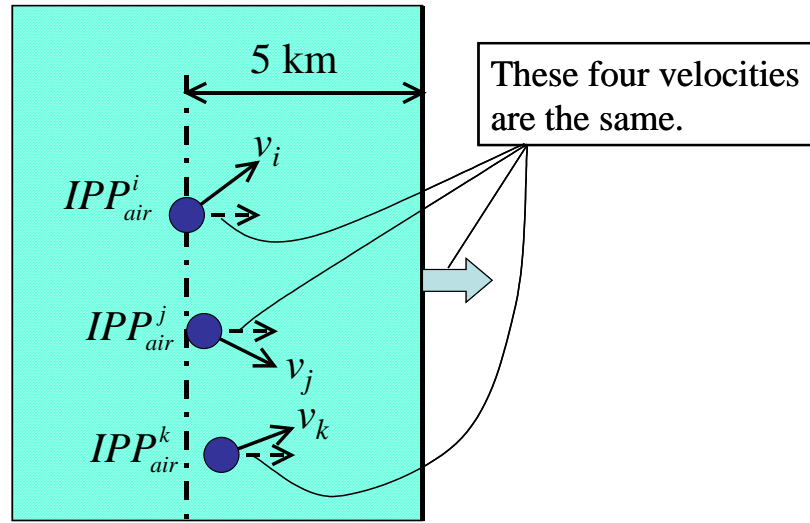


Figure C.5: Undetectable Condition for Three Satellites

Unlike the two-satellite case, an ionosphere wave front that satisfies sub-condition (1) does not always exist for any IPP triplet. Thus, the likelihood of this condition being satisfied is smaller than that for the two-satellite case. I again investigated actual satellite geometries for the same three airports in order to determine if there are IPP triplets that suffer from this undetectable condition.

Simulation Procedure

As with the two-satellite case, satellite geometries were generated at 10-minute time intervals over 24 hours using the standard 24-satellite constellation [Dod] for the three airports listed above. For each geometry, the following process was conducted.

- (1) Pick an arbitrary IPP triplet (i, j and k).
- (2) From these IPPs, select an arbitrary IPP pair, say i and j , and compute the velocity of the ionosphere front that moves with these two IPPs using equations (C-1) to (C-4). Call this velocity $v_{i,j}$. This step is illustrated in Figure C.6.

- (3) Compute the absolute difference between the front velocity from step (2) ($v_{i,j}$) and the velocity of the remaining IPP (v_k). Call this difference dv . This step is shown in Figure C.6.
- (4) Place the leading edge of a hypothetical ionosphere front having velocity $v_{i,j}$ on one of the IPPs such that all IPPs are located on one side of the leading edge, then compute the maximum distance between this edge and the three IPPs. Call this distance d_{max} . This step is also shown in Figure C.6.
- (5) Perform steps (2) to (4) for all three IPP pairs in the selected triplet.
- (6) Perform steps (1) to (5) for all IPP triplets in the satellite geometry in question.

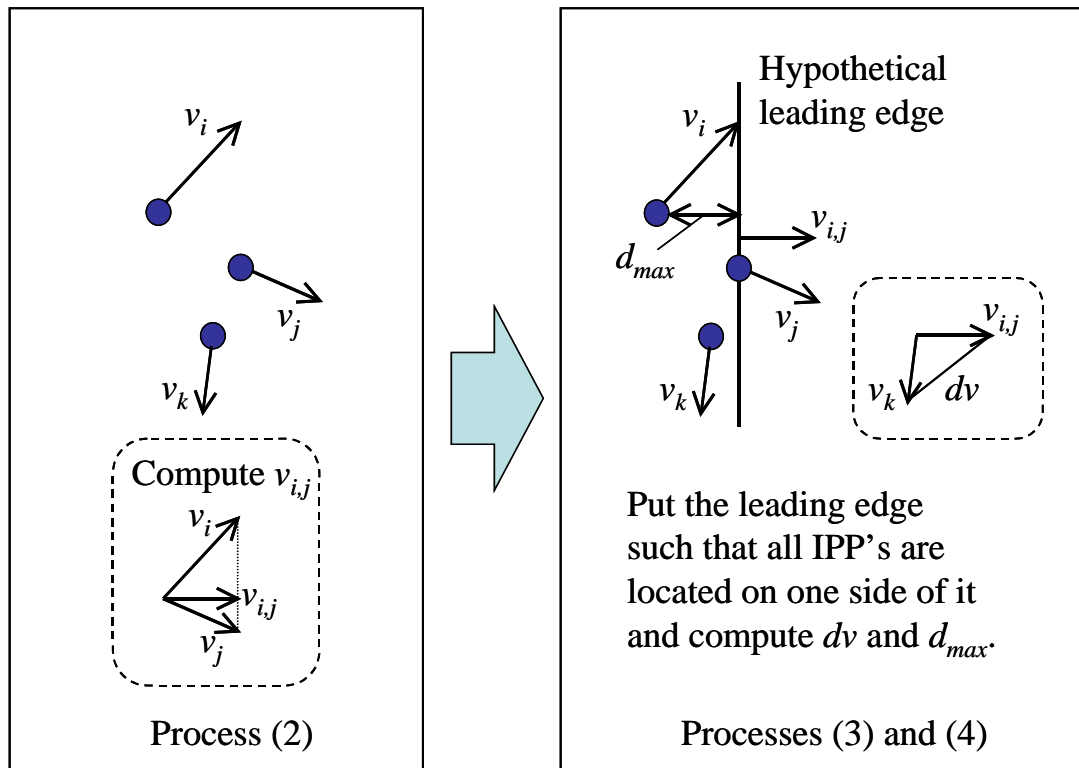


Figure C.6: Schematic of Process Steps (2) through (4) (Computing $v_{i,j}$, dv , and d_{max})

If dv is small enough, say less than 30 m/sec, the wave front that moves with $v_{i,j}$ can be considered to move with the corresponding three IPPs. If d_{max} for these three IPPs is also less than 5 km, they have the potential to be affected by an undetectable wave front.

Investigation Result

Figure C.7 shows scatter plots of d_{max} and dv for the data points corresponding to Memphis International Airport. The top figure includes all data points, and the bottom figure shows only the region with dv less than 100 m/sec and d_{max} less than 35 km. Figure C.8 shows the same type of scatter plots for John F. Kennedy International Airport (New York) and Los Angeles International Airport within the region with dv less than 100 m/sec and d_{max} less than 35 km. As these figures show, no data point that satisfies both dv less than 30 m/sec and d_{max} less than 5 km was found among the investigated geometries. This result indicates that, at least for the three airports included in the simulations, there is no three-satellite combination which could suffer from an undetectable ionosphere wave front.

Note that undetectable conditions for more than three satellites cannot occur for these airports because satisfying the three-satellite undetectable condition is a necessary condition for any more-than-three-satellite undetectable conditions.

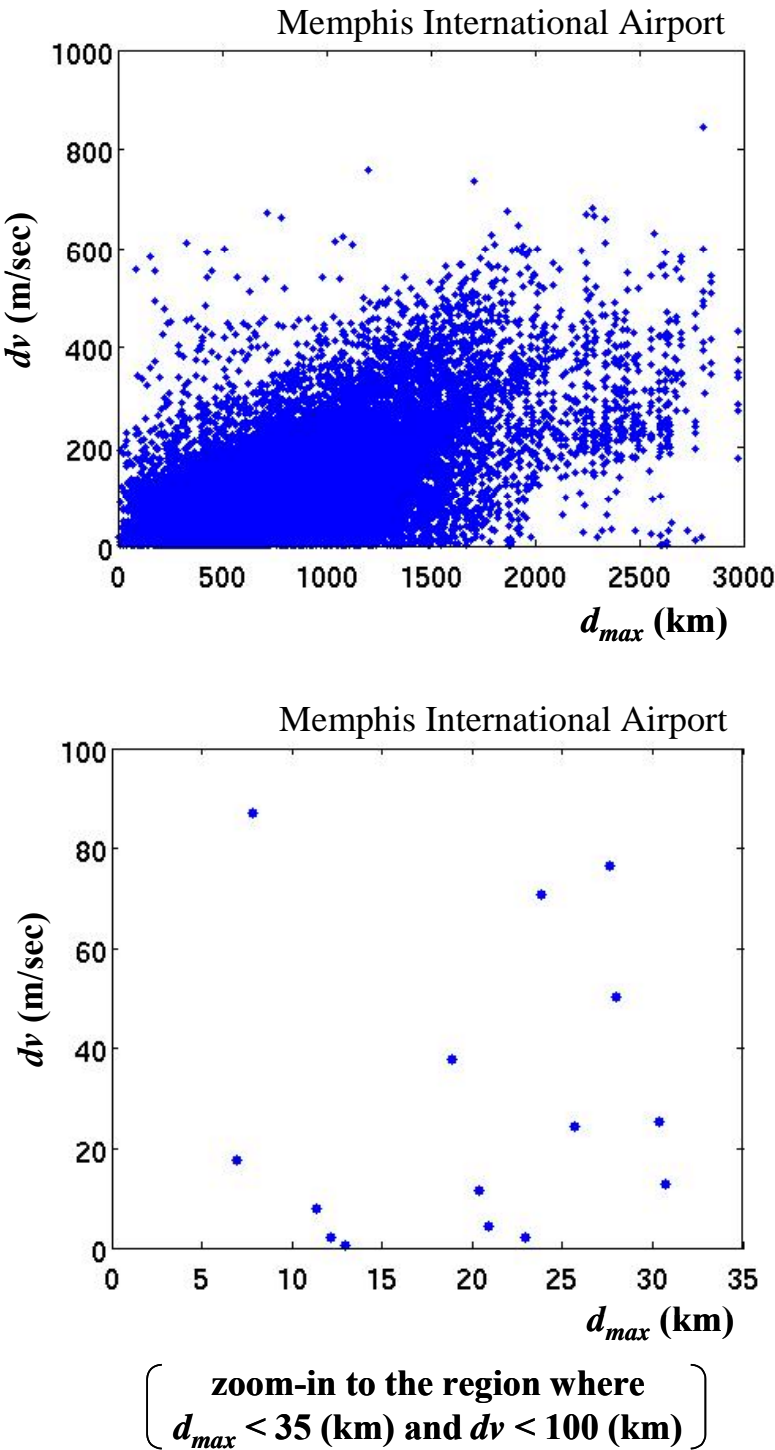


Figure C.7: Investigation Result for Memphis

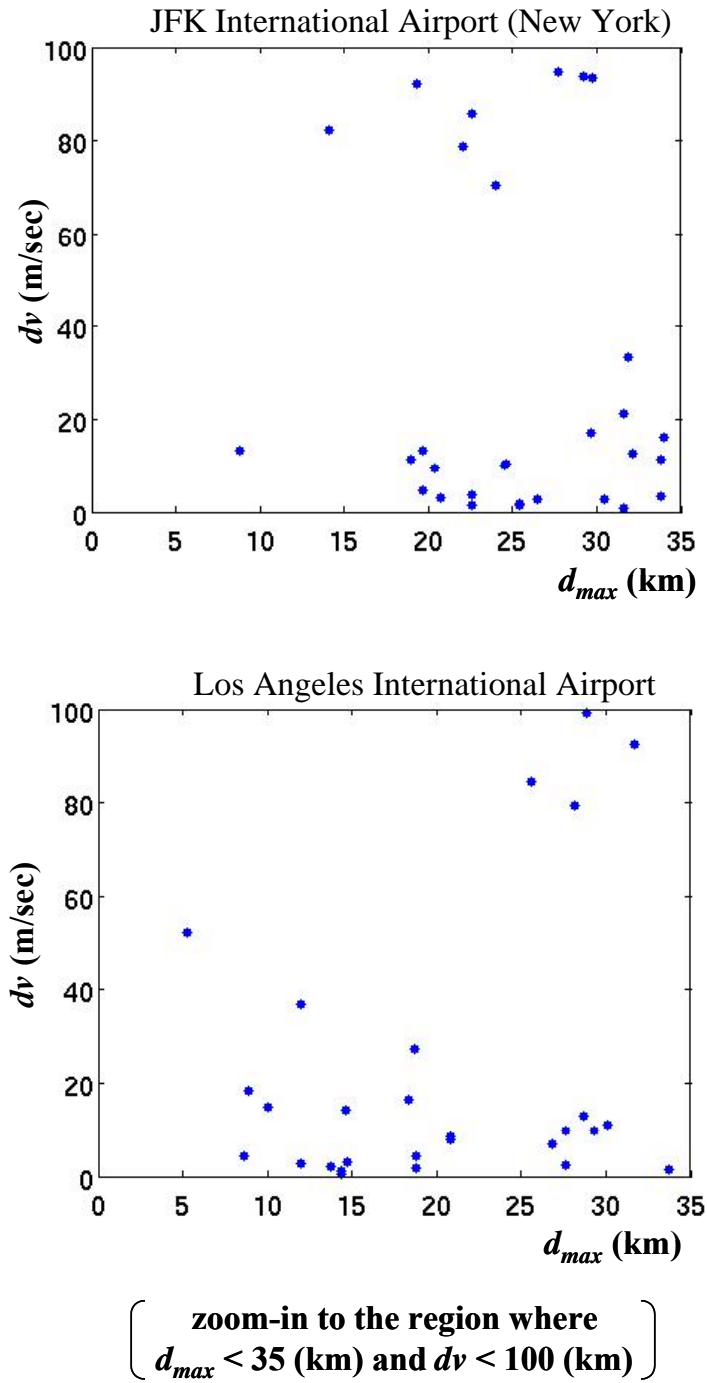


Figure C.8: Investigation Results for JFK International Airport and Los Angeles International Airport

BIBLIOGRAPHY

[Bartenev] V. Bartenev, V. Kosenko, and V. Chebotarev, “Russian GLONASS at the Stage of Active Implementation,” *Inside GNSS*, Vol. 1, No. 3, April, 2006.

[Datta-Barua02] S. Datta-Barua, T. Walter, *et al.*, “Using WAAS Ionospheric Data to Estimate LAAS Short Baseline Gradients,” *Proceedings of ION National Technical Meeting 2002*, Anaheim, CA, January 28 – 30, 2002.

[Datta-Barua05] S. Datta-Barua, T. Walter, *et al.*, “Verification of Low Latitude Ionosphere Effects on WAAS During October 2003 Geomagnetic Storm,” *Proceedings of ION 2005 Annual Meeting*, Cambridge, MA., June 27 – 29, 2005.

[Datta-Barua06] S. Datta-Barua, T. Walter, *et al.*, “Bounding Higher Order Ionosphere Errors for the Dual Frequency GPS User,” *Proceedings of ION GNSS 2006*, Fort Worth, TX, September 26 – 29, 2006.

[Dehel] T. Dehel, F. Lorge, *et al.*, “Satellite Navigation vs. the Ionosphere: Where Are We, and Where Are We Going?,” *Proceedings of ION GNSS 2004*, Long Beach, CA, September 21 – 24, 2004.

[Dod] *Global Positioning System Standard Positioning Service Performance Standard*. Washington, D.C., U.S. Department of Defense, October 2001.

[Ene] A. Ene, D. Qiu, *et al.*, “A Comprehensive Ionosphere Storm Data Analysis Method to Support LAAS Threat Model Development,” *Proceedings of ION National Technical Meeting 2005*, San Diego, CA, January 24 – 26, 2005.

[Enge96] P. Enge, T. Walter, *et al.*, “Wide Area Augmentation of the Global Positioning System,” *Proceedings of the IEEE*, Vol. 84, No. 8, August, 1996.

[Enge99] P. Enge, “Local Area Augmentation of GPS for the Precision Approach of Aircraft,” *Proceedings of the IEEE*, Vol. 87, No. 1, January, 1999.

[Enge03] P. Enge, “GPS Modernization: Capabilities of the New Civil Signals,” presented at Australian International Aerospace Congress, Brisbane, Australia, July 29 – August 1, 2003.

[FAAwebsite] <http://www.faa.gov>

[Gratton05] L. Gratton and B. Pervan, “Airborne and Ground Monitors for Ionospheric Front Detection for the Local Area Augmentation System Using Carrier Phase Measurements,” *Proceedings of ION GNSS 2005*, Long Beach, CA, September 13 – 16, 2005.

[Gratton06] L. Gratton and B. Pervan, “Carrier Phase Airborne and Ground Monitors for Ionospheric Front Detection for Category III LAAS,” *Proceedings of ION GNSS 2006*, Fort Worth, TX, September 26 – 29, 2006.

[Grohe] R. Grohe and J. Tjaden, “Galileo: Status and Way Forward,” *Proceedings of ION GPS/GNSS 2003*, Portland, OR, September 9 – 12, 2003.

[Hansen] A. Hansen, “Tomographic Estimation of the Ionosphere Using Terrestrial GPS Sensors,” *Ph.D. Dissertation*, Electrical Engineering, Stanford University, 2002.

[Hatch] R. Hatch, "The Synergism of GPS Code and Carrier Measurements," *Proceedings of 3rd International Symposium on Satellite Doppler Positioning*, Las Cruces, NM, February, 1982.

[Hein06a] G. Hein and J. Avila-Rodriguez, "Combining Galileo PRS and GPS M-Code," *Inside GNSS*, Vol. 1, No. 1, January/February, 2006.

[Hein06b] G. Hein, J. Betz, *et al.*, "MBOC: The New Optimized Spreading Modulation Recommended for Galileo L1 OS and GPS L1C," *Inside GNSS*, Vol. 1, No. 4, May/June, 2006.

[Hwang] P. Hwang, G. McGraw, and J. Bader, "Enhanced Differential GPS Carrier-Smoothed Code Processing Using Dual-Frequency Measurements," *Navigation*, Vol. 46, No. 2, Summer 1999.

[Icao] *Standards and Recommended Practices: Annex 10 – Aeronautical Telecommunications. Vol. I (Radio Navigation Aids)*. Montreal Canada, International Civil Aviation Organization (ICAO), 6th Edition, July 2006.

[Julien] O. Julien and C. Macabiau, "What are the major differences between Galileo and GPS current and forthcoming frequencies?" *Inside GNSS*, Vol. 1, No. 4, May/June, 2006.

[Kaplan] E. Kaplan and C. Hegarty, "Understanding GPS Principles and Applications," Artech House, 2nd Edition, 2006.

[Keegan] R. Keegan, "P-Code-Aided Global Positioning System Receiver," U.S. Patent 4972431, November 20, 1990.

[Klobuchar] J. Klobuchar, "Ionospheric Effects on GPS," *Global Positioning System: Theory and Applications*, Vol. I, Edited by B. Parkinson and J. Spilker, AIAA Publication, 1996.

[Kogure] S. Kogure, M. Sawabe, and M. Kishimoto, "Status of QZSS Navigation System in Japan," *Proceedings of ION GNSS 2006*, Fort Worth, TX, September 26 – 29, 2006.

[Komjathy02] A. Komjathy, L. Sparks, et al., "An Assessment of the Current WAAS Ionospheric Correction Algorithm in the South American Region," *Proceedings of ION GPS meeting 2002*, Portland, OR, September 24 – 27, 2002.

[Komjathy04] A. Komjathy, L. Sparks, et al., "The Ionospheric Impact of the October 2003 Storm Event on WAAS," *Proceedings of ION GPS 2004*, Long Beach, CA., September 21 – 24, 2004.

[Konno05] H. Konno, S. Pullen, et al., "Analysis of Ionosphere Gradient Using Japan GEONET Data," *Proceedings of ION National Technical Meeting 2005*, San Diego, CA, January 24 – 26, 2005.

[Konno06] H. Konno, S. Pullen, et al., "Ionosphere Monitoring Methodology for Hybrid Dual-Frequency LAAS," *Proceedings of ION GNSS 2006*, Fort Worth, TX, September 26 – 29, 2006.

[Lawrence] D. Lawrence, S. Cobb, and P. Montgomery, "Method for Processing in Dual Frequency Civilian GPS Receiver," U.S. Patent 5293170, August 31, 2004.

[Lee05] J. Lee, "GPS-Based Aircraft Landing Systems with Enhanced Performance: Beyond Accuracy," *Ph.D. Dissertation*, Aeronautics and Astronautics, Stanford University, 2005.

[Lee06a] J. Lee, S. Pullen, et al., "Assessment of Nominal Ionosphere Spatial Decorrelation for LAAS," *Proceedings of the IEEE/ION position location and navigation symposium 2006*, San Diego, CA, April, 2006.

[Lee06b] J. Lee, M. Luo, *et al.*, “Position-Domain Geometry Screening to Maximize LAAS Availability in the Presence of Ionosphere Anomalies,” *Proceedings of ION GNSS 2006*, Fort Worth, TX, September 26 – 29, 2006.

[Lennen] G. Lennen, “Method and Apparatus for Improved L2 Performance in Dual Frequency Semi-Codeless,” U.S. Patent 6954488, October 11, 2005.

[Luo02] M. Luo, S. Pullen, *et al.*, “Assessment of Ionospheric Impact on LAAS Using WAAS Supertruth Data,” *Proceedings of The ION 58th Annual Meeting*, Albuquerque, NM, June 24 – 26, 2002.

[Luo03] M. Luo, S. Pullen, *et al.*, “LAAS Ionosphere Spatial Gradient Threat Model and Impact of LGF and Airborne Monitoring,” *Proceedings of ION GPS/GNSS 2003*, Portland, OR, September 9 – 12, 2003.

[Luo04] M. Luo, S. Pullen, *et al.*, “Ionosphere Threat to LAAS: Updated Model, User Impact, and Mitigations,” *Proceedings of ION GNSS 2004*, Long Beach, CA, September 21 – 24, 2004.

[Luo05] M. Luo, S. Pullen, *et al.*, “LAAS Study of Slow-Moving Ionosphere Anomalies and Their Potential Impacts,” *Proceedings of ION GNSS 2005*, Long Beach, CA, September 13 – 16, 2005.

[Massatt] P. Massatt and M. Zeitzew, “The GPS Constellation Design – Current and Projected,” *Proceedings of ION National Technical Meeting 1998*, January 21 – 23, 1998.

[McGraw00] G. McGraw, T. Murphy, *et al.*, “Development of the LAAS Accuracy Models,” *Proceedings of ION GPS 2000*, Salt Lake City, UT, September 19 – 22, 2000.

[McGraw05] G. McGraw and P. Young, “Dual-Frequency Smoothing DGPS Performance Evaluation Studies,” *Proceedings of ION National Technical Meeting 2005*, San Diego, CA, January 24 – 26, 2005.

[Misra] P. Misra and P. Enge, “Global Positioning System: Signals, Measurements, and Performance,” Ganga-Jamuna Press, 2nd Edition, 2006.

[Mitelman] A. Mitelman, “Signal Quality Monitoring for GPS Augmentation Systems,” *Ph.D. Dissertation*, Electrical Engineering, Stanford University, 2004.

[Murphy05] T. Murphy and M. Harris, “More Results from the Investigation of Airborne Multipath Errors,” *Proceedings of ION GNSS 2005*, Long Beach, CA, September 13 – 16, 2005.

[Murphy06] T. Murphy and M. Harris, “Mitigation of Ionospheric Gradient Threats for GBAS to Support CAT II/III,” *Proceedings of ION GNSS 2006*, Fort Worth, TX, September 26 – 29, 2006.

[Parkinson] B. Parkinson, “Introduction and Heritage of NAVSTAR, the Global Positioning System,” *Global Positioning System: Theory and Applications*, Vol. I, Edited by B. Parkinson and J. Spilker, AIAA Publication, 1996.

[Pervan96] B. Pervan, “Navigation Integrity for Aircraft Precision Landing Using the Global Positioning System,” *Ph.D. Dissertation*, Aeronautics and Astronautics, Stanford University, 1996.

[Pervan05] B. Pervan and L. Gratton, “Orbit Ephemeris Monitors for Local Area Differential GPS,” *IEEE Transactions on Aerospace and Electronic Systems*, Vol. 41, No. 2, April, 2005.

[Phelts] E. Phelts, D. Akos, and P. Enge, “Robust Signal Quality Monitoring and Detection of Evil Waveforms,” *Proceedings of ION GPS 2000*, Salt Lake City, UT, September 19 – 22, 2000.

[Pullen01] S. Pullen, J. Lee, et al., “Ephemeris Protection Level Equations and Monitor Algorithms for GBAS,” *Proceedings of ION GPS 2001*, Salt Lake City, UT, September 11 – 14, 2001.

[Pullen02] S. Pullen, M. Luo, *et al.*, “LAAS Ground Facility Design Improvements to Meet Proposed Requirements for Category II/III Operations,” *Proceedings of ION GPS meeting 2002*, Portland, OR, September 24 – 27, 2002.

[Pullen04] S. Pullen and P. Enge, “A Civil User Perspective on Near-Term and Long-Term GPS Modernization,” *Proceedings of Japan GPS/GNSS symposium 2004*, Tokyo, Japan, November 17 – 19, 2004.

[Pullen06] S. Pullen, J. Rife, and P. Enge, “Prior Probability Model Development to Support System Safety Verification in the Presence of Anomalies,” *Proceedings of the IEEE/ION position location and navigation symposium 2006*, San Diego, CA, April, 2006.

[Rajagopal] S. Rajagopal, T. Walter, *et al.*, “Correlation Structure of the Equatorial Ionosphere,” *Proceedings of ION National Technical Meeting 2004*, San Diego, CA, January 26 – 28, 2004.

[Rife04] J. Rife, T. Walter, J. Blanch, “Overbounding SBAS and GBAS Error Distributions with Excess-Mass Functions,” presented at GNSS 2004, The 2004 International Symposium of GNSS/GPS, Sydney, Australia, December 6 – 8, 2004.

[Rife05] J. Rife, S. Pullen, *et al.*, “Vertical Protection Levels for Local Airport Monitor for WAAS,” *Proceedings of ION 2005 Annual Meeting*, Cambridge, MA., June 27 – 29, 2005.

[Rife06] J. Rife and E. Phelts, “Formulation of a Time-Varying Maximum Allowable Error for Ground-Based Augmentation Systems,” *Proceedings of ION National Technical Meeting 2006*, Monterey, CA, January 18 – 20, 2006.

[Rtca01] *Minimum Operation Performance Standards for GPS/Local Area Augmentation System Airborne Equipment*. Washington, D.C., RTCA, DO-253A, November 28, 2001.

[Rtca04] *Minimum Aviation System Performance Standards for Local Area Augmentation System (LAAS)*. Washington, D.C., RTCA SC-159, WG-4A, DO-245A, December 9, 2004.

[Saito] A. Saito, Y. Otsuka, et al., “Ionospheric Variations at Midlatitude Detected by a Dense GPS Receiver Array in Japan,” *Proceedings of The ION 61th Annual Meeting*, Cambridge, MA, June 27 – 29, 2005.

[Sakai] T. Sakai, K. Matsunaga, *et al.*, “Modified Ionospheric Correction Algorithms for the SBAS Based on Geometry Monitor Concept,” *Proceedings of ION GNSS 2005*, Long Beach, CA, September 13 – 16, 2005.

[Shallberg] K. Shallberg, P. Shloss, *et al.*, “WAAS Measurement Processing, Reducing the Effects of Multipath,” *Proceedings of ION GPS 2001*, Salt Lake City, UT, September 11 – 14, 2001.

[Shively99] C. Shively, “Derivation of Acceptable Error Limits for Satellite Signal Faults in LAAS,” *Proceeding of ION-GPS 1999*, Nashville, TN, September, 1999.

[Shively04] C. Shively and T. Hsiao, “Availability Enhancements for CAT IIIB LAAS,” *Navigation*, Vol. 51, No. 1, Spring 2004.

[Simili] D. Simili and B. Pervan, “Code-Carrier Divergence Monitoring for GPS Local Area Augmentation System,” *Proceedings of the IEEE/ION position location and navigation symposium 2006*, San Diego, CA, April, 2006.

[Spilker96a] J. Spilker, “GPS Signal Structure and Theoretical Performance,” *Global Positioning System: Theory and Applications*, Vol. I, Edited by B. Parkinson and J. Spilker, AIAA Publication, 1996.

[Spilker96b] J. Spilker, “GPS Navigation Data,” *Global Positioning System: Theory and Applications*, Vol. I, Edited by B. Parkinson and J. Spilker, AIAA Publication, 1996.

[Spilker96c] J. Spilker, "Satellite Constellation and Geometric Dilution," *Global Positioning System: Theory and Applications*, Vol. I, Edited by B. Parkinson and J. Spilker, AIAA Publication, 1996.

[Stansell] T. Stansell, P. Fenton, *et al.*, "BOC or MBOC? The Common GPS/Galileo Civil Signal Design: A Manufacturers Dialog, Part1," *Inside GNSS*, Vol. 1, No. 5, July/August, 2006.

[Stevens] J. Stevens, C. Varner, *et al.*, "LDGPS Performance Assessment Using the JPALS Availability Model," *Proceedings of ION GNSS 2004*, Long Beach, CA, September 21 – 24, 2004.

[Walter] T. Walter, S. Datta-Barua, *et al.*, "The Effects of Large Ionospheric Gradients on Single Frequency Airborne Smoothing Filters for WAAS and LAAS," *Proceedings of ION National Technical Meeting 2004*, San Diego, CA, January 26 – 28, 2004.

[Wilson] B. Wilson, *et al.*, "New and Improved The Broadcast Interfrequency Biases," *GPS World*, September, 1999.

[Xie01] G. Xie, S. Pullen, *et al.*, "Integrity Design and Updated Test Results for the Stanford LAAS Integrity Monitor Testbed," *Proceedings of ION National Technical Meeting 2001*, Albuquerque, NM, June 11 – 13, 2001.

[Xie04] G. Xie, "Optimal On-Airport Monitoring of the Integrity of GPS-Based Landing Systems," *Ph.D. Dissertation*, Electrical Engineering, Stanford University, 2004.

[Yoshihara] T. Yoshihara, T. Sakai, *et al.*, "An Investigation of Local-scale Spatial Gradient of Ionospheric Delay Using the Nation-wide GPS Network Data in Japan," *Proceedings of ION National Technical Meeting 2005*, San Diego, CA, January 24 – 26, 2005.

[Zaugg] T. Zaugg, "A New Evaluation of Maximum Allowable Errors and Missed Detection Probabilities for LAAS Ranging Source Monitors," *Proceedings of The ION 58th Annual Meeting*, Albuquerque, NM, June 24 – 26, 2002.